Quantum fluctuations in cavity BEC systems

Dissertation
zur Erlangung des Doktorgrades
an der Fakultät für Mathematik, Informatik und Naturwissenschaften
Fachbereich Physik
der Universität Hamburg

vorgelegt von
Leon Edward Mixa

Hamburg
2025

Gutachter/innen der Dissertation:	Prof. Dr. Michael Thorwart PD Dr. Axel Pelster
Zusammensetzung der Prüfungskommission:	Prof. Dr. Michael Thorwart PD Dr. Axel Pelster Prof. Dr. Andreas Hemmerich Prof. Dr. Michael Potthoff Prof. Dr. Daniela Pfannkuche
Vorsitzender der Prüfungskommission:	Prof. Dr. Michael Potthoff
Datum der Disputation:	24.09.2025
Vorsitzender des Fach-Promotionsausschusses PHYSIK:	Prof. Dr. Wolfgang J. Parak
Leiter der Fachbereichs PHYSIK:	Prof. Dr. Markus Drescher
Dekan der Fakultät MIN:	Prof. Dr.-Ing. Norbert Ritter

Abstract

This thesis investigates the role of quantum fluctuations in a cavity Bose-Einstein condensate (BEC) system, where a condensate of atoms is placed in an optical resonator. The atoms are quantum two-level systems and their transitions are pumped off-resonance by a retroreflected laser. Due to the Purcell effect, the atoms and the cavity light strongly couple by enhanced Rayleigh scattering and form strongly coupled polaritons. Weak atom-atom interactions in the BEC are modeled by s-wave scattering, resulting in quantum fluctuations in both the atomic and light fields. The system exhibits a rich phase diagram with quantum fluctuations playing a key role. Light leaving the cavity can be detected to analyze the quantum many-body system non-destructively. This setup is well suited for the study of quantum fluctuation phenomena, and we investigate decoherence effects and novel aggregate states of matter.

In the first part, we explore decoherence and its control. Damping effects arise from quantum fluctuations in the weakly interacting condensate and manifest as phonon-like damping in the form of Landau and Beliaev processes. This damping couples to both the atomic and photon modes, with stronger coupling to the photon mode. We derive exotic spectral properties of the dissipative bath, including competition between damping and antidamping channels, and sub-Ohmic signatures associated with non-Markovian dynamics. The bath is tunable via experimental parameters. We study the central polariton system and find that the quantum fluctuation bath renormalizes the light-matter system, shifting the critical point of the non-equilibrium quantum phase transition. Additional signatures of the quantum bath in the observables are uncovered and shown to be tunable by external parameters.

In the second part, we examine the formation of cavity-induced quantum droplets, a novel state of matter formed by the competition between attractive and repulsive interactions. A classification based on effective energy potentials that incorporates important finite-size effects is introduced. We study a generic long-range interaction with a periodic signature and exponential decay and develop a Bogoliubov theory to analyze the quantum corrections. The leading corrections are those from rotons, which depend on the system size, and as such compete with the mean-field, leading to the formation of a quantum droplet.

This formalism is applied to the cavity BEC setup, focusing on the long-range interaction induced by the cavity mode and the pump field. We show that the zero-point energy of a roton mode selected by the light field can induce droplet formation of the newly identified droplet class. Corrections to the infinite-range interaction are critical for droplet formation, and we develop a model that provides an analytical solution for droplet size. We also investigate droplet optimization using typical experimental parameters and offer a thermodynamic interpretation in terms of pressure, compressibility, and chemical potential. Furthermore, finite temperature effects are discussed and a critical temperature for droplet existence is found. Finally, we study how engineering the interaction, its envelope shape, and symmetries, affects droplet formation.

Zusammenfassung

In dieser Arbeit wird die Rolle von Quantenfluktuationen in einem Hohlraum-Bose-Einstein-Kondensat-System (Hohlraum-BEC) untersucht, bei dem ein Kondensat von Atomen in einem optischen Resonator platziert ist. Die Atome sind quantenmechanische Zwei-Niveau-Systeme und ihre Übergänge werden durch einen retroreflektierten Laser fern der Resonanz gepumpt. Aufgrund des Purcell-Effekts koppeln die Atome und das Resonatorlicht durch verstärkte Rayleigh-Streuung stark miteinander und formen stark gekoppelte Polaritons. Schwache Atom-Atom-Wechselwirkungen im BEC werden durch s-Wellenstreuung modelliert, was zu Quantenfluktuationen sowohl im atomaren als auch im Lichtfeld führt. Das System weist ein umfangreiches Phasendiagramm auf, in dem Quantenfluktuationen eine Schlüsselrolle spielen. Licht, das den Resonator verlässt, kann detektiert werden, um das Quanten-Vielteilchensystem nicht-destruktiv zu untersuchen. Dieser Aufbau eignet sich gut für die Untersuchung von Quantenfluktuationsphänomenen, und wir befassen uns mit Dekohärenzeffekten und neuartigen Aggregatzuständen.

Im ersten Abschnitt erforschen wir die Dekohärenz und ihre Kontrolle. Die Dämpfungseffekte entstehen durch Quantenfluktuationen im schwach wechselwirkenden Kondensat, die phononenartige Dämpfung in der Form von Landau- und Beliaev-Prozesse manifestieren. Diese Dämpfung koppelt sowohl an die atomaren als auch an die Photonenmode, wobei die Kopplung an die Photonenmode stärker ist. Wir leiten exotische spektrale Eigenschaften des Dissipationsbades her, einschließlich der Konkurrenz zwischen Dämpfungs- und Antidämpfungskanälen, sowie sub-Ohmsche Signaturen, die mit nicht-Markov'scher Dynamik verbunden sind. Das Dissipationsbad ist über experimentelle Parameter einstellbar. Wir untersuchen das zentrale Polaritonsystem und zeigen, dass das Quantenfluktuationsbad das Licht-Materie-System renormiert und den kritischen Punkt des Nicht-Gleichgewichts-Quantenphasenübergangs verschiebt. Zusätzliche Signaturen des Quantenbads in den Observablen werden aufgedeckt und es wird gezeigt, dass sie durch externe Parameter einstellbar sind.

Im zweiten Abschnitt untersuchen wir die Formation von hohlrauminduzierten Quantentröpfchen, einen neuartigen Zustand der Materie, der durch den Wettbewerb zwischen anziehenden und abstoßenden Wechselwirkungen entsteht. Wir führen eine Klassifizierung ein, die auf effektiven Energiepotentialen basiert und wichtige Effekte endlich großer Systeme berücksichtigt. Es wird eine neue Klasse von Tröpfchen identifiziert. Wir untersuchen eine generische langreichweitige Wechselwirkung mit periodischer Signatur und exponentiellem Zerfall und entwickeln eine Bogoliubov-Theorie zur Analyse der Quantenkorrekturen. Die Korrekturen führender Ordnung sind die von Rotonmoden, die von der Systemgröße abhängen, so mit dem Molekularfeld konkurrieren und zur Bildung eines Quantentröpfchens führen.

Wir wenden diesen Formalismus auf das Hohlraum-BEC-System an und konzentrieren uns dabei auf die langreichweitige Wechselwirkung erzeugt von der Resonatormode und dem Pumpfeld. Wir zeigen, dass die Nullpunktenergie einer durch das Lichtfeld ausgewählten Rotonmode die Bildung von Tröpfchen der neu identifizierten Tröpfchenklasse herbeiführen kann. Korrekturen der unendlich weiten Wechselwirkung sind für die Tröpfchenbildung entscheidend, und wir entwickeln ein Modell, das eine analytische Lösung für die Tröpfchengröße liefert. Wir untersuchen auch die Optimierung von Tröpfchen unter Verwendung typischer experimenteller Parameter und präsentieren eine thermodynamische Interpretation in Bezug auf Druck, Kompressibilität und chemisches Potenzial. Darüber hinaus diskutieren wir die Auswirkungen der endlichen Temperatur und finden eine kritische Temperatur für die Existenz von Tröpfchen. Schließlich untersuchen wir, wie sich die Konstruktion der Wechselwirkung, ihre Hüllenform und Symmetrien auf die Tröpfchenbildung auswirken.

Contents

List of Figures

1 – Introduction

It is common understanding that quantum mechanics is the fundamental framework that governs the microscopic mechanisms of our world [1]. Although it underlies the world in which we live, we cannot experience with our senses anything that adequately resembles the mechanisms at the quantum level. Mathematical tools and their development have allowed us to achieve a description of this realm [2]. In particular, it is the interactions (or measurements) that create the unhinged quantum phenomena far beyond human imagination. Yet even the mathematical description is limited and usually relies on describing an interacting system in an effective picture with the quasi absence of interactions [3]. Physics, including condensed matter physics, relies on effective mathematical descriptions [4], which are models that capture the relevant phenomena in a system while ignoring negligible microscopic details. As Phillip W. Anderson proclaimed: "The ability to reduce everything to simple fundamental laws does not imply the ability to start from those laws and reconstruct the universe." [4]. Nevertheless, similar mathematical effects such as bound states, decay, spontaneous symmetry breaking, and quantum vacuum occur in many interacting quantum systems in diverse areas of physics [5]. From very few-body to many-body physics, similar concepts, approximations, and effective models can be developed and tested. Testing the theories is paramount because once a breaking point is found, it has historically proven to be a great opportunity for new advances [3].

However, real systems can be arduous to handle and manipulate. For example, since the initial discovery of a high-temperature superconductor [6], meaning around 30 Kelvin, nearly 40 years have passed without success in developing one that does so at normal room conditions. Moreover, despite decades of dedicated work by brilliant people, no effective microscopic theory of such unconventional superconductivity has yet been established [7]. If we allow ourselves to oversimplify a bit, the bottom line is that there are just too many interactions of electrons with electrons, phonons, impurities, and magnetic fluctuations* [7]. Immediately prior to the emergence of the Bardeen-Cooper-Schrieffer theory as the effective microscopic model for conventional superconductivity [8, 9], when the community was still uncertain which of the many interactions in conventional superconductors are indispensable and which are not, Richard Feynman argued that there should be sufficient experimental detail and clues, yet no theoretical explanation had been established. He concluded his review quite critically: "The only reason that we [theoretical physicists] cannot do this problem of superconductivity is that we haven't got enough imagination" [10]. If we follow his suggestion and guess the answer without just making a long list of things that might produce a relevant effect [10], we must have a way to test and challenge our ideas.

With the increase in computing power, numerical simulations have become a powerful tool for evaluating models. However, computer simulations of quantum physics face essentially the same problem as those performed by humans. Strongly correlated systems, especially those with multiple degrees of freedom, make quantum mechanical problems intractable. Feynman concluded that if we want to study quantum phenomena in a fundamental way, we should simulate them using systems that are themselves quantum mechanical [1].

Once we have an effective model for a problem, we can look for a quantum system where the phenom-

---

[*] We do not intend to single out high-temperature superconductivity research with our opening. Rather, it seems to us to be a good example because we would argue that it is a holy grail of condensed matter research for the last half-century.

ena can be simulated and studied in more detail with greater experimental control and/or observation. This may then challenge the proposed model or reveal new phenomena. In this thesis, we deal with a controllable, non-destructively observable condensed matter system with phenomena such as (photon) mediated interaction, coupling to a vacuum, symmetry breaking, and bound states. Phenomena that arise throughout quantum physics, from the fundamental particles of the standard model to few-body systems such as atoms, many-body systems, and even the universe [3, 5].

The basis for the system studied in this thesis is one of the seemingly simplest systems in which quantum mechanics produces a fascinating phenomenon. Interactions occur at the quantum level even in situations that we would classically expect to be free of interaction. A single atom in a vacuum is not an isolated system. In fact, it forms a system with the electromagnetic field of the vacuum [11]. The effective description depicts the atom as a two-level system of states separated by the transition frequency. Such a two-level system in the vacuum, when excited to the higher energy state, sooner or later emits a photon by returning to its ground state [11]. Intricately, the vacuum provides a large reservoir of electromagnetic modes to which the two-level system is coupled. This whole system can then be described as a system-bath model, where dissipation into the large reservoir leads to irreversibility. This irreversibility is expressed in the phenomenon of spontaneous emission [11]. Spontaneous emission occurs because the two-state system has an infinite number of vacuum states into which it can emit the photon [12]. Consequently, if one were to change these states, or rather the density of states, one could control the physics by changing the dissipative bath. This can be achieved by placing the atom in a cavity, which can be constructed, for example, by two mirrors. Depending on the geometry of this construction, the spontaneous emission is inhibited or enhanced [12]. The introduction of such boundary conditions on the electromagnetic vacuum affecting atomic radiation was first mentioned historically as the Purcell effect [13].
Modifying the quantum vacuum of the electromagnetic field by constructing and controlling large macroscopic objects like mirrors has proven to be a powerful tool for studying quantum mechanics. One of the first achievements to exploit this phenomenon was the study of quantum decoherence using a microwave cavity [14].
In a similar line, simulation of quantum many-body physics, condensates of atoms have emerged as viable tools. This development was initiated in the wake of the first realization of a Bose-Einstein Condensate (BEC) [15, 16], for example, by realizing the Bose-Hubbard model using optical trapping potentials of atoms in a lattice [17]. An important goal of many-body physics is the study of phase transitions and entanglement [18, 19]. In the Bose-Hubbard model, a superfluid to Mott insulator transition can be controlled and observed to a finer degree than similar transitions in real materials [17]. Another example realized with fermionic atoms is the transition from a BEC to a Bardeen-Cooper-Schrieffer regime [20–22].

All degenerate quantum gases on their own* are governed by short-range interactions. By engineering a strong coupling to the electromagnetic vacuum, long-range, even global, interactions can be created in the condensate. In the appropriate parameter regime, the photon field does not adiabatically follow the atomic dynamics, so that rich backaction effects can arise. In addition, the dissipation of the light field can be used to non-destructively observe the system and its dynamics. Using the Purcell effect enhanced Rayleigh scattering in combination with a BEC, the driven dissipative Dicke model has been simulated [23]. The Dicke model is one of the fundamental models of light-matter interaction [24]. Furthermore, the extended Bose-Hubbard model with its rich phase diagram could be studied [25, 26].

---

*Later in the thesis we will briefly review that in certain atomic species, utilizing modification of their contact interaction with magnetic fields, long-range dipole-dipole interaction becomes significant.

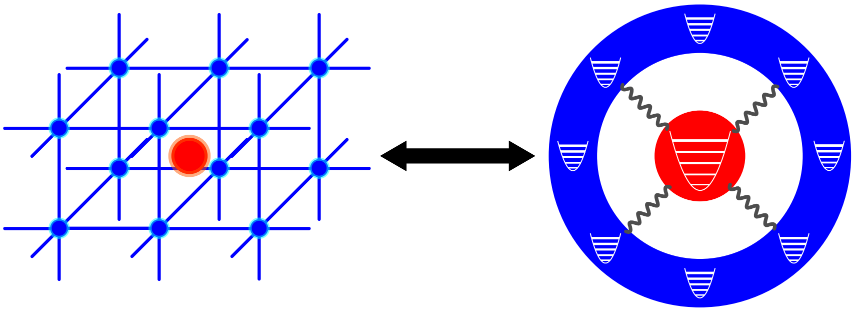

Figure 1.1: Correspondence of an electron moving through a lattice, where it interacts with lattice phonons, to a harmonic oscillator that is individually weakly coupled to an almost infinite number of harmonic oscillators at the mathematical level of description. Indeed, other physical systems share this correspondence.

In the meantime, a lot of other physical phenomena have been simulated using such a setup with a BEC coupled to an optical cavity, which we will refer to as cavity BEC [27]. We mention a selected zoo of these phenomena realized in cavity BEC in the corresponding section 2.3. The system also lends itself to the study of quantum dissipation and its impact on the phase transition and the behavior of quantum fluctuations and universal scaling [28]. Reservoir engineering is a further important aspect of quantum simulation and universal quantum computing [29–31].

1.1 – Intrinsic quantum dissipation and decoherence

The simulation of quantum systems in the presence of quantum reservoirs, where dissipation and decoherence play a crucial role, is directly related to the first project presented in this thesis. Phonons and phonon-related damping are common in real systems such as semiconductors, metals, ionic crystals, and molecular crystals [32], see figure 1.1. In unpolar crystals such as semiconductors and metals, charged particles couple to the lattice, giving rise to characteristic phonon interactions. The motion of these particles distorts the surrounding lattice, and the resulting lattice deformations propagate with them. These interactions are governed by acoustic phonons. Similarly, in ionic crystals, an electron interacts with the surrounding lattice ions, polarizing the medium. This interaction lowers the energy of the electron and its motion is accompanied by a cloud of longitudinal optical phonons. The coupling in these cases is effectively described by the Fröhlich interaction [32]. On the effective mathematical level, the particle is coupled to a bath of effectively infinitely many harmonic oscillators, which we visualize in figure 1.1.

Beyond solid state systems, phonon damping also plays a role in superfluid systems through Landau and Beliaev processes [33]. It emerges due to weak interactions between the atoms of the condensate described by s-wave scattering. Both types of superfluid damping are third-order processes in the fluctuations around the condensate mean-field. Hence they are the next-order corrections beyond the quadratic fluctuation terms of Bogoliubov theory [33]. As a consequence, they lead to significant corrections when either the density is large or the temperature is high.

We will review in the appropriate section 2.3 that in a homogeneous BEC coupled to a cavity vacuum, not all Bogoliubov modes are treated equally [34]. The cavity field mode selects certain excitations of the condensate that are commensurable. It leads to the formation of roton-like excitations [35]. Due to the strong coupling between the matter and the light field, polariton modes are formed [36]. Since the light-matter coupling can be strong and is independent of the atom-atom scattering interaction, the damping can be addressed via the light field tuning, resulting in significant corrections, as we will show. Consequently, the polariton quasiparticle is damped in a tunable way. The two modes that hybridize to the polariton are linearly coupled to a bath of the remaining excitations of the condensate. In essence, we derive a framework in which the system can be tuned to have a phononic coupling of two polariton modes, which are mathematically equivalent to harmonic oscillators. The physical description creates the intriguing situation that two coupled quantum harmonic oscillators, one for the cavity light mode and one for the matter, are damped by a phonon bath. The damping for each of them is independently tunable in the experiment. It extends the notion of a single harmonic oscillator coupled to a dissipative quantum bath as in figure 1.1 to two interacting harmonic oscillators coupled to the dissipative bath. Furthermore, it can be tuned to significant Beliaev damping even at zero temperature due to the strong coupling light field.

Mathematically, we will use the same system-bath techniques that are commonly used for the Fröhlich Hamiltonian and its lattice phonon damping for the cavity BEC damping. We will obtain a system-bath description of the central polariton system in its phonon bath with Landau and Beliaev damping, including the zero and finite temperature regimes. Our focus is then on the analysis of the quantum fluctuations of the two physical modes of the system. In particular, the cavity mode is of interest because it can be studied experimentally in situ by a non-destructive measurement of the photons lost from the cavity [23, 28]. With our results, the strong hybridization of matter and light allows us to deduce the system physics very precisely from the photon observation.

1.2 – Quantum droplets

The emergence of bound states is a remarkable property of quantum mechanics. It is essential to our humanly perceived world, which arises from fundamental particles. The effective interaction potential of two or more particles, fundamental or not, can have several bound states. They are states of negative energy, so that the energy is below the effective potential at infinity [2]. The lowest energy state, the ground state, is stable.

The formation of bound states begins at the smallest level, where the fundamental particles undergo competing interactions mediated by bosonic fields. This interplay is necessary to form the bound states of a proton and an electron cloud around it to produce the hydrogen atom [2]. Assuming that the heavy nucleus of the proton sits still at the center of mass with the fast and light electron forming a cloud around it*, its states can be derived from the Schrödinger equation with the Coulomb interaction potential between the two particles. This Coulomb potential is the effective model for the photon-mediated electromagnetic interaction between the two [2].

Simply counting up one element in the periodic table brings us to helium. Solving even the ground state of the second element in the periodic table is much more involved than for hydrogen because, in addition to the hydrogen problem, there is significant electron-electron repulsion term in the Schrödinger equation [2]. The recipe for its stable bound state requires only one additional proton, one additional electron, and one or two neutrons. The addition of just one neutron produces fermionic ^{3}He, while the addition of a second neutron means that the helium is bosonic ^{4}He [5].

Now let us imagine, as far as we can, two helium atoms. In the effective description, they interact at large distances via spontaneously induced dipole moments that lead to van der Waals attraction. At shorter distances, they must repel each other because the Pauli exclusion principle forbids overlapping wave functions. An effective potential describing this two-body interaction is of the Lennard-Jones type. It must combine both the attractive and repulsive interactions that result from the constituents of the atoms interacting with each other. If we have many helium atoms, this can quickly become an insurmountable orchestra of interactions.

---

[*] In the sense of the wave function and its absolute value the probability density so that it is like a cloud of probability and phase.

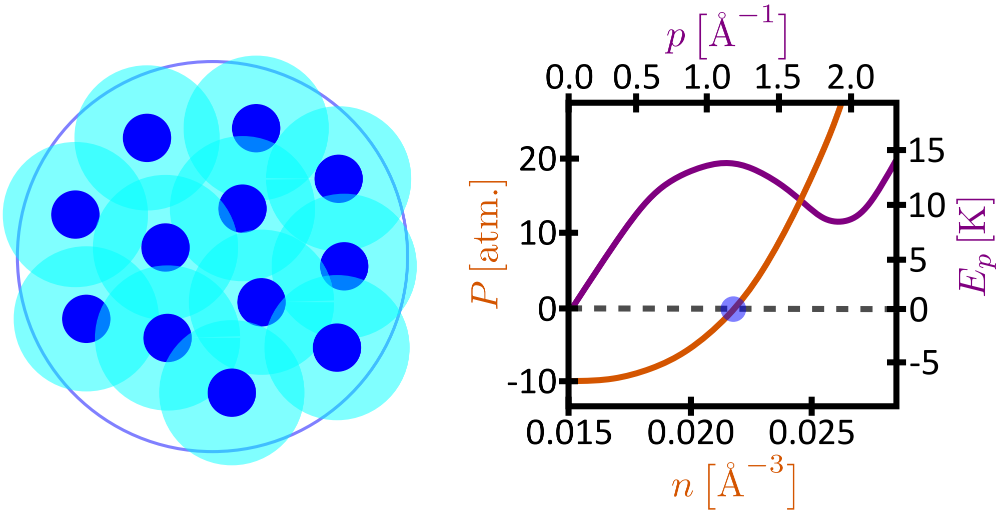

Figure 1.2: Sketch of a helium droplet of 12 ^{4}He atoms. The solid blue dots indicate their repulsive Pauli exclusion interaction, while the light blue regions visualize their van der Waals attractive range. The roton dispersion E_p and the pressure P in dependence of the density n are sketched on the right. The zero pressure marked by the blue dot determines the density of a droplet. Droplet sketch in the style of Ref. [39], dispersion and pressure sketch based on Ref. [40].

However, combining many helium atoms is a resource for versatile quantum many-body effects. Cooled below the temperature of 2.17 Kelvin, ^{4}He is in an aggregate state unpredictable by classical physics. First observed almost a century ago, the superfluid [37] has no entropy and flows without friction. It fostered the introduction of the roton dispersion relations [38] illustrated in figure 1.2, which indicate long-range interactions. Such a superfluid can also host discretized quantum vortices [41]. The competition in the superfluid between short-range repulsion and long-range attraction means that it can form a quantum droplet, sketched in figure 1.2. It is a bound state where the many-body wave function is spatially bound to a fixed size around its center of mass. Once the number of atoms in the droplet is large, it has an effectively homogeneous bulk density [40]. Now that we have many particles forming the bound state, we can invoke notions of thermodynamics. The ground state of the droplet represents the stability of the effective thermodynamic potential describing the quantum liquid. It has zero pressure and positive compressibility, see figure 1.2. Any perturbation of the size of the liquid will return it to the equilibrium value. Furthermore, the chemical potential is negative, so it does not evaporate by itself [5].

If an arrangement of quantum droplets is coherent, it forms a supersolid. A supersolid combines the properties of the liquid quantum aggregate state with the density grating of a solid. This quantum aggregate state was also originally predicted for liquid helium [42]. However, it has not yet been successfully realized [43]. A large body of theory has been developed for dilute condensed Bose gases, which also qualitatively captures superfluidity. However, the droplet state of helium requires not only an effective energy functional of the mean-field and beyond-mean-field interactions of the Lennard-Jones potential, which has to be fit to the experimental data after numerical evaluation. Furthermore, the Lennard-Jones terms are not sufficient, and gradient terms describing boundary effects have to be added for a qualitative agreement [40]. It can then be said that the helium quantum droplets and their dispersion are strongly correlated and involve long-range interactions that are beyond tractability from first principles. Liquid helium is just one of many examples of intriguing phenomena that arise from the complexity of many-body quantum physics, which makes their prediction from fundamental laws inaccessible [4].

In the middle of the last decade a new approach to quantum droplets had its dawn [44]. Bose-Einstein condensates had famously been realized two decades prior [15, 16]. These atomic condensates are dilute quantum gases, and their repulsive low-energy atom-atom interaction is precisely described by s-wave scattering. This means that their complicated Lennard-Jones-like interaction potential can be replaced by a simple effective potential, which reduces to a simple s-wave scattering length describing the strength of an effective contact interaction. In a stable three-dimensional gas, there is effectively only a repulsive interaction between the atoms, which does not allow bound many-body states. A competing interaction is therefore required. In 2016, a quantum droplet was realized using the atomic species ^{164}Dy and its Feshbach resonances [45]. The two types of interactions, dipole and scattering, and the tuning via the Feshbach resonances created an interplay of an effectively attractive mean-field and a repulsive beyond-mean-field term in the form of the Lee-Huang-Yang (LHY) correction [46–49]. Since the mean-field could be almost completely suppressed, the quantum correction could compete on an equal footing. The competition of the attractive and repulsive terms then formed the self-confined quantum droplet*. Due to the long-range nature of the dipole-dipole interaction, a roton is formed in the dispersion of the dipolar Bose gas [50–53]. When this roton is weakened, an array of droplets becomes coherent, forming a supersolid [54–56].

This minimal realization of a quantum droplet from two competing interaction terms emphasizes that it is truly quantum in nature. The mean-field approximation treats the field of the system as a complex number or function. It can therefore be considered classical because the mean-field has a trivial commutator [3]. Only beyond the mean-field the operator characteristics and its nontrivial commutation play a role. The LHY correction itself arises precisely as the sum over the zero-point energies of the quasiparticle excitations of the respective system, which in turn are a manifestation of the nontrivial commutation of the operators. To call something a quantum droplet, beyond mean-field effects must be essential for its formation.

Another aspect that we have only implicitly touched on is that the interplay is quantitatively predictable from analytical calculations using Bogoliubov theory [57]. Because the quantum liquid is dilute and weakly interacting, unlike strongly correlated helium, a model can be derived using the dilute weakly interacting approximations. For a quantum droplet, this was first worked out in 2015 in the seminal prediction of droplets of dilute quantum gases by D. S. Petrov [44]. He derived that the repulsive LHY correction in the mixture of two s-wave scattering Bose gases can compete with an almost suppressed attractive mean-field. The mixture droplets were soon realized [58, 59] and can be studied in one, two, or three dimensions [60]. We will review them in more detail in chapter 4.

For now, let us step back and take the broad view that two quantum simulations of this intriguing quantum aggregate state have been realized. They could be a fertile ground for the simulation of phenomena such as surface effects, self-binding, nucleation, and other bound many-body states [39]. However, both rely on Feshbach resonances for tuning. In cavity BEC, we have the opportunity to directly address the light field, which mediates a long-range interaction between the atoms. It can be fine-tuned to compete with the s-wave scattering of BEC, in principle without Feshbach resonances. Furthermore, the specific long-range interaction potential can even be controlled from the outside [27]. The cavity-mediated interaction also leads to the formation of roton-like excitations [35]. Admittedly, this is not straightforward. A theory for the analytical derivation of the necessary quantum corrections is developed to obtain our results. At least for global-range interactions, the model is mean-field exact in the thermodynamic limit. Thus, we present in this work a description of droplets in finite-size systems and of finite-size effects. As a caveat, this leads to a classification of droplets based on their qualitative minimal model.

---

[*] The dipole-dipole interaction is not isotropic and is attractive only along the axis in which the dipoles are aligned. Consequently, these droplets are really only in this one axis, not in all three dimensions.

1.3 – Outline

We will proceed as follows. First, in chapter 2 we review the foundations for this thesis. As described in this introduction, we start with the effective description of the interaction between two atoms at low energies. This will lead us through the derivation of s-wave scattering in section 2.1 and then quickly transfer it to the quantum many-body interaction in a dilute Bose gas. Consequently, in section 2.2 “Bogoliubov theory” we recall the effective theory for treating weakly interacting degenerate Bose gases and many other systems. It is based on an elegant expansion around the complex-valued mean-field of the system. We thus review the derivation of the Bose gas mean-field and its quantum corrections, as well as a brief look at thermal effects in the low-temperature limit.

Then, having covered the necessary basics for Bose gases, we combine them with the modified electromagnetic vacuum of a cavity in the section 2.3 aptly titled “Introduction to the cavity BEC system”. First, we need to understand the role of the electromagnetic vacuum and its modification leading to the Purcell effect. Therefore, we go over a single atom in the considered cavity setup of the Jaynes-Cummings model and then generalize it to the effective field Hamiltonian of many atoms. With the fundamental theoretical description at hand, we divert to a brief review of the experimental realization of this field Hamiltonian. Afterward, we return to the theory to evaluate which physical phenomena are realized in this setup. In view of our work presented in the following chapters of the thesis, we focus on the application of Bogoliubov theory techniques to the homogeneous mean-field of the normal superfluid phase. On the mean-field level, we review the superradiant self-assembly into a checkerboard lattice at a critical light-matter coupling. We then recall the collective excitations of the system that drive this phase transition and find the polariton modes formed by the hybridization of the cavity mode and selected matter excitations. The instability of the lower polariton mode indicates the critical value for the self-organization transition. The physics in this phase and the phase transition can be mapped to the Dicke model. Subsequently, we show that in the fast strongly dissipative cavity regime the cavity dynamics can be eliminated to find an atom-only description with a cavity-mediated global long-range atom-atom interaction. This interaction creates a roton-like excitation for the atom gas. We take a look at the cavity BEC beyond the critical point of self-organization, its realized extended Bose-Hubbard model, and its phase diagram. This is followed by a brief excursion that a similar coupling and effective Hamiltonian can be realized in hybrid atom-optomechanical setups.

In chapter 3 titled “Exotic dissipation from quantum fluctuations” we study the intrinsic damping of the cavity BEC and derive its intriguing dissipation signatures, their controllability, and observation. To this end, we review the theory of quantum dissipation around the system-bath picture and its arguably most widely applied model, the Caldeira-Leggett model. We then proceed more specifically and recall the existing literature investigating dissipation in cavity BEC and of damped Dicke models and polaritons. This then provides the foundation and motivation to derive an effective system-bath model for the quantum fluctuations from the cavity BEC field Hamiltonian that has the ambition to provide an all-encompassing investigation of the prevalent damping, dissipation, and decoherence phenomena previously reviewed. The treatment of the Landau and Beliaev damping processes as a quasiparticle bath by the system-bath formalism allows us to perform an exact analysis. It also provides us with the influence functional of the bath and hence the effective partition function of the central polariton-forming system. Mathematically, these are two bilinearly coupled harmonic oscillators in the effective dissipative bath of atomic quasiparticles formed by the s-wave scattering in the condensate.

We find a Stokes shift and signatures of the quantum fluctuations of the bath in the observables of the system. Both are controllable by tuning typical parameters of the experiments. A brief outlook on further investigations based on the presented theory and its results is provided. We conclude that we derive from first principles an intriguing system-bath model that is intrinsic to the cavity BEC due to phononic damping in the weakly interacting condensate. It is both tunable and its signatures are non-destructively observable in the experiment. Consequently, we find it to be a suitable platform for the simulation of highly nontrivial phononic damping, which, given an optimization of the setup, e.g. by particle number, should be employed to study stimulating quantum dissipation and decoherence relevant to many other condensed matter systems.

In chapter 4 we investigate cavity-induced quantum droplet formation. We start by introducing the criteria for a stable quantum liquid droplet and derive a novel droplet classification based on a minimal model for the effective ground state energy. The classification hinges on the parameter set classes of the minimal model that can satisfy the droplet conditions. Afterwards, we recapitulate the established quantum droplet realizations in Bose-Bose mixtures and dipolar Bose gases. Returning to our work, we start with a generic model for the type of long-range interactions that can be created in cavity light fields. Defining this type of long-range interaction is the envelope that captures its range, for example by exponential spatial decay. We develop an analytical Bogoliubov theory that is applicable if the interaction has a global range, but is not necessarily infinite-range. Subsequently, specific examples of cavity-induced long-range interactions are investigated.
To establish the context with the rest of the thesis, we focus on the long-range interaction induced by a single-mode cavity, where the exponential decay of the interaction emerges due to the Gaussian profile of the TEM_{00} light field. We show that the effective energy potential can fulfill the droplet criteria and analytically derive a minimal model. This allows us to directly classify the cavity quantum droplet and its tuning by external parameters. We find that it is a new type of a quantum droplet that can only form in systems of finite size. Furthermore, we investigate the low-temperature effects on the droplet formation, where we encounter a critical temperature above which no stable droplet can exist. We exploit the generality of the developed theory to study different interaction envelopes. Also, we study a translation invariant cavity-induced interaction, which leads to qualitatively equivalent results despite a different physical mechanism.
Because the cavity-induced quantum droplets are of a completely different type compared to the established ones, with a different underlying mechanism, many areas for further investigation open up. We discuss some of these aspects in the outlook. At the end of the chapter, we conclude that we generalize the minimal model of quantum droplets to finite-size systems, where we find an undiscovered droplet type. We show that quantum corrections due to the cavity-induced long-range interaction interplay with the mean-field of the Bose gas to form a droplet of this novel type. This relies on the effectively distinct roton modes having a roton depth that is dependent on the system size, making their zero-point energy quantum correction also dependent on the system size. We demonstrate that the cavity-induced droplet is controllable by many external tuning parameters, in particular those of the light field. Therefore, cavity-induced quantum droplets are an excellent basis for the simulation and study of bound many-body quantum states that occur throughout many-body physics. They could also be an interesting platform for any quantum setup that requires long-term stability and coherence due to their self-confined nature. This includes applications in quantum sensing, interferometry, or computing.

Throughout, this thesis we will set $\hbar = 1$ unless it is explicitly written. Similarly, we choose $k_B = 1$ for the Boltzmann constant and $c = 1$ for the speed of light.

2 – The atoms, the cavity, and their interplay

2.1 – Elastic collisions of quantum particles

In this section, we review the weak interaction of atoms in dilute gases. Considering the elastic collision of two slow particles leads us to s-wave scattering. It turns out to be one of the two types of coupling fundamental to the phenomena discussed throughout this thesis. Its strength U, Eq. (2.12), emerges as a key parameter for the physics presented. Thus, this introductory section of non-original work constitutes a central pillar for the entire thesis.

When one reads "collision", one classically imagines something like a billiard ball hitting another billiard ball. Such a classical elastic collision is completely determined by the velocities of the two particles, e.g. billiard balls, and the distance at which they would pass if they did not interact [61]. Quantum mechanics shatters this classical idea that is associated with the collision of two particles. In quantum mechanics, the idea of a particle with a definite velocity and a definite path has no merit due to Heisenberg's uncertainty principle. All that is accessible is to calculate the probability that the particles are scattered by any given angle ϑ [61]. During an elastic collision, the particles and their internal states must remain unchanged.

The two-body problem can be simplified to the scattering of a single effective two-body wave function in a central spherically symmetric potential $U(r)$. We consider the situation visualized in figure 2.1. A free particle is incoming, traveling along the positive direction of the z-axis, which is described by the plane wave e^{ikz}. The outgoing wave has the asymptotic form $f(\vartheta)e^{ikr}/r$ far from the scattering center $r \to \infty$. Due to its spherical wave property, it has a radial $1/r$ dependence that normalizes the probability $|\psi|^2$ on the surface of any spherical shell $\propto r^2$ of arbitrary radius r. The scattering amplitude $f(\vartheta)$ is then only a function of the scattering angle ϑ relative to the z-axis. Combining the incoming and outgoing waves we obtain the solution $\psi(\boldsymbol{r})$ of the Schrödinger equation with the

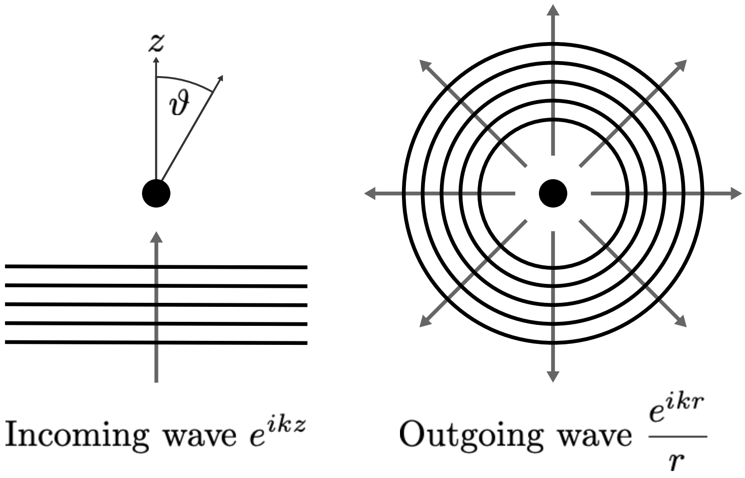

Figure 2.1: Picture of the incoming free particle and the scattering angle ϑ as well as the scattered spherical wave. The scattering center is in the large black dot.

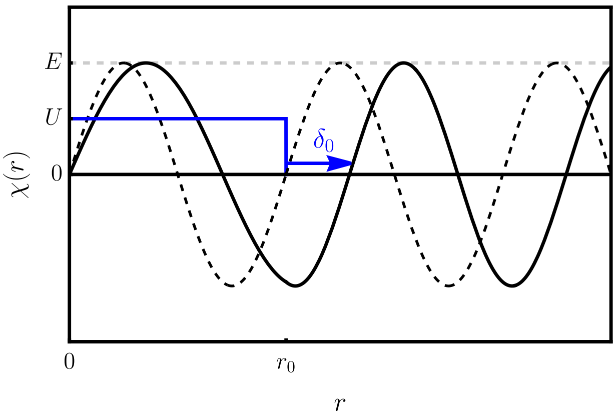

Figure 2.2: Sketch of the phase shift $\delta_{l=0}$ for a simple box potential $U(r) = E/2$ for $r \leq r_0$. The solid line draws the solution of the stationary Schrödinger equation $\chi''(r) + [E - U(r)]\chi(r) = 0$ with the boundary condition $\chi(0) = 0$, $\chi'(0) = 1$, $\lim_{r\nearrow r_0} \chi(r) = \lim_{r\searrow r_0} \chi(r)$, and $\lim_{r\nearrow r_0} \chi'(r) = \lim_{r\searrow r_0} \chi'(r)$. The wave function in the absence of the scattering potential is drawn as a dashed line.

central potential $U(r)$ in the form

$$\psi(\boldsymbol{r}) = e^{ikz} + f(\vartheta)\frac{e^{ikr}}{r}\,. \tag{2.1}$$

The probability that the scattered particle passes through the surface of a sphere in the solid angle element $d\Omega$ is determined by the effective cross-section $d\sigma$ for scattering into the solid angle $d\Omega$ [41,61]

$$d\sigma = |f(\vartheta)|^2 d\Omega = |f(\vartheta)|^2 2\pi \sin(\vartheta) d\vartheta\,, \tag{2.2}$$

where we apply that the scattering is symmetric around the z-axis, i.e. independent of the azimuthal angle.

In this thesis, we consider identical bosonic atoms occupying the same state. Due to their indistinguishable nature, the orbital part of their wave function and thus the cross section must be symmetric, so that $d\sigma = |f(\vartheta) + f(\pi - \vartheta)|^2 d\Omega$ for $0 \leq \vartheta \leq \pi/2$ [41].

In a central potential $U(r)$ the Schrödinger equation can be separated into an angular and a radial equation. The eigenfunctions for the angular momentum l are the Legendre polynomials $P_l(\cos(\vartheta))$. It is convenient to express the radial part by the functions $\chi_{kl}(r)/kr$ of the solution of the radial differential equation

$$\frac{d^2\chi_{kl}(r)}{dr^2} - \frac{l(l+1)}{r^2}\chi_{kl}(r) + m\left[E - U(r)\right]\chi_{kl}(r) = 0\,, \tag{2.3}$$

with the energy $E = k^2/m$ fixed by the incoming wave of the free particle. The mass of a single particle is m in our consideration of two identical atoms, while the reduced mass in the two-body problem takes on the value $m^* = m/2$. The solution of Eq. (2.3) can be evaluated asymptotically for large distances $r \gg r_0$, where r_0 is the range of the potential $U(r)$. For large distances relative to a short-range interaction $U(r)$, both the interaction and the centrifugal term in Eq. (2.3) are negligible, so the solution for $r \gg r_0$ is [41,62]

$$\chi_{kl}(r) = A_l \sin\left(kr - \frac{\pi l}{2} + \delta_l(k)\right)\,. \tag{2.4}$$

This solution contains a yet undefined amplitude A_l and a phase shift $\delta_l(k)$. The phase shift holds the characteristic information of how the potential acts on an incoming wave with the energy $E \propto k^2$, as can be seen from physical reasoning. In the case of a repulsive potential, such as the repulsive box potential in figure 2.2, the wave function is squeezed to the outer region, resulting in a negative phase shift $\delta_l < 0$ [62]. The "squeezing strength" or more technically the value of the phase shift δ_l is related to the strength of the interaction potential $U(r)$. An attractive potential sucks in the wave function in its outer region such that $\delta_l > 0$ [62].

The collisions of atoms that we consider in this thesis are not only non-relativistic, they are actually of low-energy in the sense that $kr_0 \ll 1$. In these low-energy collisions, one can find asymptotic solutions of Eq. (2.3) which can be used to determine the phase shift. First, for distances $r \ll 1/k$ in Eq. (2.3) it asymptotically holds that $E = 0$ and the resulting equation is independent of the incoming wavenumber k. Second, examining the solutions of Eq. (2.3) yields an iterative relation between the solutions for angular momentum $l+1$ and angular momentum l [41, 62]. This iteration manifests in $\delta_l/\delta_0 \propto k^{2l}$. Thus, in the limit $k \to 0$ it is sufficient to consider the equation for $l = 0$

$$\frac{d^2\chi_{k0}}{dr^2} - mU(r)\chi_{k0} = 0 \quad \xrightarrow{r \gg r_0} \quad \chi_{k0}(r) = c_0(1 - k_U r)\,. \tag{2.5}$$

Far from the scattering center $r \gg r_0$ the solution is asymptotically linear with free parameters c_0 and k_U depending on the choice of the interaction potential $U(r)$. The free parameters of the solution of Eq. (2.5) are found by comparison with the expansion of Eq. (2.4) for $l = 0$ at $kr \ll 1$ to linear order in kr. The solution of Eq. (2.5) is thus obtained as

$$\chi_{k0}(r) = e^{i\delta_0}\sin(\delta_0)\left(1 + kr\cot(\delta_0)\right)\,, \tag{2.6}$$

where the k-dependence arises through the free parameters. We find a linear relationship between the phase shift δ_0 and the wavenumber k by expanding $\cot(\delta_0) \approx 1/\delta_0$ so that $\delta_0 = -k/k_U$. Using the expression $\lim_{k\to 0} f(\vartheta) = -a_s$ we get the scattering length $a_s = 1/k_U$. It connects a single scalar value a_s with a potential $U(r)$ [41].
If we insert the relation $k_U = 1/a_s$ into Eq. (2.5), we can directly derive a geometric interpretation of the s-wave scattering length. We visualize this in figure 2.3. In the long wavelength limit $k \to 0$, the two-body wave function of the scattering problem with potential $U(r)$ is determined by the differential equation in Eq. (2.5). Examples are shown in figure 2.3. The asymptotic solution far beyond the potential range $r/r_0 \gg 1$ is the linear function in Eq. (2.5) independent of the shape of $U(r)$. This linear function $\chi(r) = c_0(1 - r/a_s)$ intersects the x-axis at $r = a_s$. Therefore, the scattering length a_s can be interpreted geometrically as how far the arbitrary scattering potential $U(r)$ pushes the zero crossing of the asymptotic wave function for $k \to 0$ and $r/r_0 \gg 1$ away from the scattering center $r = 0$. If the potential is attractive, the intersection of the x-axis is pulled to a negative radius value so that $a_s < 0$ [63].
Because not only the angle ϑ at which the atoms scatter, but also the shape of the interaction potential $U(r)$ itself has turned out to be irrelevant for this low-energy scattering $k \to 0$, the real potential can be replaced by a pseudopotential $\hat{U}_{\text{ps}}(r)$. This pseudopotential is constructed by stating the comparison of the two asymptotic solutions used in the derivation of Eq. (2.6) as a boundary condition [41]

$$k_U = -\left[\frac{1}{\chi_{k0}}\frac{d\chi_{k0}}{dr}\right]_{r=0}\,, \tag{2.7}$$

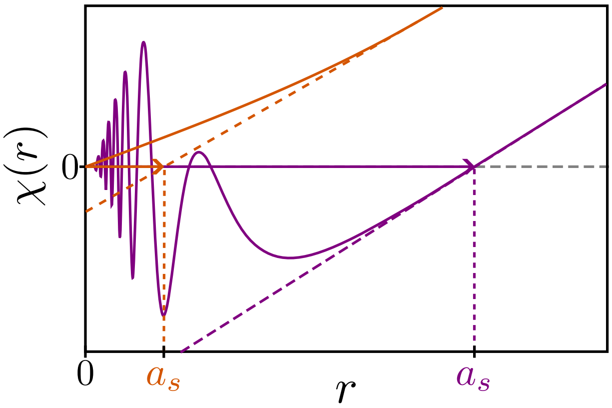

Figure 2.3: Geometric interpretation for the scattering length a_s. The plot shows the solution of the long wavelength asymptotic Schrödinger equation, Eq. (2.5), for a box potential in orange and a realistic scattering potential in purple. The dashed lines show the linear distant wavefunction as given in Eq. (2.5). This sketch blends figures from Refs. [41, 63].

so that the pseudopotential takes the form of the differential operator

$$\hat{U}_{\mathrm{ps}}(r) = \frac{4\pi a_s}{m}\delta^{(3)}(\boldsymbol{r})\frac{d}{dr}r\,. \tag{2.8}$$

Note that if the operator $\hat{U}_{\mathrm{ps}}(r)$ is applied to a function that is regular at $r = 0$, the differential operator part $(d/dr)r$ has no effect. However, if applied to a function with a $1/r$ singularity for $r \to 0$, this singularity is projected out $\hat{U}_{\mathrm{ps}}(r)[1/r] = 0$ [62]. Hence, if we can assert that there are no corresponding singularities in the many-body wave function, the differential operator can be discarded and we obtain

$$U_{\mathrm{ps}}(\boldsymbol{r}) = \frac{4\pi a_s}{m}\delta^{(3)}(\boldsymbol{r})\,. \tag{2.9}$$

2.1.1 Quantum many-body systems

In this thesis, we deal with many-body systems, usually consisting of at least several thousand indistinguishable atoms. Hence, the fact that we have just discussed the scattering of only two particles may seem a bit of a ruse. However, we are dealing only with weakly interacting dilute systems. This means that the average distance between the particles is large compared to the range of the interatomic forces. Such is assured for a small gas parameter $|a_s|^3 n \ll 1$, which consists of the scattering length a_s and the density $n = N/V$ of the N atoms occupying the volume V. If $|a_s|^3 n \ll 1$ the simultaneous interaction of three or more particles is negligible [41]. In addition, the use of asymptotic expressions for the wave function of the scattering process is justified. The interaction is thus characterized only by the s-wave scattering length. We can describe such a system with the bosonic field operator $\hat{\psi}(\boldsymbol{r})$, where $[\hat{\psi}(\boldsymbol{r}), \hat{\psi}^\dagger(\boldsymbol{r}')] = \delta^{(3)}(\boldsymbol{r} - \boldsymbol{r}')$ and $[\hat{\psi}(\boldsymbol{r}), \hat{\psi}(\boldsymbol{r}')] = [\hat{\psi}^\dagger(\boldsymbol{r}), \hat{\psi}^\dagger(\boldsymbol{r}')] = 0$ in a Hamiltonian with the two-body potential $U(r) = U(|\boldsymbol{r} - \boldsymbol{r}'|)$

$$\hat{H} = \int_V d^3\boldsymbol{r} \left\{ \hat{\psi}^\dagger(\boldsymbol{r}) \left[-\frac{\nabla^2}{2m} \right] \hat{\psi}(\boldsymbol{r}) \right\} + \frac{1}{2} \int_V d^3\boldsymbol{r} \int_V d^3\boldsymbol{r}' \left\{ \hat{\psi}^\dagger(\boldsymbol{r}) \hat{\psi}^\dagger(\boldsymbol{r}') U(|\boldsymbol{r} - \boldsymbol{r}'|) \hat{\psi}(\boldsymbol{r}') \hat{\psi}(\boldsymbol{r}) \right\}. \tag{2.10}$$

Actual interatomic potentials like the Lennard-Jones potential or the similar potential in figure 2.4 evade the solution of their Schrödinger equation. Especially for slow particles, the solutions of the Schrödinger equation cannot be calculated by perturbation theory either [41]. However, since the

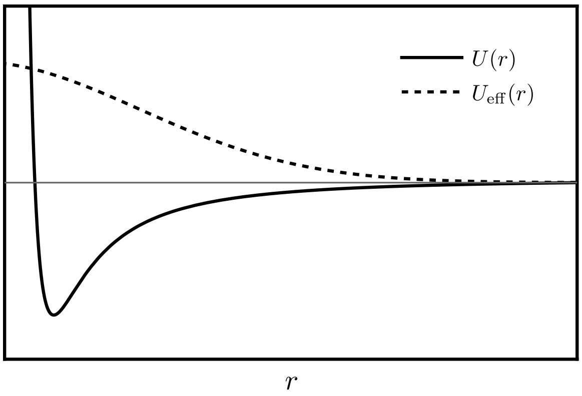

Figure 2.4: Realistic potential $U(r)$ for the two-body scattering in the many-body system with a short-range repulsion $\propto r^{-6}$ and long-range attraction term $\propto -r^{-2}$. The plot also shows an effective potential that produces the same asymptotic s-wave scattering properties a_s. The sketch is strongly based on Ref. [41].

interaction is fully characterized by the s-wave scattering length a_s, we can replace it by an effective potential U_{eff} as in figure 2.4 which yields the same interaction properties, i.e. a_s [41]. Of course, the range of the effective potential must be much smaller than the average distance between the particles $n^{-1/3}$. This adjustment to the microscopic physical reality still provides us with the correct macroscopic results for the many-body system. We can go a step further and use the pseudopotential Eq. (2.9), which yields the many-body Hamiltonian

$$\hat{H} = \int_V d^3\boldsymbol{r} \left\{ \hat{\psi}^\dagger(\boldsymbol{r}) \left[-\frac{\nabla^2}{2m} + \frac{U}{2} \hat{\psi}^\dagger(\boldsymbol{r}) \hat{\psi}(\boldsymbol{r}) \right] \hat{\psi}(\boldsymbol{r}) \right\}, \tag{2.11}$$

where $U = 4\pi a_s/m$. In the case of a potential where the Born approximation [64, 65] is applicable, like $U_{\text{eff}}(r)$, the parameter U is the value of the Fourier transform of the effective potential U_q at the origin of the Fourier space $q = 0$ [41]

$$U = U_{q=0} = \int_{\mathbb{R}^3} d^3\boldsymbol{r} \left\{ U_{\text{eff}}(r) e^{-iqr} \Big|_{q=0} \right\} = \int_{\mathbb{R}^3} d^3\boldsymbol{r} \left\{ U_{\text{eff}}(r) \right\}. \tag{2.12}$$

In this work, we encounter interactions with long-range potentials, where the range of the potential is either much larger than the average distance between atoms or more challenging if its range is comparable to the average distance.

2.2 – Bogoliubov Theory

The idea of studying a weakly interacting Bose gas posed a challenge since traditional perturbation techniques cannot be applied because the ideal Bose gas has zero ground state energy. It was the first achievement of Bogoliubov theory to circumvent this problem [57]. Subsequently, it became the standard approach to dilute gases, including many major advances in many-particle physics, ranging from the weakly interacting Bose gases, superfluidity, parametrically driven oscillators, light-matter interactions, to interacting fermions and superconductivity [3, 27, 41, 66, 67]. It is the key technique utilized throughout this thesis, so the following introduction proves to be relevant not only for the following section 2.3, but also for all subsequent chapters.

We begin with the many-body Hamiltonian for the Bose gas with weak contact interaction

$$\hat{H} = \int_V d^3\boldsymbol{r} \Big\{ \hat{\psi}^\dagger(\boldsymbol{r}) \Big[-\frac{\nabla^2}{2m} + \frac{U}{2} \hat{\psi}^\dagger(\boldsymbol{r}) \hat{\psi}(\boldsymbol{r}) \Big] \hat{\psi}(\boldsymbol{r}) \Big\} . \tag{2.13}$$

In a homogeneous Bose gas, i.e. one that occupies the volume V with uniform spatial distribution, it is advantageous to express the field operators in the plane wave basis as

$$\hat{\psi}(\boldsymbol{r}) = \frac{1}{\sqrt{V}} \sum_{\boldsymbol{p}} \hat{\psi}_{\boldsymbol{p}} e^{i\boldsymbol{p}\boldsymbol{r}} , \tag{2.14}$$

with the cyclic boundary conditions fixing the values of the momenta $\boldsymbol{p}$ in a finite volume V. Application of this expansion to Eq. (2.13) using the relation

$$\frac{1}{V} \int_V d^3\boldsymbol{r} \Big\{ e^{i\boldsymbol{p}\boldsymbol{r}} \Big\} = \delta^{(3)}_{\boldsymbol{p},\boldsymbol{0}} , \tag{2.15}$$

where $\delta^{(3)}_{\boldsymbol{p},\boldsymbol{k}}$ is the 3-dimensional Kronecker delta yields the momentum-space Hamiltonian

$$\hat{H} = \sum_{\boldsymbol{p}} \Big[\frac{\boldsymbol{p}^2}{2m} \hat{\psi}^\dagger_{\boldsymbol{p}} \hat{\psi}_{\boldsymbol{p}} + \frac{U}{2V} \sum_{\boldsymbol{p}',\boldsymbol{k}} \Big(\hat{\psi}^\dagger_{\boldsymbol{p}+\boldsymbol{k}} \hat{\psi}^\dagger_{\boldsymbol{p}'-\boldsymbol{k}} \hat{\psi}_{\boldsymbol{p}'} \hat{\psi}_{\boldsymbol{p}} \Big) \Big] . \tag{2.16}$$

Now, the brilliant trick of the Bogoliubov theory [57] is based on the realization that the ground state occupancy of the system of N_0 condensed atoms is macroscopically large and comparable to the total number of atoms N. Therefore, the creation $\hat{\psi}^\dagger_{\boldsymbol{0}}$ or annihilation $\hat{\psi}_{\boldsymbol{0}}$ of a single atom in this state leaves the macroscopic system effectively unchanged $N_0 \pm 1 \approx N_0$. Put differently, the commutator of the ground state operators $[\hat{\psi}_{\boldsymbol{0}}, \hat{\psi}^\dagger_{\boldsymbol{0}}] = 1 \ll N_0$ is negligibly small [3]. Hence, in the Bogoliubov prescription, the operators $\hat{\psi}^{(\dagger)}_0$ are replaced by a complex number, more precisely here [41]

$$\hat{\psi}_{\boldsymbol{0}} |\mathrm{GS}\rangle \approx \sqrt{N_0} |\mathrm{GS}\rangle \approx \hat{\psi}^\dagger_{\boldsymbol{0}} |\mathrm{GS}\rangle \quad \Rightarrow \quad \hat{\psi}^{(\dagger)}_{\boldsymbol{0}} = \sqrt{N_0} , \qquad \hat{\psi}^\dagger_{\boldsymbol{0}} \hat{\psi}^\dagger_{\boldsymbol{0}} \hat{\psi}_{\boldsymbol{0}} \hat{\psi}_{\boldsymbol{0}} = N_0(N_0 - 1) . \tag{2.17}$$

Note that at zero temperature with weak interactions, where almost all N atoms are condensed, we can immediately substitute $N_0 \approx N$ [41]. The number of atoms not in the ground state is given by the quantum depletion, so we have to consider this depletion to be small if we want to use the approximation $N_0 \approx N$. We then notice that this yields the same results as the mean-field approximation for the atomic field $\langle \hat{\psi}^{(\dagger)}(\boldsymbol{r}) \rangle = \sqrt{n} = \sqrt{N/V}$. A conceptually valuable remark is that since both the mean-field and Bogoliubov approximation are equivalent to neglecting nontrivial operator commutation, they constitute a classical treatment of the system [3]. The ground state energy in this classical approximation of the system, valid for a large number of atoms N, is then [41]

$$E_{\mathrm{mf}} = \frac{UN^2}{2V}\,. \tag{2.18}$$

2.2.1 Quantum fluctuations

The number of atoms in the ground state can be expressed as the total number of atoms reduced by quantum depletion. Based on this, the number operator for the ground state is expressed as $\hat{N}_0 = N - \sum_{\boldsymbol{p}}{}' \hat{\psi}^\dagger_{\boldsymbol{p}}\hat{\psi}_{\boldsymbol{p}}$ where we omit $\boldsymbol{p} = \boldsymbol{0}$ and denote this by the primed sum. We then write the ground state creation and annihilation operators as $\hat{\psi}^{(\dagger)}_{\boldsymbol{0}} = \sqrt{\hat{N}_0}$. Now we take Eq. (2.16) and where before we kept only zeroth order terms of $\boldsymbol{p} \neq \boldsymbol{0}$, we now retain the terms up to quadratic order using Eq. (2.17) and obtain

$$\begin{aligned}
\hat{H} &= \frac{U}{2V}\hat{\psi}^\dagger_{\boldsymbol{0}}\hat{\psi}^\dagger_{\boldsymbol{0}}\hat{\psi}_{\boldsymbol{0}}\hat{\psi}_{\boldsymbol{0}} + \sum_{\boldsymbol{p}}{}' \left[\left(\frac{\boldsymbol{p}^2}{2m} + 2\frac{U}{V}\hat{\psi}^\dagger_{\boldsymbol{0}}\hat{\psi}_{\boldsymbol{0}}\right)\hat{\psi}^\dagger_{\boldsymbol{p}}\hat{\psi}_{\boldsymbol{p}} + \frac{U}{2V}\left(\hat{\psi}^\dagger_{\boldsymbol{p}}\hat{\psi}^\dagger_{-\boldsymbol{p}}\hat{\psi}_{\boldsymbol{0}}\hat{\psi}_{\boldsymbol{0}} + \hat{\psi}^\dagger_{\boldsymbol{0}}\hat{\psi}^\dagger_{\boldsymbol{0}}\hat{\psi}_{-\boldsymbol{p}}\hat{\psi}_{\boldsymbol{p}}\right)\right] \\
&= \frac{U}{2V}\hat{N}_0(\hat{N}_0 - 1) + \sum_{\boldsymbol{p}}{}' \left[\left(\frac{\boldsymbol{p}^2}{2m} + 2\frac{U\hat{N}_0}{V}\right)\hat{\psi}^\dagger_{\boldsymbol{p}}\hat{\psi}_{\boldsymbol{p}} + \frac{U\hat{N}_0}{2V}\left(\hat{\psi}^\dagger_{\boldsymbol{p}}\hat{\psi}^\dagger_{-\boldsymbol{p}} + \hat{\psi}_{-\boldsymbol{p}}\hat{\psi}_{\boldsymbol{p}}\right)\right] \\
&= \frac{U}{2V}\left[N^2 - 2N\sum_{\boldsymbol{p}}{}' \left(\hat{\psi}^\dagger_{\boldsymbol{p}}\hat{\psi}_{\boldsymbol{p}}\right)\right] + \sum_{\boldsymbol{p}}{}' \left[\left(\frac{\boldsymbol{p}^2}{2m} + \frac{2UN}{V}\right)\hat{\psi}^\dagger_{\boldsymbol{p}}\hat{\psi}_{\boldsymbol{p}} + \frac{UN}{2V}\left(\hat{\psi}^\dagger_{\boldsymbol{p}}\hat{\psi}_{-\boldsymbol{p}} + \hat{\psi}_{-\boldsymbol{p}}\hat{\psi}_{\boldsymbol{p}}\right)\right] \\
&= E_{\mathrm{mf}} + \sum_{\boldsymbol{p}}\left[\left(\frac{\boldsymbol{p}^2}{2m} + 2nU - \mu_{\mathrm{mf}}\right)\hat{\psi}^\dagger_{\boldsymbol{p}}\hat{\psi}_{\boldsymbol{p}} + \frac{nU}{2}\left(\hat{\psi}^\dagger_{\boldsymbol{p}}\hat{\psi}_{-\boldsymbol{p}} + \hat{\psi}_{-\boldsymbol{p}}\hat{\psi}_{\boldsymbol{p}}\right)\right]\,,
\end{aligned} \tag{2.19}$$

with the mean-field energy $E_{\mathrm{mf}} = UN^2/2V$ and its chemical potential $\mu_{\mathrm{mf}} = (\partial E_{\mathrm{mf}}/\partial N)_V = nU$. One might think that we could now analyze the Hamiltonian Eq. (2.19) to extract the energy correction that the quantum fluctuations $\boldsymbol{p} \neq \boldsymbol{0}$ add to the ground state energy E_{mf}. However, the zero-point energy found from the eigenmodes of Eq. (2.19), which we will examine next, is a divergent sum. It turns out that Eq. (2.19) is inconsistent in the order of approximation [41, 61]. To capture the interatomic potential by the simple $U = U_{q=0}$, Eq. (2.12), we applied the lowest-order Born approximation. This is consistent if we study the ground state energy in the lowest order E_{mf}. For the quadratic-order approximation, we have to use the quadratic-order perturbation theory for the effective potential U_{eff}, which implies that instead of U we have to consider $U + (U^2/V)\sum_{\boldsymbol{p}}{}' m/\boldsymbol{p}^2$ [41, 61]. Thus, the self-consistent Hamiltonian of quadratic order is

$$\hat{H} = E_{\mathrm{mf}} + \sum_{\boldsymbol{p}}\left[\left(\frac{\boldsymbol{p}^2}{2m} + nU\right)\hat{\psi}^\dagger_{\boldsymbol{p}}\hat{\psi}_{\boldsymbol{p}} + \frac{nU}{2}\left(\hat{\psi}^\dagger_{\boldsymbol{p}}\hat{\psi}_{-\boldsymbol{p}} + \hat{\psi}_{-\boldsymbol{p}}\hat{\psi}_{\boldsymbol{p}}\right) + \frac{m(nU)^2}{2\boldsymbol{p}^2}\right]\,. \tag{2.20}$$

From it, we can uncover not only the Bogoliubov quasiparticles but also their ground state energy correction, the famous Lee-Huang-Yang (LHY) correction [46], since the additional last term in Eq. (2.20) regularizes the sum [5].

2.2.2 Excitation spectrum

The linear Bogoliubov transformation [41, 57]

$$\hat{\psi}_{\boldsymbol{p}} = u_{\boldsymbol{p}}\hat{\varphi}_{\boldsymbol{p}} - v^*_{\boldsymbol{p}}\hat{\varphi}^\dagger_{-\boldsymbol{p}}\,, \qquad \hat{\psi}^\dagger_{\boldsymbol{p}} = u^*_{\boldsymbol{p}}\hat{\varphi}^\dagger_{\boldsymbol{p}} - v_{\boldsymbol{p}}\hat{\varphi}_{-\boldsymbol{p}}\,, \tag{2.21}$$

diagonalizes the quadratic Hamiltonian Eq. (2.20). Imposing on the quasiparticle operators $\hat{\varphi}$, that they follow bosonic commutation relations, introduces the constraint $|u_{\boldsymbol{p}}|^2 - |v_{\boldsymbol{p}}|^2 = 1$ on the transfor-

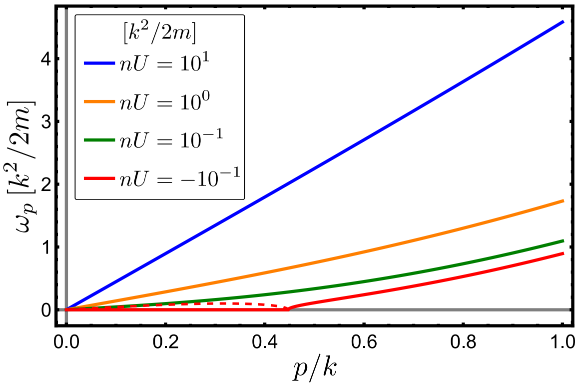

Figure 2.5: Bogoliubov dispersion ω_p, Eq. (2.25), for different strengths of the interaction nU. The momentum p is in units of some arbitrary wavenumber k, so both the dispersion ω_p and the interaction energy nU are given in units of $k^2/2m$. The dispersion for the attractive interaction $U < 0$ is pathological. In this case, the mean-field is unstable, which is reflected in the instability of the dispersion, seen in its zero real part and positive imaginary part. The latter is indicated in the plot by the dashed line.

mation coefficients. This is the characteristic equation for hyperbolic functions, so we can write [41]

$$u_{\boldsymbol{p}} = \cosh(\alpha_{\boldsymbol{p}})\,, \qquad v_{\boldsymbol{p}} = \sinh(\alpha_{\boldsymbol{p}})\,. \tag{2.22}$$

Inserting the transformation Eq. (2.21) into the quadratic Hamiltonian Eq. (2.20) yields the diagonalization condition

$$\left(\frac{\boldsymbol{p}^2}{2m} + nU\right) u_{\boldsymbol{p}} v_{\boldsymbol{p}} - \frac{nU}{2}\left(|u_{\boldsymbol{p}}|^2 + |v_{\boldsymbol{p}}|^2\right) = 0\,, \tag{2.23}$$

so that the terms of $\hat{\varphi}^\dagger_{\boldsymbol{p}}\hat{\varphi}^\dagger_{-\boldsymbol{p}}$ and $\hat{\varphi}_{-\boldsymbol{p}}\hat{\varphi}_{\boldsymbol{p}}$ are eliminated. With the hyperbolic identities $\cosh^2(\alpha_{\boldsymbol{p}}) + \sinh^2(\alpha_{\boldsymbol{p}}) = \cosh(2\alpha_{\boldsymbol{p}})$ and $2\cosh(\alpha_{\boldsymbol{p}})\sinh(\alpha_{\boldsymbol{p}}) = \sinh(2\alpha_{\boldsymbol{p}})$ the eigenmodes are found by the transformation coefficients determined by

$$\tanh(2\alpha_{\boldsymbol{p}}) = \frac{nU}{\frac{\boldsymbol{p}^2}{2m} + nU}\,. \tag{2.24}$$

The Hamiltonian Eq. (2.20) is then diagonalized with the eigenmodes following the Bogoliubov dispersion [57]

$$\omega_{\boldsymbol{p}} = \sqrt{\frac{\boldsymbol{p}^2}{2m}\left(\frac{\boldsymbol{p}^2}{2m} + 2nU\right)}\,. \tag{2.25}$$

It is shown in figure 2.5. In the long-wavelength limit, i.e. for low momentum $p^2 \ll 2mnU$, the dispersion is linear $\omega_p \sim p\sqrt{gn/m}$. This is called the phononic region with the associated speed of sound $c_s = \sqrt{gn/m}$ [41] and is shown in blue in figure 2.5. The asymptotic behavior of the dispersion at large momenta $p^2 \gg 2mnU$ is a parabola $\omega_p \sim p^2/2m$. We can identify this from the green curve in figure 2.5, which is accurately approximated by $\omega_p \approx p^2/2m + nU$.
The Hamiltonian obtained with these Bogoliubov quasiparticles of modes Eq. (2.25) is

$$\hat{H} = E_{\mathrm{mf}} + \frac{1}{2}\sum_{\boldsymbol{p}}{}' \left[\omega_{\boldsymbol{p}} - \frac{\boldsymbol{p}^2}{2m} - nU + \frac{m(nU)^2}{\boldsymbol{p}^2}\right] + \sum_{\boldsymbol{p}}{}' \left[\omega_{\boldsymbol{p}}\hat{\varphi}^\dagger_{\boldsymbol{p}}\hat{\varphi}_{\boldsymbol{p}}\right] = E_0 + \sum_{\boldsymbol{p}}{}' \left[\omega_{\boldsymbol{p}}\hat{\varphi}^\dagger_{\boldsymbol{p}}\hat{\varphi}_{\boldsymbol{p}}\right]. \tag{2.26}$$

The vacuum of the quasiparticles adds to the ground state of the system. Thus, the ground state energy $E_0 = E_{\mathrm{mf}} + E_{\mathrm{qf}}$ now includes the higher-order correction arising as the zero-point motion of the Bogoliubov quasiparticle excitations resulting from operator commutation in the derivation of Eq. (2.26), see appendix A.1.

The sum of the zero-point energies E_{qf} of the quasiparticle vacuum can be evaluated in the continuum limit $\sum_{\boldsymbol{p}}{}' \to [V/(2\pi)^3] \int_{\mathbb{R}^3} d^3\boldsymbol{p}$ to obtain the LHY correction [46] with the detailed calculation in the appendix A.2 or, e.g., in Ref. [62]. It follows that

$$E_{\mathrm{qf}} = \frac{V}{2(2\pi)^3} \int_{\mathbb{R}^3} d^3\boldsymbol{p} \left\{ \omega_{\boldsymbol{p}} - \frac{\boldsymbol{p}^2}{2m} - nU + \frac{m(nU)^2}{\boldsymbol{p}^2} \right\} = \frac{8Vm^{3/2}}{15\pi^2} (nU)^{\frac{5}{2}} \,. \tag{2.27}$$

2.2.3 Thermodynamics of the Bose gas

The weakly interacting Bose gas, even at zero temperature, has a finite pressure [41]

$$P = -\left(\frac{\partial E_0}{\partial V}\right)_N = \frac{Un^2}{2} + \frac{4m^{3/2}}{5\pi^2}(nU)^{\frac{5}{2}} = P_{\mathrm{mf}} + P_{\mathrm{qf}} \,, \tag{2.28}$$

and finite bulk modulus

$$K = V\left(\frac{\partial^2 E_0}{\partial V^2}\right)_N = \frac{3Un^2}{2} + \frac{2m^{3/2}}{\pi^2}(nU)^{\frac{5}{2}} = K_{\mathrm{mf}} + K_{\mathrm{qf}} \,, \tag{2.29}$$

with their respective mean-field values P_{mf}, K_{mf} and the corrections P_{qf}, K_{qf} stemming from the quantum fluctuations. If the scattering is repulsive $U > 0$, both the pressure and the compressibility are positive, and the gas is thermodynamically stable [5, 41]. It should be noted that the performed analysis of quantum fluctuations presumes a stable mean-field, i.e. that $U > 0$, otherwise the excitation spectrum Eq. (2.25) takes on imaginary values for $|\boldsymbol{p}| < 2\sqrt{mnU}$ as shown in figure 2.5. Below in chapter 4 we briefly review mixtures of two Bose gases where an unstable mean-field can be rescued by quantum fluctuation corrections. Thermodynamically, the sound velocity $c_s = \sqrt{K(P=0)/(mn)}$ is related to the bulk modulus at zero pressure [68]. The mean-field value $c_{s,\mathrm{mf}}$ agrees with the value obtained from the long wavelength limit $|\boldsymbol{p}| \ll mc$ properties of the dispersion relation Eq. (2.25). A result which implies that the long wavelength excitations of the Bose gas are sound waves. They are regarded as the Goldstone modes of gauge symmetry breaking due to the Bose-Einstein condensation [3, 41].

The chemical potential of the Bose gas is also finite, as we have already seen for the mean-field [41]. We have

$$\mu = \left(\frac{\partial E_0}{\partial N}\right)_V = nU + \frac{4m^{3/2}}{3\pi^2}U(nU)^{\frac{3}{2}} = \mu_{\mathrm{mf}} + \mu_{\mathrm{qf}} \,. \tag{2.30}$$

As for the pressure and compressibility modulus, the chemical potential is positive for $U > 0$ and thus in the case of a stable condensate.

2.2.4 Finite temperature

If the Bose gas is at finite temperature, an additional term contributes to E_0 and consequently to the pressure, bulk modulus, and chemical potential Eqs. (2.28), (2.29), and (2.30). The thermal contribution at the inverse temperature $\beta = 1/T$ is determined by the dispersion relation Eq. (2.25) and is

$$E_{\text{th}} = \frac{1}{\beta} \sum_{\boldsymbol{p}}{}' \ln\left(1 - e^{-\beta\omega_{\boldsymbol{p}}}\right) . \tag{2.31}$$

Like the LHY correction in Eq. (2.27), this is evaluated in the continuum limit. The addition of the low-temperature limit allows the approximation

$$\ln\left(1 - e^{-\beta\sqrt{\frac{\boldsymbol{p}^2}{2m}\left(\frac{\boldsymbol{p}^2}{2m}+2Un\right)}}\right) \approx \ln\left(1 - e^{-\beta\sqrt{\frac{Un\boldsymbol{p}^2}{m}}}\right) , \tag{2.32}$$

of the dispersion in the integrand by its phononic part [41, 62]. The detailed calculation is given in appendix A.3. The computation then can be performed analytically and yields the additional thermal contributions

$$\begin{aligned} E_{\text{th}} &= \frac{-Vm^{3/2}\pi^2}{90\beta^4(Un)^{3/2}} , & P_{\text{th}} &= \frac{m^{3/2}\pi^2}{36\beta^4(Un)^{3/2}} , \\ K_{\text{th}} &= \frac{-m^{3/2}\pi^2}{24\beta^4V(Un)^{3/2}} , & \mu_{\text{th}} &= \frac{m^{3/2}\pi^2}{60\beta^4(Un)^{3/2}n} . \end{aligned} \tag{2.33}$$

The considerations of the previous sections, starting with section 2.1, can be formulated analogously in arbitrary dimension d. We then discuss the Hamiltonian of the single interacting Bose species, where each atom occupies the same internal state Eq. (2.13), in d dimensions for equivalent low energy and small gas parameter asymptotics. This reproduces analogous results for the pseudopotential, Bogoliubov theory, ground state energy, dispersion relation, etc., which we will use in later chapters where we consider systems with spatial dimensionality other than three, or even just generic d dimensions.

2.3 – Introduction to the cavity BEC system

Placing an ultracold gas of atoms in an optical resonator has been a vastly successful endeavor in the study of condensed matter. The idea of utilizing quantum systems to simulate quantum physics and thus gain a new and deeper understanding of the phenomena of the quantum mechanical world was proposed more than 40 years ago by Richard Feynman [1].

A noteworthy first mention of the achievements in cavity BECs is the realization of the open Dicke model [23], which is the driven-dissipative pendant of the fundamental model of light-matter interaction and in quantum optics [24]. The discovery includes the second-order non-equilibrium quantum phase transition in this system [23]. This achievement already highlights the advantage of the setup, which allows in situ measurements of the light field, allowing direct observation of the superradiant order parameter from simple photon counting to elaborate correlations such as the $g^{(2)}$-function by heterodyne detection schemes [28, 69]. The occurring quantum Dicke phase transition to the superradiant phase is accompanied by a $\mathbb{Z}_2$ symmetry breaking [69] and the softening of a roton-like mode [35] into a self-organized checkerboard lattice phase [23]. With superfluid coherence prevailing between lattice sites, this phase exhibits supersolid-like properties [26, 70]. For increasingly stronger pumping, the phase diagram also shows a Mott phase in which the coherence between lattice sites has broken down in both a self-organized checkerboard [25] and a normal square lattice arrangement [26]. The driven-dissipative nature combined with the feasibility of in situ measurements lends itself to the realization of all kinds of dynamical and non-equilibrium phenomena. For example, phenomena like quantum fluctuations at a driven-dissipative phase transition [28], a dynamical Dicke phase transition with hysteresis [71], and both discrete and continuous time crystals [72–74].

Modifications of the setup allow the realization of other lattice geometries utilizing a different pumping geometry as in Refs. [70, 75]. More elaborate pumping schemes for the atoms are possible, for example, creating a Λ-state scheme of internal atomic transitions [76] instead of the usual two-state atomic system [23]. It was also predicted that in the interplay with the Rydberg atom interaction, a superglass could be formed [77]. Furthermore, it was proposed to paint effective atom-atom interaction potentials using the pump beam [78]. The step from a single cavity mode to a nearly degenerate confocal cavity yields tunable interaction ranges and, for example, the creation of an optical phonon lattice with sound [79]. This list is of course far from being complete, but rather biased towards the quantum mechanical physics on which this thesis builds. Although not directly relevant to this thesis, we would also like to mention the possibility of using fermionic atomic species instead of bosonic ones [80] and the possibilities of studying topological phenomena [81, 82].

2.3.1 Purcell effect

In this thesis, we study atoms that behave as two-level systems illustrated in figure 2.6. The two energy levels of a single atom are its ground state $|g\rangle$ and its excited state $|e\rangle$, separated by the frequency ω_A. To understand the magic of cavity quantum electrodynamics, we must first consider the two-state system in a vacuum without a cavity. When excited to the state $|e\rangle$, the two-level system will eventually emit a photon and return to the state $|g\rangle$ [11]. Quantum mechanically speaking, the vacuum is a bath of electromagnetic modes with the canonical quantization of the electrodynamic vector potential of a single radiation mode $\boldsymbol{k}$ [83, 84]

$$\hat{A}_{\boldsymbol{k}}(\boldsymbol{r},t) = \frac{\boldsymbol{\epsilon}_{\boldsymbol{k}}}{\sqrt{4\epsilon_0 \mathcal{V}\omega_{\boldsymbol{k}}}} \left[\hat{a}_{\boldsymbol{k}} e^{-i(\boldsymbol{k}\boldsymbol{r}-\omega_{\boldsymbol{k}}t)} + \hat{a}_{\boldsymbol{k}}^{\dagger} e^{i(\boldsymbol{k}\boldsymbol{r}-\omega_{\boldsymbol{k}}t)}\right] \tag{2.34}$$

where the annihilation $\hat{a}_{\boldsymbol{k}}$ and creation $\hat{a}_{\boldsymbol{k}}^{\dagger}$ operators of the second quantization formalism are akin to the quantum harmonic oscillator ladder operators $[\hat{a}_{\boldsymbol{k}}, \hat{a}_{\boldsymbol{k}'}^{\dagger}] = \delta^{(3)}_{\boldsymbol{k},\boldsymbol{k}'}$. Each radiation mode is thus interpreted as a quantum harmonic oscillator of frequency $\omega_{\boldsymbol{k}}$, so that

$$\hat{H}_{\text{field}} = \sum_{\boldsymbol{k}} \omega_{\boldsymbol{k}} \left(\hat{a}^{\dagger}_{\boldsymbol{k}} \hat{a}_{\boldsymbol{k}} + \frac{1}{2} \right) . \tag{2.35}$$

The quantization volume is $\mathcal{V}$ and we have the polarization of the mode $\boldsymbol{\epsilon_k}$ and the permittivity of free space ϵ_0. Due to its coupling to the bath, the atom dissipates energy and the photoemission is irreversible, giving rise to the phenomenon of spontaneous emission [11].

The probability Γ_0 that a photon will be emitted, i.e. the probability to find the two-level system in state $|e\rangle$ at time t from excitation at $t = 0$ is given by $P_e(t) \propto e^{-\Gamma_0 t}$ and determined by Fermi's golden rule $\Gamma_0 = 2\pi |\langle g|\hat{H}'|e\rangle|^2 \rho(\omega)$ [2]. For the atom-vacuum system, the key physical quantities are the Rabi frequency of the vacuum g_{eg} and the mode density $\rho_0(\omega_A)$ of the photon states available in the vacuum at ω_A [12]. The former $g_{eg} = d_{eg}\mathcal{E}_{\text{vac}}$ is the product of the electric dipole matrix element of the atom d_{eg} and the electric field amplitude of the vacuum $\mathcal{E}_{\text{vac}}$. Each harmonic oscillator in the radiation field contributes its zero point energy $\omega_{\boldsymbol{k}}/2$ so that the electric field amplitude of the vacuum is $E_{\text{vac}} = [\omega_A/(2\epsilon_0\mathcal{V})]^{1/2}$ for an arbitrary quantization volume $\mathcal{V}$, which is $\mathcal{V} \gg (2\pi/\omega_A)^3$ [12]. The mode density of the vacuum is given by $\rho_0(\omega_A) = \omega_A^2\mathcal{V}/\pi^2$, so the photon emission in vacuum is characterized by [12]

$$\Gamma_0 = 2\pi g_{eg}^2 \frac{\rho(\omega_A)}{3} = \frac{\omega_A^3}{3\pi} \frac{|d_{eg}|^2}{\epsilon_0} . \tag{2.36}$$

If a cavity is constructed around the two-level system by placing two mirrors, the vacuum field is modified because its mode density is altered [13,14]. A cavity tuned at resonance so that the emission is enhanced in the small solid angle covered by the mirrors has a mode density $\rho_{\text{cav}}(\omega_A) = \rho_0(\omega_A, \boldsymbol{k} \in \text{cav})\text{A}(\omega_\text{A})$ modified according to the Airy formula $A(\omega)$ [84]. The Airy formula is a function of the finesse $\mathcal{F} = \text{FSR}/2\kappa$ which characterizes the cavity by the ratio between the separation between cavity resonances called the free spectral range FSR and the cavity decay rate κ. Assuming a high finesse $\mathcal{F} \gg 1$ for the cavity of length L_C and mode volume $\mathcal{V}_C$, the Airy formula can be expanded to lowest order in $1/\mathcal{F}$ and the Purcell factor reads [14]

$$f_P = \frac{\Gamma_{\text{cav}}}{\Gamma_0} = \frac{6L_C}{4\pi^2\mathcal{V}_C} \frac{\mathcal{F}}{\omega_A^2} , \tag{2.37}$$

where the cavity frequency ω_C is resonant with the atomic transition ω_A.

However, the setups considered in this thesis operate with a large detuning between the cavity ω_C and the atomic transition ω_A, which suppresses spontaneous emission. Nonetheless, the effect of enhanced Rayleigh scattering is present [85, 86]. The enhanced Rayleigh scattering is based on a classical description of the atomic dipole, which is valid for large detuning between the light and the atomic transition and low saturation of the transition [86]. For this off-resonant cavity description of the Purcell effect, the atomic transition ω_A is replaced by the cavity frequency ω_C in Eq. (2.37). The Purcell factor of the far detuned TEM$_{00}$ cavity with the waist of the mode ξ leading to the effective mode volume $\mathcal{V}_C = \pi L_C \xi^2/4$ is [86]

$$f_P = \frac{24\mathcal{F}}{\pi(\xi k)^2} . \tag{2.38}$$

Thus, the cavity geometry, which determines the wavenumber k, its transversal mode waist ξ, and its finesse $\mathcal{F}$, also determines the enhanced emission into the cavity. Notably, in the case of Rayleigh scattering, the atomic transition ω_A does not play a role anymore compared to Eq. (2.38). The strength of the interaction between a single atom and the cavity light field is characterized by the single photon Rabi frequency, which for a cavity of length L_C with effective mode volume $\mathcal{V}_C$ is [86]

$$g_0 = d_{eg}\mathcal{E}_C = d_{eg}\sqrt{\frac{\omega_C}{2\epsilon_0\mathcal{V}_C}}\,, \tag{2.39}$$

with the effective electric field amplitude $\mathcal{E}_C$ of the cavity mode of frequency ω_C.

2.3.2 Driven Jaynes-Cummings model

The creation of a cavity BEC system begins at the single atom level as a realization of the Jaynes-Cummings model [87] in the driven form [88]. We consider the two-level atom with ground state $|g\rangle$ and excited state $|e\rangle$ separated by the frequency ω_A as shown in figure 2.6. The transition between the two states of the atom is captured by the raising operator $\hat{\sigma}^+ = |e\rangle\langle g|$ and the lowering operator $\hat{\sigma}^- = |g\rangle\langle e|$. A coherent pump of frequency ω_P drives the transition ω_A between the atomic ground state $|g\rangle$ and its excited state $|e\rangle$. The longitudinal profile of the pump is described by a standing wave of wavenumber k in the y-axis. Its maximum coupling is given by the Rabi frequency h_0. The width of the pump laser is assumed to be extremely large so that the transverse profile of the beam is assumed to be uniform and extends to infinity or beyond any position the atom can occupy. Consequently, the pump mode function has the mathematical expression $h(\boldsymbol{r}) = h_0 \cos ky$. The cavity has a single mode with frequency ω_C. It is described by a standing wave along the cavity axis x with a wavenumber effectively identical to that of the pump mode k. Its transverse mode is TEM_{00} with a waist ξ. In this chapter, we also assume that the cavity mode is broad in the sense that the atom sees a constant profile in the yz-directions. The maximum one-photon Rabi frequency of the coupling between the cavity and the atom is given by g_0, Eq. (2.39) [86]. Here we discuss the cavity with a mode function $g(\boldsymbol{r}) = g_0 \cos kx$. The annihilation of a cavity photon is performed by the bosonic operator $\hat{a}$. In the rotating-wave approximation, where the counterrotating terms with the frequency $\omega_A + \omega_C$ are omitted, the annihilation of a cavity photon is coupled to the excitation of the atom $\hat{\sigma}^+\hat{a}$ and the emission of a cavity photon to the relaxation of the atom $\hat{\sigma}^-\hat{a}^\dagger$. Finally, $\hat{\boldsymbol{p}}^2/2m$ is the kinetic term of the atom of mass m in the driven Jaynes-Cummings Hamiltonian

$$\hat{H} = \frac{\hat{\boldsymbol{p}}^2}{2m} + \omega_A\hat{\sigma}^+\hat{\sigma}^- - ih(\boldsymbol{r})\left(\hat{\sigma}^+e^{-i\omega_P t} - \hat{\sigma}^-e^{i\omega_P t}\right) + \omega_C\hat{a}^\dagger\hat{a} - ig(\boldsymbol{r})\left(\hat{\sigma}^+\hat{a} - \hat{\sigma}^-\hat{a}^\dagger\right)\,. \tag{2.40}$$

With the unitary transformation $\hat{U}(t) = \exp[i\omega_P t(\hat{\sigma}^+\hat{\sigma}^- + \hat{a}^\dagger\hat{a})]$ we change into the frame rotating with the pump [88] and obtain

$$\hat{H} = \frac{\hat{\boldsymbol{p}}^2}{2m} - \Delta_A\hat{\sigma}^+\hat{\sigma}^- - ih(\boldsymbol{r})\left(\hat{\sigma}^+ - \hat{\sigma}^-\right) - \Delta_C\hat{a}^\dagger\hat{a} - ig(\boldsymbol{r})\left(\hat{\sigma}^+\hat{a} - \hat{\sigma}^-\hat{a}^\dagger\right)\,, \tag{2.41}$$

with the detuning of the atomic transition $\Delta_A = \omega_P - \omega_A$ and of the cavity $\Delta_C = \omega_P - \omega_C$.

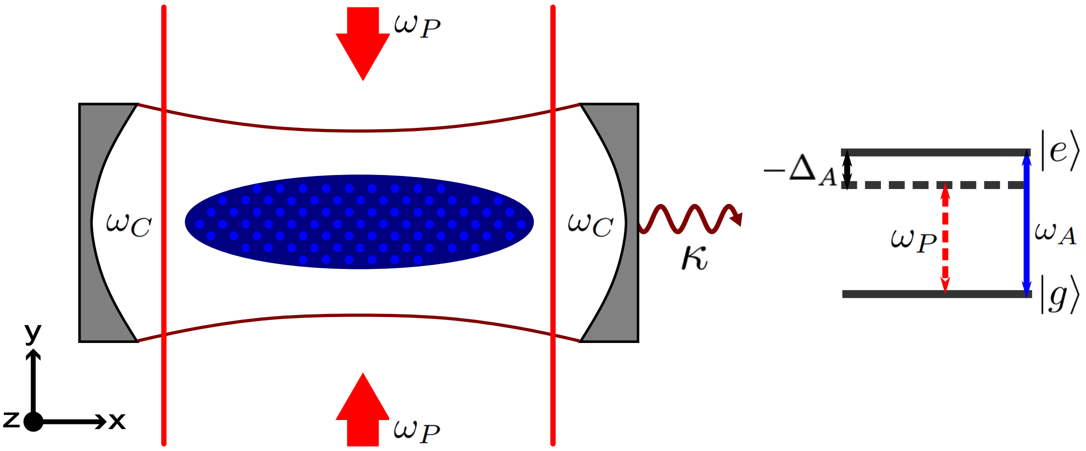

Figure 2.6: The cavity BEC setup: A condensed Bose gas (blue) is placed in the center of two mirrors creating an optical cavity. The cavity mode of frequency ω_C surrounds the condensate. The rate κ at which photons are lost from the cavity is indicated at the right mirror. Each atom is a two-level system with states $|g\rangle$ and $|e\rangle$ separated by the frequency ω_A shown on the right. The pump of frequency ω_P that excites the atoms is oriented outside the cavity mode. Without the atoms in the cavity, the cavity would always remain unoccupied. The pump drives the system equally from positive and negative y directions. It is detuned by Δ_A relative to the atomic transition ω_A. As we see in section 2.3.5, once the pump is sufficiently strong, the system self-organizes into a checkerboard lattice. This lattice is indicated by the lighter blue dots in the depiction of the condensate.

2.3.3 Field Hamiltonian of many atoms in the cavity

The generalization to N identical atoms is achieved by the second quantization field operator formalism $[\hat{\psi}_f(\boldsymbol{r}), \hat{\psi}^\dagger_{f'}(\boldsymbol{r}')] = \delta^{(3)}(\boldsymbol{r}-\boldsymbol{r}')\delta_{f,f'}$ and $[\hat{\psi}_f(\boldsymbol{r}), \hat{\psi}_{f'}(\boldsymbol{r}')] = [\hat{\psi}^\dagger_f(\boldsymbol{r}), \hat{\psi}^\dagger_{f'}(\boldsymbol{r}')] = 0$ where $f, f' \in \{g, e\}$ refer to the ground state with g and to the excited state with e [27,88]. The interaction between the atoms is included by their s-wave scattering in the form of a contact interaction of strength $U_{ff'}$. Then the generalization of the single atom Hamiltonian Eq. (2.41) to a many-body field Hamiltonian is [27,88]

$$\begin{aligned}\hat{H} = \int_V d^3\boldsymbol{r} \Big\{ & \hat{\psi}^\dagger_g(\boldsymbol{r}) \left[\frac{-\nabla^2}{2m}\right] \hat{\psi}_g(\boldsymbol{r}) + \hat{\psi}^\dagger_e(\boldsymbol{r}) \left[\frac{-\nabla^2}{2m} - \Delta_A\right] \hat{\psi}_e(\boldsymbol{r}) \\ & + \sum_{f,f'\in\{g,e\}} \left[\frac{U_{ff'}}{2} \hat{\psi}^\dagger_f(\boldsymbol{r}) \hat{\psi}^\dagger_{f'}(\boldsymbol{r}) \hat{\psi}_{f'}(\boldsymbol{r}) \hat{\psi}_f(\boldsymbol{r})\right] - ih(\boldsymbol{r}) \left[\hat{\psi}^\dagger_g(\boldsymbol{r})\hat{\psi}_e(\boldsymbol{r}) - \hat{\psi}^\dagger_e(\boldsymbol{r})\hat{\psi}_g(\boldsymbol{r})\right] \\ & - ig(\boldsymbol{r}) \left[\hat{a}^\dagger \hat{\psi}^\dagger_g(\boldsymbol{r})\hat{\psi}_e(\boldsymbol{r}) - \hat{\psi}^\dagger_e(\boldsymbol{r})\hat{\psi}_g(\boldsymbol{r})\hat{a}\right] \Big\} - \Delta_C \hat{a}^\dagger \hat{a}\,. \end{aligned} \tag{2.42}$$

To realize temperatures close to zero, heating must be avoided. Therefore, weak atomic excitation must be ensured to have negligible spontaneous emission. This is achieved by a large detuning Δ_A, which is orders of magnitude larger than the kinetic term of the atoms and the cavity dynamics [88]. It allows us to perform an adiabatic elimination of the excited state e [88] which follows the Heisenberg equation

$$i\frac{\partial \hat{\psi}_e(\boldsymbol{r})}{\partial t} = -\left[\frac{\nabla^2}{2m} + \Delta_A - U_{ee}\hat{\psi}^\dagger_e(\boldsymbol{r})\hat{\psi}_e(\boldsymbol{r}) - U_{ge}\hat{\psi}^\dagger_g(\boldsymbol{r})\hat{\psi}_g(\boldsymbol{r})\right] \hat{\psi}_e(\boldsymbol{r}) + i\left[g(\boldsymbol{r})\hat{a} + h(\boldsymbol{r})\right]\hat{\psi}_g(\boldsymbol{r})\,. \tag{2.43}$$

In the adiabatic elimination, the kinetic energy term, the time derivative, and the contact interaction are discarded relative to the large $|\Delta_\mathrm{A}|$ term to determine

$$\hat{\psi}_e(\boldsymbol{r}) = \frac{i}{\Delta_A}\left[h(\boldsymbol{r}) + g(\boldsymbol{r})\hat{a}\right]\hat{\psi}_g(\boldsymbol{r})\,. \tag{2.44}$$

We apply this to the Heisenberg equations for ground state atoms and cavity photons and find

$$\begin{aligned}
i\frac{\partial\hat{\psi}_g(\boldsymbol{r})}{\partial t} &= \left[\frac{-\nabla^2}{2m} + U_{gg}\hat{\psi}_g^\dagger(\boldsymbol{r})\hat{\psi}_g(\boldsymbol{r})\right]\hat{\psi}_g(\boldsymbol{r}) - i[h(\boldsymbol{r}) + g(\boldsymbol{r})\hat{a}^\dagger]\hat{\psi}_e(\boldsymbol{r}) \\
&= \left[\frac{-\nabla^2}{2m} + U_{gg}\hat{\psi}_g^\dagger(\boldsymbol{r})\hat{\psi}_g(\boldsymbol{r}) + \frac{h^2(\boldsymbol{r})}{\Delta_A} + \frac{g^2(\boldsymbol{r})}{\Delta_A}\hat{a}^\dagger\hat{a} + \frac{g(\boldsymbol{r})h(\boldsymbol{r})}{\Delta_A}\left(\hat{a}+\hat{a}^\dagger\right)\right]\hat{\psi}_g(\boldsymbol{r})\,, \qquad (2.45\text{a}) \\
i\frac{\partial\hat{a}}{\partial t} &= -\Delta_C\hat{a} - i\int_V d^3\boldsymbol{r}\left\{g(\boldsymbol{r})\hat{\psi}_g^\dagger(\boldsymbol{r})\hat{\psi}_e(\boldsymbol{r})\right\} \\
&= \left[-\Delta_C + \int_V d^3\boldsymbol{r}\left\{\frac{g^2(\boldsymbol{r})}{\Delta_A}\hat{\psi}_g^\dagger(\boldsymbol{r})\hat{\psi}_g(\boldsymbol{r})\right\}\right]\hat{a} + \int_V d^3\boldsymbol{r}\left\{\frac{g(\boldsymbol{r})h(\boldsymbol{r})}{\Delta_A}\hat{\psi}_g^\dagger(\boldsymbol{r})\hat{\psi}_g(\boldsymbol{r})\right\}\,. \qquad (2.45\text{b})
\end{aligned}$$

The effective Hamiltonian that describes the dynamics of Eq. (2.45) is [27,88]

$$\hat{H} = \int_V d^3\boldsymbol{r}\,\hat{\psi}^\dagger(\boldsymbol{r})\left[\frac{-\nabla^2}{2m} + \frac{h^2(\boldsymbol{r})}{\Delta_A} + \frac{g^2(\boldsymbol{r})}{\Delta_A}\hat{a}^\dagger\hat{a} + \frac{g(\boldsymbol{r})h(\boldsymbol{r})}{\Delta_A}\left(\hat{a}+\hat{a}^\dagger\right) + \frac{U}{2}\hat{\psi}^\dagger(\boldsymbol{r})\hat{\psi}(\boldsymbol{r})\right]\hat{\psi}(\boldsymbol{r}) - \Delta_C\hat{a}^\dagger\hat{a}\,, \qquad (2.46)$$

where we have suppressed the index of the ground state field operators $\hat{\psi}_g = \hat{\psi}$. First in the square brackets is the kinetic term of the atoms. This is followed by the self-interference of the pump $h^2(\boldsymbol{r})/\Delta_A$. It results from the standing wave of the pump along both the positive and negative y-directions. The third term is characterized by the coupling $U_0 = g_0^2/\Delta_A$ of a single atom to the cavity. It takes the form of an optomechanical coupling $g^2(\boldsymbol{r})\hat{\psi}^\dagger(\boldsymbol{r})\hat{a}^\dagger\hat{a}\hat{\psi}(\boldsymbol{r})$ and is the dynamical refractive index experienced by the cavity due to the presence of the atoms. The next term follows the underlying potential of the product of the pump and cavity mode functions $g(\boldsymbol{r})h(\boldsymbol{r})$ and describes the scattering of a photon between the pump and the cavity via the adiabatically eliminated absorption and emission by the atoms. Finally, there is the contact interaction between the atoms $U = 4\pi a_s/m$, Eq. (2.12). Outside the integral the cavity mode dynamics with the detuning Δ_C is given. In this thesis, we focus on systems where the atomic transition is red-detuned $\Delta_A < 0$ to the pump. This leads to a negative single atom coupling $U_0 < 0$, which means that the light field is attractive for the atoms. Given a cavity light field they will accumulate at its intensity maxima [27]. In addition, we will also consider the cavity red-detuned $\Delta_C < 0$ to the pump.

2.3.4 Setup of the experiment

The central element of the experimental setup is a vacuum chamber in which a BEC [15,16] is prepared in a trap by cooling techniques. For the experimental run, this BEC is placed in the mode of a high-finesse optical resonator cavity. Once in place, it is pumped by an additional laser beam. To go into a little more detail about the single cavity mode BEC experiment we use the example of the setup in Hamburg [89–93]. It distinguishes itself due to its small resonator linewidth, which in drastically simplified terms results from a large distance between the mirrors of about 5 cm [91], but serves here as an example for a generic cavity BEC setup. This section is only intended to give a brief insight into the experimental reality and is not a full explanation of the processes and protocols. Rather, it is designed to give an idea of how the experiment is performed, what its advantages are, and where its limitations lie. Most of the details can be found in the references [89, 90]. The transport to the quadrupole-Ioffe configuration trap is described in detail in Ref. [90] and the cavity stabilization can be studied in detail in Refs. [91,92].

To prepare a BEC, rubidium atoms ^{87}Rb are laser-cooled in a magneto-optical trap [94–96] in a separate section of the vacuum chamber. They are then cooled using the optical molasses technique and pumped to the magnetic state $|F = 2, m_f = +2\rangle$, which is optimal for later trapping in the

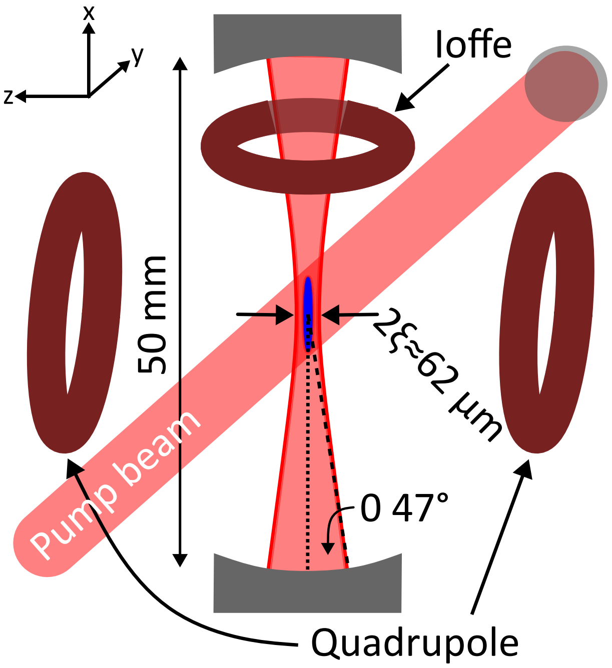

Figure 2.7: Setup in the science chamber with the trapped Bose condensate(blue) in the red light field of the pump and cavity mode. The pump beam is retroreflected by a mirror. The copper rings represent the coils of the quadrupole-Ioffe trapping configuration. In this setup, gravity is along the negative x direction. The figure is based on Refs. [25, 91].

magnetic quadrupole-Ioffe configuration [97] in the science chamber. The atoms are transported to the science chamber using transfer coils. Trapped in the quadrupole-Ioffe configuration shown in figure 2.7, the ensemble is further cooled by evaporative cooling according to the protocol described in Ref. [98]. The atoms are pumped from the state $|F = 2, m_f = +2\rangle$ via $|F = 2, m_f = +1\rangle$ to $|F = 2, m_f = 0\rangle$. In the latter state, they are no longer confined and leave the trap. The remaining ensemble thermalizes to a lower temperature due to its weak atom-atom interaction. After a second cooling phase with another radio frequency and an additional offset between the m_f states to reduce atomic losses, the remaining ensemble drops below the critical condensate temperature. Typically, the final condensate prepared in this setup has up to 10^5 atoms at a temperature of about 100 nK [91].

After the BEC is prepared, it needs to be overlapped by the TEM_{00} cavity mode. The experiment relies on a TEM_{11} reference laser, which is crucial for the stabilization of the cavity mode, and therefore needs to run permanently. Hence, the final BEC preparation step was performed about 100 μm outside the cavity mode [91]. A microtransport protocol is used to maneuver the BEC through the gap in the TEM_{11} reference mode, which is barely 10 μm wide [90, 91]. Once the BEC is placed in the center of the cavity, the experimental protocol using the pump beam can commence. The trapping frequencies during the experimental run are on the order of $2\pi \times 10$ Hz along the cavity axis x and $2\pi \times 100$ Hz in the y and z directions perpendicular to the cavity. In terms of spatial extent, the cloud is thus on the order of 10s of micrometers along the cavity axis and single-digit micrometers perpendicular to the cavity axis [93].

The optical cavity stores photons between its highly reflective mirrors, as seen in figure 2.7. How well the photons are stored is determined by the cavity field decay rate κ. In the Hamburg experiment the photons cycle on average $N_{\text{cyc}} \gtrsim 10^5$ times through the cavity [91]. Consequently, they travel a significant distance in this particularly long cavity, so their lifetime is long and conversely their decay rate $\kappa \approx 4.5$ kHz is remarkably small [91]. In fact, it is comparable to the recoil frequency $\omega_R = k^2/2m \approx 3.5$ kHz experienced by an atom when it absorbs or emits either a cavity photon or a pump photon which have approximately the same wavenumber k. Accordingly, the cavity is said to operate in the recoil-resolved regime [99]. Consequently, it is classified as an optical resonator with narrow linewidth 2κ and ultra-high finesse $\mathcal{F} = \mathrm{FSR}/2\kappa \approx \pi N_{\mathrm{cyc}}$, where FSR is the free spectral range, i.e., the separation between cavity resonances.

The key role of the optical cavity for our purposes is its influence on the vacuum fluctuation that underlies spontaneous emission [13]. This Purcell effect favors Rayleigh scattering into the cavity mode over emission into the remaining solid angle of free space. The ratio of scattering into the cavity to scattering into free space, the Purcell factor Eq. (2.38), is $\propto \mathcal{F}/(\xi k)^2$. It depends on the finesse $\mathcal{F}$, the wavenumber k, and the cavity waist ξ. The waist characterizes the width of the transverse TEM_{00} mode by the $1/e$ value of its electric field at the narrowest section of the mode, as shown in figure 2.7. The waist of the TEM_{00} cavity mode is about 31 μm [90].

The transversal pump beam is oriented along the y-axis. It is retroreflected on the other side to create the standing wave pump [91,92]. The pump is a laser of wavelength 803 nm, which is about the resonance of the cavity so that the entire light field has roughly the wavelength 803 nm, corresponding to the wavenumber $k = 7.8\ \mu\mathrm{m}^{-1}$ [89–92]. The light field is red-detuned compared to the atomic resonances of rubidium at 795 and 780 nm [91].

When the atoms are placed in the cavity, they act as a dynamic refractive index that changes the resonance frequency of the cavity. The atoms and cavity are coupled by the processes described in the effective Hamiltonian of the system Eq. (2.46). Because the cooperative coupling of many atoms leads to a resonance frequency shift greater than the cavity linewidth 2κ, the setup is classified as strongly coupled [91].

2.3.5 Mean-field approximation and self-organization

The coupled mean-field equations for the cavity $\alpha = \langle \hat{a} \rangle$ and the condensate wave function $\psi(\boldsymbol{r}) = \langle \hat{\psi}(\boldsymbol{r}) \rangle$ with the single-atom coupling $U_0 = g_0^2/\Delta_A$, the pump strength $\varpi_P = -h_0^2/4\Delta_A$, and the atom-cavity coupling $\lambda = g_0 h_0/2\Delta_A = \sqrt{-U_0 \varpi_P}$ are [100]

$$\begin{aligned} i\frac{\partial \alpha}{\partial t} &= \left[-\Delta_C + \int_V d^3\boldsymbol{r}\,\left\{U_0 \cos^2(kx)|\psi(\boldsymbol{r})|^2\right\} - i\kappa\right]\alpha \\ &\quad + \int_V d^3\boldsymbol{r}\,\left\{2\lambda \cos(kx)\cos(ky)|\psi(\boldsymbol{r})|^2\right\}\,, \end{aligned} \tag{2.47a}$$

$$\begin{aligned} i\frac{\partial}{\partial t}\psi(\boldsymbol{r},t) &= \left[-\frac{\nabla^2}{2m} + U|\psi(\boldsymbol{r})|^2 - 4\varpi_P \cos^2(ky) + U_0 \cos^2(kx)|\alpha|^2 \right. \\ &\quad \left. + 4\lambda \cos(kx)\cos(ky)\mathrm{Re}(\alpha)\right]\psi(\boldsymbol{r},t)\,, \end{aligned} \tag{2.47b}$$

where the cavity mode linewidth κ has been included. The steady state solution of the dissipative system $(\alpha_0, \psi_0(\boldsymbol{r}))$ with $\psi(\boldsymbol{r},t) = \psi_0(\boldsymbol{r})e^{-i\mu t}$ obeys the equations

$$\alpha_0 = \frac{2\lambda}{-\Delta_C + U_0 \int_V d^3\boldsymbol{r}\,\{\cos^2(kx)|\psi(\boldsymbol{r})|^2\} - i\kappa} \int_V d^3\boldsymbol{r}\,\left\{\cos(kx)\cos(ky)|\psi(\boldsymbol{r})|^2\right\}\,, \tag{2.48a}$$

$$\mu\psi_0(\boldsymbol{r}) = \left[-\frac{\nabla^2}{2m} + U|\psi_0(\boldsymbol{r})|^2 - 4\varpi_P + U_0\cos^2(kx)|\alpha_0|^2 + 4\lambda\cos(kx)\cos(ky)\mathrm{Re}(\alpha_0)\right]\psi_0(\boldsymbol{r})\,. \tag{2.48b}$$

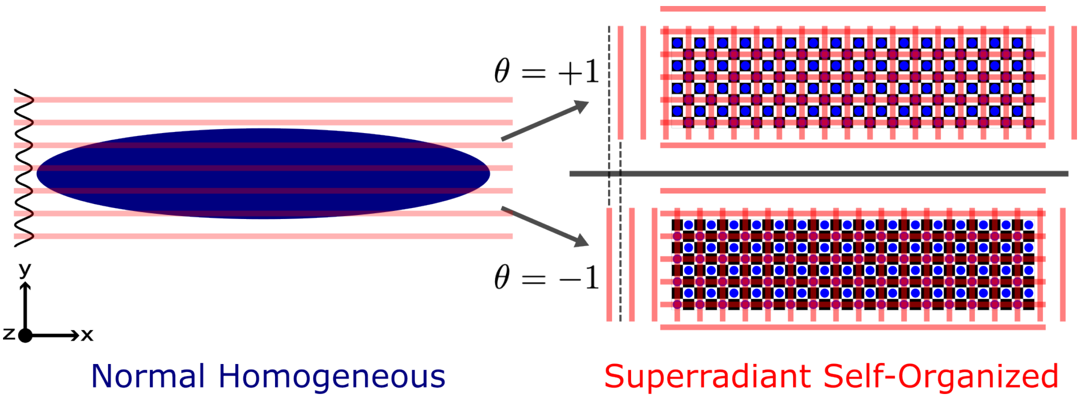

Figure 2.8: Homogeneous BEC in blue on the left with a pump wave below the critical value in red. On the right, the self-organized checkerboard of the condensate with the superradiant cavity light field along the x-axis due to the pump above the threshold. The $\mathbb{Z}_2$ symmetry-breaking can be seen both in the lattice choice on the checkerboard and in the phase of the superradiant cavity light. To visualize the phase difference, dashed lines are added to two of the cavity light maxima.

It can be solved by imaginary-time propagation [100] as typical for a Gross-Pitaevskii-like equation. The mean value

$$\theta = \int_V d^3\boldsymbol{r} \left\{ \cos(kx)\cos(ky)|\psi(\boldsymbol{r})|^2 \right\} , \tag{2.49}$$

is an order parameter for the self-organization of the condensate into either the even $\theta = +1$ or odd $\theta = -1$ sites of a lattice that then resembles a checkerboard as visualized in figure 2.8 [23, 100]. This order parameter occurs directly in Eq. (2.48a) so that the cavity steady state $\alpha_0 \propto \theta$ is connected to it. A homogeneous condensate has $\theta = 0$ and therefore in the normal phase, the cavity steady state vanishes $\alpha_0 = 0$. Each density grating $\theta = \pm 1$ in figure 2.8 satisfies the Bragg condition to maximize the coherent scattering of photons from the pump field into the cavity and vice versa [101]. It thus realizes a macroscopically large α. The resulting interference between the pump and intra-cavity light fields, as shown in figure 2.8, leads to a two-dimensional potential that stabilizes the prevailing density distribution of atoms on the checkerboard.

The kinetic energy and the collision term in the Gross-Pitaevskii type equation Eq. (2.47b) try to maximize the spread of the wave function $\psi_0(\boldsymbol{r})$. Once the coupling to the cavity $\lambda = g_0 h_0 / 2\Delta_A$ reaches a critical value λ_{cr} it can be overcome. However, one has to look at condensate and cavity photon fluctuations to understand the underlying process. The scattered field of each atom depends on its position in the cavity and on the pump field [101]. Atoms separated by half a wavelength produce the same light field but with opposite phases. Therefore their contributions cancel each other out. A density fluctuation, however, facilitates the generation of a small field with a random phase. In a red-detuned cavity, the attraction to the antinodes of the field redistributes the atoms. If the coupling between the atoms and the cavity λ is strong enough, these condensate fluctuations trigger the transition. Since the created atomic density lattice induces strong scattering into the cavity mode, the optical potential is deepened. Subsequently, the effective light field potential $\cos kx \cos ky$ is sufficiently large and the order parameter θ of the self-organized phase takes on a finite value [100]. This phase transition is accompanied by the spontaneous $\mathbb{Z}_2$ symmetry-breaking between even and odd lattice sites [69, 100]. The fluctuations then initiate a runaway process stabilizing the atomic density grating [101]. Hence, at zero temperature, quantum fluctuations determine the fate of the condensate [100]. We will review them in more detail in the next section 2.3.6. The critical coupling λ_{cr} can be determined analytically by the linear stability analysis of the trivial solution of Eq. (2.48):

$\alpha_0 = 0$, $\psi_0(\boldsymbol{r}) = \sqrt{n}$, $\mu = nU$ [100]. Equivalently, it is obtained as a by-product of examining the collective excitation spectrum, which will be reviewed next.
The self-organization was observed in the experiment [23]. In an experiment, the setup is advantageous because its cavity loss channel offers the possibility to monitor the system in situ [102–104]. This is particularly applicable to the self-organization phase transition due to the relationship between the cavity steady state and the self-organization order parameter $\alpha_0 \sim \theta$. On the other hand, the drive directly determines the light-matter coupling $\lambda \propto h_0$ via the pump Rabi frequency h_0, thus providing exceptional control over the model. The simplest experimental run would start with a condensate initialized in the absence of the external drive. Thereupon the pump is ramped up until the critical value of the phase transition λ_{cr} is reached [23]. At this point, a macroscopic number of photons is detected in the cavity output field as the atoms organize into the symmetry-broken checkerboard lattice [23]. The relation between the order parameter θ and the cavity steady state α_0 also encapsulates that the phase of the light field is linked to the sign of $\theta = \pm 1$ in the self-organized phase. The cavity light consequently carries the information on whether the atoms have organized into even or odd lattice sites. Note that even and odd sites are relative terms here, depending on the chosen definition of sites and, equivalently, the choice of zero phase in the cavity light. By measuring not only the amplitude of the outcoupled cavity light but also its phase in a heterodyne detection scheme, the spontaneous $\mathbb{Z}_2$ symmetry-breaking nature of the phase transition was verified [69].

2.3.6 Collective excitations

The cavity is damped with the rate of photon loss κ. This adds the term $i\kappa\hat{a}$ to the Heisenberg equation for the cavity operator Eq. (2.45b) as well as the fluctuation operator $\hat{\Xi}$ in accordance with the fluctuation-dissipation theorem [32]. The cavity dissipation produces white noise which means the fluctuation operator has only one nontrivial correlation function $\langle\hat{\Xi}(t)\hat{\Xi}^\dagger(t')\rangle = 2\kappa\delta(t-t')$ [32]. The collective excitations around the steady state solutions following the ansatz

$$\hat{a}(t) = \alpha_0 + \delta\hat{a}\,, \qquad\qquad \hat{\psi}(\boldsymbol{r},t) = e^{-i\mu t}\left[\psi_0(\boldsymbol{r}) + \hat{\phi}(\boldsymbol{r},t)\right], \tag{2.50}$$

obey in linear order the Heisenberg-Langevin equations [36, 100]

$$\begin{aligned} i\frac{\partial}{\partial t}\delta\hat{a} = &\left[-\Delta_C + U_0\int_V d^3\boldsymbol{r}\left\{\cos^2(kx)|\psi_0(\boldsymbol{r})|^2\right\} - i\kappa\right]\delta\hat{a} + i\hat{\Xi} \\ &+ U_0\alpha_0\int_V d^3\boldsymbol{r}\left\{\cos^2(kx)\left[\psi_0^*(\boldsymbol{r})\hat{\phi}(\boldsymbol{r}) + \hat{\phi}^\dagger(\boldsymbol{r})\psi_0(\boldsymbol{r})\right]\right\} \\ &+ 2\lambda\int_V d^3\boldsymbol{r}\left\{\cos(kx)\cos(ky)\left[\psi_0^*(\boldsymbol{r})\hat{\phi}(\boldsymbol{r}) + \hat{\phi}^\dagger(\boldsymbol{r})\psi_0(\boldsymbol{r})\right]\right\}, \end{aligned} \tag{2.51a}$$

$$\begin{aligned} i\frac{\partial}{\partial t}\hat{\phi}(\boldsymbol{r}) = &\left[-\frac{\nabla^2}{2m} + 2U|\psi_0(\boldsymbol{r})|^2 - 4\varpi_P\cos^2(ky) + U_0\cos^2(kx)|\alpha_0|^2\right. \\ &\qquad\qquad\qquad \left. + 4\lambda\cos(kx)\cos(ky)\mathrm{Re}(\alpha_0) - \mu\right]\hat{\phi}(\boldsymbol{r}) \\ &+ U\psi_0^2(\boldsymbol{r})\hat{\phi}^\dagger(\boldsymbol{r}) + U_0\cos^2(kx)\psi_0(\boldsymbol{r})\left[\alpha_0^*\delta\hat{a} + \delta\hat{a}^\dagger\alpha_0\right] + 2\lambda\psi_0(\boldsymbol{r})\left[\delta\hat{a} + \delta\hat{a}^\dagger\right]. \end{aligned} \tag{2.51b}$$

The equations couple the fluctuations to their Hermitian conjugates. Therefore, it is convenient to introduce separate operators for the propagation positive in time + and negative in time −. This yields the ansatz that doubles the operator space by adding frequencies with negative real parts [100]

$$\delta\hat{a} = e^{-i\Omega t}\delta\hat{a}_+ + e^{i\Omega^* t}\delta\hat{a}_-^\dagger\,, \qquad\qquad \hat{\phi}(\boldsymbol{r}) = e^{-i\Omega t}\hat{\phi}_+(\boldsymbol{r}) + e^{i\Omega^* t}\hat{\phi}_-^\dagger(\boldsymbol{r})\,. \tag{2.52}$$

The Langevin equations (2.51) need to be fulfilled separately for the terms $e^{-i\Omega t}$ and $e^{i\Omega^* t}$, so that the fluctuations are described by the linear eigenvalue equation [100]

$$\Omega \begin{pmatrix} \delta\hat{a}_+ \\ \delta\hat{a}_- \\ \hat{\phi}_+(\boldsymbol{r}) \\ \hat{\phi}_-(\boldsymbol{r}) \end{pmatrix} = \underline{M} \begin{pmatrix} \delta\hat{a}_+ \\ \delta\hat{a}_- \\ \hat{\phi}_+(\boldsymbol{r}) \\ \hat{\phi}_-(\boldsymbol{r}) \end{pmatrix} , \tag{2.53}$$

with the non-Hermitian stability matrix $\underline{M}$. Through some mathematical trickery elaborated on in Ref. [100] one finds that the eigenvalues describing the system dynamics come in pairs $(\Omega, -\Omega^*)$ with a real part of opposite sign and the same imaginary part, i.e. damping [100]. For an arbitrary mean-field $(\alpha_0, \psi_0(\boldsymbol{r}))$ they can only be obtained numerically. Below the self-organization threshold, though, the spectrum becomes analytically calculable. As discussed, in the normal phase the steady state is described by the trivial solution $\alpha_0 = 0$, $\psi_0 = \sqrt{n}$, and $\mu = Un$ of Eq. (2.48). The cavity couples only to the Fourier component $\cos(kx)\cos(ky)$ which is commensurable with the coupling potential in Eq. (2.51). All other modes outside this closed subspace are described approximately by the familiar condensate excitations $\omega_{\boldsymbol{p}} = \sqrt{(\boldsymbol{p}^2/2m)[(\boldsymbol{p}^2/2m) + 2Un]}$ of the Bose gas Bogoliubov dispersion Eq. (2.25) assuming that the pump ϖ_P is negligible. Next we insert the trivial mean-field along with the relevant Fourier component of the fluctuations $\hat{\phi}(\boldsymbol{r}) = 2\cos(kx)\cos(ky)\hat{\phi}_1/\sqrt{V}$ into the Langevin equations given in Eq. (2.51). Using $\int_{-L/2}^{+L/2} du \cos(ku) = 0$ and $\cos^2(ku) = [1 + \cos(2ku)]/2$, the fluctuations in the normal phase thus follow in the form

$$i\frac{\partial}{\partial t} \begin{pmatrix} \delta\hat{a} \\ \delta\hat{a}^\dagger \\ \hat{\phi}_1 \\ \hat{\phi}_1^\dagger \end{pmatrix} = \underline{M} \begin{pmatrix} \delta\hat{a} \\ \delta\hat{a}^\dagger \\ \hat{\phi}_1 \\ \hat{\phi}_1^\dagger \end{pmatrix} + i \begin{pmatrix} \hat{\Xi} \\ \hat{\Xi}^\dagger \\ 0 \\ 0 \end{pmatrix} , \tag{2.54}$$

with

$$\underline{M} = \begin{pmatrix} -\delta_C - i\kappa & 0 & +\lambda\sqrt{N} & +\lambda\sqrt{N} \\ 0 & +\delta_C - i\kappa & -\lambda\sqrt{N} & -\lambda\sqrt{N} \\ +\lambda\sqrt{N} & +\lambda\sqrt{N} & +(2\omega_R + Un - \varpi_P) & +Un \\ -\lambda\sqrt{N} & -\lambda\sqrt{N} & -Un & -(2\omega_R + Un - \varpi_P) \end{pmatrix} . \tag{2.55}$$

The stability matrix $\underline{M}$ is non-normal due to the cavity dissipation κ. Consequently, it has different left and right eigenvectors and the mentioned eigenvalue pairing $(\Omega, -\Omega^*)$. Without any coupling $\lambda = 0$ the eigenvalues $\Omega \in \mathbb{C}$ of the stability matrix are one pair for the cavity with the real part $\pm\delta_C$ with

$$\delta_C = \Delta_C - \frac{U_0 N}{2} , \tag{2.56}$$

and the negative damping which is the imaginary part $-\kappa$. The other pair is the matter mode of the real part $\pm\omega_1$ with

$$\omega_1 = \sqrt{(2\omega_R - \varpi_P)(2\omega_R - \varpi_P + 2Un)} . \tag{2.57}$$

When the coupling λ is turned on, the cavity and matter modes hybridize and form two polaritons as shown in figure 2.9. If $|\Delta_C| \gg 2\omega_R$, the mode with the larger real part of the eigenvalue will always remain predominantly cavity-like and the other predominantly matter-like.

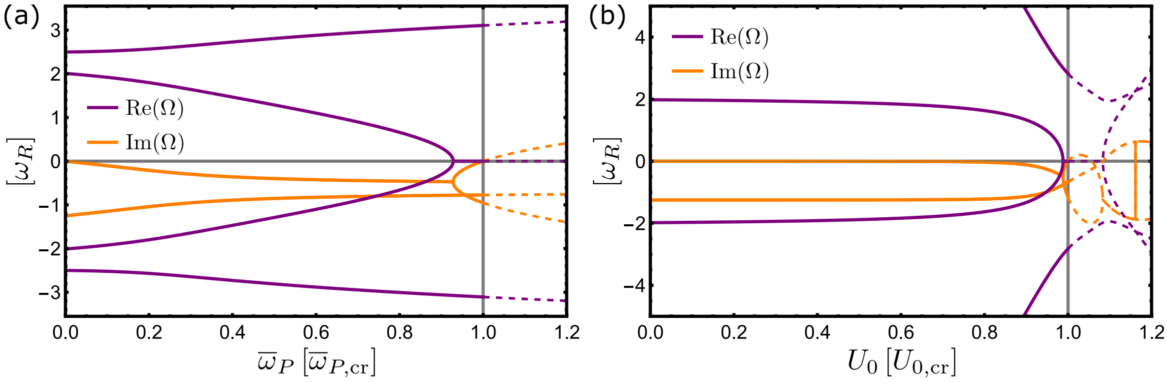

Figure 2.9: Eigenvalues Ω of the stability matrix $\underline{M}$ versus pump strength ϖ_P (a) and single atom coupling U_0 (b). The real part of Ω_M gives the dynamic frequency, while negative imaginary parts correspond to the damping of the system. The critical pump $\varpi_{P,\mathrm{cr}}$ or single atom coupling $U_{0,\mathrm{cr}}$ is at the point $\mathrm{Im}(\Omega) = 0$ where the upper branch of the damping crosses into the positive half-plane. Beyond the critical point $\lambda > \lambda_{\mathrm{cr}}$ the simple approximation that the atomic excitation is just a single Fourier mode $\hat{\phi}_1$ breaks down. Thus, the eigenvalues in this region are shown as dashed lines. Parameters are $\Delta_C = -27.5\,\omega_R$, $\kappa = 1.25\,\omega_R$, $nU = 10^{-2}\,\omega_R$, $U_0 = -10^{-3}\,\omega_R$, $\varpi_P = 2.8 \times 10^{-2}\,\omega_R$, $N = 5 \times 10^4$.

The smaller polariton mode becomes soft when the coupling between the atoms and the cavity λ reaches the critical value

$$\lambda_{\mathrm{cr}} = \left(\sqrt{-U_0\varpi_P}\right)_{\mathrm{cr}} = \sqrt{\frac{\delta_C^2 + \kappa^2}{-\delta_C}\,\frac{2\omega_R - \varpi_P + 2Un}{4N}}\,. \tag{2.58}$$

It is determined as the coupling strength for which the soft mode polariton becomes unstable. The imaginary part, i.e. the damping of the mode, acquiring a positive value in its upper branch indicates this, as can be seen in the figure 2.9. Note also that Eq. (2.58) is in principle implicit regarding the critical value for the single atom coupling U_0 and the pump strength ϖ_P. The first, U_0, is small compared to $|\Delta_C|$, and the second, ϖ_P, occurs only if the system is treated in more than one dimension. A crucial ramification of this result is that the criticality of the phase transition survives in the presence of dissipation [36]. Although, the study of the divergence of the fluctuation near the phase transition point λ_{cr} shows that the critical exponent is modified from 1/2 to 1 by the addition of the dissipative effect [36].
Here the dissipation was included because we considered the cavity loss channel. The channel allows to measure the cavity light by detecting the outgoing photons [102–104]. Since the atomic fluctuations are strongly correlated with the cavity fluctuations due to the formation of polaritons, the atomic state can also be monitored non-destructively in this way. Thus, in the cavity BEC setup, fluctuations in the matter and light sectors can be studied in situ [102–104].

2.3.7 Mapping to the Dicke model

The self-organization of the homogeneous atomic gas under a sufficiently strong coupling to the cavity light can be mapped to the Dicke model [105]. The Dicke model is one of the fundamental models of light-matter interaction [24]. It describes the coupling of a two-level system to a single bosonic light mode. The coupling is such that both the excitation and the relaxation of the two-level matter are linearly coupled to the creation and annihilation of a photon, see Eq. (2.62). From the analysis of collective excitations, it was determined that the Hilbert space of the atomic field $\hat{\psi}$ is closed below

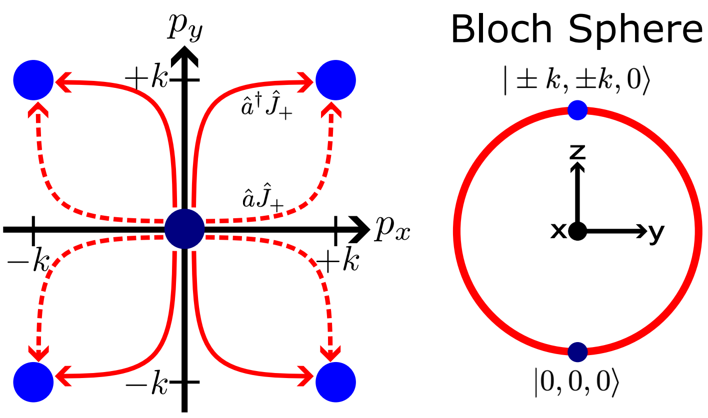

Figure 2.10: Atomic excitation paths from the condensate zero momentum mode to the checkerboard modes $\hat{\psi}_1^\dagger \hat{\psi}_0$ in momentum space. In the Dicke model, the atomic excitations are represented by $\hat{J}_+$ on the Bloch sphere sketch on the right, where according to Eq. (2.62) the coupling term is $\hat{J}_x$. Note that the spin moving on the Bloch sphere is macroscopically large $\propto N$. The left side of the plot is adapted from Ref. [23].

the critical point. Consequently, the atomic field operator is expressed in terms of this subspace [105] in the form

$$\hat{\psi}(\boldsymbol{r}) = \frac{1}{\sqrt{V}}\hat{\psi}_0 + \frac{2}{\sqrt{V}}\cos(kx)\cos(ky)\hat{\psi}_1 \,. \tag{2.59}$$

The ansatz is inserted into the field Hamiltonian of the cavity BEC Eq. (2.46) where we make again use of $\int_{-L/2}^{+L/2} du\cos(ku) = 0$ and $\cos^2(ku) = [1+\cos(2ku)]/2$ and find

$$\begin{aligned}\hat{H} = {}& \frac{k^2}{m}\hat{\psi}_1^\dagger\hat{\psi}_1 - 2\overline{\omega}_P\left(\hat{\psi}_0^\dagger\hat{\psi}_0 + \frac{3}{2}\hat{\psi}_1^\dagger\hat{\psi}_1\right) + \frac{U_0}{2}\hat{a}^\dagger\hat{a}\left(\hat{\psi}_0^\dagger\hat{\psi}_0 + \frac{3}{2}\hat{\psi}_1^\dagger\hat{\psi}_1\right) + \lambda\Big(\hat{a}+\hat{a}^\dagger\Big)\Big(\hat{\psi}_1^\dagger\hat{\psi}_0 + \hat{\psi}_0^\dagger\hat{\psi}_1\Big) \\ & + \frac{U}{2V}\left(\hat{\psi}_0^\dagger\hat{\psi}_0^\dagger\hat{\psi}_0\hat{\psi}_0 + \hat{\psi}_1^\dagger\hat{\psi}_1^\dagger\hat{\psi}_0\hat{\psi}_0 + \hat{\psi}_0^\dagger\hat{\psi}_0^\dagger\hat{\psi}_1\hat{\psi}_1 + 4\hat{\psi}_1^\dagger\hat{\psi}_0^\dagger\hat{\psi}_0\hat{\psi}_1 + \frac{9}{4}\hat{\psi}_1^\dagger\hat{\psi}_1^\dagger\hat{\psi}_1\hat{\psi}_1\right) - \Delta_C\hat{a}^\dagger\hat{a}\,.\end{aligned} \tag{2.60}$$

It is $\hat{\psi}_0^\dagger\hat{\psi}_0 + \hat{\psi}_1^\dagger\hat{\psi}_1 = N$ due to the closed subspace. For the homogeneous condensate the occupation of the zero mode $\hat{\psi}_0$ is macroscopically large $\langle\hat{\psi}_1^\dagger\hat{\psi}_1\rangle/\langle\hat{\psi}_0^\dagger\hat{\psi}_0\rangle \sim 1/N$. Furthermore, the s-wave scattering U is considered to be very weak compared to the cavity dynamics $|\Delta_C|$ and the recoil frequency $\omega_R = k^2/2m$ transferred to an atom by a pump or cavity photon. The Hamiltonian Eq. (2.60) is vastly simplified by these approximations and follows as

$$\hat{H} = \Big(2\omega_R - \overline{\omega}_P + 2Un\Big)\hat{\psi}_1^\dagger\hat{\psi}_1 + \left(-\Delta_C + \frac{U_0 N}{2}\right)\hat{a}^\dagger\hat{a} + \lambda\Big(\hat{a}+\hat{a}^\dagger\Big)\Big(\hat{\psi}_1^\dagger\hat{\psi}_0 + \hat{\psi}_0^\dagger\hat{\psi}_1\Big)\,, \tag{2.61}$$

where we have neglected constant terms like $-2\overline{\omega}_P N$ or $Un(N-1)/2$. Application of the Schwinger representation $\hat{J}_x = (\hat{\psi}_1^\dagger\hat{\psi}_0 + \hat{\psi}_0^\dagger\hat{\psi}_1)/2$, $\hat{J}_y = (\hat{\psi}_1^\dagger\hat{\psi}_0 - \hat{\psi}_0^\dagger\hat{\psi}_1)/2i$, and $\hat{J}_z = (\hat{\psi}_1^\dagger\hat{\psi}_1 - \hat{\psi}_0^\dagger\hat{\psi}_0)/2$ yields the expression for the effective Hamiltonian [105]

$$\hat{H}_{\text{Dicke}} = \left(2\omega_R - \overline{\omega}_P + 2Un\right)\hat{J}_z - \delta_C\hat{a}^\dagger\hat{a} + 2\lambda\left(\hat{a}+\hat{a}^\dagger\right)\hat{J}_x\,, \tag{2.62}$$

that has precisely the form of a Dicke Hamiltonian and we visualize this in figure 2.10. Note, however, that the realization of the model by a cavity BEC setup is technically an open Dicke model due to its driven nature. The Dicke model exhibits a quantum phase transition [106] at the critical value

$$\lambda_{\mathrm{cr}} = \sqrt{\left(-\Delta_C + \frac{U_0 N}{2}\right) \frac{2\omega_R - \overline{\omega}_P + 2Un}{4}}\,, \tag{2.63}$$

that matches the critical point from the linear stability analysis or collective excitations around the mean-field of the normal condensate phase for $\kappa \to 0$. It is the critical point of the second-order non-equilibrium Dicke quantum phase transition [106].

The Dicke model belongs to the class of infinite-range interaction models that have effectively zero dimensionality and are mean-field exact in the thermodynamic limit $N, V \to \infty$ while $n = N/V =$ const [107]. With $\hat{J}_i \sim N$ and $\langle \hat{a}^{(\dagger)} \rangle \sim \sqrt{N}$ the coupling between the cavity light and the atoms must scale as $g_0 \sim 1/\sqrt{V}$. This is supported by the equation for the Rabi frequency $g_0 = d_{eg}\sqrt{\omega_C/(2\epsilon_0 \mathcal{V}_C)}$, Eq. (2.39), if we consider that we want to keep the ratio between the cavity mode volume $\mathcal{V}_C$ and the atomic volume V constant $V/\mathcal{V}_C =$ const. It has been shown that the diagrammatic corrections to the mean-field Hamiltonian Eq. (2.46) scale as $1/V$ relative to the mean-field diagrams [107]. This verifies that the cavity BEC setup with infinite interaction range is also mean-field exact in the thermodynamic limit [107].

The effective description in the Dicke model reveals the coupling of the zero-momentum state to the degenerate superposition of states $|\pm k, \pm k\rangle$ described by $\cos(kx)\cos(ky)$ by the scattering of a photon between pump and cavity. As depicted in Figure 2.10, an excitation to the finite momentum state $\hat{J}_+ = \sum_{\pm,\pm} |\pm k, \pm k\rangle\langle 0, 0|$ can occur by two processes as exposed by replacing $\hat{J}_x = \hat{J}_+ + \hat{J}_-$ [23]. Either a standing wave pump photon is absorbed and then a photon is emitted into the cavity $\hat{a}^\dagger \hat{J}_+$ or a cavity photon is absorbed and then light is emitted into the pump field $\hat{a}\hat{J}_+$. In the superradiant phase, both the cavity field $\langle \hat{a} \rangle$ and the atomic polarization $\langle \hat{J}_x \rangle$ take on macroscopically large values and provide the order parameter for the light and matter, respectively [23].

2.3.8 Cavity-induced long-range interaction in the atom-only picture

Starting from the Heisenberg equation Eq. (2.45b), the damping of the cavity due to photon losses of the mirror is included by the white noise dissipation characterized with the cavity decay rate κ [36]. As discussed in section 2.3.6 this adds the term $i\kappa\hat{a}$ and the fluctuation operator $\hat{\Xi}$ to Eq. (2.45b). While the equation for the atomic field Eq. (2.45a) is unchanged, the cavity field is now described by

$$i\frac{\partial \hat{a}}{\partial t} = \left[-\Delta_C + \int_V d^3\boldsymbol{r} \left\{\frac{g^2(\boldsymbol{r})}{\Delta_A} \hat{\psi}^\dagger(\boldsymbol{r})\hat{\psi}(\boldsymbol{r})\right\} - i\kappa\right] \hat{a} + \int_V d^3\boldsymbol{r} \left\{\frac{g(\boldsymbol{r})h(\boldsymbol{r})}{\Delta_A} \hat{\psi}^\dagger(\boldsymbol{r})\hat{\psi}(\boldsymbol{r})\right\} + i\hat{\Xi}\,. \tag{2.64}$$

If the detuning of the cavity field is large $|\Delta_C| \gg \omega_R$, the cavity dynamics follows the atomic degrees of freedom effectively instantaneously [27, 88]. The cavity field operator $\hat{a}$ can then be eliminated in a Born-Oppenheimer approximation [27]. Alternatively, in the bad cavity limit $\kappa \gg \omega_R$, where all excitations of the cavity are rapidly damped away, the cavity field can be equivalently eliminated adiabatically [108]. Thus, if the parameter $|\Delta_C + i\kappa| \gg \omega_R$ is the steady state of Eq. (2.64), i.e. $i\frac{\partial \hat{a}}{\partial t} = 0$ and neglecting $\hat{\Xi}$, we get

$$\hat{a} = \frac{\int_V d^3\boldsymbol{r} \left\{\frac{g(\boldsymbol{r})h(\boldsymbol{r})}{\Delta_A} \hat{\psi}^\dagger \hat{\psi}\right\}}{\Delta_C + i\kappa - \int_V d^3\boldsymbol{r} \left\{\frac{g^2(\boldsymbol{r})}{\Delta_A} \hat{\psi}^\dagger \hat{\psi}\right\}}\,. \tag{2.65}$$

While this equation was perfectly fine for the complex-valued mean-field Eq. (2.47a) in its operator form, it introduces some ordering ambiguities of the operators in the numerator and denominator. However, with the normalization of the atomic field to the number of atoms N and the large parameters

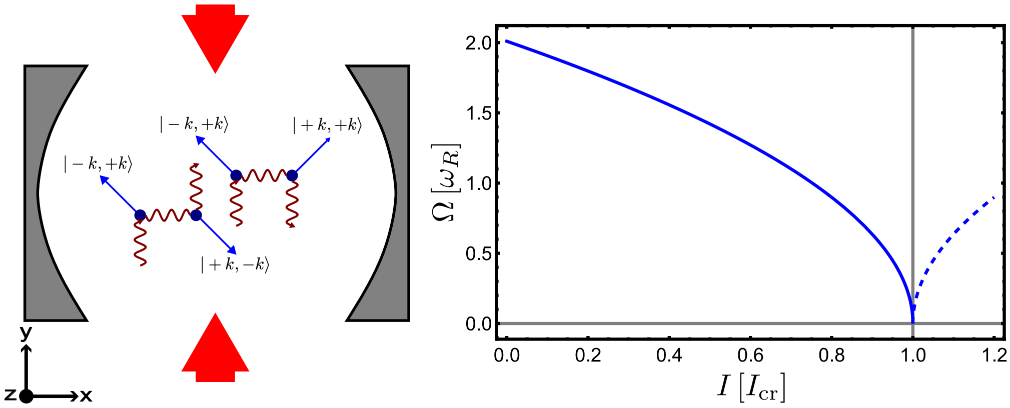

Figure 2.11: Sketch of the cavity-induced interaction in the atom-only picture Eq. (2.68). The cavity-mediated interaction by scattering of a pump photon into the cavity and subsequent scattering of a cavity photon into the pump by another atom. Note that the left diagram is momentum conserving while the right one is not. The sketch is adapted from Ref. [35]. On the right, we show the softening of the roton mode Eq. (2.69) with the increase of the cavity-induced interaction strength I to a critical value. Beyond the critical value, the roton mode is unstable with an imaginary value, which we plot as a dashed curve. The parameter is $nU = 10^{-2}\,\omega_R$.

$|\Delta_A| \gg |\Delta_C + i\kappa| \gg \omega_R$ so that $|\Delta_C \pm i\kappa| \gg |U_0| = g_0^2/|\Delta_A|$, we can expand the denominator as a harmonic series to [27]

$$\hat{a} = \frac{1}{\Delta_C + i\kappa}\int_V d^3\boldsymbol{r}\left\{\frac{g(\boldsymbol{r})h(\boldsymbol{r})}{\Delta_A}\hat{\psi}^\dagger\hat{\psi}\right\}\left[1 + \mathcal{O}\left(\frac{U_0}{|\Delta_C + i\kappa|}\right)\right]\,. \tag{2.66}$$

The order ambiguities occur only in the higher orders of the harmonic series. Insertion of Eq. (2.66) into the field Hamiltonian Eq. (2.46) yields the effective atom-only picture, although again operator ordering ambiguities occur. They are resolved correctly per Ref. [109] by the ordering

$$\begin{aligned}&\frac{1}{2}\left(\hat{a}^\dagger\int_V d^3\boldsymbol{r}\left\{\frac{g(\boldsymbol{r})h(\boldsymbol{r})}{\Delta_A}\hat{\psi}^\dagger\hat{\psi}\right\} + \int_V d^3\boldsymbol{r}\left\{\frac{g(\boldsymbol{r})h(\boldsymbol{r})}{\Delta_A}\hat{\psi}^\dagger\hat{\psi}\right\}\hat{a}\right)\\ &\quad = \frac{1}{2}\frac{2\Delta_C}{\Delta_C^2 + \kappa^2}\left(\int_V d^3\boldsymbol{r}\left\{\frac{g(\boldsymbol{r})h(\boldsymbol{r})}{\Delta_A}\hat{\psi}^\dagger\hat{\psi}\right\}\right)^2 + \mathcal{O}\left(\frac{U_0^2}{|\Delta_C \pm i\kappa|^2}\right)\,,\end{aligned} \tag{2.67}$$

for the coupling term linear in the cavity field of Eq. (2.46). In the lowest order of $U_0/|\Delta_C \pm i\kappa|$, the cavity thus induces a two-body density-density interaction between the atoms. Crucially, if the coupling between the cavity field and the atoms of the mode functions $g(\boldsymbol{r})h(\boldsymbol{r})$ is effectively infinite-range, then the induced interaction is also infinite-range. The higher orders omitted in Eq. (2.66) describe three and more body interactions of unknown operator ordering, as can be seen by considering further terms in Eq. (2.67). Conversely, even the lowest order of the optomechanical coupling term $g^2(\boldsymbol{r})\hat{a}^\dagger\hat{a}/\Delta_A$ in Eq. (2.46) is at least of three-body type and $\mathcal{O}(U_0^2/|\Delta_C \pm i\kappa|^2)$, so this term does not contribute. The effective atom-only field Hamiltonian of the cavity BEC is therefore

$$\begin{aligned}\hat{H}_{\mathrm{at}} = &\int_V d^3\boldsymbol{r}\left\{\hat{\psi}^\dagger(\boldsymbol{r})\left[-\frac{\nabla^2}{2m} + \frac{h^2(\boldsymbol{r})}{\Delta_A} + \frac{U}{2}\hat{\psi}^\dagger(\boldsymbol{r})\hat{\psi}(\boldsymbol{r})\right]\hat{\psi}(\boldsymbol{r})\right\}\\ &+ \frac{1}{2}\int_V d^3\boldsymbol{r}\int_V d^3\boldsymbol{r}'\left\{\hat{\psi}^\dagger(\boldsymbol{r})\hat{\psi}(\boldsymbol{r})\frac{2\Delta_C}{\Delta_C^2 + \kappa^2}\frac{g(\boldsymbol{r})h(\boldsymbol{r})g(\boldsymbol{r}')h(\boldsymbol{r}')}{\Delta_A^2}\hat{\psi}^\dagger(\boldsymbol{r}')\hat{\psi}(\boldsymbol{r}')\right\}\,.\end{aligned} \tag{2.68}$$

The cavity-induced interaction term of the second line in Eq. (2.68) describes an interaction that is global throughout the intersection of the pump mode and cavity mode as depicted in figure 2.11. The fast dynamical cavity field is strongly slaved to the atomic distribution Eq. (2.45a) so that a small local fluctuation of the latter significantly affects the global cavity field [27]. In a microscopic view, the induced interaction is realized by an atom scattering a pump photon into the cavity, where the photon is stored delocalized over the mode volume until another atom scatters it into the pump, as illustrated in figure 2.11. Thus, the indistinguishable atoms are globally correlated [27]. Note that the induced interaction in Eq. (2.68) is not translation invariant. While the effective Hamiltonian $\hat{H}_{\mathrm{at}}$ may appear to be a closed system, we have to remember that the underlying physics is that of a driven dissipative system. Hence, we can associate the lack of momentum conservation with the pumping of the atoms and the losses of the cavity. It should be mentioned that more complicated experimental setups succeed in engineering the cavity-induced interaction to be effectively momentum conserving [79].

Of course, below the critical pump strength, the atom-only picture is also in the homogeneous mean-field $\langle\hat{\psi}\rangle = \sqrt{n}$. The atomic excitations of the atom-only Hamiltonian can then be derived similarly by Bogoliubov theory. We generalize this derivation in the chapter 4, so we postpone the presentation of the details there and only briefly discuss the results here. Given the cavity mode function $g(\boldsymbol{r}) = g_0\cos(kx)$ and the pump mode function $h(\boldsymbol{r}) = h_0\cos(ky)$, the cavity-mediated long-range interaction affects only the checkerboard mode excitations $\hat{\phi}_1 \propto \cos(kx)\cos(ky)$. Because the interaction is infinite-range, it selects only these distinct atomic momenta $|\pm k, \pm k\rangle$. For the red-detuned cavity $\Delta_C < 0$ the interaction is locally attractive with the effective interaction parameter $I = 2\Delta_C g_0^2 h_0^2/[(\Delta_C^2+\kappa^2)\Delta_A^2] < 0$. Consequently, the excitation spectrum in the atom-only picture is the Bose gas dispersion Eq. (2.25) except for a single distinct mode as derived later as Eq. (4.55)

$$\Omega = \sqrt{2\omega_R\left(2\omega_R + 2Un + \frac{IN}{2}\right)}\,. \tag{2.69}$$

This mode Ω is roton-like because $I < 0$ and its softening with the cavity interaction I is shown in figure 2.11. At the critical point $I_{\mathrm{cr}} = -4(\omega_R + nU)/N$, the roton is completely softened $\Omega = 0$, signaling the self-organization phase transition in the atom-only description. The roton-like excitation of the atomic system and its softening have been observed in Ref. [35].

2.3.9 Short review of the cavity BEC above the critical point for self-organization

Near and beyond the self-organizing phase transition $\lambda \gtrsim \lambda_{\mathrm{cr}}$ the cavity BEC can be treated accurately as a lattice model [27, 88, 110]. The atomic field operators can then be expanded in the localized eigenfunctions at each site i given by the lowest-band expansion in Wannier functions $w(\boldsymbol{r})$ such that [88]

$$\hat{\psi}(\boldsymbol{r}) = \sum_i \hat{b}_i w(\boldsymbol{r} - \boldsymbol{r}_i)\,. \tag{2.70}$$

The lattice site index i runs over both the even and odd sites of the square checkerboard lattice shown in figure 2.8. For an overdamped light field $\kappa \gg \omega_R$, the Wannier expansion Eq. (2.70) can be applied to the effective atom-only Hamiltonian Eq. (2.68) to obtain the generalized Bose-Hubbard model [88, 111]

$$\hat{H} = \sum_{\langle i,j\rangle} t_{ij}\hat{b}_i^\dagger\hat{b}_j + \frac{U_{\mathrm{lat}}}{2}\sum_i \hat{n}_i(\hat{n}_i - 1) + \frac{I_{\mathrm{lat}}}{2}\sum_{i,j}(-1)^{i+j}\hat{n}_i\hat{n}_j\,, \tag{2.71}$$

with the cavity-mediated global interaction $I_{\mathrm{lat}} \propto \lambda^2$ and the on-site number operator $\hat{n}_i = \hat{b}_i^\dagger\hat{b}_i$. The validity of this model can be extended to the entire phase diagram, and in particular to the

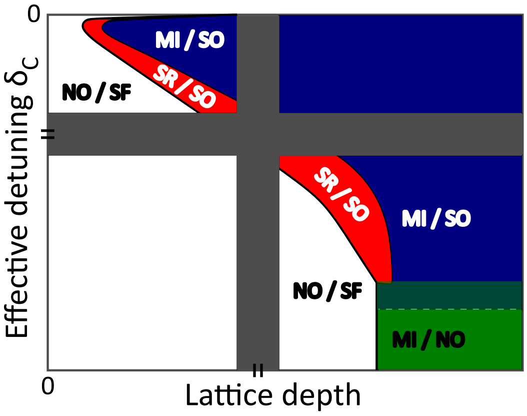

Figure 2.12: Sketch of the phase diagram of the extended Bose-Hubbard model for varying effective cavity detuning δ_C and pumped lattice depth. The cavity detuning only changes the global interaction I_{lat}, while the lattice depth increases both the on-site interaction U and the global interaction I_{lat} [26]. In the upper left is a zoom-in on the small detuning and lattice depth region to resolve the details of the phase diagram there. It shows the normal superfluid (NO/SF), the superradiant self-organized (SR/SO), and the self-organized Mott insulator phase (MI/SO). The phase diagram at large cavity detuning is shown below the gray horizontal section through the phase diagram. There is also the normal Mott insulator phase (MI/NO) with a first-order phase transition indicated by the dashed line and the shaded region. The sketch amalgamates the diagrams shown for the different regimes in Refs. [25, 26, 111]

normal ordered superfluid phase, by adding an external potential that traps the atoms initially at all possible sites, both odd and even. It adds a term with the effective on-site chemical potential $\sum_i (V_i^{\text{trap}} - \mu_i)\hat{n}_i$ to Eq. (2.71). The self-organization order parameter Eq. (2.49) takes the lattice form $\theta = (\sum_i (-1)^i n_i)/(\sum_i n_i)$ with the expectation values $n_i = \langle \hat{n}_i \rangle$ [111].

The $\mathbb{Z}_2$ symmetry-breaking into even or odd lattice sites at the self-organization transition can be emphasized in the Hamiltonian by introducing separate indices (e, o) running over the even e and odd o sites of the checkerboard [26]. We obtain

$$\hat{H} = t \sum_{\langle e,o \rangle} \left(\hat{b}_e^\dagger \hat{b}_o + \hat{b}_o^\dagger \hat{b}_e \right) + \frac{U_{\text{lat}}}{2} \sum_{i \in \{e,o\}} \hat{n}_i(\hat{n}_i - 1) + \frac{I_{\text{lat}}}{2} \left(\sum_e \hat{n}_e - \sum_o \hat{n}_o \right)^2 + \sum_{i \in \{e,o\}} (V_i^{\text{trap}} - \mu_i)\hat{n}_i \, . \tag{2.72}$$

Below the critical pump strength the system is in the usual normal superfluid phase where all lattice sites are coherent and the order parameter is $\theta = 0$. This phase is shown in white in the phase diagram of the extended Bose-Hubbard model in figure 2.12. Above the critical pump strength, the order parameter also takes finite values in the lattice model, forming the superradiant self-organized phase. In addition, when the pump strength is increased beyond the critical point, hopping between sites of the lattice is gradually hindered [111]. The system retains its superfluid properties in a small range above the critical pump value. Due to its combined superfluid properties and self-assembly into a lattice, this phase is often referred to as supersolid in the literature [26, 70, 112].

Deeper in the self-organized phase, the pump is sufficiently strong that the superfluidity breaks down because hopping is severely impeded so that there is no spatial coherence. Above this second critical pump strength, the system is in a self-organized Mott insulator phase [111]. This phase is also associated with a charge density wave [26]. The self-organized Mott phase has been experimentally verified [25].

Further studies have revealed regions of bistability and hysteresis as well as a fourth phase [26,71,112]. The phase diagram described so far is the picture for smaller cavity detunings below a certain critical off-resonance, which in Ref. [26] is about $|\Delta_C|/2\pi < 50$ MHz. When the cavity is very far red-tuned, the superfluid phase does not transition to a checkerboard phase with higher pump power. Instead, it transitions directly to a Mott insulator phase in which the atoms are equally localized on both odd and even sites [26]. In fact, the imbalance between even and odd sites θ in the self-organized phase is most pronounced for good cavity resonance. As the red-detuning Δ_C increases in absolute value, it becomes smaller until a first-order phase transition to the evenly distributed Mott insulator phase occurs in the region around $\Delta_C/2\pi \approx -50$ MHz, where blue and green overlap with a hysteresis that is independent of how fast the detuning is changed [26].

2.3.10 The hybrid atom-optomechanical setup

In the atom-optomechanical setup, a low-finesse cavity contains a semitransparent nanomechanical membrane with mass M and resonance frequency Ω_m as shown in figure 2.13. The second section of the setup contains an ultracold quasi-one-dimensional Bose gas of N atoms, each with mass m. Every atom is considered to have three internal states $|-\rangle$, $|+\rangle$, and $|e\rangle$. The transition between $|+\rangle \leftrightarrow |e\rangle$ is driven at the detuning Δ by a σ_- polarized beam of frequency ω_L. After passing through the condensate, the pump beam hits a polarizing beam splitter (PBS), where the linear π_y polarized light continues in the direction of the cavity, while the π_x light is reflected in a perpendicular direction. The π_x light is reflected back into the beam splitter, forming the vertical arm shown in figure 2.13. When the membrane in the cavity is not displaced, the π_y polarized light from the cavity returns to the beam splitter without any phase shift relative to the light of the vertical arm. However, if the membrane is displaced, it induces a phase shift between the two beams recombined at the polarized beam splitter. Then σ_+ polarized light from the beam splitter returns to the atoms and drives their internal transition $|-\rangle \leftrightarrow |e\rangle$. This produces the Λ coupling scheme shown in figure 2.13. Note that an internal transition between atomic states $|-\rangle \leftrightarrow |+\rangle$ along the Λ emits a σ_+ photon and thus affects the radiation pressure experienced by the membrane. In summary, the light field mediates coupling between the single-mode harmonic oscillator of the membrane and the atomic condensate [B].

The light field and the excited atomic state $|e\rangle$ can be adiabatically eliminated because the system is in the bad-cavity limit, i.e. the dissipation of light is the fastest time scale. In this effective picture, the Hamiltonian of the hybrid atom-optomechanical setup is [B, 113, 114]

$$\begin{aligned}\hat{H}_{\text{aom}} = \Omega_m \hat{a}^\dagger \hat{a} + \sum_{\nu=\pm} \int dz \Big\{ \hat{\psi}_\nu^\dagger(z) \Big[\nu \frac{\Omega_a}{2} - \omega_R \partial_z^2 + V_\nu(z) + \sum_{\nu'=\pm} \frac{U_{\nu\nu'}}{2} \hat{\psi}_{\nu'}^\dagger(z) \hat{\psi}_{\nu'}(z) \Big] \hat{\psi}_\nu(z) \Big\} \\ - \left(\hat{a} + \hat{a}^\dagger\right) \int dz \Big\{ \sin(2z) \Big[\lambda_{\text{ex}} \hat{\psi}_+^\dagger(z) \hat{\psi}_+(z) + \frac{\lambda}{2} \Big[\hat{\psi}_+^\dagger(z) \hat{\psi}_-(z) + \hat{\psi}_-^\dagger(z) \hat{\psi}_+(z) \Big] \Big] \Big\}, \qquad (2.73)\end{aligned}$$

with the rescaling of the position coordinate $z \to z/\omega_L$. The system is effectively a two-species Bose gas $\hat{\psi}_{\nu=\pm}$ of the $|-\rangle$ and $|+\rangle$ internal state of the atoms coupled to the single bosonic mode of the membrane Ω_m. The Bose species have atom-atom interactions by s-wave scattering intra species U_{--} and U_{++} as well as inter species $U_{+-} = U_{-+}$. Between the atoms and the membrane, there is an infinite-range coupling characterized by the light field mode $\sin(2z)$ to the displacement quadrature of the membrane $\propto (\hat{a} + \hat{a}^\dagger)$. We see that in principle there is an asymmetric coupling to the species by the parameter λ_{ex}.

The hybrid atom-optomechanical system undergoes a non-equilibrium quantum phase transition, a phenomenon that is also seen in cavity BEC as discussed in section 2.3.6. The phase diagram is rich and shows transitions from exclusive macroscopic occupation of one of the internal atomic states to phases where both are occupied [B, 113]. The transition can also be seen in the change of the membrane from a non-displaced to a constantly displaced state [B, 113]. Depending on the parameters of the

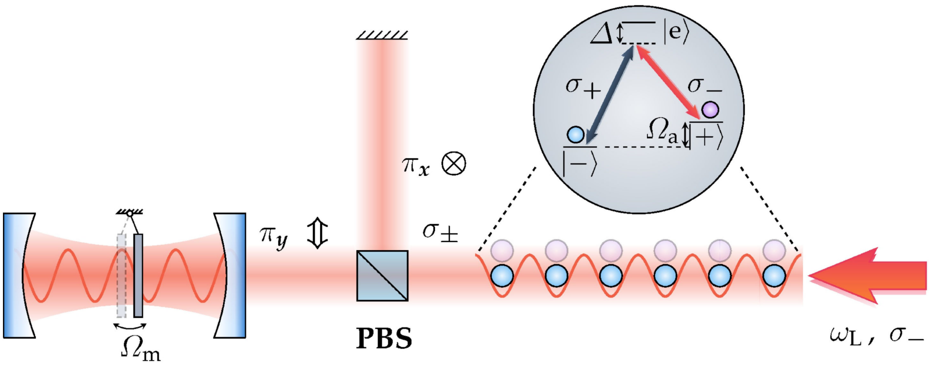

Figure 2.13: The hybrid atom-optomechanical setup with internal coupling scheme. A nanomembrane oscillates in the cavity with Ω_m. The cavity light and its outcoupled dissipative field mediate an interaction with a one-dimensional BEC on the right by addressing its internal states in the Λ scheme shown in the inset. Figure as published in Ref. [B] for which it was adapted from Ref. [113].

transition frequency Ω_a, the coupling λ and the asymmetry of the coupling $\lambda_{\rm ex}$ the transitions can be tuned to be first or second order with spontaneous breaking of the $U(1)$ symmetry of the internal states of the Bose gases [B, 113]. The first-order non-equilibrium quantum transition is accompanied by hysteresis [113]. We have associated the transition to finite membrane displacement in the steady state with the formation of a self-organized density wave state in the BEC from a homogeneous state [B], i.e. a state similar to the self-organized state in the cavity BEC. If quantum fluctuations are taken into account in this analysis, phase boundaries are likely to be affected and new phases like the quantum droplets of Bose-Bose mixtures could emerge in the already rich phase diagram [B]. We will have a brief review of Bose-Bose mixture droplets in chapter 4.

For simplicity, let us assume that $\lambda_{\rm ex} = 0$, leaving only the symmetric coupling with λ. Equivalently, the external potential is independent of the species $V_\pm(z) = -V\cos(2z)/2$ and so is the atom-atom interaction $U_{\nu\nu'} = U$. In comparison with the effective Hamiltonian of the cavity BEC Eq. (2.46), the difference comes down to the involvement of two species and their splitting Ω_a.

We now take a look at Ref. [114], where it is assumed that the atoms are in a sufficiently deep optical lattice V to expand the atomic field operators in lowest-order Wannier functions [115]. Thus a two-species Bose-Hubbard model with coupling to the membrane is found, which in momentum space gives the expression [114, 115]

$$\begin{aligned}\hat{H}_{\rm aom} = \Omega_m \hat{a}^\dagger\hat{a} + \sum_{k,\nu}\epsilon_{k\nu}\hat{b}^\dagger_{k\nu}\hat{b}_{k\nu} + \frac{U_{\rm lat}}{2l}\sum_{k,p,q}\sum_{\nu,\nu'}\hat{b}^\dagger_{k+q\nu}\hat{b}^\dagger_{p-q\nu'}\hat{b}_{p\nu'}\hat{b}_{k\nu} \\ -\frac{\Lambda}{2}(\hat{a}+\hat{a}^\dagger)\sum_k\left(\hat{b}^\dagger_{k+}\hat{b}_{k-}+\hat{b}^\dagger_{k-}\hat{b}_{k+}\right) , \end{aligned} \tag{2.74}$$

with $\epsilon_{k\nu} = \nu\Omega_a/2 - 2J\cos(k)$ where J is the hopping amplitude and with $\Lambda \propto \lambda$. The Hamiltonian Eq. (2.74), although physically completely different, is mathematically very similar to the expression we find in our work for cavity BEC in Eq. (3.28). This similarity is even more striking when the Bogoliubov theory is applied to the respective Bose gas. In the hybrid atom-optomechanical physics, the rotation of the atomic operators $\hat{b}_{k\nu} \to \hat{c}_{k\nu}$ by the Bogoliubov coefficients u_k and v_k yields [114, 115]

$$\begin{aligned}\hat{H}_{\rm aom} = \Omega_m\hat{a}^\dagger\hat{a} + \Omega_a\hat{c}^\dagger_{0+}\hat{c}_{0+} + \sum_{k\neq 0,\nu}\omega_{k\nu}\hat{c}^\dagger_{k\nu}\hat{c}_{k\nu} - \frac{\Lambda\sqrt{N}}{2}(\hat{a}+\hat{a}^\dagger)(\hat{c}_{0+}+\hat{c}^\dagger_{0+}) \\ -\frac{\Lambda}{2}(\hat{a}+\hat{a}^\dagger)\sum_{k\neq 0}\left(u_k[\hat{c}^\dagger_{k-}\hat{c}_{k+}+\hat{c}^\dagger_{k+}\hat{c}_{k-}] + v_k[\hat{c}_{k-}\hat{c}_{-k+}+\hat{c}^\dagger_{-k+}\hat{c}^\dagger_{k-}]\right) , \end{aligned} \tag{2.75}$$

with

$$\omega_{k-} = -2J[1-\cos(k)]\sqrt{1+\frac{nU_{\mathrm{lat}}}{J[1-\cos(k)]}}\,, \qquad \omega_{k+} = \Omega_a + 2J[1-\cos(k)] + nU_{\mathrm{lat}}\,. \tag{2.76}$$

In appendix A.4 the detailed derivation laid out in Ref. [115] can be found. The hybrid atom-optomechanical setup forms a phononic damping system-bath Hamiltonian similar to the Eqs. (3.38) to (3.40) derived in our work. We will explore the mathematical correspondence in more detail after deriving these equations in section 3.4. The evaluation of the dissipation characteristics of this intrinsic damping yields, among other phenomena, exciting bath spectral densities [114, 115]. The spectral density is gapped by the atomic transition frequency Ω_a, where its dominant peak lies. The quasiparticle excitations of the bath lead to enhanced squeezing in the system and nontrivial many-body states [114].

3 – Exotic quantum dissipation from fluctuations

Cavity BEC systems, with their strong coupling between the atomic and cavity sectors, provide extraordinary possibilities to study quantum phenomena in its central two harmonic modes forming a polariton system, even by in situ measurements in the cavity loss channel. We show that the presence of weak atom-atom interactions generates quantum fluctuations that act as a quantum dissipative bath of Landau and Beliaev damping on the central polariton system. The bath shows exotic spectral properties involving damping and antidamping competition as well as sub-Ohmic signatures. Using a beyond-Bogoliubov approximation on the system's field Hamiltonian, we give an analytical derivation of all relevant processes from microscopic principles. The dissipation characteristics are exactly captured by the techniques of imaginary-time path integrals. The rich influence on the physical observables of the polariton system is discussed and quantified. We determine the Stokes shift in the critical point of the Dicke quantum phase transition. The control and enhancement of the quantum bath and its influence on the quantum fluctuations of the system using external tuning parameters are described in detail. We find that the cavity BEC setup provides a great platform to study exotic quantum fluctuation and dissipation phenomena thanks to its tunability and the exploitation of its strong light-matter coupling. In this chapter we present the work published as Ref. [A] L. Mixa, H. Keßler, A. Hemmerich, and M. Thorwart, *Enhancing exotic quantum fluctuations in a strongly entangled cavity BEC system*, Phys. Rev. Res. **6**, L012024 (2024).

3.1 – Introduction

The design of the cavity BEC system discussed in this thesis realizes a setup with a strong light-matter coupling that offers both great experimental access and controllability. In situ observation of the system dynamics [102–104] is the first of these advantages. The ability to control the coupling between light and matter simply by the strength of the pump laser is another. Thus, the cavity BEC, with its rich landscape of quantum phases discussed in section 2.3.9, provides an excellent basis for studying quantum phenomena. One of these phases is the self-organized supersolid-like phase. The system passes from the superfluid normal phase to this phase via the second-order non-equilibrium Dicke phase transition, which is discussed in more detail in sections 2.3.5 and following. As a zero-temperature quantum phase transition, this requires the presence of quantum fluctuations to initiate the runaway process. These are provided by the atom-atom interaction in the BEC described by s-wave scattering. The model underlying the superradiant self-organizing phase transition is that of two quantum harmonic oscillators. One is represented by the cavity mode. The other is represented by the symmetric superposition of the condensate excitations $|\pm k, \pm k\rangle$, which carry a quantum of the light field momentum k both along the cavity axis x and along the pump axis y. If the dissipation is taken into account, as in the in situ measurement of cavity photon losses, the criticality remains [36]. However, it is qualitatively modified by the change of the critical exponent for the quantum fluctuations from 1/2 to 1.

Weak atom-atom interactions introduce processes called Landau [33, 116–122] and Beliaev damping [33, 67, 123–126] to superfluids. The Dicke system of cavity and checkerboard modes is inevitably coupled to other collective excitations of the Bose gas by these processes. Adopting a system-bath picture, we reveal that the cavity BEC provides useful experimental grounds to study a system of two bilinearly coupled quantum harmonic oscillators in the dissipative bath provided by Landau and Beliaev damping. Previous literature on this type of system already indicates peculiar bath properties leading to interesting dissipation characteristics [34, 127, 128]. The exploration of such phenomena provided in this quantum simulator setup is relevant for systems such as superconducting qubits [129,130], nanomechanical systems [131], glassy systems [132], quantum dots [133], and impurity systems [134, 135]. We review the similarity of the cavity BEC to the hybrid atom-optomechanical system in section 3.4 and the following investigation in the cavity BEC was sparked by the one performed in those systems in Ref. [114].

In this chapter, we begin with a quick review of the basics of the system-bath formalism for quantum dissipation in section 3.2, which underlies the rest of the chapter. It also contains a summary of the existing literature on describing some of the phenomena in cavity BEC and Dicke model systems. In section 3.3 we then begin our work to uncover a result that addresses all these effects by derivation from the first principles of the cavity BEC. A beyond-Bogoliubov theory ansatz to describe the quantum fluctuations in the system is the first step on this journey. In section 3.5 this is followed by invoking the system-bath notion on the collective excitations with the Landau and Beliaev processes describing the coupling between the two-harmonic-oscillators system emerging from the cavity BEC and the bath consisting of excitations of the condensate. We use the imaginary-time path integral technique to extract the influence functional of the bath. Following that, in section 3.6 we analyze the spectral densities that characterize the coupling to the bath and hence its dissipation properties. There we also explore the controllability of the bath by external tuning parameters accessible in the experiment. Having previously obtained the effective action of the system by computing the influence functional, in section 3.7 we study the fluctuations in the coupled harmonic oscillator system and, in particular, how they are affected by the bath. Again we explore the tuning of the bath so that we dive into the control and enhancement of its influence on the system and especially on the observable quantum fluctuations. Finally, we give a brief outlook in section 3.9 and conclude on our results in section 3.10.

3.2 – Quantum dissipation

The dynamics of quantum systems appear to be perfectly reversible, considering that the Schrödinger equation is a linear differential equation. Nevertheless, systems experience dissipation, damping, relaxation to equilibrium, and irreversibility. Examples are biological energy transfer [136, 137] and dissipative conical intersections [138], nanomechanical systems [B, 113, 114], molecular junctions and solvent dynamics [139–142], decoherence in Majorana wires [143], or the relaxation of a two-level system briefly touched on in section 2.3.1. Of course, the systems mentioned in the introduction to this chapter provide further examples.

As in the relaxation of the two-level system, it is crucial to consider the generic quantum system not as isolated, but in contact with an environment. This environment provides a bath consisting of a plethora of modes where the coupling to any single mode of the bath is weak. Nevertheless, due to the large number of bath modes and their dense spectrum, the influence of the bath on the system can be large [32].

In a quantum mechanical description, both the system and the bath, as well as the coupling between them, are modeled explicitly [144]. The total system is considered to be in thermal equilibrium at the inverse temperature $\beta = 1/T$ with the temperature T and the Boltzmann constant $k_B = 1$.

3.2.1 System-bath formalism

The total system-bath Hamiltonian $\hat{H} = \hat{H}_S + \hat{H}_B + \hat{H}_{SB}$ combines the isolated system $\hat{H}_S$ and the isolated bath $\hat{H}_B$ by describing the coupling between them in $\hat{H}_{SB}$. Here we focus on describing a system in equilibrium at all times. Throughout this thesis, we only stray into discussing dynamics and non-equilibrium techniques in the introductory literature review of this chapter and the outlook. We use the imaginary-time path integral technique [32, 65, 144, 145]. In this Wiener path integral formalism, the phase acquired along a path is given by the Euclidean action $S = \int_0^\beta d\tau H$, where the integrand is the Hamiltonian functional H integrated over the imaginary time τ. The Hamiltonian functional is $H[r(\tau)]$ and hence not an operator which we indicate by the omission of the hat*. The complete equilibrium system-bath ensemble is then described by the Euclidean action [32, 144]

$$S = S_S + S_B + S_{SB} = \int_0^\beta d\tau \big\{ H_S + H_B + H_{SB} \big\} \,. \tag{3.1}$$

The imaginary-time path integral of this action yields the equilibrium density matrix of the total system [32, 144]

$$W_\beta(r'', r') = \left\langle r'' \left| \frac{1}{\mathcal{Z}} e^{-\beta \hat{H}} \right| r' \right\rangle = \frac{1}{\mathcal{Z}} \int_{r(0)=r'}^{r(\beta)=r''} \mathcal{D}r(\cdot) e^{-S[r(\cdot)]} \,, \tag{3.2}$$

with the partition function of the system-bath model

$$\mathcal{Z} = \mathrm{Tr} e^{-\beta \hat{H}} = \int_{r(0)=r(\beta)} \mathcal{D}[r(\cdot)] e^{-S[r(\cdot)]} = \int_{r(0)=r(\beta)} \mathcal{D}[r(\cdot)] e^{-\int_0^\beta d\tau \{H[r(\cdot)]\}} \,. \tag{3.3}$$

We, however, are interested just in the system S_S within the environment of the bath, not the entire ensemble described by $\mathcal{Z}$. If we consider that the system's path is given by $q(\cdot)$ and that of the bath by $x(\cdot)$, it is clear that the degrees of freedom of the bath can be traced out to obtain the reduced density matrix of the system

$$\rho_\beta(q'', q') = \mathrm{tr}_B W_\beta = \int_{-\infty}^{+\infty} dx' \, W_\beta(q'', x'; q', x') \,. \tag{3.4}$$

It naturally involves the reduced partition function $Z = \mathcal{Z}/\mathcal{Z}_B$. In terms of the path integral formulation, the bath trace produces an integral over all β-periodic paths of the bath. Their period is determined by the inverse temperature β. This results in the influence functional of the bath [32, 144]

$$\mathcal{F}[q(\cdot)] = e^{-S_{\mathrm{infl}}[q(\cdot)]} = \frac{1}{\mathcal{Z}_B} \oint \mathcal{D}x(\cdot) e^{-\left(S_B[x(\cdot)] + S_{SB}[q(\cdot), x(\cdot)] \right)} \,, \tag{3.5}$$

which is determined by the influence action S_{infl} according to its definition in Eq. (3.5). The reduced density matrix thus has the expression

$$\rho_\beta(q'', q') = \frac{1}{Z} \int_{q(0)=q'}^{q(\beta)=q''} \mathcal{D}q(\cdot) e^{-S_S[q(\cdot)]} \mathcal{F}[q(\cdot)] = \frac{1}{Z} \int_{q(0)=q'}^{q(\beta)=q''} \mathcal{D}q(\cdot) e^{-S_{\mathrm{eff}}[q(\cdot)]} \,. \tag{3.6}$$

Here we have used the notation of the effective action for the system in the bath $S_{\mathrm{eff}} = S_S + S_{\mathrm{infl}}$. It is noteworthy that while the original contributions in the action S_S, S_B, and S_{SB} are local in time, the reduction of the bath to its influence on the system yields an action S_{infl} that can be, and usually is, nonlocal in time [32].

---

*See the derivation of the path integral formalism in Refs. [32, 65, 144].

Having obtained a description of the system under the influence of the bath, its equilibrium expectation values can be computed from its partition function via a source term [32, 144]

$$\begin{aligned} \langle A \rangle &= \frac{1}{Z}\frac{1}{\beta}\int_{q(0)=q(\beta)} \mathcal{D}q \int_0^\beta d\tau'\, A(q(\tau'))e^{-S_{\mathrm{eff}}[q(\tau)]} \\ &= \frac{-1}{Z\beta}\frac{\partial}{\partial\lambda}\int_{q(0)=q(\beta)} \mathcal{D}q\, e^{-(S_{\mathrm{eff}}[q(\tau)]+\int_0^\beta d\tau \lambda A(q(\tau)))} = -\frac{1}{Z\beta}\frac{\partial}{\partial\lambda}Z = -\frac{1}{\beta}\frac{\partial}{\partial\lambda}\ln Z\,. \end{aligned} \tag{3.7}$$

3.2.2 Caldeira-Leggett model

If the bath S_B consists of harmonic oscillator modes that are linearly coupled to the system in S_{SB}, the influence functional and equivalently the influence action Eq. (3.5) can be calculated exactly [32]. Even if this does not coincide with the microscopic structure of the studied system, the idea of linear coupling is usually a very good approximation due to the weak coupling between the system and a single bath mode [32]. Thus, it is a proven strategy that if the microscopic structure is not accessible or intractable, the bath can be modeled by a large number of harmonic oscillator modes linearly coupled to the system [32]. The coupling strength of each bath mode to the system can then be obtained phenomenologically from the classical system in what we will find to be the spectral density of the bath $G(\omega)$. Such a system-bath setup is described by the celebrated Caldeira-Leggett model, where the bath consists of N independent harmonic oscillators with masses m_j and frequencies ω_j

$$\hat{H}_B = \sum_{j=1}^{N} \hat{H}_j = \sum_{j=1}^{N} \frac{\hat{p}_j^2}{2m_j} + \frac{m_j\omega_j^2}{2}\hat{x}_j^2\,. \tag{3.8}$$

The system is described by a potential $V(\hat{q})$ and couples to the bath linear in the bath operators $\hat{x}_j$ given by the Hamiltonian

$$\hat{H}_{SB} = \sum_{j=1}^{N}\left(-F_j(\hat{q})\hat{x}_j + \frac{F_j^2(\hat{q})}{2m_j\omega_j^2}\right)\,. \tag{3.9}$$

The second term in the coupling Hamiltonian Eq. (3.9) counters renormalization of the system potential caused by the coupling to the bath [32, 144]. This counter-term prevents the physics from being altered by the phenomenological bath construction. Below in the thesis, a bath emerges from first principles. In that case, we can learn that the intrinsic bath renormalizes the system in a way that can even have qualitative consequences. An example is the Stokes shift where the effective dissipation into a bath shifts the photon emission spectrum of a system relative to its absorption spectrum.

We next consider the special case of a bilinear coupling between the system and the bath by setting $F_j(\hat{q}) = c_j\hat{q}$ in Eq. (3.9). To trace out the bath, the path integral over all β-periodic paths must be performed. Therefore, it is opportune to use a periodic summation of the paths based on the bosonic Matsubara frequencies $\nu_n = 2\pi n/\beta$ with $n \in \mathbb{Z}$ [144]

$$x_j(\tau) = \frac{1}{\beta}\sum_{n=-\infty}^{+\infty} x_{j,n}e^{i\nu_n\tau}\,, \qquad\qquad q(\tau) = \frac{1}{\beta}\sum_{n=-\infty}^{+\infty} q_n e^{i\nu_n\tau}\,. \tag{3.10}$$

The coefficients fulfill $x_{j,n} = x_{j,-n}^*$ and $q_n = q_{-n}^*$. Additionally, it is useful to express the paths as their stationary path $\bar{x}_j$ plus fluctuations around them. The stationary paths are obtained from the classical equations of motion [144]

$$m_j\ddot{\bar{x}}_j - m_j\omega_j^2\bar{x}_j + c_j\bar{q} = 0 \qquad \Rightarrow \qquad \bar{x}_{j,n} = \frac{c_j}{m_j(\nu_n^2+\omega_j^2)}q_n\,. \tag{3.11}$$

Because the action is extremized for the stationary paths $\bar{x}_j$, the terms linear in the fluctuations vanish and the influence action $S_{\text{infl}}[q]$ is obtained. We leave further details of the derivation to corresponding literature [32, 144, 145] and just state the result

$$S_{\text{infl}}[q(\cdot)] = \frac{1}{2\beta} \sum_{n=-\infty}^{+\infty} K_n |q_n|^2 \,. \tag{3.12}$$

The coefficients K_n express the properties of the bath influence on the system. In the continuum limit for a bath of infinitely many dense bath modes ω_j, the bath coupling characteristics are expressed via the spectral density of the bath $G(\omega)$ [144]. We have

$$K_n = \sum_{j=1}^{N} \frac{c_j^2}{m_j} \frac{1}{\nu_n^2 + \omega_j^2} = 2 \int_0^\infty d\omega \left\{ G(\omega) \frac{\omega}{\nu_n^2 + \omega^2} \right\} . \tag{3.13}$$

The fraction next to the spectral density in the integrand of Eq. (3.13) involve the Matsubara coefficients of the imaginary-time free boson propagator

$$D_\omega(\tau) = \frac{1}{\beta} \sum_{n=-\infty}^{+\infty} \frac{2\omega}{\nu_n^2 + \omega^2} e^{i\nu_n \tau} = [1 + n_B(\omega)] e^{-\omega\tau} + n_B(\omega) e^{+\omega\tau} \,, \tag{3.14}$$

with the Bose distribution $n_B(\omega) = [e^{\beta\omega} - 1]^{-1}$. It is also referred to as the free thermal Green's function $D_\omega(\tau)$. The integral kernel of the influence action Eq. (3.12)

$$K(\tau) = \frac{1}{\beta} \sum_{n=-\infty}^{+\infty} K_n e^{i\nu_n \tau} = \int_0^\infty d\omega \, G(\omega) D_\omega(\tau) \,, \tag{3.15}$$

combines the bath coupling characteristics in the spectral density $G(\omega)$ and the imaginary-time propagation of the free bath modes $D_\omega(\tau)$. With Eq. (3.15) the influence action takes the form

$$S_{\text{infl}} = \frac{1}{2} \int_0^\beta d\tau \int_0^\beta d\tau' \{ q(\tau) K(\tau - \tau') q(\tau') \} \,, \tag{3.16}$$

where the nonlocality in time of the influence action becomes apparent [32].

3.2.3 Bath spectral density

The general influence of a dissipative bath is usually studied in the spin-boson model, where a two-state system $\hat{H}_S = \Omega \hat{\sigma}_x / 2$ is bilinearly coupled to a harmonic oscillator bath via $\hat{\sigma}_z \sum_{j=1}^{N} c_j \hat{x}_j / 2$ [32, 146, 147]. The bath is classified by the low-frequency signature of its spectral density $G(\omega) \propto \gamma\omega^s$. Where γ is the coupling constant to the bath and s is the spectral exponent of the frequency dependence. A bath with $s = 1$ is called Ohmic, since it results in a time-local bath influence comparable to a series resistor [32]. As visualized in figure 3.1, the ratio of the damping rate to the oscillation frequency is constant, which manifests the time-local dynamics. By increasing the coupling γ to an Ohmic bath out of the weak regime $\gamma < 0.5$, the dynamics are tuned to be incoherent [32, 147]. In a super-Ohmic bath $s > 1$ the damping is comparatively weak for slow oscillations, but grows large for high frequencies, as shown in figure 3.1. The consequence is that no incoherent effects are induced [147]. Figure 3.1 illustrates that a sub-Ohmic spectral density $s < 1$ gives a large weight to the coupling to low-frequency oscillations and rather little to fast dynamics. Studies of the spin-

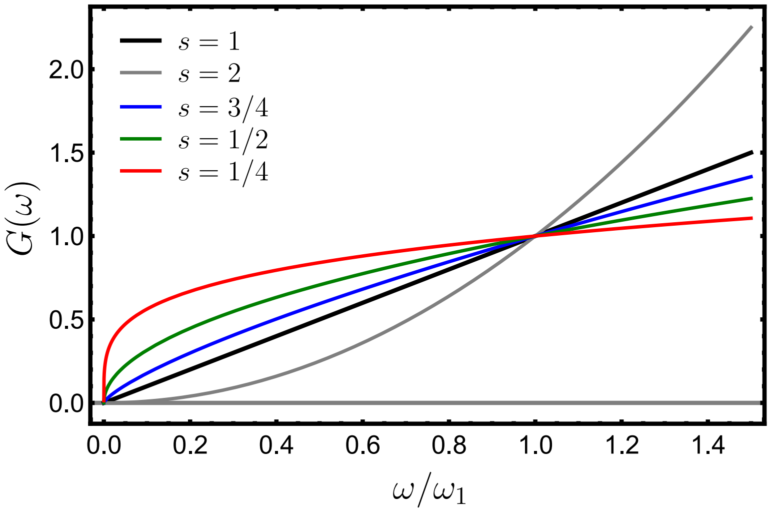

Figure 3.1: Plot of the asymptotic low-frequency behavior of the spectral densities $G(\omega)$ with Ohmic ($s = 1$), super-Ohmic ($s = 2$), and sub-Ohmic ($s = 3/4$, $1/2$, and $1/4$) bath properties.

boson model revealed that a bath with $1/2 \lesssim s \leq 1$ produces damped dynamics at small coupling*, $\gamma \lesssim 0.2$, which become incoherent with increasing coupling and finally lead to a localized phase at strong bath coupling [147–151]. For an even smaller exponent $0 \leq s \lesssim 1/2$ the bath preserves the oscillatory dynamics independent of the bath coupling γ [147, 150]. In fact, at very strong coupling, any sub-Ohmic bath $0 \leq s \leq 1$ produces pseudo-coherent dynamics as described in Ref. [147].

In the classical limit $\hbar \to 0$ an Ohmic environment produces white noise [32]. The key property of white noise is its delta-correlated bath fluctuations $\langle \hat{\Xi}^\dagger(t)\hat{\Xi}(t')\rangle = 2\kappa\delta(t - t')$, see section 2.3.6. This lack of retardation effects is the defining property for Markovian dissipation [32]. A non-Ohmic bath with its biased coupling to low frequencies for $s < 1$ or high frequencies for $s > 1$ consequently produces colored noise. Sub-Ohmic reservoirs induce strong non-Markovian dynamics and come along with exotic quantum colored noise features [32, 147].

Sub-Ohmic dissipation $s < 1$ describes phenomena such as incoherent tunneling by the open two-state description. This is valuable for example in the theory of quantum transport [32]. Sub-Ohmic effects are also the basis of ultra-slow glass dynamics [132]. In recent decades they have also been found in quantum impurity systems [134, 135] and quantum dots [133]. They can also play a role in nanomechanical oscillator systems [131] and arise from charge noise in superconducting qubits [129, 130].

In general, the dynamics under coupling to a sub-Ohmic bath are difficult to handle in computation [147] due to aspects like long-term memory effects.

3.2.4 Dissipation in the cavity BEC

The special feature of the cavity setup to allow in situ measurements of the photon dynamics [23, 69, 102–104] facilitates a real-time measurement of the cavity photon fluctuations approaching the Dicke critical point [28]. Intriguingly, the data reveal that the cavity occupation $\langle \hat{a}^\dagger \hat{a}\rangle$ exceeds that of the isolated Hamiltonian system. On the other hand, the Bogoliubov theory prediction of the dissipative system as discussed in Ref. [36], see section 2.3.6, exaggerates the fluctuations. It was concluded that additional damping of the atomic excitations, not accounted for by Bogoliubov theory, is responsible, so a phenomenological damping rate was constructed. The model was extended by the additional

---

[*] The precise boundaries for weak and strong coupling depend on the exponent s, see the phase diagram in Ref. [147], and on the cut-off frequency of the bath as well as the chosen criterium to distinguish between coherent, pseudocoherent, and incoherent dynamics.

damping channel in quantum Langevin form and fitted to data obtained from the measurement of the second-order correlation function $g^{(2)}(t,0) \propto \langle \hat{a}^\dagger(t)\hat{a}^\dagger(0)\hat{a}(0)\hat{a}(t)\rangle$ [28].
The correlation measurement shows the critical slowing of the dynamics associated with the softening of the excitation frequency, as also verified in Ref. [35], and a critical exponent of 0.9 ± 0.1 is extracted for the divergence of the fluctuations in the vicinity of the phase transition [28]. It agrees well with the theoretical prediction from the dissipative system, see section 2.3.6 [36].
The complicated phenomenological damping, which had to be nontrivially adjusted with the atom-light coupling strength λ, see figure 4 in Ref. [28], suggests an exciting non-Markovian environment that facilitates this additional damping channel. A phenomenological analysis of such an environment coupled to the Bogoliubov description of the cavity BEC setup Eq. (2.54) has been performed based on a toy model for the bath Hamiltonian [152, 153]. This model is described by

$$\hat{H} = -\delta_C \hat{a}^\dagger \hat{a} + \omega_1 \hat{\psi}_1^\dagger \hat{\psi}_1 + \lambda\sqrt{N}\left(\hat{a} + \hat{a}^\dagger\right)\left(\hat{\psi}_1 + \hat{\psi}_1^\dagger\right), \tag{3.17}$$

coupled to the usual white noise bath for the cavity of damping rate κ as employed in section 2.3.6 [36] and the colored bath for the atomic dissipation characterized by the generic ansatz for the spectral density

$$G(\omega) = \theta_H(\omega)\frac{\gamma}{\pi}\frac{(\omega/\omega_1)^s}{1 + (\omega/\omega_{\text{cut}})^2}, \tag{3.18}$$

with a cutoff at the frequency ω_{cut} and the Heaviside function $\theta_H(\omega)$. This bath is Ohmic for $s = 1$, sub-Ohmic for $0 < s < 1$, and super-Ohmic for $s > 1$, with exemplary spectral densities for these cases plotted in the figure 3.1. Note that for the super-Ohmic choice of s the exponent of the cut-off term $(\omega/\omega_{\text{cut}})^2$ must be increased to a value greater than 2 to be at least $2s$ [152, 153]. The spectral density completely characterizes the bath via the functions

$$K^{R,A}(\omega) = \mathcal{P}\int_0^\infty d\omega' \left\{\frac{G(\omega')}{\omega - \omega'}\right\} \mp i\pi G(\omega), \qquad D(\omega) = 2i\pi G(\omega). \tag{3.19}$$

The non-equilibrium dynamics of the model is represented by the action in the Keldysh formalism [67, 154–157]

$$\begin{aligned} S = \int \frac{d\omega}{2\pi} \Bigg\{ &\begin{pmatrix} a_{\text{cl}}^* & a_{\text{qu}}^* \end{pmatrix} \begin{pmatrix} 0 & \omega + \delta_C - i\kappa \\ \omega + \delta_C + i\kappa & 2i\kappa \end{pmatrix} \begin{pmatrix} a_{\text{cl}} \\ a_{\text{qu}} \end{pmatrix} \\ &+ \begin{pmatrix} \psi_{1,\text{cl}}^* & \psi_{1,\text{qu}}^* \end{pmatrix} \begin{pmatrix} 0 & \omega - \omega_1 - K^A \\ \omega - \omega_1 - K^R & D \end{pmatrix} \begin{pmatrix} \psi_{1,\text{cl}} \\ \psi_{1,\text{qu}} \end{pmatrix} \\ &- \frac{\lambda\sqrt{N}}{2}\left(a_{\text{qu}} + a_{\text{qu}}^*\right)\left(\psi_{1,\text{cl}} + \psi_{1,\text{cl}}^*\right) + \left(a_{\text{cl}} + a_{\text{cl}}^*\right)\left(\psi_{1,\text{qu}} + \psi_{1,\text{qu}}^*\right) \Bigg\}. \end{aligned} \tag{3.20}$$

Introducing fields with negative frequencies

$$\boldsymbol{v}^\dagger(\omega) = \begin{pmatrix} a_{\text{cl}}^*(\omega) & a_{\text{cl}}(-\omega) & \psi_{1,\text{cl}}^*(\omega) & \psi_{1,\text{cl}}(-\omega) & a_{\text{qu}}^*(\omega) & a_{\text{qu}}(-\omega) & \psi_{1,\text{qu}}^*(\omega) & \psi_{1,\text{qu}}(-\omega) \end{pmatrix}, \tag{3.21a}$$

and thus doubling the variable space yields the expression of the Keldysh action

$$S = \frac{1}{2}\int \frac{d\omega}{2\pi}\boldsymbol{v}^\dagger(\omega) \begin{pmatrix} 0 & \left[\boldsymbol{G}_{4\times4}^A\right]^{-1}(\omega) \\ \left[\boldsymbol{G}_{4\times4}^R\right]^{-1}(\omega) & \boldsymbol{D}_{4\times4}^K(\omega) \end{pmatrix} \boldsymbol{v}(\omega). \tag{3.22}$$

The characteristic frequencies of the system are the poles of the retarded Green's function $\boldsymbol{G}^R_{4\times4}(z)$ analytically extended into the lower complex plane. Finding an expression for the self-energies requires a choice of Riemann sheet. Here the second sheet is selected as indicated by the Roman numeral index II so that the self-energy is

$$K^R_{\mathrm{II}}(z) = \gamma \frac{e^{i\pi s}}{\sin \pi s} \left(\frac{z}{\omega_1}\right)^s . \tag{3.23}$$

Using the symmetry $K^A_{\mathrm{II}}(z) = \left[K^R_{\mathrm{II}}(z)\right]^*$ and defining $\Gamma(z) = \left[K^R_{\mathrm{II}}(z) - K^A_{\mathrm{II}}(-z^*)\right]/2i$ and $\Delta(z) = \left[K^R_{\mathrm{II}}(z) + K^A_{\mathrm{II}}(-z^*)\right]/2$, the poles of the retarded Green's function are found in the characteristic equation

$$\det\left[\boldsymbol{G}^R_{4\times4}\right]^{-1}(z) = \left[(z+i\kappa)^2 - \delta_C^2\right]\left([z - i\Gamma(z)]^2 - [\omega_1 + \Delta(z)]^2\right) + \lambda^2\sqrt{N}\delta_C\left[\omega_1 + \Delta(z)\right] = 0\,. \tag{3.24}$$

The poles are either pairs $(z, -z^*)$ with real parts of opposite sign or purely imaginary values $z \in i\mathbb{R}$. One of the solutions for the poles corresponds to the soft mode polariton which we have already seen in the Bogoliubov theory discussed in section 2.3.6. Away from the critical value λ_{cr} the damping of the soft mode polariton is significantly modified by the coupling to the bath compared to the damping seen as the real part in figure 2.9. The effect of the bath is analyzed by an exact numerical calculation of the correlation functions for the photonic mode $C_a(\omega) = i[\boldsymbol{G}^K_{4\times4}]_{11}$ and the low-frequency mode $C_{\psi_1}(\omega) = i[\boldsymbol{G}^K_{4\times4}]_{33}$, obtained as elements of $\boldsymbol{G}^K_{4\times4} = -\boldsymbol{G}^R_{4\times4}(\omega)\boldsymbol{D}^K_{4\times4}(\omega)\boldsymbol{G}^A_{4\times4}(\omega)$. If the two system modes are uncoupled $\lambda = 0$, the correlation function for the photonic mode is simply a Lorentzian peak at $\omega = -\delta_C$ with width 2κ. For $\lambda = 0$ the colored bath affects only the low-frequency mode ω_1 and its spectral peak is strictly zero for negative frequencies and has a high-frequency tail predetermined by the cutoff ω_{cut}. It is not Lorentzian. The bath modifies the bare frequency ω_1 according to the strength of the coupling to the reservoir γ. Turning on the coupling to the photonic mode λ the peak is shifted towards $\omega = 0$. If the reservoir takes influence, the real part of the soft mode polariton frequency vanishes for smaller $\lambda/\lambda_{\mathrm{cr}}$ compared to the isolated polariton system reviewed around figure 2.9. Equivalently, the imaginary part bifurcates earlier due to the bath's presence. At fairly large couplings around $\lambda = 0.8\lambda_{\mathrm{cr}}$ the spectrum of the correlation functions becomes double-peaked with one peak at positive and one at negative frequency due to the hybridization of the modes. Near the critical point $\lambda \gtrsim 0.93\,\lambda_{\mathrm{cr}}$ the spectrum of the correlation functions has only a single peak at $\omega \approx 0$. It diverges at the critical point where they are located precisely at $\omega = 0$.

To determine how the sub-Ohmic characteristics affect the universality class of the phase transition, the cavity photon number $\langle \hat{a}^\dagger(0)\hat{a}(0)\rangle$ is analyzed. It diverges near the phase transition $1 - \lambda/\lambda_{\mathrm{cr}} < 10^{-4}$ like $|1-\lambda/\lambda_{\mathrm{cr}}|^{-c}$ with the critical exponent c. Tuning the sub-Ohmic bath characteristic exponent s results in a continuous monotonic change of the critical exponent. For a sub-Ohmic reservoir $0.5 < s < 1$ the critical exponent c is less than 1 and reaches $c = 1$ when the bath is Ohmic $s = 1$ in agreement with predictions made for Markovian dissipation channels, i.e. in the absence of a colored bath [152, 153]. If the spectral density eq. (3.18) is modified to include super-Ohmic behavior $s > 1$, no significant change from the Ohmic characteristic exponent is found [153].

The analysis of the next-order terms of the fluctuations beyond the usual Bogoliubov theory unveils processes of Landau and Beliaev damping known to occur in superfluids [33, 67, 116–126]. Landau damping is a process that relies on temperature, so it vanishes as $\beta \to \infty$. Zero-temperature pure quantum damping can therefore only arise from Beliaev processes. Analysis of the one-dimensional form of the field Hamiltonian Eq. (2.46), where $y = z = 0$ is fixed and only dynamics along the cavity axis are permitted, reveals Heisenberg equations with a hierarchy in the powers of the square root of the number of atoms $\sqrt{N}$ [34, 127]. As predicted, at order N^0 the Bogoliubov spectrum reviewed in section 2.3.6 emerges, while at order $N^{-1/2}$ Landau and Beliaev processes appear and orders of N^{-1} and beyond are discarded. The fluctuations manifesting these damping processes have phonon-like properties, and for large condensate sizes, they become spectrally dense to form an intrinsic dissipative bath arising from short-range s-wave scattering. In a Landau or Beliaev process, a polariton excitation is damped by a two-phonon process in this reservoir [127]. In a system where the dynamics are constrained to be effectively one-dimensional by a harmonic trap, the spectral density function of the Beliaev bath for the atomic checkerboard mode ω_1 is found to be $G(\omega) \propto \sqrt{(\omega/\omega_R) - 1/2}$ [128]. Due to the conservation of momentum, it is gapped from $\omega = 0$. Subsequently, although it follows a sub-Ohmic power law 1/2 it does so away from zero frequency and, thus, does not modify the critical exponent at the phase transition [128].

The Beliaev process in the one-dimensional system is peaked at an atom-cavity coupling of about $\lambda = 0.8\,\lambda_{\mathrm{cr}}$ due to a resonance of the soft-mode polariton with the phononic Beliaev process. This was further analyzed by discarding all polariton modes except the soft one, creating a system analog to a single harmonic oscillator with the soft mode frequency Ω_s coupled to the phonon bath [34]. It leads to a closed set of equations for the retarded Green's functions so that the self-energies can be extracted. In the Born-Markov approximation for the self-energies $\Sigma(\omega) \approx \Sigma(\Omega_s)$, the divergent peak of the Beliaev damping is found at $\lambda = 0.8\,\lambda_{\mathrm{cr}}$ [34]. However, the Born-Markov approximation turns out to be poor in the vicinity of the spectral peak. The analysis of the poles of the Green's function of the soft-mode polaritons uncovers that at $\lambda = 0$ or $\lambda = \lambda_{\mathrm{cr}}$ the pole that can be attributed to the polariton is well separated from those of the phonon bath, especially the most relevant of the latter, which is closest to the real axis. Although at coupling parameters $0 < \lambda < \lambda_{\mathrm{cr}}$ the soft-mode polariton pole and the phonon bath pole exhibit an avoided crossing between them at about $\lambda = 0.8\lambda_{\mathrm{cr}}$ apparent in their real parts [34]. The dynamics in this region cannot be interpreted as that of a single dressed oscillator mode. Furthermore, while the Beliaev decay rate is still peaked as found in the Born-Markov approximation, the peak is an order of magnitude smaller [34]. Analysis of the correlation functions where the cavity mode is damped by the photon losses and the atomic checkerboard mode is in contact with the $G(\omega) \propto \sqrt{(\omega/\omega_R) - 1/2}$ Beliaev reservoir gives some more concrete insights into the peculiarities of the system [128]. For weak coupling to the environment, the correlation function spectrum of the low-frequency mode exhibits sharp resonance peaks for the soft polariton frequency. If the Beliaev processes are coupled stronger by an order of magnitude, the peaks are significantly broadened but strictly vanish for $\omega < \omega_R/2$. Increasing the coupling pushes this peak into the limit of the frequency range at $\omega_R/2$. For about $\lambda = 0.9\,\lambda_{\mathrm{cr}}$ the spectrum has a hole-burning effect. If the cavity is strongly damped, i.e. κ is larger, the increased linewidth of the sharp peak below $\omega_R/2$ washes out the fine structure of the Beliaev process because its tail extends into the $\omega > \omega_R/2$ region. These effects are all present in the spectrum of the photon correlation function C_a as well.

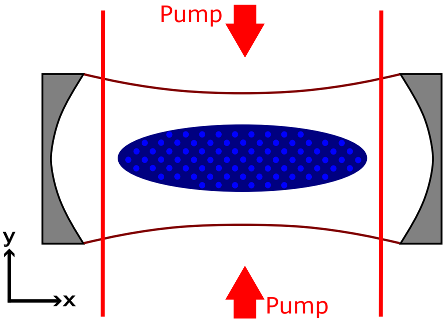

Figure 3.2: Sketch of the cavity BEC setup described by the Hamiltonian Eq. (3.25). The dynamics are constrained to the pump cavity plane xy. The checkerboard fluctuations are indicated by one of the checkerboard configurations in the blue condensate. Cavity dissipation as shown in figure 2.6 will be reintroduced when we go beyond the Hamiltonian description of the system.

In this thesis, we formulate an extension of Bogoliubov theory to microscopically derive the colored spectra of quantum statistical fluctuations. They exhibit exotic, strongly sub-Ohmic features, yielding significant non-Markovian dynamics. The imaginary-time path integral allows us to write down the bath spectral density in an exact analytical way and to study the dissipative two-mode polariton system. Finally, we determine the influence of the damping on the physical observables, illustrating the possibility of controlling and enhancing the quantum fluctuations in the system.

3.3 – Derivation of the fluctuations

We start out with the effective field Hamiltonian of the cavity BEC system Eq. (2.46) with its dynamics constrained to the xy plane of the cavity and the pump mode as in figure 3.2 [27, 88]

$$\hat{H} = \int d^2\boldsymbol{r}\, \hat{\psi}^\dagger(\boldsymbol{r}) \left[\frac{-\nabla^2}{2m} + \frac{h^2(\boldsymbol{r})}{\Delta_A} + \frac{g^2(\boldsymbol{r})}{\Delta_A} \hat{a}^\dagger \hat{a} + \frac{g(\boldsymbol{r})h(\boldsymbol{r})}{\Delta_A} \left(\hat{a} + \hat{a}^\dagger\right) + \frac{U}{2} \hat{\psi}^\dagger(\boldsymbol{r}) \hat{\psi}(\boldsymbol{r}) \right] \hat{\psi}(\boldsymbol{r}) - \Delta_C \hat{a}^\dagger \hat{a}\,. \tag{3.25}$$

From the preexisting analysis of the normal phase discussed in section 2.3.7, we can expand the atomic field operators around $\hat{\psi}_0 \sim 1$ and $\hat{\psi}_1 \sim \cos(kx)\cos(ky)$ introduced in Eq. (2.59). The expansion thus has the form of two-mode Bloch functions

$$\hat{\psi}(\boldsymbol{r}) = \frac{1}{\sqrt{V_{2D}}} \sum_{\boldsymbol{p}\in\mathcal{P}} \left[e^{i\boldsymbol{p}\boldsymbol{r}} \left(\hat{\psi}_{0,\boldsymbol{p}} + 2\cos(kx)\cos(ky) \hat{\psi}_{1,\boldsymbol{p}} \right) \right], \tag{3.26a}$$

$$\mathcal{P} = \left\{ \begin{pmatrix} \frac{2\pi j_x}{L_x} & \frac{2\pi j_y}{L_y} \end{pmatrix}^T \middle| j_x, j_y \in \mathbb{Z} \wedge |p_x|, |p_y| < \frac{k}{2} \right\}, \tag{3.26b}$$

where $\hat{\psi}_{0,\boldsymbol{0}} = \hat{\psi}_0$ and $\hat{\psi}_{1,\boldsymbol{0}} = \hat{\psi}_1$. We consider the subspace of the two Bloch modes Eq. (3.26) to be closed. When we insert the Bloch mode expansion into the cavity BEC field Hamiltonian Eq. (3.25), we have to consider

$$\frac{1}{L} \int_{-\frac{L}{2}}^{\frac{L}{2}} dx \left\{ e^{-ipx} \right\} = \delta_{p,0}\,, \tag{3.27a}$$

$$\frac{1}{L} \int_{-\frac{L}{2}}^{\frac{L}{2}} dx \left\{ e^{-i(p-k/2)x} \right\} = \delta_{2p,k} = 0\,, \tag{3.27b}$$

where the second identity follows from the definition of the quasi-momentum $|p| < k/2$ in the bands Eq. (3.26b), i.e. the Brioullin zone. Additionally, the trigonometric identity $\cos^2(kx) = [1 + \cos(2kx)]/2$ comes into play. The Hamiltonian of the cavity BEC expressed in the two Bloch modes is then

$$\begin{aligned}\hat{H} = \sum_{\boldsymbol{p}\in\mathcal{P}} \Bigg[& \left(\frac{\boldsymbol{p}^2}{2m} + \frac{h_0^2}{2\Delta_A}\right) \hat{\psi}^\dagger_{0,\boldsymbol{p}} \hat{\psi}_{0,\boldsymbol{p}} + \left(\frac{\boldsymbol{p}^2}{2m} + \frac{k^2}{m} + \frac{3h_0^2}{4\Delta_A}\right) \hat{\psi}^\dagger_{1,\boldsymbol{p}} \hat{\psi}_{1,\boldsymbol{p}} \\ & + \frac{g_0^2}{2\Delta_A} \hat{a}^\dagger \hat{a} \left(\hat{\psi}^\dagger_{0,\boldsymbol{p}} \hat{\psi}_{0,\boldsymbol{p}} + \frac{3}{2} \hat{\psi}^\dagger_{1,\boldsymbol{p}} \hat{\psi}_{1,\boldsymbol{p}} \right) + \frac{g_0 h_0}{2\Delta_A} \left(\hat{a} + \hat{a}^\dagger\right) \left(\hat{\psi}^\dagger_{1,\boldsymbol{p}} \hat{\psi}_{0,\boldsymbol{p}} + \hat{\psi}^\dagger_{0,\boldsymbol{p}} \hat{\psi}_{1,\boldsymbol{p}} \right) \\ & + \frac{U}{2V_{2D}} \sum_{\boldsymbol{q},\boldsymbol{q}'\in\mathcal{P}} \Big(\hat{\psi}^\dagger_{0,\boldsymbol{p}+\boldsymbol{q}'} \hat{\psi}^\dagger_{0,\boldsymbol{q}-\boldsymbol{q}'} \hat{\psi}_{0,\boldsymbol{q}} \hat{\psi}_{0,\boldsymbol{p}} + \hat{\psi}^\dagger_{1,\boldsymbol{p}+\boldsymbol{q}'} \hat{\psi}^\dagger_{1,\boldsymbol{q}-\boldsymbol{q}'} \hat{\psi}_{0,\boldsymbol{q}} \hat{\psi}_{0,\boldsymbol{p}} + 4 \hat{\psi}^\dagger_{1,\boldsymbol{p}+\boldsymbol{q}'} \hat{\psi}^\dagger_{0,\boldsymbol{q}-\boldsymbol{q}'} \hat{\psi}_{0,\boldsymbol{q}} \hat{\psi}_{1,\boldsymbol{p}} \\ & \qquad + \hat{\psi}^\dagger_{0,\boldsymbol{p}+\boldsymbol{q}'} \hat{\psi}^\dagger_{0,\boldsymbol{q}-\boldsymbol{q}'} \hat{\psi}_{1,\boldsymbol{q}} \hat{\psi}_{1,\boldsymbol{p}} + \frac{9}{4} \hat{\psi}^\dagger_{1,\boldsymbol{p}+\boldsymbol{q}'} \hat{\psi}^\dagger_{1,\boldsymbol{q}-\boldsymbol{q}'} \hat{\psi}_{1,\boldsymbol{q}} \hat{\psi}_{1,\boldsymbol{p}} \Big) \Bigg] - \Delta_C \hat{a}^\dagger \hat{a} \,. \end{aligned} \tag{3.28}$$

In a weakly interacting dilute BEC the occupation of the zero momentum mode $\hat{\psi}_0$ is macroscopic. Below the Dicke phase transition point λ_{cr} this remains true if the BEC is coupled to the cavity, except for a tiny region near λ_{cr} where the quantum depletion to $\hat{\psi}_1$ is large [36, 100]. Therefore, we will apply the Bogoliubov theory as reviewed for the Bose gas without the cavity in section 2.2. We know that the mean-field of the normal phase is $\langle\hat{\psi}_0\rangle = \sqrt{n}$ and $\langle\hat{\psi}_{0,\boldsymbol{p}\neq\boldsymbol{0}}\rangle = \langle\hat{\psi}_1\rangle = \langle\hat{\psi}_{1,\boldsymbol{p}\neq\boldsymbol{0}}\rangle = \langle\hat{a}\rangle = 0$ [100]. Thus, any operator other than that of the homogeneous condensate $\hat{\psi}_0$ is just the fluctuation around its trivial mean-field

$$\hat{\psi}_1 = \hat{\phi}_1 \,, \qquad \hat{a} = \delta\hat{a} \,, \qquad \hat{\psi}_{0,\boldsymbol{p}\neq\boldsymbol{0}} = \hat{\phi}_{0,\boldsymbol{p}} \,, \qquad \hat{\psi}_{1,\boldsymbol{p}\neq\boldsymbol{0}} = \hat{\phi}_{1,\boldsymbol{p}} \,. \tag{3.29}$$

We then use the closed subspace property to express the zero-momentum condensate mode by the total macroscopic number of atoms N, from which the fluctuations in the other modes are subtracted

$$\hat{\psi}_0 = \hat{\psi}_0^\dagger = \sqrt{N - \hat{\phi}_1^\dagger \hat{\phi}_1 - {\sum_{\boldsymbol{p}\in\mathcal{P}}}' \left(\hat{\phi}^\dagger_{0,\boldsymbol{p}} \hat{\phi}_{0,\boldsymbol{p}} + \hat{\phi}^\dagger_{1,\boldsymbol{p}} \hat{\phi}_{1,\boldsymbol{p}} \right)} \,, \tag{3.30}$$

where the primed sum denotes the exclusion of $\boldsymbol{p} = \boldsymbol{0}$. We insert the ansatz into Eq. (3.28) together with Eq. (3.29). We need to be careful to respect the commutator $\hat{\psi}_0^\dagger \hat{\psi}_0^\dagger \hat{\psi}_0 \hat{\psi}_0 = \hat{\psi}_0^\dagger \hat{\psi}_0 (\hat{\psi}_0^\dagger \hat{\psi}_0 - 1)$ before injecting the ansatz Eq. (3.30). Using that the quantum depletion from the homogeneous condensate is small, i.e.

$$\frac{\langle\hat{D}\rangle}{N} = \frac{\langle\hat{\phi}_1^\dagger \hat{\phi}_1\rangle + {\sum_{\boldsymbol{p}\in\mathcal{P}}}' \left(\langle\hat{\phi}^\dagger_{0,\boldsymbol{p}} \hat{\phi}_{0,\boldsymbol{p}}\rangle + \langle\hat{\phi}^\dagger_{1,\boldsymbol{p}} \hat{\phi}_{1,\boldsymbol{p}}\rangle \right)}{N} \ll 1 \,, \tag{3.31}$$

we expand the square root of Eq. (3.30) where necessary as

$$\sqrt{N}\sqrt{1 - \frac{\hat{D}}{N}} = \sqrt{N} \left[1 - \frac{\hat{\phi}_1^\dagger \hat{\phi}_1}{2N} - \frac{1}{2N} {\sum_{\boldsymbol{p}\in\mathcal{P}}}' \left(\hat{\phi}^\dagger_{0,\boldsymbol{p}} \hat{\phi}_{0,\boldsymbol{p}} + \hat{\phi}^\dagger_{1,\boldsymbol{p}} \hat{\phi}_{1,\boldsymbol{p}} \right) + \dots \right] . \tag{3.32}$$

We count each occurrence of a fluctuation operator from Eq. (3.29) or its conjugate as an order in the fluctuations. We immediately discard any term that is of fourth order or higher. The procedure is mostly based on counting orders in the square root of the large number of atoms $\sqrt{N}$ and neglecting any density-density interaction term that is not at least of order $\sqrt{N}$. For a density-density interaction term to survive this procedure, it must include the zero momentum condensate mode $\psi_{0,0}$ in Eq. (3.28). Finally, there remain a few terms that represent, for example, Umklapp processes within the bands without directly involving the cavity $\hat{a}$ or the checkerboard fluctuations $\hat{\phi}_1$. We neglect these few terms as well as the constant mean-field energy shift $UnN/2$ with $n = N/V_{2D}$. Thus, we acquire

$$\begin{aligned}\hat{H} =& \left(\frac{k^2}{m} + \frac{h_0^2}{4\Delta_A} + Un\right)\hat{\phi}_1^\dagger\hat{\phi}_1 + \frac{Un}{2}\left(\hat{\phi}_1\hat{\phi}_1 + \hat{\phi}_1^\dagger\hat{\phi}_1^\dagger\right) \\ &+ {\sum_{\boldsymbol{p}\in\mathcal{P}}}' \left[\left(\frac{\boldsymbol{p}^2}{2m} + Un\right)\hat{\phi}_{0,\boldsymbol{p}}^\dagger\hat{\phi}_{0,\boldsymbol{p}} + \frac{Un}{2}\left(\hat{\phi}_{0,-\boldsymbol{p}}\hat{\phi}_{0,\boldsymbol{p}} + \hat{\phi}_{0,\boldsymbol{p}}^\dagger\hat{\phi}_{0,-\boldsymbol{p}}^\dagger\right)\right] \\ &+ {\sum_{\boldsymbol{p}\in\mathcal{P}}}' \left[\left(\frac{\boldsymbol{p}^2}{2m} + \frac{k^2}{m} + \frac{h_0^2}{4\Delta_A} + Un\right)\hat{\phi}_{1,\boldsymbol{p}}^\dagger\hat{\phi}_{1,\boldsymbol{p}} + \frac{Un}{2}\left(\hat{\phi}_{1,-\boldsymbol{p}}\hat{\phi}_{1,\boldsymbol{p}} + \hat{\phi}_{1,\boldsymbol{p}}^\dagger\hat{\phi}_{1,-\boldsymbol{p}}^\dagger\right)\right] \\ &+ 2\frac{U\sqrt{N}}{V_{2D}} {\sum_{\boldsymbol{p}\in\mathcal{P}}}' \left[\left(\hat{\phi}_1 + \hat{\phi}_1^\dagger\right)\left(\hat{\phi}_{1,\boldsymbol{p}}^\dagger\hat{\phi}_{0,\boldsymbol{p}} + \hat{\phi}_{0,\boldsymbol{p}}^\dagger\hat{\phi}_{1,\boldsymbol{p}}\right) + \hat{\phi}_1^\dagger\hat{\phi}_{0,-\boldsymbol{p}}\hat{\phi}_{1,\boldsymbol{p}} + \hat{\phi}_{1,\boldsymbol{p}}^\dagger\hat{\phi}_{0,-\boldsymbol{p}}^\dagger\hat{\phi}_1\right] \\ &+ \frac{g_0 h_0}{2\Delta_A}\sqrt{N}\left(\hat{a} + \hat{a}^\dagger\right)\left(\hat{\phi}_1 + \hat{\phi}_1^\dagger\right) + \frac{g_0 h_0}{2\Delta_A}\left(\hat{a} + \hat{a}^\dagger\right) {\sum_{\boldsymbol{p}\in\mathcal{P}}}' \left[\hat{\phi}_{1,\boldsymbol{p}}^\dagger\hat{\phi}_{0,\boldsymbol{p}} + \hat{\phi}_{0,\boldsymbol{p}}^\dagger\hat{\phi}_{1,\boldsymbol{p}}\right] \\ &+ \left(-\Delta_C + \frac{g_0^2 N}{2\Delta_A}\right)\hat{a}^\dagger\hat{a} + \text{const}\,. \end{aligned} \tag{3.33}$$

We reintroduce the effective parameters that have already appeared in the review of the cavity BEC Bogoliubov theory in section 2.3.6. They are the recoil frequency ω_R, the pumping strength $\overline{\omega}_P$, and the coupling U_0 of a single atom to the cavity. Based on these, there is the coupling λ between the atoms and the cavity and the effective cavity detuning δ_C modified by the refractive index of the atoms $\propto U_0 N$. There is also a new parameter η for the coupling of the checkerboard mode $\hat{\phi}_1$ to the bands

$$\begin{aligned} \omega_R &= \frac{k^2}{2m}\,, & \overline{\omega}_P &= -\frac{h_0^2}{4\Delta_A}\,, & U_0 &= \frac{g_0^2}{\Delta_A}\,, \\ \lambda &= \frac{g_0 h_0}{2\Delta_A} = \sqrt{-U_0\overline{\omega}_P}\,, & \delta_C &= \Delta_C - \frac{g_0^2 N}{2\Delta_A} = \Delta_C - \frac{U_0 N}{2}\,, & \eta &= 2\frac{U\sqrt{N}}{V_{2D}}\,. \end{aligned} \tag{3.34}$$

The Bogoliubov modes, which represent the eigenmodes of the BEC without the cavity ($\lambda = 0$), are found by the usual transformation, see section 2.2.2 [57],

$$\hat{\phi}_{0,\boldsymbol{p}} = u_{0,\boldsymbol{p}}\hat{\varphi}_{0,\boldsymbol{p}} - v_{0,\boldsymbol{p}}\hat{\varphi}_{0,-\boldsymbol{p}}^\dagger\,, \qquad \hat{\phi}_{1,\boldsymbol{p}} = u_{1,\boldsymbol{p}}\hat{\varphi}_{1,\boldsymbol{p}} - v_{1,\boldsymbol{p}}\hat{\varphi}_{1,-\boldsymbol{p}}^\dagger\,, \tag{3.35}$$

with the Bogoliubov transformation coefficients for the bands $i = 0, 1$ given by

$$\begin{aligned} u_{i,\boldsymbol{p}} &= \cosh(\alpha_{i,\boldsymbol{p}})\,, & v_{i,\boldsymbol{p}} &= \sinh(\alpha_{i,\boldsymbol{p}})\,, \\ \tanh(2\alpha_{0,\boldsymbol{p}}) &= \frac{nU}{\frac{\boldsymbol{p}^2}{2m} + nU}\,, & \tanh(2\alpha_{1,\boldsymbol{p}}) &= \frac{nU}{\frac{\boldsymbol{p}^2}{2m} + 2\omega_R - \overline{\omega}_P + nU}\,. \end{aligned} \tag{3.36}$$

The eigenfrequencies of these quasiparticles are

$$\omega_{0,\boldsymbol{p}} = \sqrt{\frac{\boldsymbol{p}^2}{2m}\left(\frac{\boldsymbol{p}^2}{2m} + 2nU\right)}\,, \quad \omega_{1,\boldsymbol{p}} = \sqrt{\left(\frac{\boldsymbol{p}^2}{2m} + 2\omega_R - \overline{\omega}_P\right)\left(\frac{\boldsymbol{p}^2}{2m} + 2\omega_R - \overline{\omega}_P + 2nU\right)}\,. \tag{3.37}$$

Taking into account that $u_{i,-\boldsymbol{p}} = u_{i,\boldsymbol{p}}$ and $v_{i,-\boldsymbol{p}} = v_{i,\boldsymbol{p}}$ the resulting Hamiltonian consists exclusively of harmonic oscillators and linear couplings between two or three of them, see Eqs. (3.38), (3.39), and (3.40) or Appendix A.5. We invoke the system-bath model $\hat{H} = \hat{H}_S + \hat{H}_B + \hat{H}_{SB}$ as introduced in section 3.2.1, where we obtain a system of two harmonic oscillators in a phonon-like bath provided by the two Bloch bands [32]. The system is provided by the effective Bogoliubov level model of two

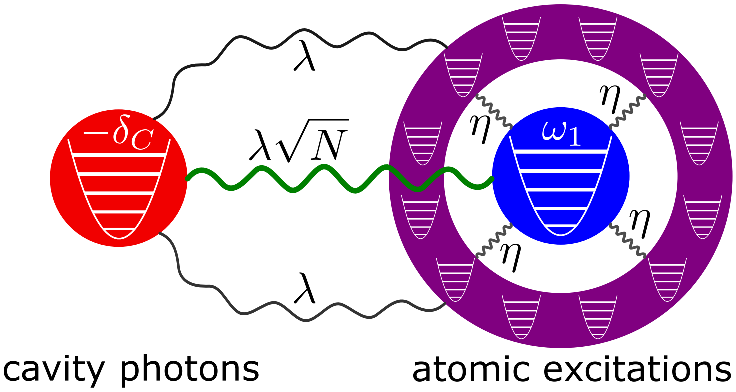

Figure 3.3: Sketch of the effective cavity BEC model in terms of the system-bath formalism $\hat{H} = \hat{H}_S + \hat{H}_B + \hat{H}_{SB}$. The cavity mode $-\delta_C$ is shown as the red subsystem. The checkerboard mode ω_1 is the blue subsystem. These two modes are coupled by their bilinear coupling $\lambda\sqrt{N}$ in green and form the system $\hat{H}_S$, Eq. (3.38). The bath modes, which are the band excitations of the atomic condensate $\hat{H}_B$, Eq. (3.39), are represented in purple surrounding the checkerboard on the atomic subsystem side of the sketch. To this bath, the checkerboard mode couples with the parameter η and the cavity mode couples with the coupling parameter λ, creating the linear system-bath coupling $\hat{H}_{SB}$, Eq. (3.40).

bilinearly coupled harmonic modes of the cavity fluctuations $\hat{a}$ and the checkerboard fluctuations $\hat{\varphi}_1$

$$\hat{H}_S = -\delta_C \hat{a}^\dagger \hat{a} + \omega_1 \hat{\varphi}_1^\dagger \hat{\varphi}_1 + \lambda_0 \big(\hat{a} + \hat{a}^\dagger\big)\big(\hat{\varphi}_1 + \hat{\varphi}_1^\dagger\big) \, . \tag{3.38}$$

The quantum fluctuation bath is given by the phonon-like modes

$$\hat{H}_B = \sum_{\boldsymbol{p}\in\mathcal{P}}{}' \left[\omega_{0,\boldsymbol{p}} \hat{\varphi}_{0,\boldsymbol{p}}^\dagger \hat{\varphi}_{0,\boldsymbol{p}} + \omega_{1,\boldsymbol{p}} \hat{\varphi}_{1,\boldsymbol{p}}^\dagger \hat{\varphi}_{1,\boldsymbol{p}}\right] . \tag{3.39}$$

In the visualization of the system-bath in figure 3.3 they are portrayed as a bath surrounding the matter mode ω_1 of the system due to their nature as excitations of a weakly s-wave scattering BEC. The coupling Hamiltonian between the harmonic two-mode system and the harmonic phonon bath is

$$\begin{aligned} \hat{H}_{SB} = &\left[\lambda\big(\hat{a} + \hat{a}^\dagger\big) + \eta\big(\hat{\varphi}_1 + \hat{\varphi}_1^\dagger\big)\right] \big(\hat{L}_1 - \hat{B}_1\big) \\ &+ \eta\big(u_1\hat{\varphi}_1 - v_1\hat{\varphi}_1^\dagger\big)\big(-\hat{L}_2^\dagger + \hat{B}_2^\dagger\big) + \eta\big(u_1\hat{\varphi}_1^\dagger - v_1\hat{\varphi}_1\big)\big(-\hat{L}_2 + \hat{B}_2\big) \, , \end{aligned} \tag{3.40}$$

with the operators

$$\hat{L}_1 = \sum_{\boldsymbol{p}\in\mathcal{P}}{}' \left[\left(u_{0,\boldsymbol{p}} u_{1,\boldsymbol{p}} + v_{0,\boldsymbol{p}} v_{1,\boldsymbol{p}}\right) \left(\hat{\varphi}_{0,\boldsymbol{p}}^\dagger \hat{\varphi}_{1,\boldsymbol{p}} + \hat{\varphi}_{1,\boldsymbol{p}}^\dagger \hat{\varphi}_{0,\boldsymbol{p}}\right)\right] , \tag{3.41a}$$

$$\hat{B}_1 = \sum_{\boldsymbol{p}\in\mathcal{P}}{}' \left[\left(v_{0,\boldsymbol{p}} u_{1,\boldsymbol{p}} + u_{0,\boldsymbol{p}} v_{1,\boldsymbol{p}}\right) \left(\hat{\varphi}_{1,-\boldsymbol{p}} \hat{\varphi}_{0,\boldsymbol{p}} + \hat{\varphi}_{0,\boldsymbol{p}}^\dagger \hat{\varphi}_{1,-\boldsymbol{p}}^\dagger\right)\right] , \tag{3.41b}$$

$$\hat{L}_2 = \sum_{\boldsymbol{p}\in\mathcal{P}}{}' \left[v_{0,\boldsymbol{p}} u_{1,\boldsymbol{p}} \hat{\varphi}_{0,\boldsymbol{p}}^\dagger \hat{\varphi}_{1,\boldsymbol{p}} + u_{0,\boldsymbol{p}} v_{1,\boldsymbol{p}} \hat{\varphi}_{1,\boldsymbol{p}}^\dagger \hat{\varphi}_{0,\boldsymbol{p}}\right] , \tag{3.41c}$$

$$\hat{B}_2 = \sum_{\boldsymbol{p}\in\mathcal{P}}{}' \left[u_{0,\boldsymbol{p}} u_{1,\boldsymbol{p}} \hat{\varphi}_{1,-\boldsymbol{p}} \hat{\varphi}_{0,\boldsymbol{p}} + v_{0,\boldsymbol{p}} v_{1,\boldsymbol{p}} \hat{\varphi}_{0,\boldsymbol{p}}^\dagger \hat{\varphi}_{1,-\boldsymbol{p}}^\dagger\right] , \tag{3.41d}$$

describing the Landau $\hat{L}$ and Beliaev $\hat{B}$ processes in the phonon bath. Note that the coupling is always linear as shown in figure 3.4 with one (de)excitation each of the system $(\hat{a}, \hat{\varphi}_1)$, the lower band $\hat{\varphi}_{0,\boldsymbol{p}}$, and the upper band $\hat{\varphi}_{1,\boldsymbol{p}}$. The bath-coupling Hamiltonian already proves to be quite exceptional

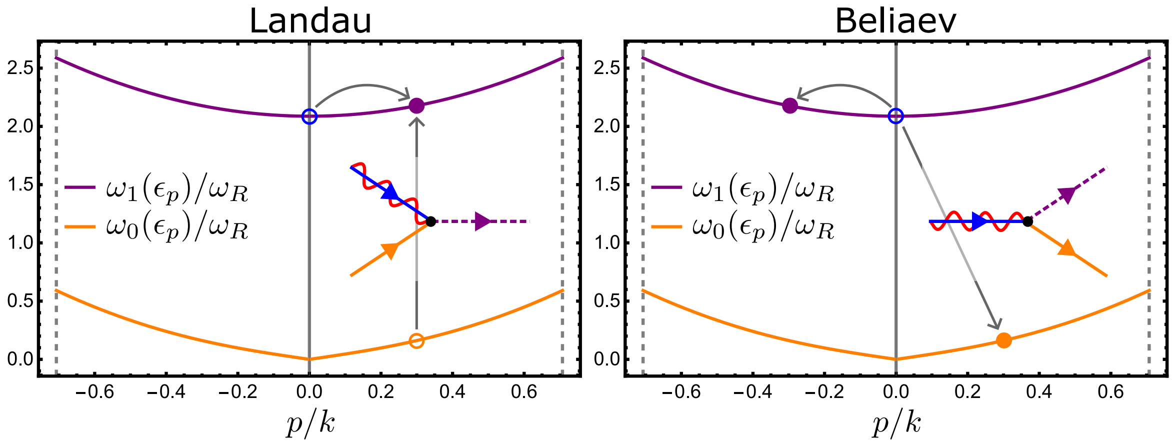

Figure 3.4: Band structure of the two considered bands based on Eq. (3.26) and the subsequent Bogoliubov transformation to $\omega_0(\epsilon_p)$ and $\omega_1(\epsilon_p)$, Eq. (3.37), with $\epsilon_p = \boldsymbol{p}^2/2m$. The boundaries of the quasimomentum are indicated by the dashed vertical lines. In the figure on the left, the Landau process $\hat{\varphi}^\dagger_{1,\boldsymbol{p}}\hat{\varphi}_{0,\boldsymbol{p}}\hat{\varphi}_1$ is sketched by denoting the annihilation of a quasiparticle by an empty circle and the creation by a filled circle. The inset shows a diagram of such a Landau process, where the annihilation of a system excitation either $\hat{\varphi}_1$ (blue propagator) or $\hat{a}$ (red photon propagator) combines with annihilation in the lower band $\hat{\varphi}_{0,\boldsymbol{p}}$ to create a quasiparticle in the upper band $\hat{\varphi}^\dagger_{1.\boldsymbol{p}}$. On the right, the Beliaev process $\hat{\varphi}^\dagger_{0.\boldsymbol{p}}\hat{\varphi}^\dagger_{1,-\boldsymbol{p}}\hat{\varphi}_1$ is sketched. The inset shows how the annihilation of a system excitation $(\hat{a}, \hat{\varphi}_1)$ leads to the creation of two quasiparticles in the bath with opposite quasimomentum, one in the lower band $\hat{\varphi}^\dagger_{0,\boldsymbol{p}}$ and one in the upper band $\hat{\varphi}^\dagger_{1,-\boldsymbol{p}}$. The parameters for the band structure are $nU = 10^{-1}\,\omega_R$, $\overline{\omega}_P = 10^{-2}\,\omega_R$. Figure inspired by Ref. [127].

here, even beyond its occurrence from microscopic processes intrinsic to the cavity BEC setup. The interaction of the system with the quantum fluctuation bath Eq. (3.40) manifests either a Landau or a Beliaev damping process where the quasi-momentum $\boldsymbol{p}$ is conserved. In a Landau process, the creation or annihilation of a system fluctuation leads to the creation of a phonon in one band, while a phonon with the same quasi-momentum is annihilated in the other band. In a Beliaev process, the creation or annihilation of a system fluctuation simultaneously annihilates or creates a phonon in each band but with opposite quasi-momentum. The processes are weighted by the Bogoliubov transformation coefficients $u_{i,\boldsymbol{p}}$ and $v_{i,\boldsymbol{p}}$ intrinsic to the weakly scattering Bose gas [57]. Remarkably, as shown in figure 3.3, the Landau and Beliaev damping, originally known as the damping of a superfluid [33,67,116–126] also couple to the photon fluctuations of the cavity. The coupling parameter to the bath is different depending on whether the bath is acting on the cavity fluctuations or on the checkerboard fluctuations. For the checkerboard it is given by the parameter $\eta = 2U\sqrt{N}/V_{2D} = 2Un/\sqrt{N}$, while for the cavity it is the light-matter coupling via the pump $\lambda = g_0 h_0/2\Delta_A$ that determines the bath coupling strength. Although physically there is only a single bath, in the following we will treat it from the point of view of the two-harmonic-oscillators system Eq. (3.38). We will then decompose it according to which degrees of freedom of Eq. (3.38) it is coupled to, as shown in figure 3.3.

3.4 – Interlude: Similarity to the hybrid atom-optomechanical system*

We make a few assumptions for the coupling parameters in the system-bath model described by Eqs. (3.38) to (3.41), which simplify the model and yield a direct mapping to the effective model of the hybrid atom-optomechanical setup, see section 2.3.10. One of the assumptions is that for the system-bath coupling, the coupling to the cavity λ dominates over the coupling to the checkerboard mode η. Given $\eta \ll \lambda$ the bath is effectively only coupled to the cavity. Our second assumption is that both the

---

*This discussion is not published, neither in Ref. [A] nor other work.

pump strength $\overline{\omega}_P$ and the energy of the s-wave scattering nU are tiny relative to the recoil frequency ω_R. Utilizing $nU, \overline{\omega}_P \ll \omega_R$ yields a plethora of simplifications: $u_{1\boldsymbol{p}} = 1$, $v_{1\boldsymbol{p}} = 0$, $\omega_{1\boldsymbol{p}} = 2\omega_R + \boldsymbol{p}^2/2m$, and $\lambda_0 = \lambda\sqrt{N}$. If we now apply all this to Eqs. (3.38) to (3.41) the system-bath model takes the form

$$\begin{aligned}\hat{H} = &- \delta_C \hat{a}^\dagger \hat{a} + 2\omega_R \hat{\varphi}_1^\dagger \hat{\varphi}_1 + {\sum_{\boldsymbol{p}\in\mathcal{P}}}' \left[\omega_{0,\boldsymbol{p}} \hat{\varphi}_{0,\boldsymbol{p}}^\dagger \hat{\varphi}_{0,\boldsymbol{p}} + \omega_{1,\boldsymbol{p}} \hat{\varphi}_{1,\boldsymbol{p}}^\dagger \hat{\varphi}_{1,\boldsymbol{p}}\right] + \sqrt{N}\lambda(\hat{a} + \hat{a}^\dagger)(\hat{\varphi}_1 + \hat{\varphi}_1^\dagger) \\ &+ \lambda(\hat{a} + \hat{a}^\dagger) {\sum_{\boldsymbol{p}\in\mathcal{P}}}' \left[u_{0,\boldsymbol{p}} \left(\hat{\varphi}_{0,\boldsymbol{p}}^\dagger \hat{\varphi}_{1,\boldsymbol{p}} + \hat{\varphi}_{1,\boldsymbol{p}}^\dagger \hat{\varphi}_{0,\boldsymbol{p}}\right) - v_{0,\boldsymbol{p}} \left(\hat{\varphi}_{1,-\boldsymbol{p}} \hat{\varphi}_{0,\boldsymbol{p}} + \hat{\varphi}_{0,\boldsymbol{p}}^\dagger \hat{\varphi}_{1,-\boldsymbol{p}}^\dagger\right)\right] . \end{aligned} \tag{3.42}$$

We identify $\Omega_m = -\delta_C$, $\Omega_a = 2\omega_R$, $\hat{\varphi}_{0/1,\boldsymbol{p}} = \hat{c}_{k\mp}$, $\omega_{0/1,\boldsymbol{p}} = \omega_{k,\mp}$, $u_{0,\boldsymbol{p}} = u_k$, $v_{0,\boldsymbol{p}} = -v_k$, and $\Lambda/2 = -\lambda$. This is straightforward except for the mapping between the momenta $\boldsymbol{p} \in \mathcal{P}$ to the momenta of the atom-optomechanical system k. The momenta k run from $-\pi$ to π in equidistant steps of $2\pi/l$ where l is the one-dimensional number of lattice sites of the setup. Therefore, we have to find a fitting l for our (L_x, L_y) so that we can have a bilinear map between the momenta. We should note that this issue is circumvented if the cavity BEC is treated as quasi-one-dimensional from the outset. By inserting the identities it becomes apparent that the effective Bogoliubov theory Hamiltonian of the cavity BEC, Eq. (3.42), has the same mathematical structure as the Bogoliubov theory Hamiltonian of the hybrid atom-optomechanical system Eq. (2.75)

$$\begin{aligned}\hat{H}_{\mathrm{aom}} = \Omega_m \hat{a}^\dagger \hat{a} + \Omega_a \hat{c}_{0+}^\dagger \hat{c}_{0+} + \sum_{k\neq 0,\nu} \omega_{k\nu} \hat{c}_{k\nu}^\dagger \hat{c}_{k\nu} - \frac{\Lambda\sqrt{N}}{2}(\hat{a} + \hat{a}^\dagger)(\hat{c}_{0+} + \hat{c}_{0+}^\dagger) \\ - \frac{\Lambda}{2}(\hat{a} + \hat{a}^\dagger) \sum_{k\neq 0} \left(u_k[\hat{c}_{k-}^\dagger \hat{c}_{k+} + \hat{c}_{k+}^\dagger \hat{c}_{k-}] + v_k[\hat{c}_{k-} \hat{c}_{-k+} + \hat{c}_{-k+}^\dagger \hat{c}_{k-}^\dagger]\right) . \end{aligned} \tag{3.43}$$

We should point out that below the surface, the difference in the excitation spectra $\omega_{0/1,\boldsymbol{p}}$ and $\omega_{k\mp}$, Eq. (2.76), of the two physical realizations remains. In the cavity BEC, as we treat it, it is determined by the dispersion of a homogeneous Bose gas while in the hybrid atom-optomechanical setup it is determined by the hopping J of a Bose gas confined to a lattice. Put differently, in the latter the atomic field operators are expanded in Wannier functions while in the cavity BEC we have applied the two-mode Bloch functions Eq. (3.26). It has a qualitative impact on the bath spectral densities we obtain in the following section.

3.5 – Quasiparticle dissipative bath

We use the imaginary-time integral technique described in section 3.2 to extract the influence functional $\mathcal{F}$, Eq. (3.5), and the properties of the bath encoded in the spectral density of the bath $G(\omega)$, Eq. (3.15). Tracing out the bath degrees of freedom $\varphi_{i,\boldsymbol{p}\neq\boldsymbol{0}}$ is performed using the bath expectation value

$$\langle\cdot\rangle_B = \frac{1}{\mathcal{Z}_B} \int \mathcal{D}\left[\varphi^*, \varphi\right] (\cdot)\, e^{-S_B[\varphi^*, \varphi]} . \tag{3.44}$$

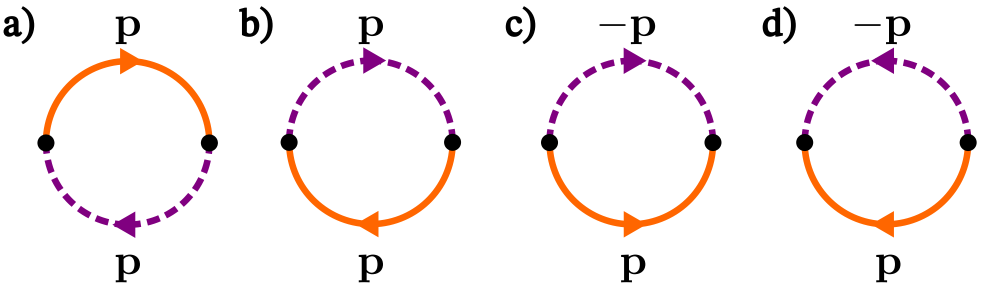

Figure 3.5: Diagrams of the bath expectation values that enter into Eq. (3.48). An external line of the system (a, φ_1) is coupled to each vertex as in figure 3.4. The arrow $\langle \varphi_{i,\boldsymbol{p}}\varphi^*_{i,\boldsymbol{p}}\rangle_B$. The solid lines are for $\varphi_{0,\boldsymbol{p}}$ while the dashed lines are for $\varphi_{1,\boldsymbol{p}}$. The Landau damping consists of loops a) and b). The Beliaev damping consists of loops c) and d).

Due to the coupling of the phonon bath containing only linear terms, the influence functional of the bath decomposes into quadratic correlators by using the Wick theorem [32, 158] and we find

$$\begin{aligned} e^{-S_{\text{infl}}[a^*,a,\varphi_1^*,\varphi_1]} &= \left\langle e^{-S_{SB}[a^*,a,\varphi_1^*,\varphi_1,\varphi^*,\varphi]}\right\rangle_B \\ &= \sum_{j=0}^{\infty} \frac{\langle(-S_{SB})^j\rangle_B}{j!} = \sum_{m=0}^{\infty} \frac{\left[\langle(-S_{SB})^2\rangle_B\right]^m}{m!} = e^{+\langle S_{SB}^2\rangle_B}\,. \end{aligned} \tag{3.45}$$

Therefore, we only have to evaluate the correlator $\langle H_{SB}(\tau)H_{SB}(\tau')\rangle$ of the system-bath coupling Eq. (3.40). Any correlation of a Beliaev and Landau process like $\langle L(\tau)B(\tau')\rangle_B = 0$ is trivial. The bath average of two Landau operators $\langle L^{(*)}_{1,2}(\tau)L^{(*)}_{1,2}(\tau')\rangle_B$ or of two Beliaev operators $\langle B^{(*)}_{1,2}(\tau)B^{(*)}_{1,2}(\tau')\rangle_B$ is a linear combination of single-loop diagrams depicted in the figure 3.5. We need the phonon bath to be in equilibrium to evaluate the influence functional in imaginary time. For this we invoke detailed balance [32] by constructing the correlators symmetric in the imaginary time arguments (τ, τ'), for example,

$$\begin{aligned} \langle B_1(\tau)B_2(\tau')\rangle_B = \sum_{\boldsymbol{p}\in\mathcal{P}}{}' \Big\{ (v_{0,\boldsymbol{p}}u_{1,\boldsymbol{p}} + u_{0,\boldsymbol{p}}v_{1,\boldsymbol{p}}) \Big[& v_{0,\boldsymbol{p}}v_{1,\boldsymbol{p}} n_B(\omega_{0,\boldsymbol{p}}) n_B(\omega_{1,\boldsymbol{p}}) e^{+(\omega_{0,\boldsymbol{p}}+\omega_{1,\boldsymbol{p}})(\tau-\tau')} \\ & + u_{0,\boldsymbol{p}}u_{1,\boldsymbol{p}} (1+n_B(\omega_{0,\boldsymbol{p}}))(1+n_B(\omega_{1,\boldsymbol{p}})) e^{-(\omega_{0,\boldsymbol{p}}+\omega_{1,\boldsymbol{p}})(\tau-\tau')} \Big] \Big\}\,, \end{aligned} \tag{3.46a}$$

$$\begin{aligned} \langle B_2(\tau)B_1(\tau')\rangle_B = \sum_{\boldsymbol{p}\in\mathcal{P}}{}' \Big\{ (v_{0,\boldsymbol{p}}u_{1,\boldsymbol{p}} + u_{0,\boldsymbol{p}}v_{1,\boldsymbol{p}}) \Big[& u_{0,\boldsymbol{p}}u_{1,\boldsymbol{p}} n_B(\omega_{0,\boldsymbol{p}}) n_B(\omega_{1,\boldsymbol{p}}) e^{+(\omega_{0,\boldsymbol{p}}+\omega_{1,\boldsymbol{p}})(\tau-\tau')} \\ & + v_{0,\boldsymbol{p}}v_{1,\boldsymbol{p}} (1+n_B(\omega_{0,\boldsymbol{p}}))(1+n_B(\omega_{1,\boldsymbol{p}})) e^{-(\omega_{0,\boldsymbol{p}}+\omega_{1,\boldsymbol{p}})(\tau-\tau')} \Big] \Big\}\,. \end{aligned} \tag{3.46b}$$

The symmetric correlator satisfying the equilibrium invariance under $\tau \to \beta - \tau$ is

$$\begin{aligned} K^B_{12}(\tau-\tau') &= \frac{1}{2}\left[\langle B_1(\tau)B_2(\tau')\rangle_B + \langle B_2(\tau)B_1(\tau')\rangle_B\right] \\ &= \frac{1}{2}\sum_{\boldsymbol{p}\in\mathcal{P}}{}' \Big\{ (v_{0,\boldsymbol{p}}u_{1,\boldsymbol{p}} + u_{0,\boldsymbol{p}}v_{1,\boldsymbol{p}})(u_{0,\boldsymbol{p}}u_{1,\boldsymbol{p}} + v_{0,\boldsymbol{p}}v_{1,\boldsymbol{p}}) \left[1 + n_B(\omega_{0,\boldsymbol{p}}) + n_B(\omega_{1,\boldsymbol{p}})\right] \times \\ &\qquad \times \Big[n_B(\omega_{0,\boldsymbol{p}}+\omega_{1,\boldsymbol{p}}) e^{+(\omega_{0,\boldsymbol{p}}+\omega_{1,\boldsymbol{p}})(\tau-\tau')} + [1 + n_B(\omega_{0,\boldsymbol{p}}+\omega_{1,\boldsymbol{p}})] e^{-(\omega_{0,\boldsymbol{p}}+\omega_{1,\boldsymbol{p}})(\tau-\tau')} \Big] \Big\}\,. \end{aligned} \tag{3.47}$$

Further details and the remaining correlators can be found in the appendix A.5. We sort the correlators according to which part of the system S_S they couple to. This is either the displacement quadrature of the cavity $q_C = (a + a^*)/\sqrt{-2\delta_C}$ or of the checkerboard quasiparticle $q_A = (\varphi_1 + \varphi_1^*)/\sqrt{2\omega_1}$. Hence the second order correlator of the coupling Hamiltonian $\hat{H}_{SB}$ between the bath and the system, Eq. (3.40), has the form

$$\begin{aligned}\left\langle H_{SB}(\tau)H_{SB}(\tau')\right\rangle_B = &-\delta_C K_C(\tau-\tau')q_C(\tau)q_C(\tau')\\ &+\sqrt{-\delta_C\omega_1}K_{AC}(\tau-\tau')\left[q_A(\tau)q_C(\tau')+q_C(\tau)q_A(\tau')\right]\\ &+\omega_1 K_A(\tau-\tau')q_A(\tau)q_A(\tau')+\frac{1}{\omega_1}K_{\dot{A}}(\tau-\tau')\dot{q}_A(\tau)\dot{q}_A(\tau')\,,\end{aligned} \tag{3.48}$$

where we denote the respective bath correlation functions K_ν with $\nu=\{C,AC,A,\dot{A}\}$. The exception is the last term in Eq. (3.48), where the bath mediates between the momentum quadrature of the checkerboard excitation. In the Lagrangian of a harmonic mode, this becomes $\dot{q}_A(\tau)$. The correlators which provide the integral kernels in each term of the influence functional resulting from the combination of Eqs. (3.45) and (3.48) take the general form

$$K_\nu(\tau-\tau')=\gamma_\nu\sum_{\boldsymbol{p}\in\mathcal{P}}{}'\left[f_\nu^L(\boldsymbol{p})\mathcal{N}_{\boldsymbol{p}}^L D_{\omega_{\boldsymbol{p}}^L}(\tau-\tau')+f_\nu^B(\boldsymbol{p})\mathcal{N}_{\boldsymbol{p}}^B D_{\omega_{\boldsymbol{p}}^B}(\tau-\tau')\right]\,, \tag{3.49}$$

for $\nu\in\{C,AC,A,\dot{A}\}$. They are composed of a bath coupling parameter γ_ν

$$\gamma_C=\lambda^2\,,\qquad \gamma_{AC}=\lambda\eta(u_1-v_1)\,,\qquad \gamma_A=\eta^2(u_1-v_1)^2\,,\qquad \gamma_{\dot{A}}=\frac{\eta^2}{(u_1-v_1)^2}\,, \tag{3.50}$$

and the free thermal Green's function $D_\omega(\tau)$, Eq. (3.14), of the frequencies $\omega_{\boldsymbol{p}}^L=\omega_{1,\boldsymbol{p}}-\omega_{0,\boldsymbol{p}}$ for the Landau and $\omega_{\boldsymbol{p}}^B=\omega_{0,\boldsymbol{p}}+\omega_{1,\boldsymbol{p}}$ for the Beliaev terms. Moreover, they also contain the respective combination of Bose-Einstein distributions $n_B(\omega)=(e^{\beta\omega}-1)^{-1}$ for the Landau $\mathcal{N}_{\boldsymbol{p}}^L$ and Beliaev processes $\mathcal{N}_{\boldsymbol{p}}^B$

$$\mathcal{N}_{\boldsymbol{p}}^L=n_B(\omega_{0,\boldsymbol{p}})-n_B(\omega_{1,\boldsymbol{p}})\,,\qquad\qquad \mathcal{N}_{\boldsymbol{p}}^B=1+n_B(\omega_{0,\boldsymbol{p}})+n_B(\omega_{1,\boldsymbol{p}})\,, \tag{3.51}$$

and finally, most importantly, the coefficients of the bath kernels $f_\nu^{L,B}(\boldsymbol{p})$. The specific characteristics of the bath kernels $K_\nu(\tau)$ for the influence functional, Eq. (3.45), are encoded in the coefficients $f_\nu^{L,B}(\boldsymbol{p})$, which are given by combinations of the Bogoliubov transformation coefficients of the phonon bands, Eq. (3.36),

$$f_C^L(\boldsymbol{p})=2\left(u_{0,\boldsymbol{p}}u_{1,\boldsymbol{p}}+v_{0,\boldsymbol{p}}v_{1,\boldsymbol{p}}\right)^2\,,\qquad f_C^B(\boldsymbol{p})=2\left(v_{0,\boldsymbol{p}}u_{1,\boldsymbol{p}}+u_{0,\boldsymbol{p}}v_{1,\boldsymbol{p}}\right)^2\,, \tag{3.52a}$$

$$\begin{aligned}f_{AC}^L(\boldsymbol{p})&=2\left(u_{0,\boldsymbol{p}}u_{1,\boldsymbol{p}}+v_{0,\boldsymbol{p}}v_{1,\boldsymbol{p}}\right)^2-\left(u_{0,\boldsymbol{p}}u_{1,\boldsymbol{p}}+v_{0,\boldsymbol{p}}v_{1,\boldsymbol{p}}\right)\left(v_{0,\boldsymbol{p}}u_{1,\boldsymbol{p}}+u_{0,\boldsymbol{p}}v_{1,\boldsymbol{p}}\right)\,,\\ f_{AC}^B(\boldsymbol{p})&=2\left(v_{0,\boldsymbol{p}}u_{1,\boldsymbol{p}}+u_{0,\boldsymbol{p}}v_{1,\boldsymbol{p}}\right)^2-\left(u_{0,\boldsymbol{p}}u_{1,\boldsymbol{p}}+v_{0,\boldsymbol{p}}v_{1,\boldsymbol{p}}\right)\left(v_{0,\boldsymbol{p}}u_{1,\boldsymbol{p}}+u_{0,\boldsymbol{p}}v_{1,\boldsymbol{p}}\right)\,,\end{aligned} \tag{3.52b}$$

$$\begin{aligned}f_A^L(\boldsymbol{p})&=\frac{5}{2}\left(u_{0,\boldsymbol{p}}u_{1,\boldsymbol{p}}+v_{0,\boldsymbol{p}}v_{1,\boldsymbol{p}}\right)^2-2\left(u_{0,\boldsymbol{p}}u_{1,\boldsymbol{p}}+v_{0,\boldsymbol{p}}v_{1,\boldsymbol{p}}\right)\left(v_{0,\boldsymbol{p}}u_{1,\boldsymbol{p}}+u_{0,\boldsymbol{p}}v_{1,\boldsymbol{p}}\right)-\frac{1}{2}\,,\\ f_A^B(\boldsymbol{p})&=\frac{5}{2}\left(v_{0,\boldsymbol{p}}u_{1,\boldsymbol{p}}+u_{0,\boldsymbol{p}}v_{1,\boldsymbol{p}}\right)^2-2\left(u_{0,\boldsymbol{p}}u_{1,\boldsymbol{p}}+v_{0,\boldsymbol{p}}v_{1,\boldsymbol{p}}\right)\left(v_{0,\boldsymbol{p}}u_{1,\boldsymbol{p}}+u_{0,\boldsymbol{p}}v_{1,\boldsymbol{p}}\right)+\frac{1}{2}\,,\end{aligned} \tag{3.52c}$$

$$f_{\dot{A}}^L(\boldsymbol{p})=\frac{1}{2}\left(u_{0,\boldsymbol{p}}v_{1,\boldsymbol{p}}-v_{0,\boldsymbol{p}}u_{1,\boldsymbol{p}}\right)^2\,,\qquad f_{\dot{A}}^B(\boldsymbol{p})=\frac{1}{2}\left(u_{0,\boldsymbol{p}}u_{1,\boldsymbol{p}}-v_{0,\boldsymbol{p}}v_{1,\boldsymbol{p}}\right)^2\,. \tag{3.52d}$$

We proceed by capturing the properties of each bath correlation integral kernel $K_\nu(\tau)$, Eq. (3.49), in its spectral density $G_\nu(\omega)$, as prescribed by Eq. (3.15)

$$K_\nu(\tau)=\int_0^\infty d\omega\,G_\nu(\omega)D_\omega(\tau)\,. \tag{3.53}$$

Due to the finite interval in which the quasi-momenta $|\boldsymbol{p}|\in(0,k/\sqrt{2})$ of the Brillouin zone lie, see Eq. (3.26b), the frequencies of the Landau $\omega_{\boldsymbol{p}}^L$ and the Beliaev damping $\omega_{\boldsymbol{p}}^B$ are also confined to finite intervals. For the former, one has $\omega^L_{\boldsymbol{p}} = \omega_{1,\boldsymbol{p}} - \omega_{0,\boldsymbol{p}} \in I_L = (2\omega_R - \overline{\omega}_P, \omega_1)$, while for the latter it is $\omega^B_{\boldsymbol{p}} = \omega_{0,\boldsymbol{p}} + \omega_{1,\boldsymbol{p}} \in I_B = (\omega_1, 3\omega_R + 2nU - \overline{\omega}_P)$. The boundary between the intervals is the frequency ω_1 of the checkerboard quasiparticles of $\boldsymbol{p} = 0$ in Eq. (3.37). For weak s-wave scattering and small pump strength $nU, \overline{\omega}_P \ll \omega_R$ it is $\omega_1 \approx 2\omega_R - \overline{\omega}_P + nU$. The width of the Landau damping frequency range I_L is thus determined by the small energy nU from s-wave scattering. This results in a narrow frequency range for the Landau processes, as shown in figure 3.6. On the other hand, the extent of the frequency range of the Beliaev damping I_B is dominated by the recoil energy ω_R for $nU, \overline{\omega}_P \ll \omega_R$ making it comparatively wide. The recoil energy ω_R and the s-wave scattering energy nU are parameters that are difficult to change in the experiment. However, the pump energy $\overline{\omega}_P$ is easily manipulated. As the pump strength is increased, the frequency bands of the quantum fluctuations are shifted to lower frequencies. They maintain their respective widths to a good approximation as long as $\overline{\omega}_P \ll \omega_R$. Another noteworthy result is that the frequency ranges are gapped from zero frequency $\omega = 0$ for reasonable choices of parameters. If one wants to explore the case $\overline{\omega}_P \lessapprox 2\omega_R$, it comes with the caveat that the optical potential created by the self-interference of the pump $h^2(\boldsymbol{r})$ in Eq. (3.25) would be significant. Physically, the atomic cloud would then be cut into pancakes stacked along the y axis, with each pancake occupying one period of the $\cos^2(ky)$ pump potential. In its wake, modes of the atomic field operators not included in the calculation would be significantly occupied, especially the $\cos(2ky)$ Fourier component.

The spectral densities obtained by Eq. (3.53) decompose at the borderline into a Landau and a Beliaev part as

$$G_\nu(\omega) = G^L_\nu(\omega)\theta_H(\omega_1 - \omega) + G^B_\nu(\omega)\theta_H(\omega - \omega_1)\,. \tag{3.54}$$

Matching Eq. (3.53) to Eq. (3.49) unveils that the constituents must follow the generic formula

$$G^{L,B}_\nu(\omega) = \gamma_\nu \sum_{\boldsymbol{p}\in\mathcal{P}}{}' \left[f^{L,B}_\nu(\boldsymbol{p}) \mathcal{N}^{L,B}_{\boldsymbol{p}} \delta(g_{L,B}(\epsilon(\boldsymbol{p}))) \right] , \tag{3.55a}$$

$$g_{L,B}(\epsilon(\boldsymbol{p})) = \omega - \omega^{L,B}_{\boldsymbol{p}}\,, \tag{3.55b}$$

where $\epsilon(\boldsymbol{p}) = \boldsymbol{p}^2/2m$. To further extract the properties of the bath coupling, we invoke the continuum limit $\sum'_{\boldsymbol{p}\in\mathcal{P}} \to [V_{2D}/(2\pi)^2] \int_{\mathcal{P}} d^2\boldsymbol{p}$ on the phononic bath and thus the spectral densities Eq. (3.55a) as reviewed in section 3.2.2 [32]. The corresponding function $g_{L,B}$, Eq. (3.55b), in the argument of the delta distribution is continuously differentiable $g'_{L,B}(\epsilon) = -d\omega^{L,B}(\epsilon)/d\epsilon$. Its derivative is non-zero on the intervals I_L and I_B. Therefore, the relation $\delta(g(\epsilon)) = \sum_i \delta(\epsilon - W_i)/|g'(W_i)|$ holds for the roots of $g(\epsilon = W_i) = 0$. The roots of $g_{L,B}(\epsilon)$ in the respective frequency ranges of $\omega^L_{\boldsymbol{p}}$ and $\omega^B_{\boldsymbol{p}}$ are

$$W(\omega) = -\frac{2\omega_R - \overline{\omega}_P + 2nU}{2} + \frac{\omega}{2}\sqrt{1 + \frac{(2nU)^2}{\omega^2 - (2\omega_R - \overline{\omega}_P)^2}}\,. \tag{3.56}$$

They are plotted in figure 3.6. We can now evaluate the quasi-momentum integral in polar coordinates with $\rho = |\boldsymbol{p}|$ as

$$\begin{aligned} G^{L,B}_\nu(\omega) &= \gamma_\nu \frac{V_{2D}}{2\pi} \int_0^{k/\sqrt{2}} d\rho \left\{ \rho f^{L,B}_\nu(\rho) \mathcal{N}^{L,B}_\rho \frac{\delta(\epsilon(\rho) - W(\omega))}{|g'_{L,B}(W(\omega))|} \right\} = \frac{V_{2D}}{2\pi} m\gamma_\nu f^{L,B}_\nu(W(\omega)) \frac{\mathcal{N}^{L,B}(W(\omega))}{|g'_{L,B}(W(\omega))|} \\ &= \frac{V_{2D}}{2\pi} m\gamma_\nu f^{L,B}_\nu(\omega) \frac{\mathcal{N}^{L,B}(\omega)}{|g'_{L,B}(\omega)|}\,, \end{aligned} \tag{3.57}$$

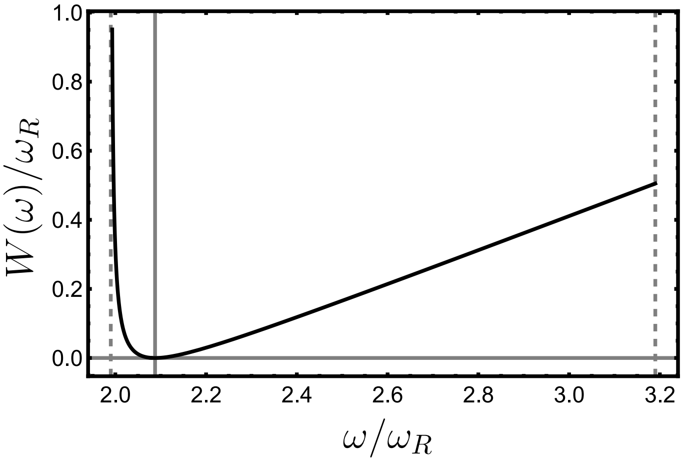

Figure 3.6: Roots $W(\omega)$, Eq. (3.56), of the argument of the delta distribution in the spectral densities Eq. (3.55). The solid vertical line marks the ω_1 boundary between the Landau I_L and Beliaev I_B frequency intervals. The dashed lines indicate the lower bound of I_L and the upper bound of I_B. The parameters are $\overline{\omega}_P = 10^{-2}\,\omega_R$ and $nU = 10^{-1}\,\omega_R$.

and find the exact analytical expression of the bath spectral densities shown in figure 3.7. This is the key result of this chapter since the spectral densities carry the complete information about the quantum fluctuation processes.

3.6 – Discussion of the spectral characteristics of the bath

The spectral densities Eq. (3.57) derived in the previous section and shown for exemplary parameters in figure 3.7 differ drastically from any of the usual textbook examples, some of which were discussed in section 3.2.3. We start with the feature of finite frequency ranges analyzed just before. The Landau processes G_C^L, G_{AC}^L, and $G_{\dot{A}}^L$ are all strongly peaked near the lower bound of their frequency range. This peak decays rapidly toward the boundary to the Beliaev region. The Landau damping of $G_{\dot{A}}$ is small compared to other damping channels. It is paramount that any Landau process is inherently thermal and vanishes for zero temperature $\beta = T^{-1} \to \infty$, as is easily deduced from Eq. (3.51), which carry the complete temperature dependence of any Landau and Beliaev channel. The temperature in figure 3.7 has been deliberately chosen to be $\beta\omega_R = 17.1$ or $T = 10$ nK, a value at which the Beliaev and Landau channels couple on a similar scale. For larger temperatures, the spectral weight of the Landau damping dominates, effectively placing the fluctuations in the Landau channels. Although in the pathological case of a BEC, at very large temperatures $\beta\omega_R \ll 1$, the Landau damping is again suppressed compared to Beliaev due to the signs in Eq. (3.51). If the temperature is zero, only the Beliaev damping remains. As soon as the temperature of the atomic cloud is such that $n_B(\omega_0(\omega)) + n_B(\omega_1(\omega)) \ll 1$ for $\omega \in I_B$, i.e. in the Beliaev frequency range, we can state that the fluctuations are of pure quantum nature.

The Beliaev channel G_C^B, which damps the cavity by coupling to $q_C(\tau)q_C(\tau')$, is strongest near the boundary to the Landau range $\omega = \omega_1$ and decreases rapidly towards higher frequencies. This is similar to the shape of the Landau process with its minimum value at the upper bound of the Beliaev domain. Over the entire frequency range, $G_C^B(\omega \in I_B)$ is positive and the fluctuations thus act in a damping manner on the cavity. Studying the coefficients characterizing this spectral weight Eq. (3.52) we find that G_C^B contains a specific phonon channel by its Bogoliubov coefficient weight

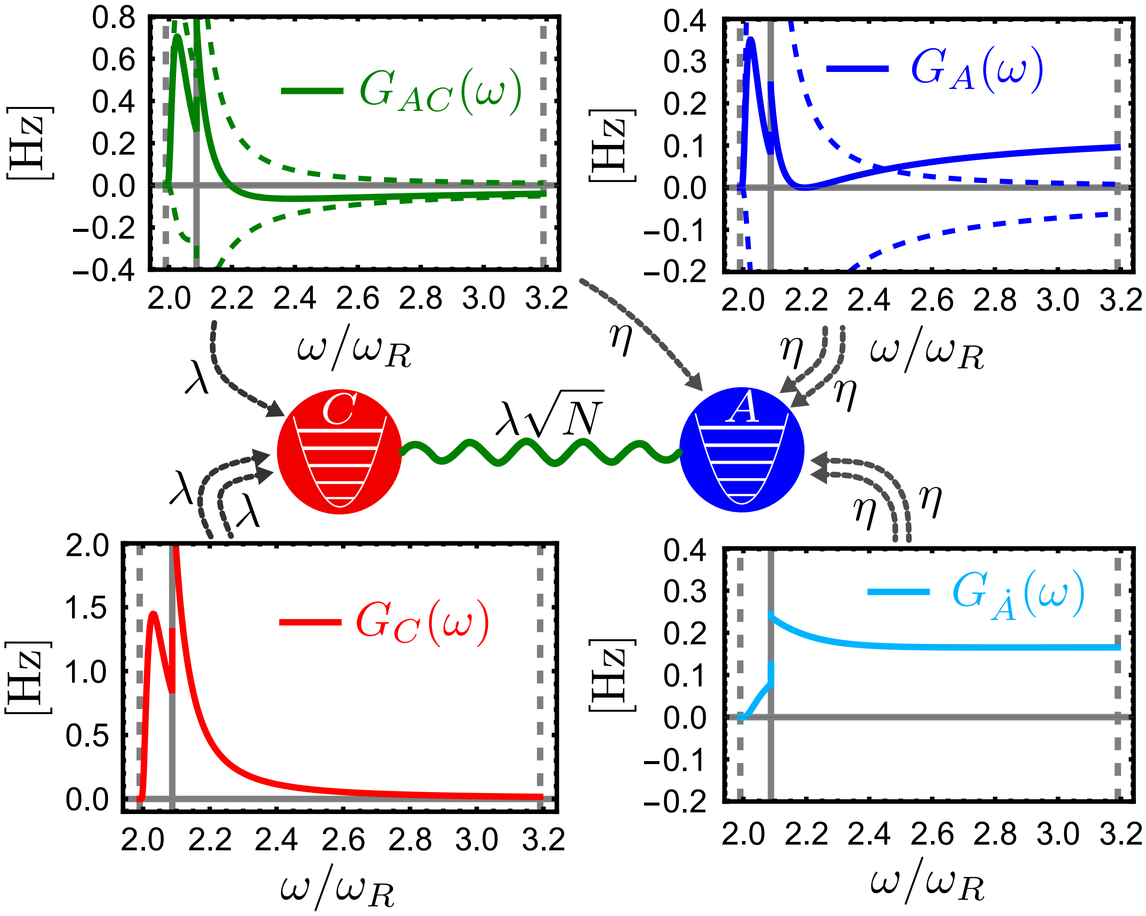

Figure 3.7: Spectral densities G_ν of the four different coupling channels to the bath $(C, AC, A, \dot{A})$ as given by Eq. (3.48). The dashed lines visualize the competing phonon channels. Their sum results in the spectral density shown as the solid line with a constant offset in $G_A(\omega)$, see Eq. (3.52c). The data have been scaled by $2\pi\hbar\omega_R/V_{2D}m$ to compensate for the global prefactor in Eq. (3.57). The vertical solid gray line in each plot marks the boundary $\omega = \omega_1$ between the Landau damping frequency range on the left $\omega < \omega_1$ and the Beliaev range $\omega > \omega_1$ on the right. Gray dashed lines indicate the lower bound $\omega = 2\omega_R - \overline{\omega}_P$ of the Landau range and the upper bound $\omega = 3\omega_R + 2nU - \bar{\omega}_P$ of the Beliaev range. The parameters are $\overline{\omega}_P = 10^{-2}\,\omega_R$, $U_0 = -10^{-3}\,\omega_R$, $nU = 10^{-1}\omega_R$, $N = 10^4$, $\beta\omega_R = 17.1$, $L_x = 60\,\mu\text{m}$, $L_y = 11\,\mu\text{m}$, $m = 87$ u, $\omega_R = 2\pi \times 3560$ Hz.

$\propto (u_{0,\boldsymbol{p}}u_{1,\boldsymbol{p}} + v_{0,\boldsymbol{p}}v_{1,\boldsymbol{p}})^2$. This channel also enters the spectral density, which influences the atomic checkerboard mode $G_A(\omega)$ and the coupling between it and the cavity fluctuations $G_{AC}(\omega)$.

The analog is true for the Landau part, see Eq. (3.52). Note that although a connection between the cavity damping channel G_C^B and the s-wave scattering nU may not be obvious at first glance, the Beliaev damping of the cavity only exists if there is a nontrivial rotation to the quasiparticle excitations $\hat{\varphi}$. This is evident from the comparison of the cavity coupling term in Eq. (3.33) with Eq. (3.40). The bare atomic fluctuations $\hat{\phi}$ in Eq. (3.33) couple to the cavity only as a Landau channel. It follows that at zero temperature $\beta \to \infty$ and in the absence of an interaction between the atoms $U \to 0$ none of the derived fluctuation channels exist, not even the one influencing the cavity.

As teased, the bath channel G_{AC} coupling the cavity and the checkerboard mode combines the spectral characteristics of the cavity damping channel f_C with a competing phonon fluctuation channel with spectral weight $\propto -(u_{0,\boldsymbol{p}}u_{1,\boldsymbol{p}} + v_{0,\boldsymbol{p}}v_{1,\boldsymbol{p}})(v_{0,\boldsymbol{p}}u_{1,\boldsymbol{p}} + u_{0,\boldsymbol{p}}v_{1,\boldsymbol{p}})$, see Eq. (3.52b). We analyze the continuum limit of the spectral characteristics of each bath by plotting $f_\nu(\omega)/|g'(\omega)|$ as they occur as part of Eq. (3.57) in figure 3.8. The competition within the spectral density leads to even more

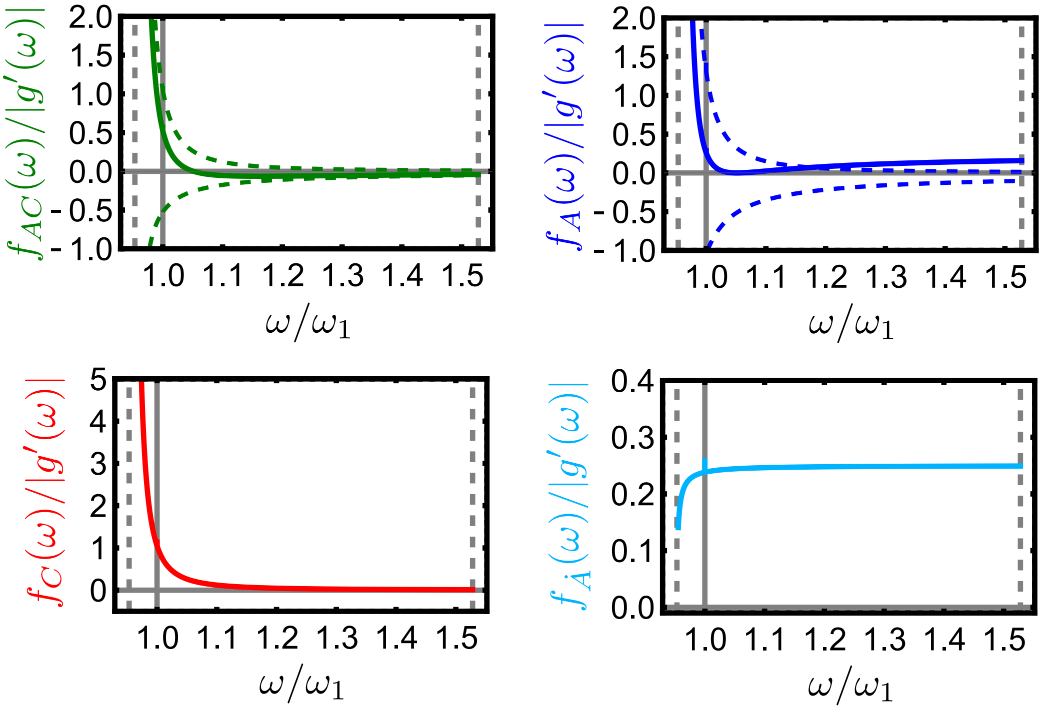

Figure 3.8: The functions characterizing the spectral densities Eq. (3.55) in the continuum limit, see Eq. (3.57), plotted as solid lines. If more than one phonon channel contributes, the individual channels are plotted as dashed lines. The sum of the channels (dashed) yields the overall function (solid), see Eq. (3.52). Note that there is an offset in $f_A(\omega)$, see Eq. (3.52c). Again, the solid vertical line visualizes the boundary ω_1, while the dashed vertical lines mark the lower boundary of I_L and the upper boundary of I_B.

exotic spectral weighting properties of its Beliaev fluctuations. In the lower frequency region near the ω_1 boundary, the phonon channel, which is the same as for the cavity damping, dominates. Towards higher frequencies, however, the Beliaev damping turns into anti-damping, as the G^B_{AC} spectral density is dominated by the second phonon channel, i.e. the second term in Eq. (3.52b). Figure 3.8 is helpful to visualize this competition. The frequency at which the crossover between damping and anti-damping occurs can be tuned by parameters such as ϖ_P and nU. Both contributing phonon channels have the maximum of their absolute magnitude at the low-frequency end of the Beliaev range and decrease in their absolute spectral weight towards higher frequencies, see figure 3.8. The damping channel G_A coupled to the displacement quadrature of the checkerboard excitation is composed of the same phonon channels as G_{AC} as evident from Eq. (3.52c). However, the weight between the channels is different and there is a constant offset that is positive for the Beliaev part and negative for the Landau part. Since the same phonon channels occur, the Beliaev damping G^B_A is similar to G^B_{AC} over the frequency range. Although, due to the relatively larger weight of the second channel in Eq. (3.52c), it becomes the dominant channel at a lower frequency in G^B_A compared to G^B_{AC}, see figures 3.7 and 3.8. The final Beliaev damping spectral density $G^B_{\dot{A}}$ is magnificent for its nearly constant value throughout the frequency range. Note that the difference in spectral weight seen in figure 3.7 for different spectral densities like G_C and G_{AC} goes beyond the difference in phonon channel weight in Eq. (3.52). Also the difference in the global bath coupling parameters γ_ν, Eq. (3.50), is significant. The cavity-atom coupling λ is stronger than η. As a consequence, the bath is most strongly coupled to the cavity quadrature q_C.

For deeper insight, we analyze the functions Eq. (3.52) as they determine the qualities of the different damping channels. We find

$$
\begin{aligned}
f_C^L(\omega) &= \cosh^2\left(\frac{A_+(\omega)}{2}\right), \qquad f_C^B(\omega) = \sinh^2\left(\frac{A_+(\omega)}{2}\right), && \text{(3.58a)}\\
f_{AC}^L(\omega) &= \cosh\left(\frac{A_+(\omega)}{2}\right)\left[2\cosh\left(\frac{A_+(\omega)}{2}\right) - \sinh\left(\frac{A_+(\omega)}{2}\right)\right], &&\\
f_{AC}^B(\omega) &= \sinh\left(\frac{A_+(\omega)}{2}\right)\left[2\sinh\left(\frac{A_+(\omega)}{2}\right) - \cosh\left(\frac{A_+(\omega)}{2}\right)\right], && \text{(3.58b)}\\
f_A^L(\omega) &= \frac{1}{2}\left[\sinh\left(\frac{A_+(\omega)}{2}\right) - 2\cosh\left(\frac{A_+(\omega)}{2}\right)\right]^2, &&\\
f_A^B(\omega) &= \frac{1}{2}\left[\cosh\left(\frac{A_+(\omega)}{2}\right) - 2\sinh\left(\frac{A_+(\omega)}{2}\right)\right]^2, && \text{(3.58c)}
\end{aligned}
$$

where

$$
\begin{aligned}
A_+(\omega) =& \operatorname{artanh}\left(\frac{nU}{W(\omega)+nU}\right) + \operatorname{artanh}\left(\frac{nU}{W(\omega)+2\omega_R-\overline{\omega}_P+nU}\right)\\
=&\frac{1}{2}\ln\left(1+\frac{nU}{W(\omega)+nU}\right) + \frac{1}{2}\ln\left(1-\frac{nU}{W(\omega)+nU}\right) + \frac{1}{2}\ln\left(1+\frac{nU}{W(\omega)+2\omega_R-\overline{\omega}_P+nU}\right)\\
&+\frac{1}{2}\ln\left(1-\frac{nU}{W(\omega)+2\omega_R-\overline{\omega}_P+nU}\right), \qquad \text{(3.59)}
\end{aligned}
$$

using that the arguments of these $\operatorname{artanh}(u)$ fulfill $0 \leq u < 1$. For the sake of completeness, we have

$$
f_{\tilde{A}}^L(\omega) = \frac{1}{2}\sinh^2\left(\frac{A_-(\omega)}{2}\right), \qquad f_{\tilde{A}}^B(\omega) = \frac{1}{2}\cosh^2\left(\frac{A_-(\omega)}{2}\right), \tag{3.60}
$$

with

$$
\begin{aligned}
A_-(\omega) =& \operatorname{artanh}\left(\frac{nU}{W(\omega)+nU}\right) - \operatorname{artanh}\left(\frac{nU}{W(\omega)+2\omega_R-\overline{\omega}_P+nU}\right)\\
=&\frac{1}{2}\ln\left(1+\frac{nU}{W(\omega)+nU}\right) + \frac{1}{2}\ln\left(1-\frac{nU}{W(\omega)+nU}\right) - \frac{1}{2}\ln\left(1+\frac{nU}{W(\omega)+2\omega_R-\overline{\omega}_P+nU}\right)\\
&-\frac{1}{2}\ln\left(1-\frac{nU}{W(\omega)+2\omega_R-\overline{\omega}_P+nU}\right). \qquad \text{(3.61)}
\end{aligned}
$$

We note that $\cosh^2(u) = (e^{2u} + e^{-2u} + 2)/4$, $\sinh^2(u) = (e^{2u} + e^{-2u} - 2)/4$, and $\cosh(u)\sinh(u) = (e^{2u} - e^{-2u})/2$. So we have derived via Eqs. (3.58), (3.59), and (3.60) that the functions $f_\nu^{L,B}(\omega)$ are sums of the root expressions

$$
\left(1 \pm \frac{nU}{W(\omega)+nU}\right)^{\pm\frac{1}{2}}, \quad \text{and} \quad \left(1 \pm \frac{nU}{W(\omega)+2\omega_R-\overline{\omega}_P+nU}\right)^{\pm\frac{1}{2}}. \tag{3.62}
$$

Of these eight different building blocks, seven are well behaved for ω in the frequency range of the Landau and Beliaev processes $\omega \in (2\omega_R - \overline{\omega}_P, 3\omega_R - \overline{\omega}_P + 3nU)$. The exception is where the radicant in the denominator can attain zero value $(1 - nU/[W(\omega) + nU])^{-1/2}$. If $\omega \to \omega_1$, then $W(\omega) \to 0$ and this term diverges. In other words, it diverges at the boundary $\omega = \omega_1$ between the Landau and Beliaev domains. However, this is not the origin of the divergence of the spectral functions at $\omega = \omega_1$ that we see in the figure 3.7. This is due to the pole of order 1 of the Bose-Einstein distribution $n_B(\omega_0(W(\omega)))$ at $W(\omega = \omega_1) = 0$ in the thermal distributions $\mathcal{N}^{L,B}(W(\omega))$, Eq. (3.51).

The $W^{-1/2}$ divergence of the functions $f_\nu^{L,B}(W(\omega))$ is lifted by $g'_{L,B}(W)$, which also diverges like $W^{-1/2}$ for $W \to 0$. Thus, the functions of the Bogoliubov coefficients that give the spectral densities

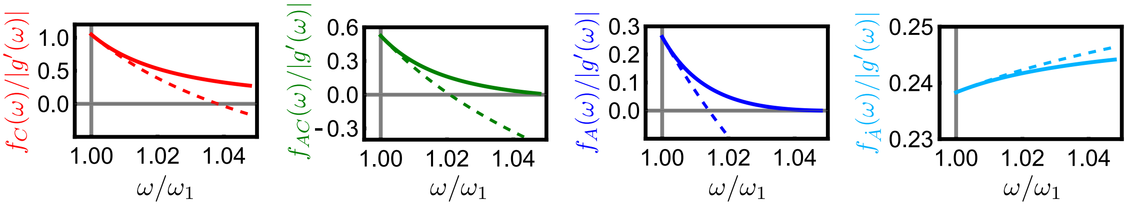

Figure 3.9: Comparison of the approximated spectral densities near the critical point at zero temperature Eq. (3.64) (dashed lines) and the exact ones (solid lines). The latter are identical to those shown in figure 3.7.

their characteristics $f_\nu^{L,B}/|g'_{L,B}|$ are finite at the boundary, as apparent in figure 3.8.

If we focus on the purely quantum fluctuations at zero temperature $\beta \to \infty$, so that the Bose distributions vanish, it is $G_\nu^B(\omega) \propto f_\nu^B(\omega)/|g'_B(\omega)|$ and the spectral densities maintain a finite value at the boundary $\omega = \omega_1$. To get a deeper understanding of the shape of the spectral densities, we analyze them at the boundary and find the expansion

$$\frac{d}{dW}\frac{f_\nu^B(W)}{|g'_B(W)|} \sim -\frac{a_\nu}{\sqrt{W}} + b_\nu\,, \tag{3.63}$$

with the expansion coefficients a_ν and b_ν functions of ω_R, $\overline{\omega}_P$, and nU, see Appendix A.6. The coefficients a_ν and b_ν for $\nu = C, AC, A$ are all positive and only those for $\dot{A}$ are negative. Based on Eq. (3.63), we can approximate the spectral densities near $W = 0$ by the antiderivatives

$$\frac{f_\nu^B(W)}{|g'_B(W)|} \sim -2a_\nu\sqrt{W} + b_\nu W + C_\nu\,, \tag{3.64}$$

where the constants C_ν are determined by $f_\nu^B(0)/|g'_B(0)|$, see the appendix A.6. An analogous analysis can be done for the Landau damping side, but it is physically irrelevant since at zero temperature, where the pole of $\mathcal{N}^L(\omega)$ is absent, the total Landau damping is also zero. In figure 3.9 we show the approximation for the Beliaev spectral densities obtained in Eq. (3.64). Approximating $W(\omega)$ as roughly $\propto (\omega - \omega_1)$, we find that the zero temperature $\beta \to \infty$ spectral densities are characterized by $G_\nu^B(\omega) \propto (\omega - \omega_1)^{1/2}$. They thus follow a spectral exponent $s = 1/2$, which is a sub-Ohmic characteristic. Hence, we have derived from first principles the sub-Ohmic bath introduced phenomenologically in existing studies [152, 153]. Sub-Ohmic quantum fluctuations induce strong, exotic, non-Markovian real-time dynamics, as we have reviewed in section 3.2.3.

It is striking in figure 3.9 that they approximate the spectral densities only in the very vicinity of the singular point $\omega = \omega_1$. The discrepancy indicates the complicated nature of the damping that occurs in the cavity BEC system. It is particularly pronounced in f_{AC} and f_A, where we find the multichannel competition.

3.7 – Effective partition function

In the preceding sections we dealt with and discussed the characteristics of the dissipative bath based on the spectral densities we derived. Via Eqs. (3.5), (3.15), and (3.16) these spectral densities determine the influence functional so that we can investigate the two-mode polariton system $\hat{H}_S$, Eq. (3.38), coupled to the bath. Within the Bogoliubov and system-bath techniques of the previous sections, we have obtained an effective Euclidean action that is quadratic in the system path $(q_A \; q_C)^T$

$$S_{\text{eff}}\left[q_{A,C}\right] = \frac{1}{2}\int_0^\beta d\tau \int_0^\beta d\tau' \left\{ \dot{q}_A(\tau) \left[\delta(\tau-\tau') - \frac{K_{\dot{A}}(\tau-\tau')}{\omega_1}\right] \dot{q}_A(\tau') + \dot{q}_C(\tau)\delta(\tau-\tau')\dot{q}_C(\tau') \right. \\ \left. + \begin{pmatrix} q_A(\tau) & q_C(\tau) \end{pmatrix} \underline{S}(\tau-\tau') \begin{pmatrix} q_A(\tau') \\ q_C(\tau') \end{pmatrix} \right\}, \tag{3.65}$$

with

$$\underline{S}(\tau) = \begin{pmatrix} \omega_1^2\delta(\tau) - \omega_1 K_A(\tau) & \sqrt{-\delta_C\omega_1}\left[\lambda\sqrt{N}(u_1-v_1)\delta(\tau) - K_{AC}(\tau)\right] \\ \sqrt{-\delta_C\omega_1}\left[\lambda\sqrt{N}(u_1-v_1)\delta(\tau) - K_{AC}(\tau)\right] & \delta_C^2\delta(\tau) + \delta_C K_C(\tau) - \delta_C K_{C\text{env}}(\tau) \end{pmatrix}. \tag{3.66}$$

We have included the damping of the cavity by photon loss at the experimentally determined rate κ by an additional Ohmic bath $G_{C\text{env}} \sim \omega$ for the cavity fluctuations. The high-frequency cutoff $\omega_D^2/(\omega^2+\omega_D^2)$ for the cavity photon loss is of the Drude type with an appropriate cutoff frequency $\omega_D \gg |\delta_C|$. Furthermore, it has to satisfy $\int_0^\infty d\omega G_{C\text{env}}(\omega) = \kappa^2/(-\delta_C)$.

We expand S_{eff} in periodic eigenfunctions of the bosonic Matsubara frequencies, $\nu_n = 2\pi n/\beta$ with $n \in \mathbb{Z}$ as introduced in section 3.2.2,

$$q_{A,Cn}(\tau) = \frac{1}{\beta}\sum_{i\nu_n} q_{A,Cn} e^{i\nu_n\tau}, \qquad K_\nu(\tau) = \frac{1}{\beta}\sum_{i\nu_n} K_{\nu n} e^{i\nu_n\tau}. \tag{3.67}$$

The expansion coefficients obey the symmetry $q_{-n} = q_n^*$, so the expanded action has the form

$$S_{\text{eff}}(q_{An}, q_{Cn}) = \frac{1}{2\beta}\sum_{i\nu_n}\left\{ \begin{pmatrix} q_{An}^* & q_{Cn}^* \end{pmatrix} \underline{S}_n \begin{pmatrix} q_{An} \\ q_{Cn} \end{pmatrix} \right\}, \tag{3.68}$$

with the (2×2)-matrix

$$\underline{S}_n = \begin{pmatrix} \nu_n^2[1 - K_{\dot{A}n}/\omega_1] + \omega_1^2 - \omega_1 K_{An} & \sqrt{-\delta_C\omega_1}\left[\lambda\sqrt{N}(u_1-v_1) - K_{ACn}\right] \\ \sqrt{-\delta_C\omega_1}\left[\lambda\sqrt{N}(u_1-v_1) - K_{ACn}\right] & \nu_n^2 + \delta_C^2 + \delta_C K_{Cn} - \delta_C K_{C\text{env}n} \end{pmatrix}. \tag{3.69}$$

The determinant of $\underline{S}_n$ is

$$D_n = \left(\nu_n^2[1 - K_{\dot{A}n}/\omega_1] + \omega_1^2 - \omega_1 K_{An}\right)\left(\nu_n^2 + \delta_C^2 + \delta_C K_{Cn} - \delta_C K_{C\text{env}n}\right) \\ + \delta_C\omega_1\left(\lambda\sqrt{N}(u_1-v_1) - K_{ACn}\right)^2. \tag{3.70}$$

It is invariant under the change of sign $n \to -n$. The partition function is given with some normalization $\mathcal{N}$ by the simple expression [32]

$$Z = \frac{\mathcal{N}}{\sqrt{D_0}}\prod_{n>1} D_n^{-1}, \tag{3.71}$$

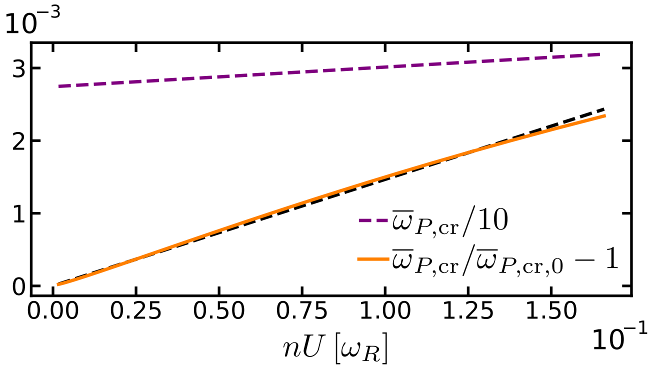

Figure 3.10: Shift of the critical point (purple, dashed) and its deviation due to the Stokes shift (solid, orange) of the quantum phase transition determined by the atom-atom interaction nU. The black dashed line shows a linear fit to the growth of the Stokes shift. Parameters for the recoil resolved experimental setup of Ref. [99, 159] are used: $\delta_C = -2\,\omega_R$, $U_0 = -10^{-3}\,\omega_R$, $nU = 1.6\times 10^{-2}\,\omega_R$, $N = 5\times 10^4$, $\kappa = 1.25\,\omega_R$, $\omega_D = 10^9\,\omega_R$, $\omega_R = 2\pi\times 3560$ Hz.

3.7.1 Role of the Stokes shifts

If the coupling $\lambda = \sqrt{-U_0\overline{\omega}_P}$ between cavity and atomic fluctuations is gradually increased, the first determinant to go to zero is $D_{n=0}$. From $D_0 = 0$, we derive the modified Dicke critical point in the presence of the fluctuations

$$\lambda_{\mathrm{cr}}^2 = \frac{\delta_C^2+\kappa^2}{-\delta_C}\,\frac{\omega_1 - R_A}{\big(R_C/\lambda^2\big)\big(\omega_1 - R_A\big) + \big(\sqrt{N}[u_1 - v_1] - [R_{AC}/\lambda]\big)^2}\,, \tag{3.72}$$

where the reorganization energies $R_\nu = \int_0^\infty d\omega G_\nu(\omega)$ encode the influence of the bath based on the bath spectral densities Eq. (3.57). We have done our best to remove any λ dependence on the right-hand side of the equation. However, it remains an implicit equation due to the occurrence of $\overline{\omega}_P$ in ω_1 and the phonon dispersion affecting the bath reorganization energies, as well as U_0 contributing in δ_C. In figure 3.10 we show how λ_{cr} changes under the modification of the s-wave scattering which is the basis for the existence of the bath. If we artificially remove the bath by setting $R_\nu = 0$, we find the bare critical point of the system $\lambda_{\mathrm{cr},0}^2 = (\delta_C^2+\kappa^2)\omega_1/[-\delta_C N(u_1 - v_1)^2]$, which agrees with the mean-field stability analysis and the prediction of the Bogoliubov theory discussed in section 2.3.6. [36]. The dashed purple line in figure 3.10 shows a linear growth of the critical value for $\lambda_{\mathrm{cr}}^2 \sim \overline{\omega}_{P,\mathrm{cr}}$ when the s-wave scattering strength U is increased. This quality is no different from the bare critical value without the fluctuation bath $\lambda_{\mathrm{cr},0}^2 = U_0\overline{\omega}_{P,\mathrm{cr},0} \sim nU$ as can be seen from Eqs. (2.58) or (2.63). However, by comparing the critical value of the whole system $\overline{\omega}_{P,\mathrm{cr}}$ with the naked system $\overline{\omega}_{P,\mathrm{cr},0}$ in figure 3.10 we find a linear increase of the relative critical pumping strength $\overline{\omega}_{P,\mathrm{cr}}/\overline{\omega}_{P,\mathrm{cr},0} - 1$. The presence of the quasiparticle dissipative bath induces a Stokes shift to the two-mode system, which also leads to a shift of the critical point. With increasing interaction energy nU the Stokes shift becomes stronger. In the region where the Stokes shift starts to deviate from the linear influence on the critical point, the prerequisite of the Bogoliubov approximation $nU/\omega_R \ll 1$ breaks down.

3.8 – Observables of the quantum fluctuations

Given the partition function Eq. (3.71), we have direct information about the observables for the quantum fluctuations of both the cavity q_C and the checkerboard mode q_A. We consider

$$\langle q_C^2 \rangle = -\frac{1}{\beta\delta_C}\frac{\partial \ln Z}{\partial \delta_C} = \frac{1}{2\beta(-\delta_C)}\sum_{n=-\infty}^{+\infty}\Bigg[\frac{\left(\nu_n^2[1-K_{\dot{A}n}/\omega_1]+\omega_1^2-\omega_1 K_{An}\right)\left(-2\delta_C+K_{Cn}-K_{C\mathrm{envn}}\right)}{D_n} + \frac{\omega_1(\lambda\sqrt{N}[u_1-v_1]-K_{ACn})^2}{D_n}\Bigg], \tag{3.73a}$$

$$\langle q_A^2 \rangle = -\frac{1}{\beta\omega_1}\frac{\partial \ln Z}{\partial \omega_1} = \frac{1}{2\beta\omega_1}\sum_{n=-\infty}^{+\infty}\Bigg[\frac{\left(\nu_n^2 K_{\dot{A}n}/\omega_1^2+2\omega_1-K_{An}\right)\left(\nu_n^2+\delta_C^2+\delta_C K_{Cn}-\delta_C K_{C\mathrm{envn}}\right)}{D_n} + \frac{\delta_C(\lambda\sqrt{N}[u_1-v_1]-K_{ACn})^2}{D_n}\Bigg], \tag{3.73b}$$

respectively. Due to the high polynomial order in ν_n^2 of the expectation values with the bath as revealed by Eq. (3.13), an analytical solution in the zero temperature limit $\beta \to \infty$ is not available. Instead, we numerically evaluate the sums $\sum_{n=-n_{\max}}^{n_{\max}}$ up to the Matsubara terms $n_{\max}$. We choose $n_{\max}$ depending on the inverse temperature β so that the values are converged. From our bath spectral density analysis, we know that at temperatures $\beta\omega_R \gtrsim 10^3$ the thermal spectral weight is orders of magnitude smaller than the quantum weight that remains at zero temperature. Therefore, we consider our bath to be effectively at zero temperature for such a large β.

The light and matter sectors become strongly entangled as we approach the critical point λ_{cr} from below by increasing either the coupling of a single atom to the cavity U_0 or the strength of the pump $\overline{\omega}_P$ in $\lambda = \sqrt{-U_0\overline{\omega}_P}$. A pair of polaritons is formed, which we find in the naked system S_S, from Eq. (3.38), by the transformation

$$\begin{pmatrix} q_C \\ q_A \end{pmatrix} = \begin{pmatrix} \cos(\chi) & \sin(\chi) \\ -\sin(\chi) & \cos(\chi) \end{pmatrix}\begin{pmatrix} q_1 \\ q_2 \end{pmatrix}, \qquad \tan(2\chi) = \frac{-\lambda\sqrt{-\delta_C\omega_1 N}(u_1-v_1)}{|\delta_C^2-\omega_1^2|}. \tag{3.74}$$

Its application to Eq. (3.38) yields the effective action

$$S_{\mathrm{eff}} = \frac{1}{2}\sum_{s,s'=1}^{2}\int_0^\beta d\tau\Bigg\{\delta_{s,s'}\left[\dot{q}_s^2(\tau)+\Omega_s^2 q_s^2(\tau)\right] - \int_0^\beta d\tau'\Big\{q_s(\tau)K_{ss'}(\tau,\tau')q_{s'}(\tau')+\dot{q}_s K_{\dot{s}\dot{s}'}(\tau,\tau')\dot{q}_{s'}(\tau)\Big\}\Bigg\}. \tag{3.75}$$

Figure 3.11 displays the respective expectation values of the observables $\langle q_{A,C}^2\rangle$ as the pump strength $\overline{\omega}_P$ is increased. If the cavity and BEC are uncoupled, $\overline{\omega}_P = 0$, there are no cavity fluctuations. The quantum fluctuations in the BEC originate from the s-wave scattering and are thus already present without the cavity through K_A and $K_{\dot{A}}$. However, they are comparatively weak. By introducing the coupling to the atoms, fluctuations are created in the cavity. As the coupling $\lambda = \sqrt{-U_0\overline{\omega}_P}$ is gradually increased, the fluctuations in both sectors grow monotonically. At the critical value of the phase transition λ_{cr} given by Eq. (3.72), the quantum fluctuations diverge. We can see this in the figure 3.12 for a selection of temperatures. Near the phase transition, the fluctuations of the system diverge with the critical exponent $c = 1$. This result is consistent with the prediction for the bare system, i.e. the Bogoliubov theory discussed in section 2.3.6. The reason for this is that the fluctu-

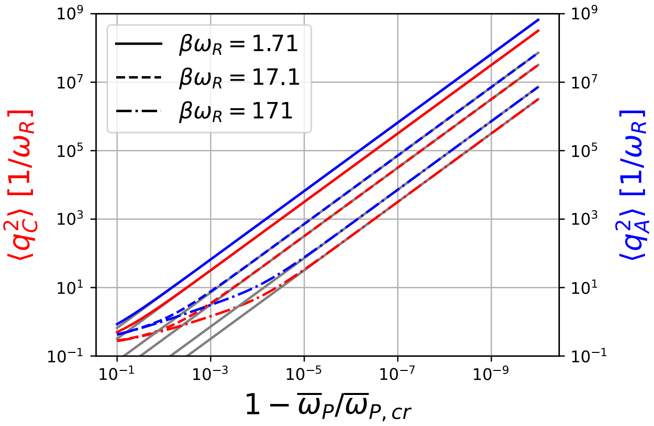

Figure 3.11: Expectation values for the light $\langle q_A^2 \rangle$ and the matter sector $\langle q_C^2 \rangle$ of the system as it approaches its Dicke phase transition by increasing the pump strength ϖ_P. The plot shows data for three different inverse temperatures from $\beta\omega_R = 1.71$, where thermal fluctuations dominate the bath, to $\beta\omega_R = 171$, where zero temperature quantum fluctuations are significant. The parameters are the same as in figure 3.10 with $n_{\max} = 10^3$.

ation bath is gapped from $\omega = 0$, see figure 3.7, so it does not affect the soft polariton while it is close to zero frequency, see figure 2.9. Thus the sub-Ohmic signature of the bath does not affect the critical exponent [128, 152]. Finite temperature extends the region where the expectation values grow according to the universal phase transition behavior. In this way, the additional thermal fluctuation on top of the quantum fluctuation increases the expectation values for both the photon $\langle q_C^2 \rangle$ and the atomic sector $\langle q_A^2 \rangle$ equivalently.

We now examine the influence of the quantum fluctuation bath on these observables in figure 3.12 by comparing their value $\langle \cdot \rangle$ in the presence of the bath with the value $\langle \cdot \rangle_0$ observed when we artificially turn off the fluctuation bath $G_\nu = 0$. Because the cavity fluctuations vanish without any coupling $\varpi_P = 0$, there is no difference in the cavity photon observable $\langle q_C^2(\varpi_P = 0) \rangle$. The observable of the matter sector $\langle q_A^2 \rangle$ however is already influenced at $\varpi_P = 0$, so that we spot a small deviation in figure 3.12. From there on, the influence of the fluctuation bath increases in both sectors as the coupling between them is increased. If we compare $\langle q_{A,C}^2 \rangle$ and $\langle q_{A,C}^2 \rangle_0$ at the same absolute pump strength ϖ_P in units of the recoil frequency ω_R, as shown by the dashed lines in figure 3.12, the bath-induced deviation of the observables diverges at the critical point because the presence of the bath moves the critical point λ_{cr} through the Stokes shift, as discussed around figure 3.10. Consequently, the two expectation values reach the phase transition at different values of ϖ_P. The relative deviation of the critical values caused by the Stokes shift is 2.3×10^{-4} for the parameters of figure 3.12.

Once we account for the Stokes shift by comparing the observables at the same relative value to their respective critical points, i.e. the solid lines of figure 3.12 where ϖ_P in units of $\varpi_{P,\text{cr}}$ for $\langle q_{A,C}^2 \rangle$ and $\varpi_{P,\text{cr},0}$ for $\langle q_{A,C}^2 \rangle_0$, we gain further insights. The deviation still largely increases over the ramp-up of the coupling λ by increasing the pump strength ϖ_P. However, it saturates near the critical point λ_{cr}, indicating that the quantum fluctuation bath does not change the critical exponent of the phase transition as seen in figure 3.11. In figure 3.12 we see that the bath affects the atomic sector of the system more than the photonic sector. This seems to contradict the conclusions drawn from the analysis of the bath spectral densities. There we found that the spectral weight G_C of the cavity bath is larger than the other coupling channels due to the difference in the coupling parameter $\lambda > \eta$, see figure 3.7. For the parameters in figure 3.12, the bath coupling for the checkerboard mode is $\eta = 2Un/\sqrt{N} \approx 1.4 \times 10^{-4}\,\omega_R$. With $U_0 = -10^{-3}\,\omega_R$ the cavity bath coupling $\lambda = \sqrt{-U_0\varpi_P}$ is

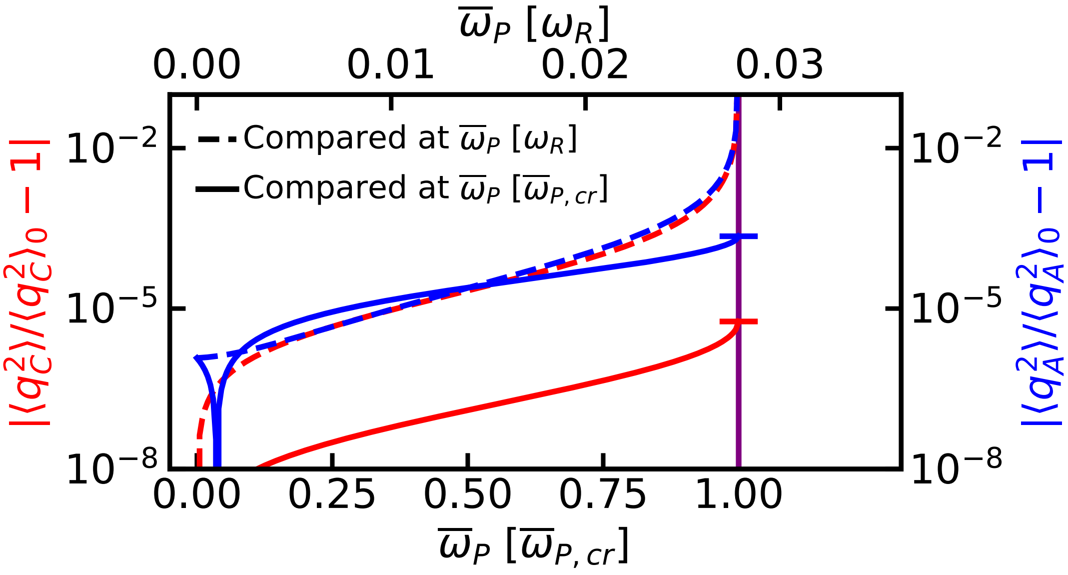

Figure 3.12: Relative difference between the quantum fluctuations in the photon (red, left) and atom (blue, right) sectors with quasiparticle-damping $\langle\cdot\rangle$ and without quasiparticle-damping $\langle\cdot\rangle_0$ for varying pump strengths. The upper axis is scaled to the recoil frequency ω_R and the result is shown as dashed lines. Thus, these data include the effect of the Stokes shift. On the other hand, the lower axis is scaled in units of the critical pumping strength and the results shown as solid lines do not include the Stokes shift. The purple vertical line marks the critical point of the modified Dicke phase transition. The temperature is $\beta\omega_R = 1.71 \times 10^3$ so that thermal fluctuations are negligible and only quantum fluctuations prevail. The parameters are again those for the recoil resolved experimental setup as in figure 3.10 with $n_{\max} = 10^4$.

already larger than η if $\overline{\omega}_P > 2 \times 10^{-5}\,\omega_R$. The effect must be due to the hybridization of the cavity photons and the checkerboard mode in the creation of the polaritons. Unless $-\delta_C$ and ω_1 are on resonance, one polariton is necessarily more photon-like while the other is more matter-like. As the polariton frequencies change, they resonate better or worse with the damping processes described in the bath of fluctuations. Thus, the actual expectation values for the two sectors $\langle q_C^2\rangle$ and $\langle q_A^2\rangle$ are entangled by the bath, see Eq. (3.75).

So far, we have studied the case of pure quantum fluctuations at zero temperature in figure 3.12, where we have chosen a parameter set of a weakly damped optical cavity of the Hamburg experiment [99,159] introduced in section 2.3.4. However, the derived theory also works at finite temperatures and for strongly damped cavities. In figure 3.13 we analyze the quantum fluctuations of the system for the finite temperature $\beta\omega_R = 1.71$. In the chosen setup this is about 100 nK and the thermal fluctuations are dominant in the bath. In the left panel, all parameters except the temperature are the same as in figure 3.12. We find that the addition of thermal fluctuations to the quantum fluctuations increases the observable system fluctuations by orders of magnitude. No qualitative differences to the case of effectively zero temperature are found. The relative deviation of the critical point induced by the Stokes shift is 8.7×10^{-2}, almost 10 percent of the required pump strength. For the right plot, we change the cavity detuning $\delta_C = -20\,\omega_R$ to be significantly away from resonance with the checkerboard mode $\omega_1 \approx 2\omega_R$. The fluctuations observed in the cavity are more strongly influenced by the bath for the larger cavity detuning. In particular, near the phase transition, the data for the relative deviation at $\overline{\omega}_P\,[\overline{\omega}_{P,\mathrm{cr}}]$ catches up with that in the atomic sector. The Stokes shift induced change in the critical point is slightly reduced to a relative change in pump strength of 8×10^{-2}. Note that the fluctuations in the atomic sector are largely unaffected.

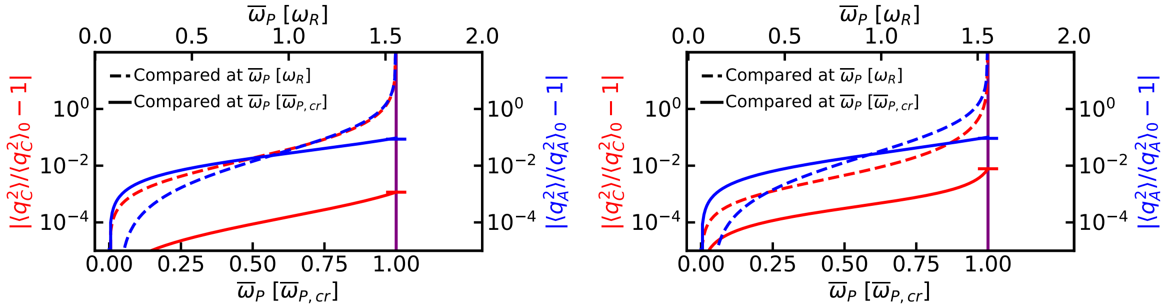

Figure 3.13: Relative difference between the quantum fluctuations in the sectors of the system against the pump strength $\overline{\omega}_P$ as also shown in figure 3.12. Here, however, for a finite temperature typical of contemporary experiments $\beta\omega_R = 1.71$. On the left, all other parameters are the same as in figure 3.12. In the right plot, the cavity detuning has been changed to $\delta_C = -20\,\omega_R$.

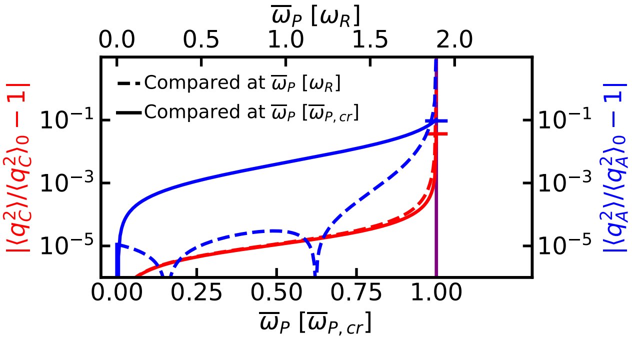

Figure 3.14: Relative difference in the quantum fluctuations as the pump strength $\overline{\omega}_P$ is tuned as in figure 3.12. However, here the cavity parameter set is that of the non-recoil resolved (overdamped) regime, and for a typical experimental temperature, i.e., $\delta_C = -2000\omega_R$, $\kappa = 1250\omega_R$ and $\beta\omega_R = 1.71$.

A fast ($|\delta_C|/\omega_R \gg 1$) and strongly damped ($\kappa/\omega_R \gg 1$) cavity is also realized in experiments. For example, in the setup at ETH Zürich in Refs. [23, 28, 35, 69]. We analyze such a setup in figure 3.14. Over most of the pumping range $\overline{\omega}_P$ [ω_R] the bath-induced fluctuations are significantly suppressed compared to the other parameter sets of figure 3.13. Except at the phase transition where the fluctuations diverge. The change in fluctuations due to bath influence without Stokes shift, i.e. using $\overline{\omega}_P/\overline{\omega}_{P,\mathrm{cr}}$, is also smaller over most of the pumping range. However, they grow faster up to the saturation value at the critical point marked by the horizontal bar in the plot. This saturation value of the atomic sector $\langle q_A^2\rangle$ is roughly the same as in figure 3.13. In the cavity photon sector, the data catch-up with the atomic sector is even more pronounced than in figure 3.13, corresponding to the much larger cavity detuning $|\delta_C|$. The Stokes shift at the critical pump strength is a relative deviation of 2.6×10^{-3} and thus significantly smaller than in the recoil resolved regime.

3.8.1 Tuning the contact interaction

The central characteristics of the bath is the strength of the s-wave scattering U. We next explore how its spectral densities and its influence are shaped by tuning this parameter. In the experiment, one would have to utilize different atomic species or different hyperfine levels, and ideally, Feshbach resonances, to achieve this kind of control. Figure 3.15 shows the change of the quantum fluctuations as U is varied. We keep the density n of the atomic gas constant. A larger scattering parameter U leads to more fluctuations and consequently to a larger value of the observables $\langle q^2_{A.C}\rangle$. Nevertheless, we have to keep in mind that even if we again artificially eliminate the bath fluctuations $G_\nu = 0$, the

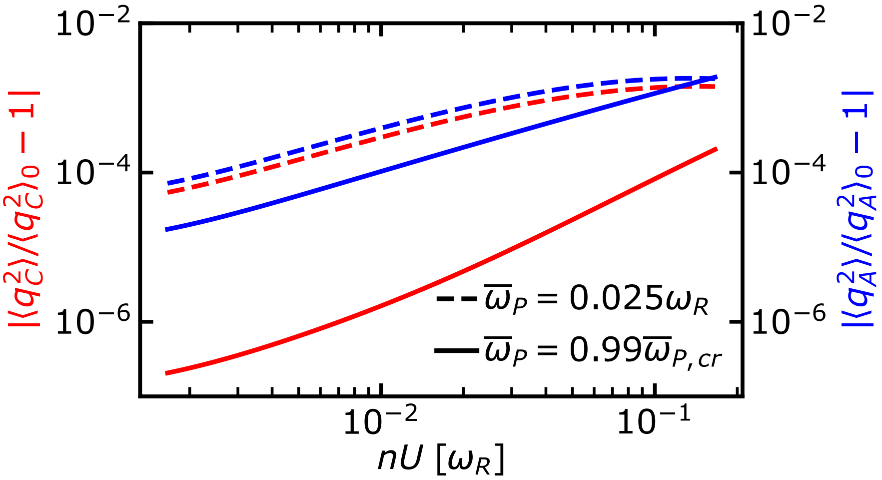

Figure 3.15: Relative difference between the quantum fluctuations in the photon (red, left) and the atom (blue, right) sectors as a function of the atom-atom interaction nU for two different values of $\overline{\omega}_P$ and for the same parameters as in figure 3.12.

magnitude of the fluctuations and the observables are changed, since the checkerboard mode ω_1 is directly dependent on nU, see Eq. (3.37). Thus, any increase in U leads to a larger pump strength $\overline{\omega}_{P,\mathrm{cr}}$ needed to reach the critical fluctuations for the phase transition, Eq. (3.72). If we again adjust for the shifted critical point, which grows approximately linearly with U, see figure 3.10, as in figure 3.12 by comparing the value with and without the bath not at the same absolute pump strength $\overline{\omega}_P/\omega_R$ but at the same relative value to the critical point $\overline{\omega}_P/\overline{\omega}_{P,\mathrm{cr}}$, we find a much more pronounced response of the observables to changing U. In figure 3.15 we find, when we examine this influence, that the difference in influence observed in the cavity and checkerboard sectors is greatly reduced for larger s-wave scattering strengths. We find that if the Stokes shift is taken into account, the strength of the fluctuations is increased by two orders of magnitude while the atom-atom interaction U is modulated by two orders of magnitude inbetween $2 \times 10^{-3}\,\omega_R \leq nU \leq 2 \times 10^{-1}\,\omega_R$. In fact, the cavity observable $\langle q_C^2\rangle$ increases by almost three orders of magnitude in that range.

3.9 – Outlook

So far we have only analyzed equilibrium correlation functions $\langle q_{A,C}^2 \rangle$ to study the response of the system to the bath. In principle, it is feasible to obtain the dynamics by modeling the system as two harmonic oscillators with different couplings to the quantum fluctuation bath, e.g. using the Keldysh approach [67,154–157]

$$\begin{aligned} S_S = \int_{-\infty}^{+\infty} dt \Bigg\{ & \begin{pmatrix} a_{\mathrm{cl}}^* & a_{\mathrm{qu}}^* \end{pmatrix} \underline{G}_{C,0}^{-1} \begin{pmatrix} a_{\mathrm{cl}} \\ a_{\mathrm{qu}} \end{pmatrix} + \begin{pmatrix} \varphi_{1\mathrm{cl}}^* & \varphi_{1\mathrm{qu}}^* \end{pmatrix} \underline{G}_{A,0}^{-1} \begin{pmatrix} \varphi_{1\mathrm{cl}} \\ \varphi_{1\mathrm{qu}} \end{pmatrix} \\ & - \lambda_0 \left[a_{\mathrm{cl}}^* \varphi_{1\mathrm{qu}}^* + a_{\mathrm{qu}}^* \varphi_{1\mathrm{cl}}^* + a_{\mathrm{cl}}^* \varphi_{1\mathrm{qu}} + a_{\mathrm{qu}}^* \varphi_{1\mathrm{cl}} \right. \\ & \left. + \varphi_{1\mathrm{cl}}^* a_{\mathrm{qu}} + \varphi_{1\mathrm{qu}}^* a_{\mathrm{cl}} + \varphi_{1\mathrm{cl}} a_{\mathrm{qu}} + \varphi_{1\mathrm{qu}} a_{\mathrm{cl}} \right] \Bigg\} , \end{aligned} \tag{3.76a}$$

$$S_B = \sum_{\boldsymbol{p} \in \mathcal{P}}{}' \int_{-\infty}^{+\infty} dt \left\{ \begin{pmatrix} \varphi_{0\boldsymbol{p}\mathrm{cl}}^* & \varphi_{0\boldsymbol{p}\mathrm{qu}}^* \end{pmatrix} \underline{G}_{0\boldsymbol{p}}^{-1} \begin{pmatrix} \varphi_{0\boldsymbol{p}\mathrm{cl}} \\ \varphi_{0\boldsymbol{p}\mathrm{qu}} \end{pmatrix} + \begin{pmatrix} \varphi_{1\boldsymbol{p}\mathrm{cl}}^* & \varphi_{1\boldsymbol{p}\mathrm{qu}}^* \end{pmatrix} \underline{G}_{1\boldsymbol{p}}^{-1} \begin{pmatrix} \varphi_{1\boldsymbol{p}\mathrm{cl}} \\ \varphi_{1\boldsymbol{p}\mathrm{qu}} \end{pmatrix} \right\} , \tag{3.76b}$$

$$\begin{aligned} S_{SB} = \frac{-1}{\sqrt{2}} \int_{-\infty}^{+\infty} dt \Bigg\{ & \left[\lambda \left(a_{\mathrm{cl}}^* + a_{\mathrm{cl}} \right) + \eta \left(\varphi_{1\mathrm{cl}}^* + \varphi_{1\mathrm{cl}} \right) \right] \left(L_1^{\mathrm{cl,qu}} + L_1^{\mathrm{qu,cl}} - B_1^{\mathrm{cl,qu}} - B_1^{\mathrm{qu,cl}} \right) \\ & + \left[\lambda \left(a_{\mathrm{qu}}^* + a_{\mathrm{qu}} \right) + \eta \left(\varphi_{1\mathrm{qu}}^* + \varphi_{1\mathrm{qu}} \right) \right] \left(L_1^{\mathrm{cl,cl}} + L_1^{\mathrm{qu,qu}} - B_1^{\mathrm{cl,cl}} - B_1^{\mathrm{qu,qu}} \right) \\ & + \eta (u_1 \varphi_{1\mathrm{cl}} - v_1 \varphi_{1\mathrm{cl}}^*) \left[-\left(L_2^{\mathrm{cl,qu}} \right)^* - \left(L_2^{\mathrm{qu,cl}} \right)^* + \left(B_2^{\mathrm{cl,qu}} \right)^* + \left(B_2^{\mathrm{qu,cl}} \right)^* \right] \\ & + \eta (u_1 \varphi_{1\mathrm{qu}} - v_1 \varphi_{1\mathrm{qu}}^*) \left[-\left(L_2^{\mathrm{cl,cl}} \right)^* - \left(L_2^{\mathrm{qu,qu}} \right)^* + \left(B_2^{\mathrm{cl,cl}} \right)^* + \left(B_2^{\mathrm{qu,qu}} \right)^* \right] \\ & + \eta (u_1 \varphi_{1\mathrm{cl}}^* - v_1 \varphi_{1\mathrm{cl}}) \left[-L_2^{\mathrm{cl,qu}} - L_2^{\mathrm{qu,cl}} + B_2^{\mathrm{cl,qu}} + B_2^{\mathrm{qu,cl}} \right] \\ & + \eta (u_1 \varphi_{1\mathrm{qu}}^* - v_1 \varphi_{1\mathrm{qu}}) \left[-L_2^{\mathrm{cl,cl}} - L_2^{\mathrm{qu,qu}} + B_2^{\mathrm{cl,cl}} + B_2^{\mathrm{qu,qu}} \right] \Bigg\} , \end{aligned} \tag{3.76c}$$

with the notation

$$L_1^{\mu,\nu} = \sum_{\boldsymbol{p} \in \mathcal{P}}{}' \left[\left(u_{0,\boldsymbol{p}} u_{1,\boldsymbol{p}} + v_{0,\boldsymbol{p}} v_{1,\boldsymbol{p}} \right) \left(\varphi_{0\boldsymbol{p}\mu}^* \varphi_{1\boldsymbol{p}\nu} + \varphi_{1\boldsymbol{p}\mu}^* \varphi_{0\boldsymbol{p}\nu} \right) \right] , \tag{3.77}$$

and for the other operators defined in Eq. (3.41) analog. Although the system S_S and the bath S_B are still quadratic and their coupling S_{SB} linear, the computation from Eq. (3.76) is tedious. Alternatively, having already obtained the bath spectral densities Eq. (3.57), we can use them to solve the dynamics of the two harmonic oscillators in the real-time form of the action S_{eff}, Eq. (3.65) [160]. However, both approaches are computationally tedious and never purely analytical, since the self-energies or damping kernels associated with the spectral densities are nonelementary integrals.

One might simplify the elaborate model of the damping channels. Studying figure 3.7 and the spectral density approximations in Eq. (3.64) quantitatively, we find that the cavity is most strongly coupled to the fluctuating bath in common parameter regimes, see our discussion in sections 3.5 and 3.8 on λ and η. This is a remarkable result, considering that the bath is essentially an effect of the atoms and their interactions with one another. However, it is simply because the cavity-atom coupling λ is significantly larger than the coupling of the checkerboard mode to the phonon bath η. Hence, the coupling parameter of the spectral density $G_C(\omega)$ is much larger compared to the other spectral densities. From this point of view we can discard the terms coupled by η in the system-bath Hamiltonian Eq. (3.40), leaving us with $H_{SB} = \lambda(\hat{a} + \hat{a}^\dagger)(\hat{L}_1 - \hat{B}_1)$. We have mentioned this and further approximations already in section 3.4. In the effective action picture Eq. (3.65) the much simplified form

$$S_{\text{eff}} = \frac{1}{2}\int_0^\beta d\tau \Bigg\{ \dot{q}_A^2(\tau) + \omega_1^2 q_A^2(\tau) + \dot{q}_C^2(\tau) + \delta_C^2 q_C^2(\tau) + \lambda\sqrt{N}(u_1 - v_1) q_A(\tau) q_C(\tau) \\ - \int_0^\beta \Big\{ q_C(\tau)\delta_C K_C(\tau,\tau') q_C(\tau') \Big\} \Bigg\}, \tag{3.78}$$

is obtained. Here we have again included the cavity loss with rate κ through the Ohmic bath $G_C \to G_C + G_{C\text{env}}$ with Drude cutoff. Analogously, this reduction of the bath can be performed for $\eta \gg \lambda$, but this limit is physically less likely since it would require strong scattering interaction U or small volumes V_{2D}, or conversely a large number of atoms in the same volume, all of which tend to contradict the dilute weakly interacting gas assumption of Bogoliubov theory.

Even in the reduced bath picture of Eq. (3.78) it still requires great effort to obtain the dynamics of the two coupled oscillator system [160]. Fortunately, there is a simpler way. Applying the technique developed in Ref. [161], one of the harmonic oscillators can be eliminated and reduced to an effective spectral density $G_{\text{eff}}(\omega)$. The dynamics of a single harmonic oscillator coupled to a bath is well understood [32, 162].

Determining an effective spectral density by including the system modes in the bath also opens the possibility of studying the backaction of a detector on the system. In the experiment, this detector setup is placed behind a cavity mirror and thus directly detects only the light lost through that of the mirror. For a detector capable of observing single photons, an appropriate simple approach for its modeling could be an effective harmonic oscillator mode or two-state system. In turn, the application of the effective bath technique could also allow us to predict the actual dynamic measurement performed at the detector and to study it in relation to the actual cavity BEC system dynamics.

3.10 – Conclusions

In this chapter, we explore effects arising from quantum fluctuations due to weak scattering interaction in the BEC. Some aspects of this work have been studied in the existing literature [28, 34, 127, 128, 152, 153], but here we present an all-encompassing picture of these phenomena starting from first principles.

Starting from the field Hamiltonian of the cavity BEC setup, we consider the dynamics in the two-dimensional cavity pump plane Eq. (3.25). In the intersection of the cavity and the pump beam, a weakly interacting condensate with interaction strength U is placed. This interaction is the physical foundation for quantum fluctuations in the system and thus for the quantum phase transition to the self-organized state to occur. Based on existing literature [34, 36, 100, 105, 128] analyzing such systems, we identify a Bloch band structure of the atomic field and pinpointed the two relevant bands for the dominant dynamics, see Eq. (3.26). From there, we have carried out a beyond-Bogoliubov approximation around the macroscopically occupied condensate, which allows for higher-order fluctuations than the standard Bogoliubov theory. We thus find a description of the quantum fluctuations that are of quadratic order equivalent to the existing Bogoliubov theory discussed in sections 2.3.6 and 2.3.7. However, we additionally find in the next order terms of Landau and Beliaev damping within the phononic band structure, which is coupled to the Dicke model-like system of the common Bogoliubov approach. Because the key cavity BEC features and their measurement are centered on the Dicke model system of cavity photons and checkerboard excitations, the resulting total microscopic

Hamiltonian is interpreted in a system-bath model. We show that the quasiparticle bath of quantum fluctuations couples via independent coupling parameters λ and η to the photon and atom sectors of the two-mode system, respectively. Both parameters are tunable in an experiment, the former by light field properties such as the strength $\overline{\omega}_P$ of the transversal pump beam and the latter by Feshbach resonances to modify the strength U of the atom-atom scattering.
We extract the characteristics of the quantum bath and its influence on the Dicke system by deriving the influence functional in the imaginary-time path integral approach. Within our beyond-Bogoliubov approximation, this can be done analytically exactly due to the linear coupling in all modes. It provides us with bath spectral densities for each type of coupling between the system and the bath. The spectral densities are defined on finite frequency intervals determined by the Brillouin zone related to the Bloch bands. The frequency interval for Landau damping is different from that for Beliaev damping. However, they meet at the boundary defined by the frequency of the checkerboard mode ω_1, Eq. (3.37). We have discussed in detail how the spectral densities and their frequency intervals can be controlled by the tuning external parameters $\overline{\omega}_P$ and U. We would like to emphasize that the possibility of using the pump strength to tune the atomic excitation bands only presents itself in a system with dynamics in more than one dimension as we consider it in our calculation taking into account the two-dimensional dynamics in the pump-cavity plane. The spectral densities reveal exotic coupling properties of the quantum bath to the system. Key results of our analysis are peculiar competitions between different quasiparticle channels leading to frequency regions of damping and antidamping induced by the bath. Zero-temperature pure quantum effects exist exclusively in the channels of Beliaev damping. These peak at the boundary $\omega = \omega_1$ with a finite valued cusp singularity if $\beta \to \infty$. Since the boundary represents the point of zero quasi-momentum $\boldsymbol{p} = \boldsymbol{0}$ in the system, we discovered analytically that in the immediate vicinity of the boundary the dominant expansion term of the spectral densities is sub-Ohmic. Thus, if the coupling to the bath is significant, the dynamics of the system can acquire strong non-Markovian signatures. Finally, we also analyzed the competition between the thermal weight of the bath influence and that of the quantum fluctuations. This led to the conclusion that temperatures of $\beta\omega_R \gtrsim 10^3$ are required to effectively eliminate all thermal effects.
We furthermore analyzed the effective partition function of the system as its expansion in Matsubara frequencies. First, we note that the system parameters are renormalized by the bath in terms of its Stokes shift. It is observed in the shift of the critical point for the Dicke phase transition Eq. (3.72). In fact, for realistic parameters of contemporary experimental setups, this shift is up to almost 10 percent of the critical pump strength $\overline{\omega}_P$. We proceeded by analyzing the fluctuations in the system observables using their equilibrium expectation values. We found that while finite temperatures quantitatively change the measurement, it has no qualitative effect. Likewise, the bath with its gap to the zero frequency of the soft mode polariton does not change the universality class of the system at the phase transition. On the other hand, the quantum bath qualitatively affects the system beyond the Stokes shift. The magnitude of the fluctuations in the system observables is changed by taking into account the intrinsic quantum fluctuations from the bath. Although this effect appears to be small for most parameter ranges in contemporary experimental setups, it is straightforward to increase its significance. The coupling to the bath is suppressed compared to the Bogoliubov level by $\sqrt{N}$, see Eq. (3.33) or figure 3.3. Thus, systems with fewer particles $N \lesssim 10^3$ will open the door to study the enhancement and control of the fluctuation bath influence and the non-Markovian dynamics induced by it on the polariton system. The control is performed by tuning external parameters such as the pump laser strength $\overline{\omega}_P$, the single-atom-cavity coupling U_0 and the atom-atom scattering strength U.

We have demonstrated that the cavity BEC platform intrinsically offers a simulation of an intriguing system-bath model with exceptional control over the quantum fluctuations and nondestructive access to the dynamics. Therefore, it constitutes a great platform to study stimulating dissipative dynamics with time-nonlocal signatures. Their investigation and exploitation are not just relevant for the cavity BEC, polariton, or Dicke systems but in a broader scope throughout condensed matter physics. This includes fields such as superconductor qubits, quantum information, nanomechanical and glassy systems, and quantum dots.

4 – Cavity-induced quantum droplet formation

Quantum droplets are formed in quantum many-body systems when the competition of quantum corrections with the mean-field interaction yields a stable self-bound quantum liquid. We predict the emergence of a quantum droplet in a dilute Bose gas with both a short-range and an effective long-range interaction between the atoms. The long-range interaction is spatially characterized by a periodic signature and a tunable envelope. We formulate a Bogoliubov theory based on a homogeneous mean-field description and quantum fluctuations around it where roton modes emerge. We find that the repulsive mean-field contact interaction could be destabilized by quantum fluctuation corrections rooted in the long-range interaction. The competition between both facilitates the formation of self-bound quantum droplets. This generic approach is applied to setups where a BEC is placed in an optical cavity. The cavity induces an effective long-range interaction between the atoms with different interaction profiles and symmetries depending on the specific setup. The favorable scaling of the quantum fluctuations with respect to the system size is determined by the envelope of the long-range interaction potential. We show analytically how the size and the central density of the cavity-induced quantum droplets depend on the contact interaction strength, the long-range interaction strength, and the shape of the spatial envelope. In this chapter we present the work published as Ref. [C] L. Mixa, M. Radonjić, A. Pelster, M. Thorwart, *Cavity-induced quantum droplets*, Phys. Rev. Res. **7**, 033216 (2025) and Ref. [D] L. Mixa, M. Radonjić, A. Pelster, M. Thorwart, *Engineering quantum droplet formation by cavity-induced long-range interactions*, Phys. Rev. Res. **7**, 023204 (2025).

4.1 – Introduction to and classification of droplets

In classical physics, matter exists uniquely in the solid, liquid, or gas phase. Once quantum mechanics takes effect, a variety of further aggregate states emerge. In 1938 Kapitza published his findings on ultracold helium-4 [37], where at temperatures below 2.17 Kelvin he discovered the superfluid state, a liquid that flows without friction and has no entropy. This sparked a widespread and enduring interest in exploring the intricate macroscopic quantum states of helium. Landau provided the roton mode in the dispersion relation of superfluid ^{4}He [38] as the explanation of the superfluid properties. The quantum liquid helium can also realize a free droplet state [5]. This state is characterized by zero pressure at a certain density, which leads to a self-trapping quantum liquid. A self-trapping liquid of N atoms occupying the volume V and avoiding self-evaporation can be understood by its effective energy $E_0(V,N)$ satisfying the minimal generic conditions [5]

$$\text{(C1) zero pressure: } \left(\frac{\partial E_0}{\partial V}\right)_N = 0 \;\Rightarrow\; V_0 > 0\,, \tag{4.1a}$$

$$\text{(C2) positive bulk compressibility: } \left(\frac{\partial^2 E_0}{\partial V^2}\right)_N \bigg|_{V=V_0} > 0\,, \tag{4.1b}$$

$$\text{(C3) negative chemical potential: } \left(\frac{\partial E_0}{\partial N}\right)_{V=V_0} < 0\,. \tag{4.1c}$$

At the equilibrium volume V_0, the effective energy of the liquid is minimized, which determines the size of the droplet. The discussion within the effective ground state energy E_0 generalizes the notion

of a droplet in the thermodynamic limit to finite systems with significant finite-size effects.
A model must contain at least two terms to possibly satisfy the conditions. Usually, the first term is the mean-field energy $\propto N^2/V$. For finite volume it cannot fulfill (C1), Eq. (4.1a), by itself. Therefore, a contact interaction BEC has $V_0 \to \infty$ as we depict in figure 4.1. It needs competition that contributes an energy term with a different algebraic dependence on the volume V. To amount to a quantum droplet, this player against the mean-field must be of a quantum fluctuation nature. We denote the difference in the exponent of the volume by the parameter c and introduce the parameters $a(N)$ for the mean-field prefactor and $b(N)$ for the quantum competition prefactor so that we can write the minimal energy model of a droplet in the form

$$E_0(V,N) = a(N)V^{-1} + b(N)V^{-(1+c)} + d(N)\,, \tag{4.2}$$

with an atom number dependent offset $d(N)$. For a true *minimal* model we should set $d(N) = 0$ and indeed it would suffice to fulfill (C1) to (C3) but its inclusion allows us a wider range of choices for $a(N)$ and $b(N)$ while still satisfying condition (C3). We find from Eq. (4.1a) the generic solution for the droplet size of the model $E_0(V,N)$

$$V_0^c = -\frac{(1+c)b(N)}{a(N)}\,, \tag{4.3}$$

and three classes of parameters (a,b,c) that satisfy (C1) and (C2), i.e. Eqs. (4.1a) and (4.1b) so that $V_0 > 0$,

$$\text{(D1)}\ a(N) < 0\,,\ b(N) > 0\,,\ c > 0\,, \tag{4.4a}$$

$$\text{(D2)}\ a(N) > 0\,,\ b(N) < 0\,,\ 0 > c > -1\,, \tag{4.4b}$$

$$\text{(D3)}\ a(N) > 0\,,\ b(N) > 0\,,\ c < -1\,. \tag{4.4c}$$

Figure 4.1 illustrates their qualitative difference in satisfying the conditions. Starting with (D1) we find that in the large system or equivalently dilute system limit $1/V \to 0$ the curve follows an inverse parabola $-(1/V)^2$ due to $a < 0$ and $c > 0$. In the small system limit $1/V \to \infty$ the curve is described by the convex function $(1/V)^{2+c}$ since $b > 0$ and $c > 0$. In the particular example sketched in figure 4.1 the asymptotic behavior is $(1/V)^{5/2}$ for $1/V \to \infty$. The second class of droplets (D2), because it has the parameter $c < 0$, follows its correction term $-(1/V)^{2+c}$ in the large system limit $1/V \to 0$. Its negative parameter $b < 0$ means that it has concave asymptotic behavior at $1/V \to 0$. The plot shows $(1/V)^{3/2}$. For the dense system limit $1/V \to \infty$ the parabola $+(1/V)^2$ of the mean-field term in E_0 with positive parameter $a > 0$ dominates. Studying the sketch of the third droplet class (D3) it is again $c < 0$, so that in the dilute limit $1/V \to 0$ the correction term $-(1/V)^{2+c}$ rules. The sketch in figure 4.1 shows an example where $-2 < c < -1$, so the exponent $\tilde{c} = 2 + c \in (0, 1)$ is some fraction, provided $c \in \mathbb{Q}$. Therefore, the pressure in the large system limit $1/V \to 0$ shown for (D3) is given by some root expression $-(1/V)^{\tilde{c}=1/3}$. In class (D3), if the exponent parameter c has a larger absolute value $c < -2$, the pressure is given by a function diverging to negative infinity as $-V^{|c|-2}$ for $V \to \infty$. Finally, the limit of small system size $1/V \to \infty$ for the droplet model (D3) is dominated by the positive parabola $(1/V)^2$ resulting from the mean-field term with $a > 0$. Figure 4.1 also underpins the mathematical interpretation of conditions (C1) and (C2) that the effective energy of the system is minimized with respect to the system size V in the droplet state given by V_0. The third droplet condition (C3), Eq. (4.1c), implies that the dependence of $a(N)$ and $b(N)$ on the number of atoms N

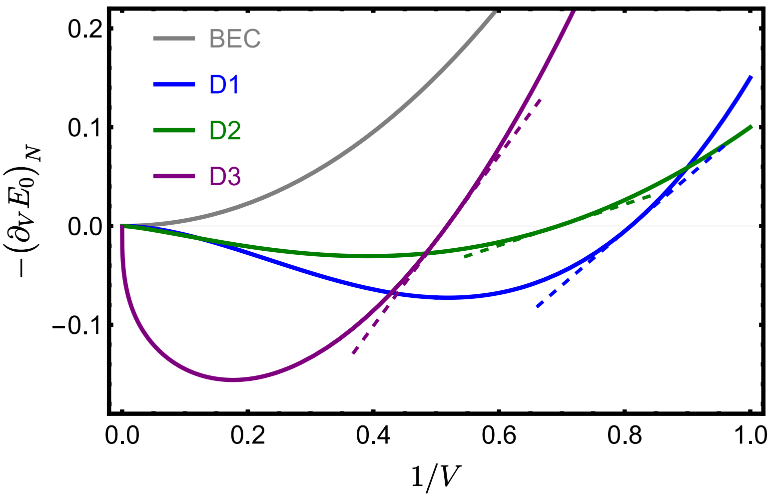

Figure 4.1: Pressure $-(\partial E_0/\partial V)_N$ of the minimal energy model E_0, Eq. (4.2), against the inverse of the system size V for a stable BEC and the three droplet classes Eq. (4.4). It visualizes the qualitative differences between the classes (D1)-(D3). More precisely, the plot shows the derivative of the minimal energy model E_0 with respect to the system size V: $(-\partial E_0/\partial V)_N$ plotted against the inverse system size $1/V$ for (BEC): $a = 0.5$, $b = 0.01$, $c = +1/2$, (D1): $a = -1.35$, $b = +1$, $c = +1/2$, (D2): $a = +0.6$, $b = -1$, $c = -1/2$, and (D3): $a = +1$, $b = +1/2$, $c = -5/3$. The parameters for a and b were picked for optimal visual presentation. The dashed lines show the tangents to the pressure curves at droplet equilibrium volume V_0, i.e. $(-\partial E_0/\partial V)_N = 0$. Their positive slopes demonstrate the stability of the zero pressure points or, in other words, the positive compressibility of the respective droplet.

follows

$$\begin{aligned}\left(\frac{\partial E_0}{\partial N}\right)_{V=V_0} &= \frac{1}{V_0}\frac{\partial a(N)}{\partial N} + \frac{1}{V_0^{1+c}}\frac{\partial b(N)}{\partial N} + \frac{\partial d(N)}{\partial N} < 0 \\ &\Rightarrow \frac{\partial a(N)}{\partial N} - \frac{a(N)}{(1+c)b(N)}\frac{\partial b(N)}{\partial N} + \frac{\partial d(N)}{\partial N} < 0\,, \end{aligned} \tag{4.5}$$

to prevent self-evaporation of the droplet. We believe it is important to note that if the dependence of the parameters on the number of particles is such that $a(N) \propto N^2$, $b(N) \propto N^{2+c}$, and $d(N) = 0$, then the condition given in Eq. (4.5) can only be satisfied for $c > -1$. In particular, this excludes the droplet class (D3), Eq. (4.4c). This may seem benign, but only if the model parameters have these proportionalities $a(N) \propto N^2$ and $b(N) \propto N^{2+c}$, the pressure can be expressed as a function $P(n)$ only depending on the particle density $n = N/V$. Solely if this is given, the droplet can survive the thermodynamic limit $N \to \infty$, $V \to \infty$ with $n = N/V = \text{const}$ and in fact this also relates to whether we can express the effective droplet model as an energy density $\epsilon_0(n)$. Hence, our notion based on the energy potential Eq. (4.2) generalizes the notion of droplets existing in the thermodynamic limit [5] and additionally covers those arising in systems of finite size.

For the strongly interacting and highly correlated liquid helium, the derivation of the specific long-range correlations and quantum many-body interactions is concealed from the first-principles derivation. For superfluid helium effective energy functionals have been applied [40,163–165] to achieve great progress. Over the past decade, quantum droplets have been established as a novel macroscopic quantum state of matter through their discovery in weakly interacting dilute atom gases. This was sparked by the seminal prediction of a quantum droplet state in Bose-Bose mixtures by D. S. Petrov [44]. In the description of the ground state energy, their three-dimensional realization is of class (D1) with $c = +1/2$, as follows from Eq. (4.8) in the next section. The one-dimensional mixture droplets are of class (D2) with $c = -1/2$ [60]. The isolated droplets formed in a dipolar BEC [45, 166–168] are

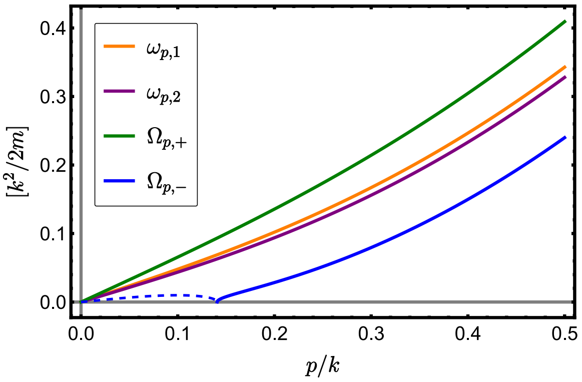

Figure 4.2: Excitation spectrum of the Bose-Bose mixture. The Bogoliubov dispersion of each species is shown as $\omega_{p,s=1,2}$ with $U_{11}n_1$ and $U_{22}n_2$ respectively. The two branches of the mixture $\Omega_{p,\pm}$, Eq. (4.7), are shown. As for the single Bose gas dispersion figure 2.5 the units are determined by an arbitrary wavenumber k and any finite imaginary part in the dispersion is shown as a dashed curve. The parameters are $U_{11}n_1 = 0.11\,k^2/2m$, $U_{22}n_2 = 0.09\,k^2/2m$, and $U_{12} = -1.1\sqrt{U_{11}U_{22}}$.

another manifestation of class (D1) with $c = +1/2$ as follows from Eq. (4.14). Dipolar BECs have a roton mode in their excitation spectrum [50–53], which enables the spontaneous formation of a spatial density modulation of the superfluid in a narrow parameter window [54–56]. Such a quantum aggregate state called a supersolid, which combines the signatures of both a liquid and a solid, has long been predicted to exist in ultracold helium [42]. However, supersolid properties have not yet been demonstrated in ^{4}He.

4.2 – Quantum liquid droplets

In this section, we want to explore what constitutes a quantum droplet and what physical systems they can be realized and observed in. In recent years, quantum droplets have been a rapidly developing and exciting field, and there is much more to say than we take space for. However, in the context of this thesis, where we are dealing with different kinds of systems, our aim should be to give an intuitive but probably incomplete picture based on the current state of research and not the intricate details of every derivation or experimental setup. Of course, reference is made to the necessary literature where this information can be found.

4.2.1 Bose-Bose mixtures

A way to realize a dilute droplet in a weakly interacting system was devised by D. S. Petrov in the seminal Ref. [44]. Consider two Bose gases of two different atoms, called species $s = 1$ and $s = 2$. In such a mixture there is both intraspecies U_{ss} and interspecies $U_{12} = U_{21}$ contact interaction, so that the single species Hamiltonian Eq. (2.11) is generalized to [44, 169]

$$\hat{H} = \int_V d^3\boldsymbol{r} \sum_{s=1}^{2} \left\{ \hat{\psi}_s^\dagger(\boldsymbol{r}) \left[-\frac{\nabla^2}{2m} + \sum_{s'=1}^{2} \frac{U_{ss'}}{2} \hat{\psi}_{s'}^\dagger(\boldsymbol{r}) \hat{\psi}_{s'}(\boldsymbol{r}) \right] \hat{\psi}_s(\boldsymbol{r}) \right\} . \tag{4.6}$$

Thus, the homogeneous mean-field $\langle \hat{\psi}_s^{(\dagger)} \rangle = \sqrt{n_s}$ of the Bose-Bose mixture is stable if the quadratic form of the interaction term is positive definite. Mean-field stability can only be obtained if both intraspecies scattering parameters $U_{11}, U_{22} > 0$ are positive and $U_{12}^2 < U_{11}U_{22}$ so that $\delta U = U_{12} + \sqrt{U_{11}U_{22}} > 0$. Note that the two species are miscible if $U_{12} < \sqrt{U_{11}U_{22}}$. By performing the Bogoliubov theory, two excitation branches are found [44]

$$\Omega_{\boldsymbol{p},\pm} = \sqrt{\frac{\omega_{\boldsymbol{p},1}^2 + \omega_{\boldsymbol{p},2}^2}{2} \pm \sqrt{\frac{(\omega_{\boldsymbol{p},1}^2 - \omega_{\boldsymbol{p},2}^2)^2}{4} + \frac{U_{12}^2 n_1 n_2 \boldsymbol{p}^4}{m_1 m_2}}}\,, \tag{4.7}$$

with $\omega_{\boldsymbol{p},s} = \sqrt{(\boldsymbol{p}^2/2m_s)^2 + U_{ss} n_s \boldsymbol{p}^2/m_s}$ the Bogoliubov dispersion of the individual species, Eq. (2.25). We show these in figure 4.2. The LHY correction arising from the excitation spectrum Eq. (4.7) of the mixture is

$$\begin{aligned} E_{\mathrm{qf}} &= \frac{V}{2(2\pi)^3} \int_{\mathbb{R}^3} d^3\boldsymbol{p} \Big\{ \Omega_{\boldsymbol{p},-} + \Omega_{\boldsymbol{p},+} - \frac{\boldsymbol{p}^2}{2m^*} - U_{11} n_1 - U_{22} n_2 \\ &\qquad + \frac{m_1 U_{11}^2 n_1^2 + m_2 U_{22}^2 n_2^2 + 4m^* U_{12}^2 n_1 n_2}{\boldsymbol{p}^2} \Big\} \\ &= \frac{8 V m_1^{3/2}}{15\pi^2} (U_{11} n_1)^{\frac{5}{2}} f\left(\frac{m_1}{m_2}, \frac{U_{12}^2}{U_{11} U_{22}}, \frac{U_{22} n_2}{U_{11} n_1} \right), \end{aligned} \tag{4.8}$$

where $m^* = m_1 m_2/(m_1 + m_2)$ and $f > 0$ is a dimensionless, in general nonelementary function [44]. However, for equal masses $m_1 = m_2$, the integral Eq. (4.8) can be solved analytically and results in

$$f(1, x, y) = \frac{1}{4\sqrt{2}} \sum_{\pm} \left(1 + y \pm \sqrt{(1 - y^2) + 4xy} \right)^{5/2}. \tag{4.9}$$

Petrov then argues that the mean-field collapse due to a small negative $\delta U < 0$, visualized in the unstable lower excitation branch of figure 4.2, is cured by the LHY correction of the mixture Eq. (4.8) [44]. The competition between the attractive mean-field $\propto \delta U n^2$ and the repulsive quantum correction $\propto [(U_{11} + U_{22})n/2]^{5/2}$ with their different dependence on the mixture density n and the interaction parameters U_{11}, U_{22}, and U_{12} leads to an equilibrium density which, for small $|\delta U|$, has the form [44]

$$n_{1,0} = \frac{25\pi}{1024} \left[f\left(\frac{m_2}{m_1}, 1, \sqrt{\frac{U_{22}}{U_{11}}} \right) \right]^{-2} a_{11}^{-3} \frac{\delta U}{U_{11} U_{22}}\,, \tag{4.10}$$

with the scattering length a_{11} of $U_{11} = 4\pi a_{11}/m_1$. The other component $n_{2,0}$ is then determined by the ratio locking of the mixture $n_2/n_1 = \sqrt{U_{11}/U_{22}}$ [44].

For this dilute droplet, the wavelength of the dominant excitations is much smaller than the droplet size $p \ll 1/\xi_h$. Therefore, the local density approximation can be applied. Thereby, the competition between the mean-field term and the LHY correction in the low-energy regime of the system can be cast into an extended Gross-Pitaevskii equation for the ground state of the mixture condensate wave function $\phi_0(\tilde{\boldsymbol{r}})$, which has the expression [44]

$$0 = \left(-\frac{\nabla_{\tilde{\boldsymbol{r}}}^2}{2} - 3|\phi_0|^2 + \frac{5}{2}|\phi_0|^3 - \tilde{\mu} \right) \phi_0\,, \tag{4.11}$$

in rescaled units denoted by a tilde. For a large number of particles, the ground state is a spherical droplet of large radius with uniform bulk. When the number of atoms is not large, the wave function can be found numerically, leading to the results in figure 4.3, where we see that for larger numbers of atoms, the droplet approximates a uniform bulk with a small surface. It also shows that the addition of particles only extends the radial size of the wave functions, but leaves its local density in the bulk unchanged. Below a rescaled number of atoms $\tilde{N}_{\mathrm{cr}} \approx 18.65$ the droplet is unstable due to the kinetic energy contribution in Eq. (4.11). Slightly above the critical number of atoms, it is just meta-stable

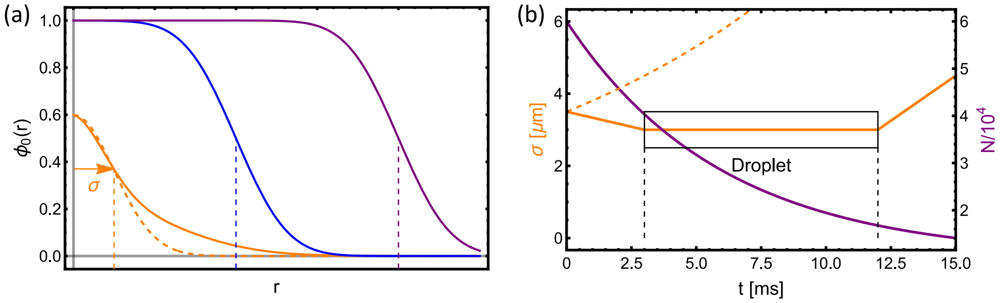

Figure 4.3: (a) Sketch of the wave function $\phi_0(r)$ of the mixture condensate droplet for different numbers of particles based on the numerical evaluation of the extended Gross-Pitaevskii Eq. (4.11) in Ref. [44]. In orange, the wave function of a droplet that is metastable barely above the critical number of particles is sketched. The central part of its wave function is well approximated by a Gaussian curve in dashed orange. Hence the droplet size, indicated by the vertical dashed line, can be evaluated by a Gaussian fit $\propto e^{-r^2/\sigma^2}$ from the fit parameter σ [58]. Once the number of particles is large enough for the droplet to be stable, the addition of particles creates a flat top, shown as the blue wave function. Further addition of particles creates a larger droplet, shown in purple, without changing the bulk density. On the right (b) the features observed in the experiment are sketched, see Refs. [58,59]. If the parameters can stabilize a droplet, the prepared atomic condensate maintains its size σ over time t. In the experiment, at some time t effects like three-body losses put an end to the stability of the droplet, from when on its size σ grows [58,59]. For comparison, the results for a stable Bose gas are shown in an orange dashed curve. It expands immediately after the preparation of the experiment $t = 0$ [58,59]. In purple, we sketch the evolution of the number of particles N. In the mean-field attractive parameter regime, the number of atoms decays due to three-body recombination until it falls below the critical minimum number of atoms for the droplet, which here is about 10^4 based on Ref. [58].

and only truly stable at $\tilde{N} > 22.55$ [44].

The excitation branches of the mixture condensate are obtained for identical mass $m_1 = m_2 = m$ by the transformation $\hat{\psi}_c = (\sqrt{n_1}\hat{\psi}_1 + \sqrt{n_2}\hat{\psi}_2)/\sqrt{n_0}$ and $\hat{\psi}_d = (\sqrt{n_2}\hat{\psi}_1 - \sqrt{n_1}\hat{\psi}_2)/\sqrt{n_0}$ [170]. This produces the lower condensate branch $\langle\hat{\psi}_c\rangle = \sqrt{n_0}$ and the upper spin branch $\langle\hat{\psi}_d\rangle = 0$. It is deduced that the leading quantum correction is the LHY energy of the upper branch [171]. The excitation of the lower branch with the collapsing mean-field is renormalized by the one-loop self-energy of the Beliaev coupling to the upper branch [170]. The Beliaev damping through the upper branch then cures the instability in the condensate branch [170, 171]. An alternative route to a consistent theory for the droplet phase is that of bosonic pairing as applied in Ref. [172, 173], a common technique in fermionic BEC-BCS theory as discussed in these references.

The droplets of Bose-Bose mixtures were experimentally verified in Refs. [58,59,174]. In the experiment of Ref. [58] a mixture of ^{39}K is prepared in the two hyperfine states $|F, m_F\rangle = |1, -1\rangle$ and $|1, 0\rangle$. The Feshbach resonance tunes the intraspecies interaction of the state $|1, 0\rangle$, which in turn changes the parameter δU. After the preparation of the atomic cloud in a red-detuned radial optical dipole trap and a blue-detuned optical lattice in the vertical z direction, the radial trap is opened and in situ images are taken at times t. Such an experimental protocol is designed around the key property of a droplet to be a self-confined quantum liquid [44]. The imaged distribution is fitted by a Gaussian e^{-r^2/σ^2} to extract its size from the Gaussian $1/e$ width σ. This distinguishes the droplet state from that of a gas $\delta U > 0$ which expands as shown in figure 4.3. Reference [59] uses a very similar approach, where they prepare the ^{39}K mixture in a trap of three red-detuned laser beams, creating a crossed dipole trap. In addition, they use a modulated beam to create an effective gradient that compensates for gravity. The picture of a quantum liquid that maintains its average size σ without any additional confinement is verified, as shown in figure 4.3. Once it has lost too many atoms $N < N_{\text{cr}}$

due to three-body losses, the droplet is not a stable or even meta-stable state and turns into a Bose gas [58, 59].

4.2.2 Dipolar Bose gas

Although their first theoretical prediction was in Bose-Bose mixtures, dilute quantum droplets were first observed in dipolar gases [45]. Using an atomic species with a significant magnetic dipole moment μ_m creates an atomic system in which the atoms interact not only via the contact interaction $U(\boldsymbol{r}, \boldsymbol{r}') = 4\pi a_s \delta^{(3)}(\boldsymbol{r} - \boldsymbol{r}')/m$ but also via the long-range dipole-dipole interaction [167, 168]

$$V_{\mathrm{dd}}(\boldsymbol{r} - \boldsymbol{r}') = \frac{\mu_0 \mu_m^2}{4\pi} \frac{1 - 3\cos^2(\vartheta)}{|\boldsymbol{r} - \boldsymbol{r}'|^3} \,. \tag{4.12}$$

Here ϑ is the angle between the chosen polarization direction z and the relative position of the dipoles $\boldsymbol{r} - \boldsymbol{r}'$. The Gross-Pitaevskii equation of the mean-field wave function $\psi(\boldsymbol{r}, t)$ in the dipolar system is

$$i\partial_t \psi = \left[-\frac{\nabla^2}{2m} + V_{\mathrm{ext}}(\boldsymbol{r}) + U|\psi|^2 + \int d^3\boldsymbol{r}' \Big\{ V_{\mathrm{dd}}(\boldsymbol{r} - \boldsymbol{r}') |\psi(\boldsymbol{r}', t)|^2 \Big\} \right] \psi \,. \tag{4.13}$$

The balance between the contact interaction with the scattering length a_s and the dipolar interaction is expressed by the relation $\epsilon_{\mathrm{dd}} = a_{\mathrm{dd}}/a_s = m\mu_0\mu_m^2/(12\pi a_s)$, which assigns an effective scattering length a_{dd} to the dipolar interaction [49]. If the attractive dipolar interaction dominates the contact repulsion $\epsilon_{\mathrm{dd}} > 1$ the mean-field is unstable [167, 168, 175]. Bogoliubov theory for this weakly interacting system reveals the quantum correction [47–49]

$$E_{\mathrm{qf}} = V \frac{256\sqrt{\pi}}{15m} (a_s n)^{\frac{5}{2}} \mathcal{Q}_5(\epsilon_{\mathrm{dd}}) \,, \tag{4.14}$$

where the nonelementary function

$$\mathcal{Q}_5(\epsilon_{\mathrm{dd}}) = \frac{1}{2} \int_0^{\pi} d\vartheta \left\{ \sin(\vartheta) \left[1 + \epsilon_{\mathrm{dd}} \left(3\cos^2(\vartheta) - 1 \right) \right]^{\frac{5}{2}} \right\} \,, \tag{4.15}$$

provides the average angular contribution of the dipolar interaction with ϵ_{dd} [49]. Similar to the LHY correction in the mixture case, the dipolar LHY correction Eq. (4.14) is dominated by hard modes [175]. Therefore it can provide a stabilizing mechanism against the unstable mean-field associated with unstable soft modes, i.e. the instability of the roton.

To obtain the extended Gross-Pitaevskii equation, the term $|\psi|^3$ is added in the local density approximation with the appropriate prefactor from Eq. (4.14) to Eq. (4.13). Again, this is possible because the LHY correction Eq. (4.14) is dominated by wavelengths much smaller than the size of the atomic system. The solution of this extended Gross-Pitaevskii equation shows that the dipolar quantum correction E_{qf}, Eq. (4.14), indeed compensates for the collapsing mean-field and a droplet density distribution is formed along the axis of polarization z [167, 168, 175].

Remarkably, the long-range dipolar interaction V_{dd}, Eq. (4.12), yields Bogoliubov excitations with a roton dispersion similar to that of liquid helium [50]. Albeit, due to the anisotropy of the interaction, the roton is exactly in the magnetization direction where the potential is attractive. The dipolar roton formation was measured in the experiment with highly magnetic erbium atoms in Ref. [52, 53]. Because the dispersion relation of the superfluid forms a potentially soft roton from its interaction characteristics, density modulation as in a classical solid should be achievable. Such a system combining superfluid and solid properties called a supersolid, was first proposed more than 50 years ago [42]. Helium-4, the only known bosonic quantum liquid at the time, with its roton dispersion already known from neutron scattering experiments, was the subject of early attempts to create a supersolid [176,177]. However, efforts with helium have not yet been successful [43,178]. To create a supersolid from a quantum liquid, one has to create an array of droplets in which the droplets are coherent with each other. It was shown that in dipolar gases there exists a narrow parameter regime where the conditions are fulfilled when three groups realized the dipolar supersolid in experiment [54–56]. The setups in Refs. [54,55] used ^{162}Dy atoms, strongly exploiting the Feshbach resonance of the atoms to reach the required interaction parameter range at the cost of increased three-body losses [176,177]. The third experiment Ref. [56] achieved with one of their two choices of atomic species ^{164}Dy supersolids that existed as long as 150 ms thanks to the dominant dipolar interactions compared to the weak contact interaction in ^{164}Dy [176,177]. Curiously, a dipolar superfluid can also be heated to a supersolid phase [179].

Throughout this work, we have explored the quantum fluctuations in the cavity BEC setup associated with a roton mode in the effective atom-only picture. The emergence of droplets by a long-range interaction engineered in a cavity has been studied in the extended Bose-Hubbard model created by confining the BEC in an external optical lattice, see section 2.3.9. Initially, the energetic competition of an alternating long-range interaction with the entropy of the possible states at finite temperature was considered [180]. Later, quantum Monte Carlo calculations were performed for the extended Bose Hubbard model, where the long-range interaction interplays with the on-site repulsion [181]. Also, the mean-field emergence of a single droplet and the mean-field supersolid with phonon-like excitations have been studied for ring cavities, where multimode cavity physics is generated with interaction ranges such that the rotons extend over multiple modes in reciprocal space [182]. Here we show that a generic long-range interaction such as that induced by the cavity can compete with the atomic contact interaction to give rise to quantum droplets. We explore this mechanism at length in the example of the specific long-range interaction induced by a single-mode cavity but also survey other forms of interactions that can be engineered in cavity BEC setups.

4.3 – Generic model

In section 2.3.8 the long-range density-density interaction induced on the atoms by the scattering of photons between the pump and the cavity was reviewed. Its interaction potential in the atom-only Hamiltonian Eq. (2.68) can be abstracted as the effective interaction parameter I and a dimensionless periodic potential $v(\boldsymbol{r},\boldsymbol{r}')$. In the example of the Hamiltonian Eq. (2.68) it would be $I = 2\Delta_C g_0^2 h_0^2/([\Delta_C^2+\kappa^2]\Delta_A^2)$ and $v(\boldsymbol{r},\boldsymbol{r}') = \cos(kx)\cos(ky)\cos(kx')\cos(ky')$. In general, we assign to the periodic signature that it is real, symmetric in its arguments $v(\boldsymbol{r}',\boldsymbol{r}) = v(\boldsymbol{r},\boldsymbol{r}')$, even $v(-\boldsymbol{r},-\boldsymbol{r}') = v(\boldsymbol{r},\boldsymbol{r}')$, and bounded $|v(\boldsymbol{r},\boldsymbol{r}')| \leq 1$. We explicitly point out that in general, we do not have translational invariance to discuss interactions mediated by dissipative degrees of freedom. These do not necessarily conserve momentum, and the cavity-induced interaction Eq. (2.68) is indeed an example of this. The interaction described by the periodic potential $v(\boldsymbol{r},\boldsymbol{r}')$ would be infinite-range. For our generic model, we add a real dimensionless envelope $f_{\boldsymbol{\xi}}(\boldsymbol{r},\boldsymbol{r}')$ of widths $\boldsymbol{\xi}$ to the long-range interaction potential. We give this function the properties that it is argument symmetric $f_{\boldsymbol{\xi}}(\boldsymbol{r}',\boldsymbol{r}) = f_{\boldsymbol{\xi}}(\boldsymbol{r},\boldsymbol{r}')$, even $f_{\boldsymbol{\xi}}(-\boldsymbol{r},-\boldsymbol{r}') = f_{\boldsymbol{\xi}}(\boldsymbol{r},\boldsymbol{r}')$, and that it has its maximum value 1 at the origin of the coordinate system $|f_{\boldsymbol{\xi}}(\boldsymbol{r},\boldsymbol{r}')| \leq f_{\boldsymbol{\xi}}(\boldsymbol{0},\boldsymbol{0}) = 1$ with a well-defined limit to the infinite-range case $\lim_{\boldsymbol{\xi}\to\infty} f_{\boldsymbol{\xi}}(\boldsymbol{r},\boldsymbol{r}') = 1$. The resulting generic long-range interaction potential

$$V_C(\boldsymbol{r},\boldsymbol{r}') = I v(\boldsymbol{r},\boldsymbol{r}') f_{\boldsymbol{\xi}}(\boldsymbol{r},\boldsymbol{r}')\,, \tag{4.16}$$

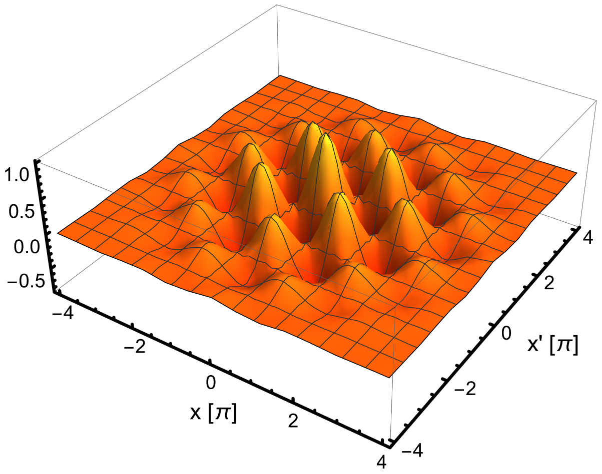

Figure 4.4: Sketch of the cavity-induced long-rang interaction potential in one dimension as $V_C(x,x') = \cos(x)\cos(x')e^{-x^2/50}e^{-x'^2/50}$.

shares therefore substantial similarities with a stationary wave packet. This also sticks out in its visualization shown in figure 4.4. We discuss below how the envelope in the interaction $f_{\boldsymbol{\xi}}(\boldsymbol{r},\boldsymbol{r}')$ actually arises naturally in the single-mode cavity but has been discarded until now.

The generic field Hamiltonian of a d-dimensional system, which we study in this section, is

$$\begin{aligned}\hat{H} = &\int_V d^d\boldsymbol{r} \left\{ \hat{\psi}^\dagger(\boldsymbol{r}) \left[-\frac{\nabla^2}{2m} + \frac{U}{2}\hat{\psi}^\dagger(\boldsymbol{r})\hat{\psi}(\boldsymbol{r}) \right] \hat{\psi}(\boldsymbol{r}) \right\} \\ &+ \frac{1}{2}\int_V d^d\boldsymbol{r} \int_V d^d\boldsymbol{r}' \left\{ \hat{\psi}^\dagger(\boldsymbol{r})\hat{\psi}(\boldsymbol{r}) V_C(\boldsymbol{r},\boldsymbol{r}') \hat{\psi}^\dagger(\boldsymbol{r}')\hat{\psi}(\boldsymbol{r}') \right\}, \end{aligned} \tag{4.17}$$

for the N atoms of mass m and their contact interaction strength U.

4.3.1 Transformation to momentum space

As a periodic function, we can express $v(\boldsymbol{r},\boldsymbol{r}')$ by its Fourier series

$$v(\boldsymbol{r},\boldsymbol{r}') = \sum_{\boldsymbol{k},\boldsymbol{k}'} e^{i\boldsymbol{k}\boldsymbol{r}} e^{i\boldsymbol{k}'\boldsymbol{r}'} v_{\boldsymbol{k},\boldsymbol{k}'} \,. \tag{4.18}$$

The symmetries that we have given to $v(\boldsymbol{r},\boldsymbol{r})$ result in real Fourier coefficients $v_{\boldsymbol{k},\boldsymbol{k}'}$ with

$$v_{\boldsymbol{k},\boldsymbol{k}'} = v_{\boldsymbol{k}',\boldsymbol{k}} = v_{-\boldsymbol{k},-\boldsymbol{k}'} \,. \tag{4.19}$$

We assume periodic boundary conditions, so the atomic field operators $\hat{\psi}^{(\dagger)}(\boldsymbol{r})$ can be expanded in their respective Fourier series as well resulting in the expression

$$\hat{\psi}(\boldsymbol{r}) = \frac{1}{\sqrt{V}} \sum_{\boldsymbol{p}} e^{i\boldsymbol{p}\boldsymbol{r}} \hat{\psi}_{\boldsymbol{p}} \,. \tag{4.20}$$

For our d-dimensional system of volume $V = \prod_{\nu=1}^{d} L_\nu$ the momenta have the discrete values $p_\nu = 2\pi j_\nu / L_\nu$ with the integers $j_\nu \in \mathbb{Z}$. We assume that the periods of the periodic signature $v(\boldsymbol{r},\boldsymbol{r}')$ are integer fractions of the system extensions, i.e. L_ν / l_ν for $l_\nu \in \mathbb{Z} \setminus \{0\}$. Hence the set of wave vectors $\boldsymbol{k} \in \mathcal{K}_C$ is a proper sublattice of the atomic momenta set because of the commensurability of the respective periods. The Fourier coefficients for $v(\boldsymbol{r},\boldsymbol{r}')$ can be expressed as

$$v_{\boldsymbol{k},\boldsymbol{k}'} = \int_V \frac{d^d\boldsymbol{r}}{V}\int_V \frac{d^d\boldsymbol{r}'}{V}\left\{e^{-i\boldsymbol{k}\boldsymbol{r}}e^{-i\boldsymbol{k}'\boldsymbol{r}'}v(\boldsymbol{r},\boldsymbol{r}')\right\}\,, \tag{4.21}$$

with $k_\nu = 2\pi j_{k,\nu}l_\nu/L_\nu$ and $k'_\nu = 2\pi j'_{k,\nu}l_\nu/L_\nu$.

In the infinite-range limit of the envelope $f_{\boldsymbol{\xi}\to\infty}(\boldsymbol{r},\boldsymbol{r}') \to 1$ the second line in Eq. (4.17) describes an infinite-range interaction between the atoms with a periodic potential $v(\boldsymbol{r},\boldsymbol{r}')$. Using the Fourier expansions Eqs. (4.18) and (4.20) we find with the Kronecker delta

$$\int_V \frac{d^d\boldsymbol{r}}{V}\left\{e^{-i(\boldsymbol{p}_1-\boldsymbol{p}_2-\boldsymbol{k})\boldsymbol{r}}\right\} = \delta^{(d)}_{\boldsymbol{p}_1-\boldsymbol{p}_2-\boldsymbol{k},\boldsymbol{0}}\,, \tag{4.22}$$

that such an infinite-range interaction selects distinct momenta $\boldsymbol{p}$ from the field operators $\hat{\psi}^{(\dagger)}(\boldsymbol{r})$ with its wave vectors $\boldsymbol{k}$. More precisely, each wave vector $\boldsymbol{k}$ of $v(\boldsymbol{r},\boldsymbol{r}')$ determines commensurable sets $\{(\boldsymbol{p}_1,\boldsymbol{p}_2),(\boldsymbol{p}'_1,\boldsymbol{p}'_2)\}$ of atomic momenta $\boldsymbol{p}$ under the Kronecker delta Eq. (4.22). Trivially, sets like $\{(\boldsymbol{k},\boldsymbol{0}),(\boldsymbol{k}',\boldsymbol{0})\}$ are elements of these combinations of commensurable momenta. Consequently, a subset of the atomic momenta $\boldsymbol{p}$ coincides with the wave vectors $\boldsymbol{k}$ and this subset is denoted as $\mathcal{K}_\mathrm{C}$. The Fourier coefficients $v_{\boldsymbol{k},\boldsymbol{k}'}$ encode the symmetries of the periodic potential $v(\boldsymbol{r},\boldsymbol{r}')$ and thus control which combinations of $(\boldsymbol{p}_1,\boldsymbol{p}_2)$ with $(\boldsymbol{p}'_1,\boldsymbol{p}'_2)$ are possible under the respective long-range interaction. To give an example: If $v(\boldsymbol{r},\boldsymbol{r}')$ is translation invariant, then $v_{\boldsymbol{k},\boldsymbol{k}'}$ is non-zero only if $\boldsymbol{k}' = -\boldsymbol{k}$. Consequently, the selected momentum sets must satisfy $\delta^{(d)}_{\tilde{\boldsymbol{p}},0}$ with $\tilde{\boldsymbol{p}} = \boldsymbol{p}_1+\boldsymbol{p}_2-\boldsymbol{p}'_1-\boldsymbol{p}'_2$ in addition to the Kronecker delta given in Eq. (4.22).

If we relax the infinite-range limit so that the envelope is a nontrivial part of the integrand in Eq. (4.17), the long-range interaction will in principle couple to atomic momenta other than those selected by the infinite-range interaction. Crucially, though, these selected momenta will always be those modes to which the long-range interaction $V_C(\boldsymbol{r},\boldsymbol{r}')$ couples most strongly. Therefore, the atomic momenta that are elements of $\mathcal{K}_C$ are maximally coupled by the long-range interaction. Moreso, if the long-range interaction leads to the emergence of rotons as we will find below it is energetically favorable for the system to satisfy the assumption that $\mathcal{K}_C$ is a proper sublattice of the discrete set of atomic momenta because of the maximized coupling.

We now anticipate what is required to transform the long-range interaction term of the Hamiltonian Eq. (4.17) into momentum space. We find that we have to solve integrals related to the Fourier coefficients of the envelope function

$$\tilde{f}_{\boldsymbol{\xi}}(\boldsymbol{p},\boldsymbol{p}') = \int_V \frac{d^d\boldsymbol{r}}{V}\int_V \frac{d^d\boldsymbol{r}'}{V}\left\{e^{-i\boldsymbol{p}\boldsymbol{r}}e^{-i\boldsymbol{p}'\boldsymbol{r}'}f_{\boldsymbol{\xi}}(\boldsymbol{r},\boldsymbol{r}')\right\}\,. \tag{4.23}$$

We choose to deal with envelopes that vary slowly compared to the complex exponentials $e^{i\boldsymbol{p}\boldsymbol{r}}$ for $\boldsymbol{p} \neq 0$. The integral Eq. (4.23) can thus be approximated by the spatial average of the envelope. In the volume V, the spatial average of the envelope function is precisely the $\boldsymbol{p} = \boldsymbol{p}' = \boldsymbol{0}$ coefficient $\tilde{f}_{\boldsymbol{\xi}}(\boldsymbol{0},\boldsymbol{0})$, so we get

$$\tilde{f}_{\boldsymbol{\xi}}(\boldsymbol{p},\boldsymbol{p}') \approx \tilde{f}_{\boldsymbol{\xi}}(\boldsymbol{0},\boldsymbol{0})\int_V \frac{d^d\boldsymbol{r}}{V}\int_V \frac{d^d\boldsymbol{r}'}{V}\left\{e^{-i\boldsymbol{p}\boldsymbol{r}}e^{-i\boldsymbol{p}'\boldsymbol{r}'}\right\} = \delta^{(d)}_{\boldsymbol{p},\boldsymbol{0}}\delta^{(d)}_{\boldsymbol{p}',\boldsymbol{0}}\tilde{f}_{\boldsymbol{\xi}}(\boldsymbol{0},\boldsymbol{0})\,. \tag{4.24}$$

Consequently, for an envelope that varies sufficiently slowly on the scale of the atomic system, the only relevant property is $\tilde{f}_{\boldsymbol{\xi}}(\boldsymbol{0},\boldsymbol{0})$ and the limit $\lim_{\boldsymbol{\xi}\to\infty} f_{\boldsymbol{\xi}}(\boldsymbol{r},\boldsymbol{r}') = 1$ to the infinite-range case directly implies the textbook relation $\lim_{\boldsymbol{\xi}\to\infty}\tilde{f}_{\boldsymbol{\xi}}(\boldsymbol{p},\boldsymbol{p}') = \delta^{(d)}_{\boldsymbol{p},\boldsymbol{0}}\delta^{(d)}_{\boldsymbol{p}',\boldsymbol{0}}$. The approximation Eq. (4.24) is the key technical result that we use in the following analysis and that allows us to perform it analytically.

For an extended discussion, it is useful to express Eq. (4.23) as a convolution

$$\begin{aligned}\tilde{f}_{\boldsymbol{\xi}}(\boldsymbol{p},\boldsymbol{p}') &= \left\{\bar{f}_{\boldsymbol{\xi}} * \bar{g}_V\right\}(\boldsymbol{p},\boldsymbol{p}') \\ &= \int_{\mathbb{R}^d} d^d\boldsymbol{q} \int_{\mathbb{R}^d} d^d\boldsymbol{q}' \left\{ \bar{f}_{\boldsymbol{\xi}}(\boldsymbol{q},\boldsymbol{q}') \prod_{\nu=1}^{d} \frac{\sin([p_\nu - q_\nu]L_\nu/2)}{[p_\nu - q_\nu]L_\nu/2} \frac{\sin([p'_\nu - q'_\nu]L_\nu/2)}{[p'_\nu - q'_\nu]L_\nu/2} \right\} , \qquad (4.25)\end{aligned}$$

of the Fourier transformation of the envelope

$$\bar{f}_{\boldsymbol{\xi}}(\boldsymbol{q},\boldsymbol{q}') = \int_{\mathbb{R}^d} \frac{d^d\boldsymbol{r}}{(2\pi)^d} \int_{\mathbb{R}^d} \frac{d^d\boldsymbol{r}'}{(2\pi)^d} \left\{ e^{-i\boldsymbol{q}\boldsymbol{r}} e^{-i\boldsymbol{q}'\boldsymbol{r}'} f_{\boldsymbol{\xi}}(\boldsymbol{r},\boldsymbol{r}') \right\} , \qquad (4.26)$$

and the product of the sampling function of the spatial system extension $\mathrm{sinc}(q_\nu L_\nu/2)$ which is the Fourier transformation of the Heaviside function. Our assumption of a slowly varying envelope can be elaborated by noting that the Fourier transform $\bar{f}_{\boldsymbol{\xi}}(\boldsymbol{q},\boldsymbol{q}')$ is narrow in $(\boldsymbol{q},\boldsymbol{q}')$ space. More quantitatively, we want it to be exponentially small for $|q_\nu|, |q'_\nu| \geq 2\pi/L_\nu$ in all $\nu = 1,\ldots,d$. Then we can expand the denominators, where $p_\nu, p'_\nu \neq 0$ in Eq. (4.25), as a harmonic series to obtain

$$\begin{aligned}\tilde{f}(\boldsymbol{p},\boldsymbol{p}') = \int_{\mathbb{R}^d} d^d\boldsymbol{q} \int_{\mathbb{R}^d} d^d\boldsymbol{q}' \Bigg\{ \bar{f}_{\boldsymbol{\xi}}(\boldsymbol{q},\boldsymbol{q}') \prod_{\nu=1}^{d} (-1)^{j_\nu + j'_\nu} \frac{\sin(q_\nu L_\nu/2)}{\pi j_\nu} \left[1 + \frac{q_\nu L_\nu}{2\pi j_\nu} + \mathcal{O}\left(\left(\frac{q_\nu L_\nu}{2\pi j_\nu} \right)^2 \right) \right] \\ \times \frac{\sin(q'_\nu L_\nu/2)}{\pi j'_\nu} \left[1 + \frac{q'_\nu L_\nu}{2\pi j'_\nu} + \mathcal{O}\left(\left(\frac{q'_\nu L_\nu}{2\pi j'_\nu} \right)^2 \right) \right] \Bigg\} , \qquad (4.27)\end{aligned}$$

where we use that the momenta $p_\nu = 2\pi j_\nu/L_\nu$ in the finite system only take on discrete values with $j_\nu \in \mathbb{Z} \setminus \{0\}$. For narrow $\bar{f}_{\boldsymbol{\xi}}(\boldsymbol{q},\boldsymbol{q}')$, we effectively perform the integration of the q-integrals only in the intervals $\mathcal{P}_\nu = (-2\pi/L_\nu, +2\pi/L_\nu)$. We can then compare the integrands of the spatial average $\tilde{f}_{\boldsymbol{\xi}}(\boldsymbol{0},\boldsymbol{0})$ of Eq. (4.25) with the highest order in Eq. (4.27) to see why $|\tilde{f}_{\boldsymbol{\xi}}(\boldsymbol{p},\boldsymbol{p}')|/\tilde{f}_{\boldsymbol{\xi}}(\boldsymbol{0},\boldsymbol{0}) \ll 1$ so that Eq. (4.24) holds. The function $\mathrm{sinc}(q_\nu L_\nu/2)$ in the spatial average integral is greater everywhere than $\sin(q_\nu L_\nu/2)/\pi$ on the interval $q_\nu \in \mathcal{P}_\nu$, as visualized in figure 4.5. Since $\sin(q_\nu L_\nu/2)/\pi$ is the leading order contribution of Eq. (4.27), we investigate the ratio of this term to the sinc function given by $q_\nu L_\nu/2\pi$ on the interval $\mathcal{P}_\nu = (-2\pi/L_\nu, +2\pi/L_\nu)$. The modulus of the ratio is less than 1 everywhere in the interval, but crucially it is much less than one in the center $q_\nu \approx 0$ and approaches 1 only near the edges of the interval, as seen in figure 4.5. If the interaction potential Eq. (4.16) is constructed faithfully so that all oscillatory behavior is in the periodic signature $v(\boldsymbol{r},\boldsymbol{r}')$, such that $f_{\boldsymbol{\xi}}(\boldsymbol{r},\boldsymbol{r}')$ is a smooth slowly varying envelope, we can combine this to estimate the integrands and thus the ratio of the integrals. Because we demand that $\bar{f}_{\boldsymbol{\xi}}(\boldsymbol{q},\boldsymbol{q}')$ is exponentially small for $|q_\nu|, |q'_\nu| \geq 2\pi/L_\nu$ relative to $\bar{f}_{\boldsymbol{\xi}}(\boldsymbol{0},\boldsymbol{0})$ and slowly varies at the edges of the interval, $\mathcal{P}_\nu = (-2\pi/L_\nu, +2\pi/L_\nu)$, where the integrands are of similar size, the outer region of $\mathcal{P}_\nu$ contributes very little to each integral. On the other hand, we notice that in the central region, the integrand of $\boldsymbol{p} \neq 0$ is much smaller than that for $\boldsymbol{p} = \boldsymbol{0}$ because the leading term of the ratio behaves like $|q|/\pi$. Therefore, since the integrand of $\tilde{f}_{\boldsymbol{\xi}}(\boldsymbol{0},\boldsymbol{0})$ is much larger than that for $\boldsymbol{p} \neq \boldsymbol{0}$ in the region that contributes significantly to the integral $\mathcal{P}_\nu$, we conclude that $\tilde{f}_{\boldsymbol{\xi}}(\boldsymbol{0},\boldsymbol{0})$ itself is much greater than $\tilde{f}_{\boldsymbol{\xi}}(\boldsymbol{p},\boldsymbol{p}')$ for $\boldsymbol{p} \neq \boldsymbol{0}$. In other words, Eq. (4.24) holds for a generic envelope $f_{\boldsymbol{\xi}}(\boldsymbol{r},\boldsymbol{r}')$ with the properties introduced at the beginning of this section. Such an envelope has a Fourier transform that is narrow and therefore $\bar{f}_{\boldsymbol{\xi}}(\boldsymbol{q},\boldsymbol{q}')$ acts in the lowest order as a multidimensional delta distribution in the integral of Eq. (4.25). Note that it acts like a delta distribution but is not one. It is more akin to a narrow function out of a sequence that converges to the delta distribution in the distributional sense. The effective distribution takes into account the symmetries of the specific envelope choice $f_{\boldsymbol{\xi}}(\boldsymbol{r},\boldsymbol{r}')$. Applying this picture of the delta distribution to the Fourier analysis Eq. (4.25) yields a d-dimensional function similar to a $\mathrm{sinc}(\boldsymbol{p},\boldsymbol{p}')$ function that

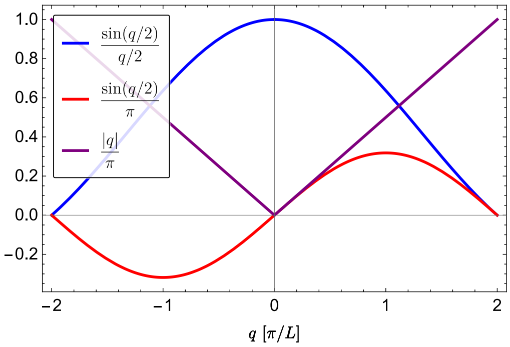

Figure 4.5: Estimates of the integrands of the convolution Eqs. (4.25) and (4.27). The integrand for the spatial average $(\boldsymbol{p}, \boldsymbol{p}') = (\mathbf{0}, \mathbf{0})$ based on Eq. (4.25) is represented by $\sin(q/2)/(q/2)$ (blue). The integrand for $(\boldsymbol{p}, \boldsymbol{p}') \neq (\mathbf{0}, \mathbf{0})$ is embodied by the zeroth order of the expansion of the harmonic series in Eq. (4.27), i.e. $\sin(q/2)/\pi$ (red). The modulus of the fraction of both, i.e. red divided by blue $|q|/\pi$, is displayed in purple.

is well localized around the center $(\boldsymbol{p}, \boldsymbol{p}') = (\mathbf{0}, \mathbf{0})$. This property of localization around the center implies Eq. (4.24).

A more rigorous mathematical formulation of this notion is likely possible but is beyond the scope of this thesis, where we verify Eq. (4.24) anyway for the specific envelopes we study in sections 4.4 and 4.5.

4.3.2 Mean field

We study the generic system described by the Hamiltonian Eq. (4.17) in its homogeneous mean-field phase, where the expectation value of the field operators is the square root of the particle density $n = N/V$, i.e. $\langle \hat{\psi}^{(\dagger)}(\boldsymbol{r}) \rangle = \sqrt{n}$. In the following, we look at the quantum fluctuations around it in a Bogoliubov theory. The expansion of the atomic field operator with the fluctuations $\hat{\phi}(\boldsymbol{r})$ is

$$\hat{\psi}(\boldsymbol{r}) = \sqrt{n} + \hat{\phi}(\boldsymbol{r}) = \sqrt{n} + \frac{1}{\sqrt{V}} \sum_{\boldsymbol{p}}{}' e^{i\boldsymbol{p}\boldsymbol{r}} \hat{\phi}_{\boldsymbol{p}} \,, \tag{4.28}$$

where we have applied the Fourier series expansion of the fluctuations in the second identity. The primed sum indicates again the omission of $\boldsymbol{p} = \mathbf{0}$.

With Eq. (4.28) the mean-field energy of the Hamiltonian Eq. (4.17) is promptly found in the zeroth order of the quantum fluctuations in the form

$$\begin{aligned} E_{\mathrm{mf}} &= \frac{Un^2}{2} \int_V d^d\boldsymbol{r} \Big\{ 1 \Big\} + \frac{In^2}{2} \sum_{\boldsymbol{k},\boldsymbol{k}'} \int_V d^d\boldsymbol{r} \int_V d^d\boldsymbol{r}' \Big\{ v_{\boldsymbol{k},\boldsymbol{k}'} e^{i\boldsymbol{k}\boldsymbol{r}} e^{i\boldsymbol{k}'\boldsymbol{r}'} f_{\boldsymbol{\xi}}(\boldsymbol{r}, \boldsymbol{r}') \Big\} \\ &= \frac{UN^2}{2V} + \frac{IN^2}{2} v_{\mathbf{0},\mathbf{0}} \tilde{f}_{\boldsymbol{\xi}}(\mathbf{0}, \mathbf{0}) \,, \end{aligned} \tag{4.29a}$$

$$E_{\mathrm{mf,U}} = \frac{UN^2}{2V} \,, \qquad E_{\mathrm{mf,C}} = \frac{IN^2}{2} v_{\mathbf{0},\mathbf{0}} \tilde{f}_{\boldsymbol{\xi}}(\mathbf{0}, \mathbf{0}) \,, \tag{4.29b}$$

using Eqs. (4.18) and (4.24). The first term $E_{\mathrm{mf,U}}$ in the mean-field energy is the familiar contribution from s-wave scattering in a homogeneous Bose gas Eq. (2.18). The long-range interaction gives rise to the energy $E_{\mathrm{mf,C}}$, which is finite only if $v_{\mathbf{0},\mathbf{0}} \neq 0$, i.e. the periodic signature has a constant background. We are interested in the quantum fluctuation contribution of this long-range interaction and therefore declare $v_{\mathbf{0},\mathbf{0}} = 0$. This leaves us with systems where $E_{\mathrm{mf,C}} = 0$ the mean-field is unaffected by the long-range interaction V_C. The chemical potential is $\mu_{\mathrm{mf}} = nU$.

4.3.3 First-order quantum fluctuations

To validate the assumption of a homogeneous phase, we check whether the first order in the quantum fluctuations vanishes when the ansatz for the field operator Eq. (4.28) is applied to the Hamiltonian Eq. (4.17). Using Eqs. (4.18), (4.24) and (4.28) we find

$$\begin{aligned}\hat{H}_1 &= I n^{3/2} \int_V d^d\boldsymbol{r} \left\{ \left[\hat{\phi}(\boldsymbol{r}) + \hat{\phi}^\dagger(\boldsymbol{r})\right] \int_V d^d\boldsymbol{r'} \Big\{ v(\boldsymbol{r},\boldsymbol{r'}) f_{\boldsymbol{\xi}}(\boldsymbol{r},\boldsymbol{r'}) \Big\} \right\} \\ &= I N^{3/2} \tilde{f}_{\boldsymbol{\xi}}(\boldsymbol{0},\boldsymbol{0}) \sum_{\boldsymbol{k}\in\mathcal{K}_C} \left(\hat{\phi}_{-\boldsymbol{k}} + \hat{\phi}^\dagger_{\boldsymbol{k}} \right) v_{\boldsymbol{k},\boldsymbol{0}} \,, \end{aligned} \tag{4.30}$$

so we have to require $v_{\boldsymbol{k},\boldsymbol{0}} = 0$, which means we set $\boldsymbol{0} \notin \mathcal{K}_C$. Thus, due to the symmetry Eq. (4.19), $v(\boldsymbol{r},\boldsymbol{r'})$ has no constant background in any of its arguments $(\boldsymbol{r},\boldsymbol{r'})$.

4.3.4 Second-order quantum fluctuations

We now derive the energy correction due to quantum fluctuations in the second order. The second-order quantum fluctuations contribute to the total system the Hamiltonian term

$$\begin{aligned}\hat{H}_2 = \frac{1}{2} {\sum_{\boldsymbol{p}}}' &\left[\frac{\boldsymbol{p}^2}{2m} \left(\hat{\phi}^\dagger_{\boldsymbol{p}} \hat{\phi}_{\boldsymbol{p}} + \hat{\phi}_{-\boldsymbol{p}} \hat{\phi}^\dagger_{-\boldsymbol{p}} \right) + nU \left(\hat{\phi}_{-\boldsymbol{p}} + \hat{\phi}^\dagger_{\boldsymbol{p}} \right) \left(\hat{\phi}_{\boldsymbol{p}} + \hat{\phi}^\dagger_{-\boldsymbol{p}} \right) - \frac{\boldsymbol{p}^2}{2m} - nU \right] \\ &+ \frac{IN}{2} \tilde{f}_{\boldsymbol{\xi}}(\boldsymbol{0},\boldsymbol{0}) {\sum_{\boldsymbol{p},\boldsymbol{p'}}}' \sum_{\boldsymbol{k},\boldsymbol{k'}\in\mathcal{K}_C} \left[\left(\hat{\phi}_{\boldsymbol{p}} \delta^{(d)}_{-\boldsymbol{p},\boldsymbol{k}} + \hat{\phi}^\dagger_{\boldsymbol{p}} \delta^{(d)}_{\boldsymbol{p},\boldsymbol{k}} \right) v_{\boldsymbol{k},\boldsymbol{k'}} \left(\hat{\phi}_{\boldsymbol{p'}} \delta^{(d)}_{-\boldsymbol{p'},\boldsymbol{k'}} + \hat{\phi}^\dagger_{\boldsymbol{p'}} \delta^{(d)}_{\boldsymbol{p'},\boldsymbol{k'}} \right) \right] . \end{aligned} \tag{4.31}$$

The detailed derivation is discussed in the appendix A.7. To proceed, we transform Eq. (4.31) to its representation in the quasi-position operator $\hat{x}_{\boldsymbol{p}}$ and the quasi-momentum operator $\hat{y}_{\boldsymbol{p}}$ [183]

$$\hat{x}_{\boldsymbol{p}} = \sqrt{\frac{m}{\boldsymbol{p}^2}} \left(\hat{\phi}_{\boldsymbol{p}} + \hat{\phi}^\dagger_{-\boldsymbol{p}} \right) , \qquad \hat{y}_{\boldsymbol{p}} = -i \sqrt{\frac{\boldsymbol{p}^2}{4m}} \left(\hat{\phi}_{-\boldsymbol{p}} - \hat{\phi}^\dagger_{\boldsymbol{p}} \right) , \tag{4.32a}$$

$$[\hat{x}_{\boldsymbol{p}}, \hat{y}_{\boldsymbol{p}}] = i \delta^{(d)}_{\boldsymbol{p},\boldsymbol{p'}} \,, \qquad \hat{x}_{-\boldsymbol{p}} = \hat{x}^\dagger_{\boldsymbol{p}} \,, \qquad \hat{y}_{-\boldsymbol{p}} = \hat{y}^\dagger_{\boldsymbol{p}} \,. \tag{4.32b}$$

It turns Eq. (4.31) into

$$\hat{H}_2 = \frac{1}{2} {\sum_{\boldsymbol{p}}}' \left[\hat{y}_{-\boldsymbol{p}} \hat{y}_{\boldsymbol{p}} + \omega^2_{\boldsymbol{p}} \hat{x}_{-\boldsymbol{p}} \hat{x}_{\boldsymbol{p}} - \frac{\boldsymbol{p}^2}{2m} - nU \right] + \frac{IN}{2} \tilde{f}_{\boldsymbol{\xi}}(\boldsymbol{0},\boldsymbol{0}) \sum_{\boldsymbol{k},\boldsymbol{k'}\in\mathcal{K}_C} \left[v_{\boldsymbol{k},-\boldsymbol{k'}} \frac{|\boldsymbol{k}||\boldsymbol{k'}|}{m} \hat{x}_{-\boldsymbol{k}} \hat{x}_{\boldsymbol{k'}} \right] , \tag{4.33}$$

with the Bogoliubov dispersion in the presence of a contact interaction U, Eq. (2.25),

$$\omega_{\boldsymbol{p}} = \sqrt{\frac{\boldsymbol{p}^2}{2m} \left(\frac{\boldsymbol{p}^2}{2m} + 2nU \right)} \,. \tag{4.34}$$

Thus we have already found the eigenfrequencies of the modes $\boldsymbol{p} \notin \mathcal{K}_C$ as Eq. (4.34). We continue with the modes affected by the long-range interaction $\mathcal{K}_C = \{\boldsymbol{k}_1, \ldots, \boldsymbol{k}_{\tilde{d}}\}$ where $\tilde{d} = |\mathcal{K}_C|$ is the number of these modes. In this notation we define $\hat{\vec{x}} = (\hat{x}_1 \cdots \hat{x}_{\tilde{d}})^T$, $\hat{\vec{y}} = (\hat{y}_1 \cdots \hat{y}_{\tilde{d}})^T$, and the $(\tilde{d} \times \tilde{d})$ matrix $\underline{\tilde{v}}$ with the elements $\tilde{v}_{ij} = v_{\boldsymbol{k}_i,-\boldsymbol{k}_j} |\boldsymbol{k}_i||\boldsymbol{k}_j|/m$. We split the Hamiltonian Eq. (4.33) into the modes that are already uncoupled $\boldsymbol{p} \notin \mathcal{K}_C$ and those that couple to the long-range interaction potential

$$\hat{H}_2 = \frac{1}{2} {\sum_{\boldsymbol{p}\notin\mathcal{K}_C}}' \left[\hat{y}^\dagger_{\boldsymbol{p}} \hat{y}_{\boldsymbol{p}} + \omega^2_{\boldsymbol{p}} \hat{x}^\dagger_{\boldsymbol{p}} \hat{x}_{\boldsymbol{p}} - \frac{\boldsymbol{p}^2}{2m} - nU \right] + \frac{1}{2} \left[\hat{\vec{y}}^\dagger \mathbb{I}_{\tilde{d}\times\tilde{d}} \hat{\vec{y}} + \hat{\vec{x}}^\dagger \underline{h} \hat{\vec{x}} - \sum_{\boldsymbol{k}\in\mathcal{K}_C} \left(\frac{\boldsymbol{k}^2}{2m} + nU \right) \right] , \tag{4.35}$$

with the real symmetric matrix

$$\underline{h} = \mathrm{diag}\left(\omega_1^2, \ldots, \omega_{\tilde{d}}^2\right) + IN\tilde{f}_{\boldsymbol{\xi}}(\mathbf{0},\mathbf{0})\underline{\tilde{v}}\,. \tag{4.36}$$

Some remarks about the second square bracket of Eq. (4.35) are in order. The long-range interaction couples exclusively to the quasi-position operators, since $v(\boldsymbol{r},\boldsymbol{r}')$ is even and symmetric Eq. (4.19). That $\underline{h}$ is real and symmetric also follows directly from the properties of the periodic signature $v(\boldsymbol{r},\boldsymbol{r}')$ via Eq. (4.19). Finally, as is evident from Eq. (4.31), the Fourier coefficient of the envelope $\tilde{f}_{\boldsymbol{\xi}}(\mathbf{0},\mathbf{0})$ is a prefactor of the long-range coupling, i.e. it is the same for all long-range coupled modes. Because it carries the dependence on the system extensions L_ν, it can be thought of as a system size dependent modification of the long-range interaction strength I between the momentum modes.
The orthogonal diagonalization of $\underline{h}$ yields $\tilde{d}$ eigenvalues $\Omega_{\boldsymbol{k}}^2$, which are the squares of the eigenfrequencies of the modes $\boldsymbol{k} \in \mathcal{K}_C$ coupled by the long-range interaction V_C. Each eigenfrequency $\Omega_{\boldsymbol{k}} \neq \omega_{\boldsymbol{k}}$ that is changed by V_C compared to the dispersion Eq. (4.34) necessarily carries the dependence on the spatial extension of the system via $\tilde{f}_{\boldsymbol{\xi}}(\mathbf{0},\mathbf{0})$. The familiar expression of the diagonalized Hamiltonian $\hat{H}_2$ in annihilation and creation operators $\hat{\varphi}_{\boldsymbol{p}}^{(\dagger)}$ of its eigenmodes is obtained by the transformation [183]

$$\hat{x}_{\boldsymbol{p}\notin\mathcal{K}_C} = \sqrt{\frac{1}{2\omega_{\boldsymbol{p}}}}\left(\hat{\varphi}_{\boldsymbol{p}} + \hat{\varphi}_{-\boldsymbol{p}}^\dagger\right), \qquad \hat{y}_{\boldsymbol{p}\notin\mathcal{K}_C} = -i\sqrt{\frac{\omega_{\boldsymbol{p}}}{2m}}\left(\hat{\varphi}_{-\boldsymbol{p}} - \hat{\varphi}_{\boldsymbol{p}}^\dagger\right), \tag{4.37a}$$

$$\hat{x}_{\boldsymbol{k}\in\mathcal{K}_C} = \sqrt{\frac{1}{2\Omega_{\boldsymbol{k}}}}\left(\hat{\varphi}_{\boldsymbol{k}} + \hat{\varphi}_{-\boldsymbol{k}}^\dagger\right), \qquad \hat{y}_{\boldsymbol{k}\in\mathcal{K}_C} = -i\sqrt{\frac{\Omega_{\boldsymbol{k}}}{2m}}\left(\hat{\varphi}_{-\boldsymbol{k}} - \hat{\varphi}_{\boldsymbol{k}}^\dagger\right). \tag{4.37b}$$

After this transformation, we integrate out the fluctuations $\hat{\varphi}$ and can easily read off the zero-point energy they leave behind as a quantum fluctuation correction to the ground state energy of the system

$$E_{\mathrm{qf}} = \frac{1}{2}\sum_{\boldsymbol{p}\notin\mathcal{K}_C}{}' \left(\omega_{\boldsymbol{p}} - \frac{\boldsymbol{p}^2}{2m} - nU\right) + \frac{1}{2}\sum_{\boldsymbol{k}\in\mathcal{K}_C}\left(\Omega_{\boldsymbol{k}} - \frac{\boldsymbol{k}^2}{2m} - nU\right). \tag{4.38}$$

Finally, as in the case of the mean-field, the energy correction $E_{\mathrm{qf}} = E_{\mathrm{qf,U}} + E_{\mathrm{qf,C}}$ is separated into the contribution $E_{\mathrm{qf,U}}$ which is exclusively due to the contact interaction and the term which is only present if there is a long-range interaction $E_{\mathrm{qf,C}}$. To do this, we complete the sum in the first term of Eq. (4.38) by extracting the respective summands from the second term and obtain

$$E_{\mathrm{qf,U}} = \frac{1}{2}\sum_{\boldsymbol{p}}{}' \left(\omega_{\boldsymbol{p}} - \frac{\boldsymbol{p}^2}{2m} - nU\right), \qquad E_{\mathrm{qf,C}} = \frac{1}{2}\sum_{\boldsymbol{k}\in\mathcal{K}_C}\left(\Omega_{\boldsymbol{k}} - \omega_{\boldsymbol{k}}\right). \tag{4.39}$$

We evaluate the contact interaction correction $E_{\mathrm{qf,U}}$ in the continuum limit $\sum_{\boldsymbol{p}}{}' \to [V/(2\pi)^{d/2}]\int_{\mathbb{R}^d} d^d\boldsymbol{p}$ with the appropriate renormalization, see discussion in section 2.2.1. This then yields the Lee-Huang-Yang correction Eq. (2.27) [46]. In a weakly interacting dilute Bose gas the quantum correction due to the contact interaction U is small $E_{\mathrm{qf,U}} \ll E_{\mathrm{mf,U}}$ compared to the mean-field contribution from the contact interaction. Thus we neglect this subleading correction and deal only with $E_{\mathrm{mf,U}}$, Eq. (4.29b), and $E_{\mathrm{qf,C}}$, Eq. (4.39). The dependence on the spatial extension of the former is given by $\propto V^{-1}$, while for the latter it is encoded in the spatial average of the envelope $\tilde{f}_{\boldsymbol{\xi}}(\mathbf{0},\mathbf{0})$, which appears in the long-range interacting modes $\Omega_{\boldsymbol{k}}$. Next, we discuss two generic examples of long-range interaction in which we can analytically find the eigenmodes $\Omega_{\boldsymbol{k}}$. We achieve this by imposing an additional symmetry on the long-range interaction $V_C(\boldsymbol{r},\boldsymbol{r}')$.

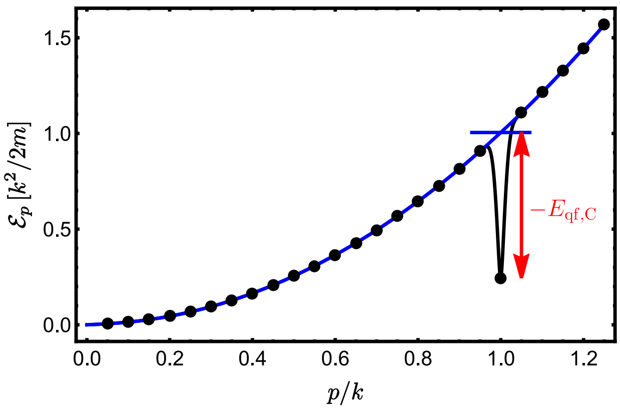

Figure 4.6: Dispersion relation Eq. (4.41) for the simple example of $\mathcal{K}_{\mathrm{C}} = \{-k, +k\}$. The dots mark the discrete modes of the finite system with the distinct roton at $p = k$. The black line indicates the continuum of the discrete modes marked by the dots. The blue curve shows the continuum of the dispersion without the long-range interaction, $I = 0$. The horizontal blue line marks the roton mode value for $I = 0$. Consequently, the difference between the actual roton value and the horizontal blue line given by the red arrow represents the roton contribution to the long-range induced quantum correction $E_{\mathrm{qf,C}}$.

4.3.5 Examples of generic long-range interactions

The first additional symmetry we impose on the interaction is that of momentum conservation. Technically, it must be a translation invariant interaction $V_C(\boldsymbol{r} + \boldsymbol{R}, \boldsymbol{r}' + \boldsymbol{R}) = V_C(\boldsymbol{r}, \boldsymbol{r}')$ for all $\boldsymbol{R} \in \mathbb{R}^d$. The translation invariance of the periodic signature $v(\boldsymbol{r}, \boldsymbol{r}')$ implies that its only non-zero Fourier coefficients in Eq. (4.18) are $v_{-\boldsymbol{k},\boldsymbol{k}}$, so that the matrix $\underline{\tilde{v}}$ in Eq. (4.36) is diagonal. Actually, within the conditions for Eq. (4.24) to hold so that only the spatial average of the envelope $\tilde{f}_{\boldsymbol{\xi}}(\boldsymbol{0}, \boldsymbol{0})$ needs to be considered, we can weaken the criterium of translation invariance of the total interaction V_C. To obtain a momentum-conserving fluctuation Hamiltonian $\hat{H}_2$ it is sufficient that the periodic function $v(\boldsymbol{r}, \boldsymbol{r}')$ is translation invariant. Any term that is not momentum conserving due to the lack of translation invariance of the envelope $f_{\boldsymbol{\xi}}(\boldsymbol{r}, \boldsymbol{r}')$ and thus $V_C(\boldsymbol{r}, \boldsymbol{r}')$ becomes a subleading correction to the momentum conserving terms in $\hat{H}_2$ as long as $v(\boldsymbol{r}, \boldsymbol{r}')$ is translation invariant. Since $\underline{\tilde{v}}$ is diagonal, Eq. (4.35) immediately takes the form

$$\hat{H}_2 = \frac{1}{2} \sum_{\boldsymbol{p}}{}' \left[\hat{y}^{\dagger}_{\boldsymbol{p}} \hat{y}_{\boldsymbol{p}} + \mathcal{E}^2_{\boldsymbol{p}} \hat{x}^{\dagger}_{\boldsymbol{p}} \hat{x}_{\boldsymbol{p}} - \frac{\boldsymbol{p}^2}{2m} - nU \right] , \tag{4.40}$$

with the dispersion including the long-range interaction unveiled to be

$$\mathcal{E}_{\boldsymbol{p}} = \sqrt{\omega^2_{\boldsymbol{p}} + \frac{\boldsymbol{p}^2}{m} I N \tilde{f}_{\boldsymbol{\xi}}(\boldsymbol{0}, \boldsymbol{0}) \sum_{\boldsymbol{k} \in \mathcal{K}_C} \delta^{(d)}_{\boldsymbol{p},\boldsymbol{k}} v_{-\boldsymbol{k},\boldsymbol{k}}} \, . \tag{4.41}$$

The modes altered by the presence of the long-range interaction are therefore $\Omega_{\boldsymbol{k}} = \mathcal{E}_{\boldsymbol{k}}$. For a negative long-range interaction parameter $I < 0$, a roton is created in the dispersion, Eq. (4.41). Figure 4.6 shows such a dispersion for the simplest one-dimensional example $\mathcal{K}_C = \{-k, +k\}$. The quantum fluctuation correction of the long-range interaction with a translation invariant periodic signature $v(\boldsymbol{r}, \boldsymbol{r}')$ is given by Eq. (4.39) to be

$$E^{(\mathrm{ti})}_{\mathrm{qf,C}} = \frac{1}{2} \sum_{\boldsymbol{k} \in \mathcal{K}_C} \left[\sqrt{\omega^2_{\boldsymbol{k}} + \frac{\boldsymbol{k}^2}{m} I N \tilde{f}_{\boldsymbol{\xi}}(\boldsymbol{0}, \boldsymbol{0}) v_{-\boldsymbol{k},\boldsymbol{k}}} - \omega_{\boldsymbol{k}} \right] . \tag{4.42}$$

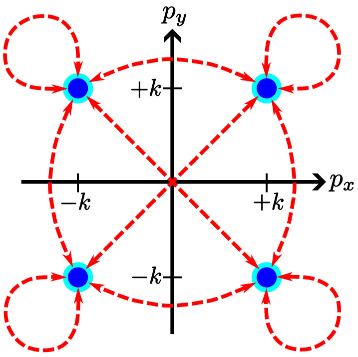

Figure 4.7: Visualization of the four modes in $\mathcal{K}_C = \{(\pm k \ \ \pm k \ \ 0)^T\}$ in the $(p_x \ \ p_y)$ momentum plane. They interact bilinearly all to all via the red arrows. The value of the red arrows is determined by $IN\tilde{f}_{\boldsymbol{\xi}}(\mathbf{0},\mathbf{0})\underline{\tilde{v}}$ of Eq. (4.36). As discussed in the text, all elements of $\tilde{v}$ are equal, so $\underline{\tilde{v}} = \tilde{v}\boldsymbol{k}^2/(m)\underline{J}$, where $\underline{J}$ is the matrix of all elements equal to 1. In the example discussed in the next section 4.4, it is $\tilde{v} = 1/16$.

If the interaction parameter is such that rotons are formed when $I < 0$, then $E^{(\mathrm{ti})}_{\mathrm{qf,C}} < 0$ is negative. A roton is soft, $\mathcal{E}_{\boldsymbol{k}} = 0$, as soon as the critical interaction

$$I^{(\mathrm{ti})}_{\mathrm{cr}}(\boldsymbol{k}) = -\frac{\boldsymbol{k}^2/2m + 2nU}{2Nv_{-\boldsymbol{k},\boldsymbol{k}}\tilde{f}_{\boldsymbol{\xi}}(\mathbf{0},\mathbf{0})}\,, \tag{4.43}$$

is reached. Next, we consider a periodic signature $v(\boldsymbol{r},\boldsymbol{r'})$ that couples modes with the same modulus, i.e., $|\boldsymbol{k}| = |\boldsymbol{k'}|$ for all $\boldsymbol{k},\boldsymbol{k'} \in \mathcal{K}_C$. Furthermore, we add that the Fourier coefficients of $v(\boldsymbol{r},\boldsymbol{r'})$ are equal, so that $\tilde{v}_{ij} = \tilde{v}\boldsymbol{k}^2/m$ for all $\boldsymbol{k}_i,\boldsymbol{k}_j \in \mathcal{K}_C$ and all elements of the interaction matrix $\underline{\tilde{v}}$ are equal. Since the contact dispersion, Eq. (4.34), depends only on $\boldsymbol{k}^2$, we also get $\omega_{\boldsymbol{k}} = \omega_{\boldsymbol{k'}}$ for all $\boldsymbol{k},\boldsymbol{k'} \in \mathcal{K}_C$. Taken together, these are then the properties of the long-range interaction induced by the single-mode cavity, Eq. (2.68), and lead to a coupling between the modes as shown in the figure 4.7. After applying these additional constraints to the matrix $\underline{h}$, Eq. (4.36), the $\tilde{d}$ eigenmodes are easily found analytically with the details in appendix A.7. First, note that $\underline{h} - \omega^2_{\boldsymbol{k}}\mathbb{I}_{\tilde{d}\times\tilde{d}}$ is singular with rank 1, so $(\tilde{d}-1)$ eigenvalues are unaffected by the presence of the long-range interaction. They lie in the contact interaction dispersion $\omega_{\boldsymbol{k}}$, Eq. (4.34). The final eigenvalue is revealed when we realize that $\underline{h} - (\omega^2_{\boldsymbol{k}} + \tilde{d}IN\tilde{f}_{\boldsymbol{\xi}}(\mathbf{0},\mathbf{0})\tilde{v}\boldsymbol{k}^2/m)\mathbb{I}_{\tilde{d}\times\tilde{d}}$ is singular. A long-range interaction with these constraints thus produces a single distinct mode

$$\Omega = \sqrt{\omega^2_{\boldsymbol{k}} + \frac{\boldsymbol{k}^2}{m}IN\tilde{f}_{\boldsymbol{\xi}}(\mathbf{0},\mathbf{0})\tilde{d}\tilde{v}}\,, \tag{4.44}$$

that is roton-like if $I < 0$ and becomes soft at the critical point

$$I_{\mathrm{cr}} = -\frac{\boldsymbol{k}^2/2m + 2nU}{2N\tilde{d}\tilde{v}\tilde{f}_{\boldsymbol{\xi}}(\mathbf{0},\mathbf{0})}\,. \tag{4.45}$$

Consequently, the quantum fluctuation correction from this long-range interaction is the zero-point energy of this single mode

$$E_{\mathrm{qf,C}} = \frac{1}{2}\left(\Omega - \omega_{\boldsymbol{k}}\right)\,. \tag{4.46}$$

If Ω is roton-like as $I < 0$, this energy correction is negative $E_{\mathrm{qf,C}} < 0$.

4.3.6 Discussion

Let us study in more detail how the rotons in Eqs. (4.41) and (4.44) emerge from the long-range interaction in the Hamiltonian, Eq. (4.17). Previously we discussed that the momenta $\boldsymbol{p} = \boldsymbol{k}$ at which a roton is located in the reciprocal space follow the selection from the periodic signature $v(\boldsymbol{r}, \boldsymbol{r}')$ of the long-range interaction potential, Eq. (4.16). In a sense, the envelope $f_{\boldsymbol{\xi}}(\boldsymbol{r}, \boldsymbol{r}')$ measures the system extensions L_ν in units of its interaction ranges ξ_ν under the spatial integrals $\int_V d^d\boldsymbol{r}$. This information is encoded in the spatial average $\tilde{f}_{\boldsymbol{\xi}}(\boldsymbol{0}, \boldsymbol{0})$, which is a function of the ratios L_ν/ξ_ν. Expressing the spatial average $\tilde{f}_{\boldsymbol{\xi}}(\boldsymbol{0}, \boldsymbol{0})$ as the convolution, Eq. (4.25), highlights this notion that the envelope scans the size of the system. In the derivation of the quantum fluctuations, we found that the spatial average enters as a coupling prefactor into the momentum-space expression of the Hamiltonian, for example in Eq. (4.31). Therefore, the effective interaction strength in reciprocal space depends on the system size. Since the long-range interaction is responsible for the formation of the rotons, the roton modes, Eqs. (4.41) and (4.44), depend on the spatial extension of the system. More specifically, the depth of the rotons is varied by changing the size of the system. Consequently, the zero-point energies of the rotons are system-size dependent, and these provide the energy correction given in Eq. (4.39). Crucially, this means that its derivative $(\partial E_{\mathrm{qf,C}}/\partial V)_N$ is nontrivial if the envelope $f_{\boldsymbol{\xi}}(\boldsymbol{r}, \boldsymbol{r}')$ is nontrivial and can compete with the mean-field so that a droplet can form, see Eq. (4.1).

We deal with the quantum fluctuation energy of an individual mode or a few distinct modes, and thus face the fact that this energy is not extensive but intensive. It is therefore expected to vanish in a proper thermodynamic limit. However, the thermodynamic limit of the kind of system we stated in Eq. (4.17) turns out to be a delicate matter, which we have already discussed in the context of Dicke model mapping, see section 2.3.7. A physical thermodynamic limit requires not only $N \to \infty$ and $V \to \infty$, while $N/V = \mathrm{const}$, but also the widths of the envelope should be $\xi_\nu \to \infty$ under the constraint that $L_\nu/\xi_\nu = \mathrm{const}$, which leads to some issues with our analytical approach. Namely, for finite-size systems we could argue for Eq. (4.24) that the Fourier transform of the envelope $\bar{f}_{\boldsymbol{\xi}}(\boldsymbol{q}, \boldsymbol{q}')$ is exponentially small for $|q_\nu| > 2\pi/L_\nu$. However, to maintain this while $L_\nu \to \infty$, the Fourier transform of the envelope must essentially become a delta distribution. This erases any information about the spatial shape of the envelope. It is like the delta distribution, independent of the chosen sequence of functions that converges to it in the sense of distributions. Based on this intricate property of $E_{\mathrm{qf,C}}$ there are some consequences for the effective ground state energy $E_0 = E_{\mathrm{mf,U}} + E_{\mathrm{qf,U}} + E_{\mathrm{qf,C}}$. Let us first recall that we have already figured out that we can discard $E_{\mathrm{qf,U}}$ due to $E_{\mathrm{qf,U}} \ll E_{\mathrm{mf,U}}$. Moreover, we noticed that the mean-field term $\propto V^{-1}$ cannot realize a droplet by itself. To satisfy conditions (C1)-(C3), Eq. (4.1), the competition must come from the long-range correction $E_{\mathrm{qf,C}}$. With the dependence of the spatial extension encoded in the spatial mean of the envelope $\tilde{f}_{\boldsymbol{\xi}}(\boldsymbol{0}, \boldsymbol{0})$ this is feasible in a finite system.

The spatial average of the envelope $\tilde{f}_{\boldsymbol{\xi}}(\boldsymbol{0}, \boldsymbol{0})$ can be expanded around $\xi_\nu \to \infty$. This expansion can subsequently be applied to the eigenmodes $\Omega_{\boldsymbol{k}}$ and their zero-point energy $E_{\mathrm{qf,C}}$. Such an expansion allows us not only to better understand the qualitative influence of the shape of the envelope on the quantum fluctuations but also to compare the realized E_0 with the minimal model Eq. (4.2) and its classification Eq. (4.4), as well as to analytically find the solution Eq. (4.3) for the droplet size V_0. Due to the constraints, we imposed to derive Eq. (4.24), so that the atoms see only the spatial average of the center of the envelope, we get a good quantitative agreement even if we only expand to the first nontrivial order in $1/\xi_\nu$.

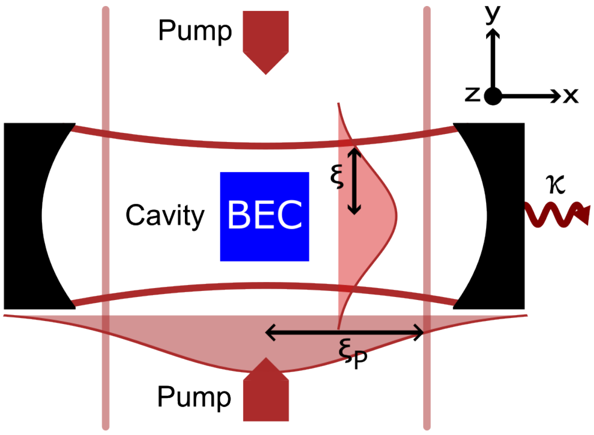

Figure 4.8: Sketch of a cavity BEC setup with a single mode cavity. The BEC in blue is pumped by a broad beam along both directions of the y-axis. The cavity axis is along the x-axis with photon loss rate κ through the right mirror. The cavity mode has a Gaussian transverse profile with waist ξ.

4.4 – Spatial self-confinement in the single-mode cavity setup

We consider the setup discussed in previous chapters of a BEC that is coupled by a transversal pumping scheme to a single mode cavity described by the field Hamiltonian, Eq. (2.46), [27, 88]

$$\hat{H} = \int_V d^3\boldsymbol{r}\, \hat{\psi}^\dagger(\boldsymbol{r}) \left[-\frac{\nabla^2}{2m} + \frac{h^2(\boldsymbol{r})}{\Delta_A} + \frac{g^2(\boldsymbol{r})}{\Delta_A} \hat{a}^\dagger \hat{a} + \frac{g(\boldsymbol{r})h(\boldsymbol{r})}{\Delta_A} \left(\hat{a} + \hat{a}^\dagger\right) + \frac{U}{2} \hat{\psi}^\dagger(\boldsymbol{r}) \hat{\psi}(\boldsymbol{r}) \right] \hat{\psi}(\boldsymbol{r}) - \Delta_C \hat{a}^\dagger \hat{a}\,, \tag{4.47}$$

where we study a three-dimensional BEC in this section. However, unlike in the previous chapters, we here consider the transverse shape of the light modes. Namely, a TEM$_{00}$ cavity mode with waist ξ and the same for the pump laser shape with width ξ_P as sketched in figure 4.8. The spatial dependence of the light mode profiles influences the respective Rabi frequency that couples the light to the atoms. We consider

$$g(\boldsymbol{r}) = g_0 \cos(kx) \exp\left(-\frac{y^2+z^2}{\xi^2}\right), \qquad h(\boldsymbol{r}) = h_0 \cos(ky) \exp\left(-\frac{x^2+z^2}{\xi_P^2}\right). \tag{4.48}$$

The derivation of the effective atom-only Hamiltonian is analogous to that performed in section 2.3.8 to obtain Eq. (2.68). Taking into account the transverse profile, we obtain for the adiabatic elimination of the cavity mode

$$\hat{a} = \frac{g_0 h_0}{\Delta_A(\Delta_C + i\kappa)} \int_V d^3\boldsymbol{r} \left\{ \cos(kx)\cos(ky) \exp\left(-\frac{y^2+z^2}{\xi^2}\right) \exp\left(-\frac{x^2+z^2}{\xi_P^2}\right) \hat{\psi}^\dagger(\boldsymbol{r})\hat{\psi}(\boldsymbol{r}) \times \right.$$
$$\left. \times \left[1 + \mathcal{O}\left(\frac{U_0}{|\Delta_C + i\kappa|}\right)\right] \right\}. \tag{4.49}$$

Subsequently, up to order $\mathcal{O}(U_0^2/[\Delta_C^2+\kappa^2])$, the effective atom-only Hamiltonian [109], Eq. (4.17), is realized with the long-range interaction

$$V_C(\boldsymbol{r}, \boldsymbol{r}') = \frac{2\Delta_C g_0^2 h_0^2}{(\Delta_C^2+\kappa^2)\Delta_A^2} \cos(kx)\cos(ky)\cos(kx')\cos(ky') \exp\left(-\frac{y^2+z^2}{\xi^2} - \frac{x^2+z^2}{\xi_P^2}\right) \times$$
$$\times \exp\left(-\frac{y'^2+z'^2}{\xi^2} - \frac{x'^2+z'^2}{\xi_P^2}\right). \tag{4.50}$$

For the brevity of the equations, we now assume that the width ξ_P of the pump is much larger than the cavity waist ξ and that the condensate occupies a cube $V = L^3$ contained within the cavity waist $L < \xi$. Neglecting the pump and thus the entire envelope along the cavity axis x may seem far-fetched. However, if one imagines a tabletop experiment, external levitation of the atomic cloud against gravity is likely required. Now imagine that the cavity axis x is the vertical axis, and we do not need any self-confinement along this axis, which would result from the pump profile alone. Theoretically, of course, this choice is arbitrary. We could just as well consider the cavity width $\xi \gg \xi_P$ and study the confinement from the pump profile with ξ_P and get the same results for the box of atoms $V^{1/3} < \xi_P$. To reiterate, we choose $L = V^{1/3} < \xi \ll \xi_P$ and investigate the confinement from the TEM_{00} profile of the cavity with waist ξ. Furthermore, we recall the parameter hierarchy for the atom-only picture to hold in the presented form $|\Delta_A| \gg |\Delta_C|, \kappa \gg \omega_R = k^2/2m \gg nU, |U_0|$. We decompose the long-range interaction Eq. (4.50) into its constituents after applying $\xi_P \to \infty$ and obtain

$$\begin{aligned} I &= \frac{2\Delta_C g_0^2 h_0^2}{(\Delta_C^2 + \kappa^2)\Delta_A^2}\,, \qquad v(\boldsymbol{r}, \boldsymbol{r}') = \cos(kx)\cos(ky)\cos(kx')\cos(ky')\,, \\ f_\xi^{(2)}(\boldsymbol{r}, \boldsymbol{r}') &= \exp\left(-\frac{y^2 + z^2}{\xi^2}\right)\exp\left(-\frac{y'^2 + z'^2}{\xi^2}\right)\,. \end{aligned} \tag{4.51}$$

The superscript (2) denotes the algebraic order of the exponent and thus the specific form of the exponential envelope Eq. (4.51) of the TEM_{00} mode. Having determined the constituents of the long-range interaction Eq. (4.51), we can apply the formalism developed in section 4.3. First, we verify Eq. (4.24) for $\tilde{f}_\xi^{(2)}(\boldsymbol{p}, \boldsymbol{p}')$, which is given by nonelementary integrals. Therefore, for the one-dimensional integrals of which $\tilde{f}_\xi^{(2)}(\boldsymbol{p}, \boldsymbol{p}')$ is composed, we study their Taylor series, which is in principle given by integrating the Taylor series of the integrand term by term. The derivation, which is presented in the appendix A.8.1, yields the estimate

$$\left| \int_{-\frac{L}{2}}^{+\frac{L}{2}} \frac{dx}{L} \left\{ e^{i\frac{2\pi j}{L}x} e^{-\frac{x^2}{\xi^2}} \right\} \right| < \frac{L^2}{2\pi^2 j^2 \xi^2} \int_{-\frac{L}{2}}^{+\frac{L}{2}} \frac{dx}{L} \left\{ e^{-\frac{x^2}{\xi^2}} \right\}. \tag{4.52}$$

The spatial average of the Gaussian envelope Eq. (4.51) is

$$\tilde{f}_\xi^{(2)}(\boldsymbol{0}, \boldsymbol{0}) = \left[\frac{\sqrt{\pi}\xi}{L} \mathrm{erf}\left(\frac{L}{2\xi}\right) \right]^4, \tag{4.53}$$

and we can verify Eq. (4.24) for $\boldsymbol{p}, \boldsymbol{p}' \neq \boldsymbol{0}$ and $L < \xi$, i.e.

$$\frac{|\tilde{f}_\xi(\boldsymbol{p}, \boldsymbol{p}')|}{\tilde{f}_\xi(\boldsymbol{0}, \boldsymbol{0}')} < {\prod_{\nu=1}^{2}}' \frac{1}{(\pi j_\nu)^2} {\prod_{\nu'=1}^{2}}' \frac{1}{(\pi j'_{\nu'})^2}\,. \tag{4.54}$$

The primed product denotes the omission of $j_\nu = 0$.
By confirming that Eq. (4.24) holds, we can simply use the results of the generic theory, see section 4.3. The wavenumber k of the light field and the associated recoil frequency $\omega_R = k^2/2m$ are finite. Consequently, there is no mean-field contribution from the cavity-induced long-range interaction V_C, Eq. (4.50). This interaction couples the four modes $\mathcal{K}_C = \{(\pm k \;\; \pm k \;\; 0)^T\}$ with the same absolute momentum $\sqrt{2}k$ and identical Fourier coefficient $v_{\boldsymbol{k},\boldsymbol{k}'} = 1/16$ for all $\boldsymbol{k}, \boldsymbol{k}' \in \mathcal{K}_C$. This means that the conditions of Eq. (4.44) are fulfilled and the cavity induces a single roton-like mode

$$\Omega = \sqrt{2\omega_R \left(2\omega_R + 2nU + \frac{IN}{2} \left[\frac{\sqrt{\pi}\xi}{L} \mathrm{erf}\left(\frac{L}{2\xi}\right) \right]^4 \right)}\,. \tag{4.55}$$

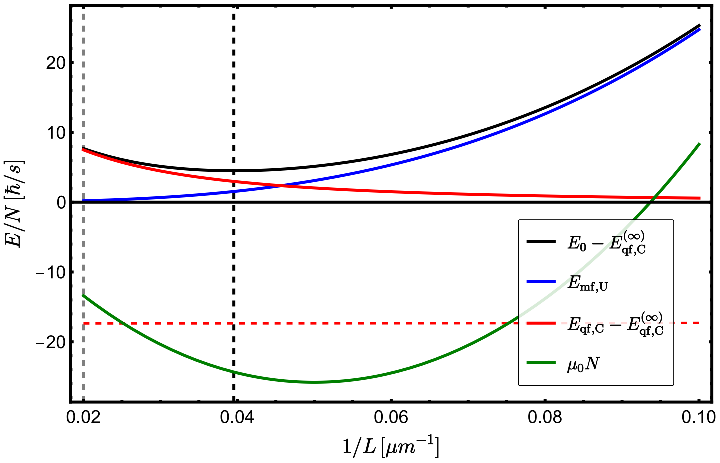

Figure 4.9: Effective energy per particle E_0/N against the inverse of the spatial extent of the system $1/L$. We also show the contributions to E_0, Eq. (4.58), which are the Bose gas mean-field energy $E_{\rm mf,U}$ and the cavity-induced quantum correction $E_{\rm qf,C}$. The gray dashed line marks the equilibrium system size where the competition between the mean-field $E_{\rm mf,U}$ and the correction $E_{\rm qf,C}$ produces a minimum in the effective energy E_0. From the quantum correction $E_{\rm qf,C}$ we have subtracted the infinite-range correction, which is shown as the dashed red line. Additionally, the effective chemical potential μ_0 is displayed. The parameters are $N = 10^3$, $\xi = 50\,\mu$m, $I = -85$ Hz, $a_s = 100\,a_0$, $m = 87$ u, $\omega_R = 2\pi \times 3560$ Hz.

The roton characteristic results from the red-detuned cavity $\Delta_C < 0$, which implies that the effective cavity-induced interaction strength $I < 0$ is negative. This interaction strength then determines the softness of the roton Ω with the critical point given by Eq. (4.45) as

$$I_{\rm cr} = -\frac{4\,(\omega_R + nU)}{N\,[\sqrt{\pi}\mathrm{erf}(L/2\xi)\xi/L]^4}\,. \tag{4.56}$$

In the limit of $\xi \to \infty$, where the square bracket in the denominator approaches 1, this is the established critical point for cavities with infinite-range interaction [36], see section 2.3.8. In the following study of the effective energy, we must choose the system parameters such that we stay below this critical point to maintain the homogeneous mean-field condensate phase. To change the interaction strength I realized in the cavity setup of Eq. (4.51) the most accessible parameters are the pump strength h_0 or the cavity detuning Δ_C. Of course, in principle, one can change any of the cavity parameters in Eq. (4.51) to control the strength of the induced interaction and thus the softness of the roton. The roton Ω directly determines the leading quantum fluctuation correction according to Eq. (4.46)

$$E_{\rm qf,C} = \frac{1}{2}\,(\Omega - \omega_{\boldsymbol{k}})\;, \tag{4.57}$$

from its softness relative to the s-wave scattering dispersion $\omega_{\boldsymbol{k}}$, Eq. (2.25/4.34). Due to the roton property, the energy correction is negative $E_{\rm qf,C} < 0$. The effective beyond mean-field energy of the condensate is therefore

$$E_0 = E_{\rm mf,U} + E_{\rm qf,C} = \frac{UN^2}{2V} + \frac{1}{2}\,(\Omega - \omega_{\boldsymbol{k}})\;, \tag{4.58}$$

with the scattering mean-field contribution $E_{\rm mf,U}$, Eq. (4.29b), and the cavity-induced quantum fluctuation term $E_{\rm qf,C}$.

4.4.1 Evaluation of the effective energy under the droplet criteria

We now examine how the effective energy E_0, Eq. (4.58), can realize the conditions for a quantum droplet (C1) to (C3), Eq. (4.1). To satisfy (C1), a system for a fixed number of atoms N must have an energy extremum with respect to its size V. If there is no cavity interaction $I = 0$ then the quantum correction vanishes $E_{\mathrm{qf,C}} = 0$, but for a stable BEC, i.e. $U > 0$, the mean-field energy $E_{\mathrm{mf,U}} \propto 1/V$ is positive and grows strictly monotonously with the inverse of the system size. Only if there is a significant correction $E_{\mathrm{qf,C}}$ rooted in the quantum fluctuations of the cavity, can (C1) be satisfied. Their competition is shown in figure 4.9 and we see that a minimum of energy is created. This means that we have also fulfilled (C2), Eq. (4.1b). The system extension at which the effective energy E_0 is minimal determines the equilibrium volume V_0 of the atomic system, which is the size of the droplet. Figure 4.9 also shows that the effective chemical potential

$$\mu_0 = nU + \left(\frac{\partial E_{\mathrm{qf,C}}}{\partial N}\right)_V , \tag{4.59}$$

is negative in the vicinity of the equilibrium $1/L_0$.

4.4.2 Analytical Investigation

We perform the analytical expansion around $L/\xi = 0$ mentioned in the discussion of the generic correction, section 4.3.6, on the specific example for $E_{\mathrm{qf,C}}$. Due to the constraint $L < \xi$, the system experiences only the center of the envelope $f_\xi^{(2)}(\boldsymbol{r}, \boldsymbol{r}')$, so we can expand it to second order in L/ξ, or equivalently expand its spatial average Eq. (4.53) for our needs and have

$$\tilde{f}_\xi^{(2)}(\mathbf{0}, \mathbf{0}) = 1 - \frac{L^2}{3\xi^2} + \mathcal{O}\left(\left(\frac{L}{\xi}\right)^4\right) . \tag{4.60}$$

For $L < \xi$ the approximation is also quantitatively accurate. First, we use this on the roton mode Eq. (4.55) and obtain

$$\Omega = \sqrt{2\omega_R\left(2\omega_R + 2nU + \frac{IN}{2}\right)} - \frac{IN}{12\sqrt{1 + (4nU + IN)/4\omega_R}}\frac{L^2}{\xi^2} + \mathcal{O}\left(\frac{L^4}{\xi^4}\right) . \tag{4.61}$$

In the limit of an infinitely broad envelope $\xi \to \infty$, only the first term prevails. We consequently denote it by $\Omega^{(\infty)}$. It demonstrates that since we can apply the expansion around $L/\xi = 0$ in the sense of $\xi \to \infty$ as in Eq. (4.60), we can recover the results for the well-established infinite-range cavity interaction at any point of the derivation presented in section 4.3. The succeeding term encapsulates the leading dependence on the system extension that is characteristic of the specific envelope. Here, the Gaussian shape of $f_\xi^{(2)}(\boldsymbol{r}, \boldsymbol{r}')$ yields a term of order L^2/ξ^2. Based on its similarity to a harmonic oscillator potential due to the quadratic dependence on the system length L, we denote the prefactor by the effective spring constant

$$k_\Omega = \frac{-IN}{12\xi^2\sqrt{1 + (4nU + IN)/4\omega_R}} . \tag{4.62}$$

The expansion applied to the quantum energy correction $E_{\mathrm{qf,C}}$ yields

$$\begin{aligned} E_{\mathrm{qf,C}} &= \frac{1}{2}\left[\sqrt{2\omega_R\left(2\omega_R + 2nU + \frac{IN}{2}\right)} - 2\omega_R - nU\right] - \frac{IN}{24\sqrt{1 + (4nU + IN)/4\omega_R}}\frac{L^2}{\xi^2} + \mathcal{O}\left(\frac{L^4}{\xi^4}\right) \\ &= E^{(\infty)}_{\mathrm{qf,C}} + \frac{k_\Omega}{2}L^2 + \mathcal{O}\left(\frac{L^4}{\xi^4}\right) , \end{aligned} \tag{4.63}$$

which we dissect again into the term $E^{(\infty)}_{\mathrm{qf,C}}$ for infinite width $\xi \to \infty$ and the leading spatial extension dependence term of order L^2/ξ^2. Yet analytically we cannot compare the effective energy E_0 obtained from Eq. (4.58) with this approximation to the minimal effective model Eq. (4.2) due to the dependence on the system volume V in the s-wave scattering terms nU. In figure 4.9 we can see that this dependence cannot be significant for $nU/\omega_R \ll 1$, since the dashed line of the infinite-range correction $E^{(\infty)}_{\mathrm{qf,C}}$ is almost perfectly horizontal, i.e. independent of $1/L = V^{-1/3}$. Analytically speaking, as long as the radicants in Eq. (4.61) or equivalently Eq. (4.63) are not close to zero $\Omega^{(\infty)} \gg nU$, we can discard any occurrence of nU in the roton Ω and its zero-point motion $E_{\mathrm{qf,C}}$. Due to the way the roton approaches zero near the Dicke critical point, see figure 2.11, this is a good approximation except in the very vicinity of I_{cr}, Eq. (4.56).

We now have obtained an analytically solvable effective potential

$$E_0(N,V) = E^{(\infty)}_{\mathrm{qf,C}} + \frac{UN^2}{2V} + \frac{k_\Omega}{2}V^{2/3} , \tag{4.64}$$

with the terms induced by cavity quantum fluctuations

$$E^{(\infty)}_{\mathrm{qf,C}} \approx \frac{1}{2}\left[\sqrt{2\omega_R\left(2\omega_R + \frac{IN}{2}\right)} - 2\omega_R\right] , \qquad k_\Omega \approx \frac{-IN}{12\xi^2\sqrt{1 + IN/4\omega_R}} . \tag{4.65}$$

Next we can directly compare Eq. (4.64) with the minimal droplet model Eq. (4.2). The infinite-range correction $E^{(\infty)}_{\mathrm{qf,C}} = d(N)$ is independent of the spatial extent of the atomic system V and therefore acts as a system size-independent shift in Eq. (4.64), as we see in figure (4.9). The other two terms are akin to the remaining minimal model terms. Thus, from the mean-field term linear in $1/V$ we find the model parameter $a(N) = UN^2/2$. For the quantum correction proportional to $V^{2/3}$ we get $b(N) = k_\Omega/2$ and $c = -5/3$ from the comparison with the term $\propto V^{-1-c}$. According to our analysis of the droplet parameter classes in Eq. (4.4), it must be (D3), since $c < -1$. If we restrict ourselves to a stable BEC, then $a(N) > 0$. A red-detuned cavity $\Delta_C < 0$ implies the roton characteristic due to a negative effective interaction parameter I and thus $b(N) > 0$. Indeed, we match the model parameter class of (D3), Eq. (4.4c).

On the analytical model Eq. (4.64) we can directly use the generic solution Eq. (4.3) to obtain the droplet size as the equilibrium system volume

$$V_0 = \left(-\frac{18\xi^2 UN}{I}\sqrt{1 + \frac{IN}{4\omega_R}}\right)^{3/5} . \tag{4.66}$$

Equation (4.66) now reveals how the droplet size is influenced by the respective system parameters to leading order. In figure 4.10 we show the dependence of the droplet density $n_0 = N/V_0$ on the interaction parameters U and I. From Eq. (4.66) we get the relation of $V_0 \propto U^{3/5} \propto a_s^{3/5}$ for the contact interaction parameter U given by the s-wave scattering length a_s. For the effective strength of the cavity-induced interaction away from the Dicke critical point I_{cr} we find the proportionality $V_0 \propto |I|^{-3/5}$. When the interaction is $I \gtrsim 0.6\, I_{\mathrm{cr}}$ the square root in Eq. (4.66) is significant and

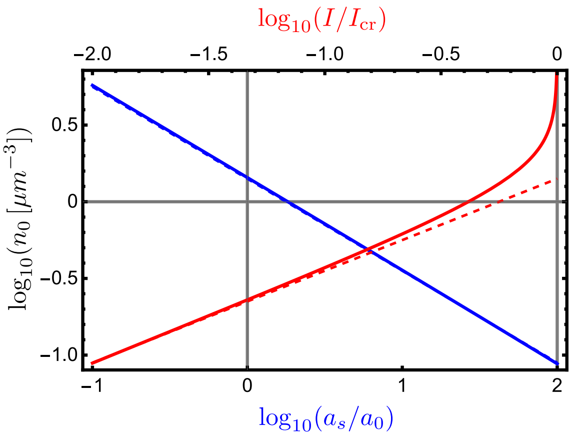

Figure 4.10: Dependence of the droplet density n_0 on the interaction parameters, i.e. the cavity interaction strength I (red, top scale) and the s-wave scattering length $a_{\rm s}$ (blue, bottom scale). We set $a_{\rm s} = 0.1\,a_0$ and $I = 0.99\,I_{\rm cr}$, respectively. The lower bound of the y-axis is given by the self-consistency constraint $V_0 < \xi^3$. The parameters are $N = 10^4$, $\xi = 50\,\mu$m, and $m = 87\,u$.

therefore the relation between the droplet density n_0 and the effective interaction parameter I deviates from the simple relation $V_0 \propto |I|^{-3/5}$, as we can see in figure 4.10. The dependence on the number of atoms N works similarly and is $V_0 \propto N^{3/5}$ when the deviation of the square root of the radicant from 1 is negligible. Finally, the droplet size also varies with the width of the envelope ξ, which here is given by the cavity waist in the proportionality $V_0 \propto \xi^{6/5}$. Note, however, that the theory behind Eq. (4.66) involves the restriction to $V_0 < \xi^3$, which must be respected for self-consistency.

If we consider a stable BEC of rubidium-87 atoms with the s-wave scattering length a_s as in figure 4.9, the theory predicts a quantum droplet that is orders of magnitude more dilute than those observed in both dipolar gases and Bose-Bose mixtures [45, 58, 59, 166, 174] as well as the BEC prepared in cavity BEC experiments [23, 25, 35]. This is primarily because, in the droplet presented here, the quantum fluctuation correction competes with a normal mean-field contact interaction. In the established droplet realizations, however, the mean-field is almost completely suppressed by the use of Feshbach resonances. Figure 4.10 indicates that a similar suppression of the mean-field would result in an increase of the droplet density by one to two orders of magnitude due to the relation $n_0 \propto U^{-3/5}$.

4.4.3 Thermodynamic Interpretation

We study how the creation of the droplet by the cavity-induced quantum fluctuations can be interpreted in terms of thermodynamic concepts typically applied to liquids. The droplet conditions Eq. (4.1) each have a physical interpretation to make a droplet a thermodynamically stable state [5]. First (C1), Eq. (4.1a), a self-bound liquid must have zero pressure $P_0 = -(\partial E_0/\partial V)_N = 0$ so that it neither expands nor collapses. In the mean-field, the system has a positive pressure $P_{\rm mf,U} = Un^2/2$ due to the repulsive contact interaction mean-field. However, the quantum fluctuations of the cavity-induced roton mode contribute the correction which acts as a negative pressure $P_{\rm qf,C} = -k_\Omega/(3L)$. Their competition can facilitate the vanishing of the effective pressure

$$P_0 = P_{\rm mf,U} + P_{\rm qf,C} = \frac{UN^2}{2L^3} - \frac{k_\Omega(N)}{3L}\,. \tag{4.67}$$

This is shown in figure 4.11, where the effective pressure P_0 is plotted in the plane of the number of atoms N and the spatial extent of the system L. The magenta line denotes zero pressure P_0 and thus the equilibrium system size L_0 for any number of atoms N. Figure 4.11(b) shows the density n_0 of

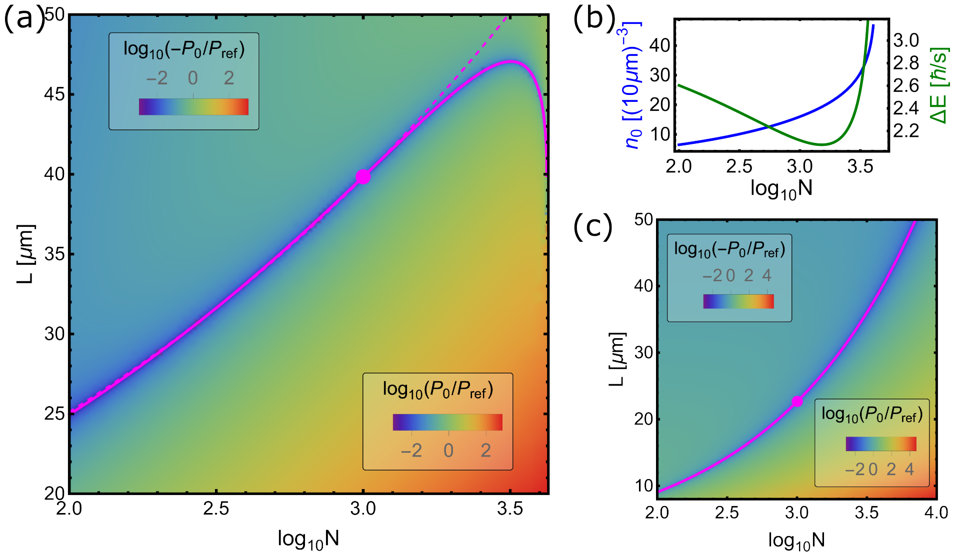

Figure 4.11: (a) Logarithm of the system pressure P_0 as a function of the number of atoms N and the system size L for $I = -25$ Hz. The magenta line marks zero pressure. Above the line of zero pressure, P_0 is negative, and below, it is positive. The pressure is displayed relative to the reference pressure $P_{\text{ref}} = 6.5 \times 10^{-19}$ Pa, which is the mean-field pressure of a BEC with 10^3 atoms and a cube edge length of $L = 38.8\,\mu$m, i.e. the mean-field pressure at the point indicated by the magenta dot. The dashed magenta line shows $L_0 \propto N^{1/5}$ as discussed in section 4.4.2 based on the analytical solution Eq. (4.66). Where the dashed line deviates from the solid magenta line, the square root in Eq. (4.66) has a value significantly different from one. (b) Droplet density $n_0 = N/L_0^3$ (blue) and the single particle energy difference $\Delta E = [E_0(N-1, V_0) - E_0(N, V_0)]|_{P_0(N,V_0)=0}$ (green) realized along the magenta line $P_0 = 0$ of (a). (c) System pressure P_0 for a relative cavity interaction strength $I = 0.95\,I_{\text{cr}}$. The absolute value of I decreases with increasing N. The reference pressure is again the mean-field pressure of the Bose gas at the magenta point $P_{\text{ref}} = 1.9 \times 10^{-17}$ Pa. Remaining parameters are as in figure 4.9.

the droplet along this line of zero pressure. It increases monotonically as $n_0 = N/V_0 \propto N^{2/5}$ with increasing number of atoms N, as predicted by the analytical model Eq. (4.66), until it diverges at about $N_{\text{cr}} \approx 4000$. The phenomenon is due to the cavity-induced interaction being a collective effect, and thus the critical interaction strength I_{cr} for the Dicke phase transition, Eq. (4.56), decreases with a larger number of atoms. In the approximations for the analytical model, it is $I_{\text{cr}} \propto N^{-1}$. At the critical point, where the roton becomes soft, the radicant vanishes in the square root of Eq. (4.66), leading to an arbitrarily dense droplet. This is due to the divergence of the quantum fluctuations and the negative pressure $P_{\text{qf,C}}$ they induce. Note, however, that this divergence also indicates a divergence of the quantum depletion, which is not taken into account in the presented theory. If we adjust the effective interaction strength $I = 0.95\,I_{\text{cr}}$ to remain relatively constant to the critical point of self-organization I_{cr}, we obtain the results shown in figure 4.11(c). This is because the value of the square root in Eq. (4.66) is held at a constant value throughout the diagram figure 4.11(c).

A common feature we observe in both pressure plots of figure 4.11(a) and (c) is that we have negative effective pressure above the magenta line of zero pressure, i.e., for system extensions greater than the equilibrium size, and positive pressure for any system extension smaller than the equilibrium one. This is the realization of (C2) a positive bulk modulus $K_0(P_0 = 0) = -V(\partial P_0/\partial V)_N|_{V=V_0} > 0$, Eq. (4.1b). A system with an extension greater than the equilibrium L_0 will collapse back to equilibrium due to the negative effective pressure. Equivalently, a system that is too dense, i.e. smaller than the equilibrium size, expands to the equilibrium size because it has a positive effective pressure. This balance renders the droplet mechanically stable. Although the effective compressibility of the droplet at $P_0 = 0$ is positive, it is modified compared to the bulk compressibility resulting from the mean-field, see Eq. (2.29). It is straightforward to derive these two statements from the analytical model Eq. (4.64)

$$K(P_0 = 0) = V \left(\frac{\partial^2 E_0}{\partial V^2}\right)_N \bigg|_{V=V_0} = \left[Un^2 - \frac{k_\Omega(N)}{9L}\right] \bigg|_{V=V_0} = \frac{5}{6} U n_0^2 > 0\,, \tag{4.68}$$

where we have entered $P_0 = 0$ from Eq. (4.67). The compressibility of any cavity-induced droplet is therefore positive. It follows that the speed of sound $c_s = \sqrt{K(P_0 = 0)/mn}$ is correspondingly reduced by the cavity-induced interaction compared to the homogeneous Bose gas $c_s^{\mathrm{gas}} = \sqrt{Un/m}$, see section 2.2.3.

Figure 4.11(b) also displays the energy difference $\Delta E = [E_0(N-1) - E_0(N)]|_{P_0(N)=0}$ due to the loss of a single particle. Since it is positive, it ensures that the droplet is not self-evaporating (C3), Eq. (4.1c). In thermodynamic terms, a positive $\Delta E/N$ is a negative chemical potential $\mu_0 = (\partial E_0/\partial N)_{V_0} < 0$. We analyze this for the effective energy $E_0(N, V)$, Eq. (4.64), analytically in addition to the graphical presentation in figure 4.11. Based on the effective potential, Eq. (4.64), we get three contributions to the effective chemical potential. The first is the standard mean-field chemical potential of the weakly interacting Bose gas $\mu_{\mathrm{mf}} = Un$. The second is the cavity quantum correction term for the spatial extension $b(N)V^{2/3} = k_\Omega V^{2/3}/2$, which yields the contribution

$$\left(\frac{\partial b(N) V^{2/3}}{\partial N}\right)_{V=V_0} = -\frac{I V_0^{2/3}}{24\xi^2\sqrt{1 + INm/2k^2}} + \frac{I^2 N V_0^{2/3} m/2k^2}{48\xi^2[1 + INm/2k^2]^{3/2}}\,. \tag{4.69}$$

For interaction parameters $U > 0$ and $I < 0$ all these terms of the chemical potential are strictly positive. The negative effective chemical potential seen in figure 4.9 must therefore be due to the third contribution to the chemical potential which is the infinite-range cavity correction

$$\mu_{\mathrm{qf,C}}^{(\infty)} = \frac{\partial E_{\mathrm{qf,C}}^{(\infty)}}{\partial N} = \frac{I}{8\sqrt{1 + INm/2k^2}}\,. \tag{4.70}$$

With $I < 0$, it is indeed negative. We note that $Im/2k^2 \lesssim 1$ based on the self-organization critical point, Eq. (4.56), and that we consider the system in a dilute weakly interacting regime, so $gmN/2V_0k^2 \ll 1$ must always be valid. Estimating the contributions to the effective chemical potential for the droplet $\mu_0(P_0 = 0)$ under these restrictions reveals that the negative infinite-range part of the chemical potential is significantly larger than both Eq. (4.69) and μ_{mf}. This ensures a negative chemical potential at the equilibrium point that determines the droplet size and verifies (C3). As figure 4.9 shows, this is not true far from the equilibrium system size.

4.4.4 Finite temperature

Any experiment will inadvertently involve a gas of finite temperature. In a system of finite temperature T, the effective energy E_0, Eq. (4.58), has an additional term E_{th} [62, 179], i.e.

$$E_0(N, V, T) = E_{\mathrm{mf}} + E_{\mathrm{ac}} + E_{\mathrm{th}}\,. \tag{4.71}$$

For the cavity BEC this additional term E_{th} consists of a term for the Bose gas excitations, as discussed in section 2.2.4, and a term for the deviation of the roton mode Ω from the Bose gas dispersion. In this way, we have separated E_{th} in the same notion as the zero-point motion E_{qf}, Eq. (4.39), into a Bose gas term and a cavity-induced term, so that the latter vanishes when there is no cavity-mediated

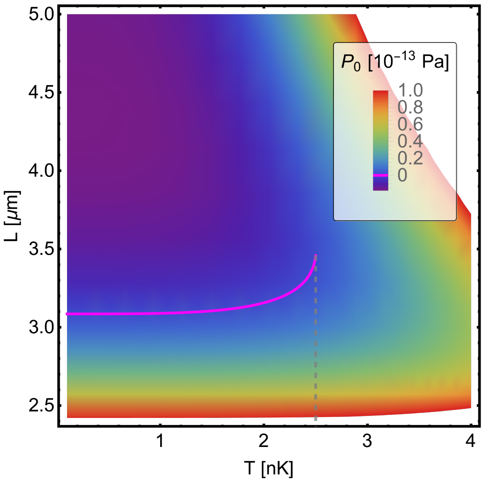

Figure 4.12: System pressure $P_0(N,V,T) = P_{\mathrm{mf,U}} + P_{\mathrm{qf,C}} + P_{\mathrm{th,U}}$ in the plane of temperature T and system extension L. The magenta line indicates zero pressure $P_0 = 0$. The dashed vertical line indicates the critical temperature above which the parameter set can no longer realize a stable droplet. The parameters are $N = 10^2$, $\xi = 5\,\mu$m, $a_s = 100\,a_0$, $I = 0.99\,I_{\mathrm{cr}}$, $m = 87\,u$, $\omega_R = 2\pi \times 3560$ Hz.

interaction. We have

$$E_{\mathrm{th}} = \frac{1}{\beta}\sum_{\boldsymbol{p}}{}' \ln\left(1 - e^{-\beta\omega_{\boldsymbol{p}}}\right) + \frac{1}{\beta}\ln\left(\frac{1-e^{-\beta\Omega}}{1-e^{-\beta\omega_{\boldsymbol{k}}}}\right) = E_{\mathrm{th,U}} + E_{\mathrm{th,C}}\,. \tag{4.72}$$

The sum over the momenta $\boldsymbol{p}$ is evaluated in the continuum and the low-temperature limit as discussed in section 2.2.4 and Refs. [41,62]. We find

$$E_{\mathrm{th}} = -\frac{Vm^{3/2}\pi^2}{90\beta^4(Un)^{3/2}} + \frac{1}{\beta}\ln\left(\frac{1-e^{-\beta\Omega}}{1-e^{-\beta\omega_{\boldsymbol{k}}}}\right). \tag{4.73}$$

The thermal pressure from the Bose gas is Eq. (2.33) and reads

$$P_{\mathrm{th,U}} = \frac{m^{3/2}\pi^2}{36\beta^4(Un)^{3/2}}\,. \tag{4.74}$$

In comparison, the cavity-induced thermal pressure $P_{\mathrm{th,C}} = (-\partial E_{\mathrm{th,C}}/\partial V)_{N,T}$ is very small, and from now on we omit the cavity-induced thermal contributions.

The positive thermal pressure of the Bose gas $P_{\mathrm{th,U}}$, Eq. (4.74), will shift the zero pressure point to a lower density, see figure 4.12, that is, if a minimum of effective energy can be realized at all for a given temperature. As figure 4.12 shows, no droplet can form above a critical temperature T_{cr}. The critical temperature depends naturally on the other parameters. We also find that the window below the critical temperature where the thermal contribution to the pressure is significant is very narrow due to $P_{\mathrm{th,U}} \propto T^4$. In figure 4.12 the droplet is effectively zero temperature below 2 nK, so the region for a droplet with significant thermal effects is just half a nanokelvin. Finally, we note that there is a second solution for zero pressure at larger system size L, which can be seen in figure 4.12. However, it is not stable because of its negative compressibility.

Optimization of the experiment should focus on enabling a denser droplet to raise the critical temperature because $P_{\mathrm{th,U}} \propto T^4/n^{3/2}$. We have already chosen optimized parameters for figure 4.12, where the droplet can be sustained up to nanokelvin temperature. Compared to figure 4.9 we have reduced the number of particles N, chosen a narrower light field ξ resulting in a shorter interaction range, and moved closer to the Dicke phase transition $I = 0.99\,I_{\mathrm{cr}}$ to obtain a softer roton. If we want droplet formation for the same parameters as in figure 4.9 we must have a system below the critical temperature of about 0.1 nK where $\beta\omega_R \approx 10^3$. It has been demonstrated that condensates can be prepared at these temperatures [184]. Recently, even tens of picokelvins have been reached with matter wave lensing techniques [185, 186], albeit we admit that this requires great experimental effort. Hence, temperature is probably the biggest obstacle to verifying the proposed droplet in an experiment. Nevertheless, our results show that a finite temperature is not a no-go for the formation of a droplet.

4.4.5 Other envelope shapes: Quartic exponent

Now we want to explore further how the shape of the envelope influences the self-confinement mechanism of the cavity-induced quantum liquid. We have already established in our theory in section 4.3 that the envelope directly determines the dependence of the quantum correction on the spatial extension of the system through its spatial average $\tilde{f}_{\boldsymbol{\xi}}(\mathbf{0},\mathbf{0})$. Here, we consider the same setup as before, figure 4.8 and Eq. (4.47), but change the exponents in the envelope to quartic as

$$f_\xi^{(4)}(\boldsymbol{r},\boldsymbol{r}') = \exp\left(-\frac{y^4+z^4}{\xi^4}\right)\exp\left(-\frac{y'^4+z'^4}{\xi^4}\right) . \tag{4.75}$$

We obtain the estimate, see appendix A.8.2, i.e.

$$\left|\int_{-\frac{L}{2}}^{+\frac{L}{2}} \frac{dx}{L}\left\{e^{i\frac{2\pi j}{L}x}e^{-\frac{x^4}{\xi^4}}\right\}\right| < \frac{L^4}{4\pi^2 j^2\xi^4}\int_{-\frac{L}{2}}^{+\frac{L}{2}} \frac{dx}{L}\left\{e^{-\frac{x^4}{\xi^4}}\right\} , \tag{4.76}$$

and thus can verify Eq. (4.24) explicitly for $\boldsymbol{p},\boldsymbol{p}' \neq \mathbf{0}$ and $L < \xi$

$$\frac{|\tilde{f}_\xi(\boldsymbol{p},\boldsymbol{p}')|}{\tilde{f}_\xi(\mathbf{0},\mathbf{0})} < {\prod_{\nu=1}^{2}}' \frac{1}{(\pi j_\nu)^2} {\prod_{\nu'=1}^{2}}' \frac{1}{(\pi j'_{\nu'})^2} , \tag{4.77}$$

where the primed product indicates the omission of $j_\nu = 0$. Hence, we have satisfied the condition to apply Eq. (4.24) and only require the spatial average of the envelope

$$\tilde{f}_\xi^{(4)}(\mathbf{0},\mathbf{0}) = \left[\frac{2\xi}{L}\Gamma\left(\frac{5}{4}\right) - \frac{\xi}{2L}\Gamma\left(\frac{1}{4},\frac{L^4}{16\xi^4}\right)\right]^4 , \tag{4.78}$$

where $\Gamma(s,x)$ is the upper incomplete gamma function. Thus we get the single distinct roton from Eq. (4.44) and its zero-point motion from Eq. (4.46) with $\tilde{d} = 4$ and $\tilde{v} = 1/16$.

The obtained effective energy $E_0 = E_{\mathrm{mf,U}} + E_{\mathrm{qf,C}}$ can be analyzed in the same way as for the Gaussian envelope. Its competition to realize the equilibrium of a droplet is presented in figure 4.13. The effective energy E_0 is molded by the spatial extension dependence of the cavity-induced quantum correction $E_{\mathrm{qf,C}}$ determined by the envelope shape. We have chosen identical system parameters in figure 4.13 as for the Gaussian envelope, figure 4.9. Yet the density of the droplet in the quartic exponent envelope is only about 40 % of that realized in the Gaussian envelope. This indicates a weaker self-confinement of the system.

We expand the envelope in Eq. (4.75) or its spatial average, Eq. (4.78), around $L/\xi = 0$ and find that the first nontrivial order is L^4/ξ^4. Matching the effective energy E_0 to the minimal model, we obtain here $c = -7/3$. The quartic exponent envelope still realizes the same droplet class (D3), Eq. (4.4c), as for the Gaussian envelope. However, since it creates a significantly more dilute droplet, we have an indication that an exponent parameter c closer to its upper limit -1 optimizes the density of a (D3) droplet.

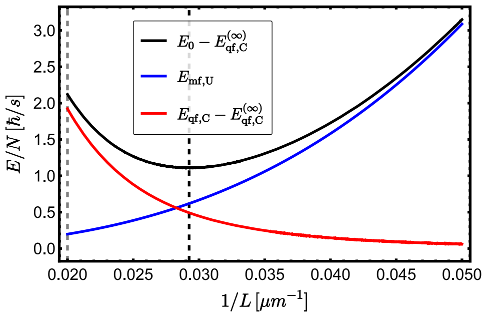

Figure 4.13: Effective system energy E_0 per particle with its mean-field $E_{\mathrm{mf,U}}$ and quantum fluctuation cavity contribution $E_{\mathrm{qf,C}}$ for the quartic exponent envelope, Eq. (4.75), as a function of the inverse of the atomic system extension $1/L$. The constant shift due to the infinite-range cavity correction $E_{\mathrm{qf,C}}^{(\infty)}$ has already been subtracted. An equilibrium droplet size L_0 is realized at the energy minimum marked by the gray dashed line. The remaining parameters are the same as figure 4.9.

4.4.6 Other envelope shapes: Generic exponent

We explore tunability and control by the exponent γ in the envelope further with the generic ansatz

$$f_\xi^{(\gamma)}(\boldsymbol{r},\boldsymbol{r}') = \exp\left(-\frac{|y|^\gamma + |z|^\gamma}{\xi^\gamma}\right)\exp\left(-\frac{|y'|^\gamma + |z'|^\gamma}{\xi^\gamma}\right). \tag{4.79}$$

Assuming that the approximation of Eq. (4.24) holds for an arbitrary $\gamma > 0$, we need only the zero Fourier coefficient

$$\tilde{f}_\xi^{(\gamma)}(\mathbf{0},\mathbf{0}) = \left(\frac{2\xi}{\gamma L}\left[\Gamma\left(\frac{1}{\gamma}\right) - \Gamma\left(\frac{1}{\gamma},\left(\frac{L}{2\xi}\right)^\gamma\right)\right]\right)^4 = 1 - \frac{4}{1+\gamma}\left(\frac{L}{2\xi}\right)^\gamma + \mathcal{O}\left(\left(\frac{L}{2\xi}\right)^{2\gamma}\right). \tag{4.80}$$

From Eq. (4.44) the roton mode is determined by $\tilde{f}_\xi^{(\gamma)}(\mathbf{0},\mathbf{0})$ with $\tilde{d} = 4$ and $\tilde{v} = 1/16$ and hence the quantum correction, Eq. (4.46). Analyzing the right-hand side of Eq. (4.80) we deduce that the first nontrivial term in the cavity-induced pressure is $P_{\mathrm{qf,C}} \propto L^{\gamma-3}$. We also find that the parameter γ is related to the droplet classification by $c = -(1+\gamma/3)$ for the three-dimensional system under investigation $V = L^3$.

We analyze the interplay between the Bose gas mean-field $E_{\mathrm{mf,U}}$, Eq. (4.29b), and the quantum correction $E_{\mathrm{qf,C}}$ as a function of the envelope exponent γ in figure 4.14. In subfigure (a) we find that the exponent parameter γ does affect the droplet size L_0. As suspected in the previous section 4.4.5, a larger exponent γ such as $\gamma = 4$ or 3 results in a more dilute droplet than the Gaussian envelope $\gamma = 2$. In figure 4.14(a) we find that decreasing the exponent below $\gamma = 2$ indeed leads to further improvement. The maximum droplet density is obtained at the peculiar value $\gamma = 1.36$. This is further investigated in figure 4.14(b). We observe that the optimal exponent γ to create the densest possible droplet is sensitive to the remaining set of parameters. In figure 4.14(b), taking only half of the atoms $N/2$ leads to an optimal γ of about 1.02. Conversely, increasing the s-wave scattering by a factor of 5 shifts the optimal exponent to $\gamma \approx 1.85$. In the limit $\gamma \to 0$ the envelope Eq. (4.79) becomes spatially constant, so the interaction becomes infinite-range. Consequently, if $\gamma \to 0$ a droplet can no longer be generated and $1/L_0 \to 0$. Although the initial growth around $\gamma = 0$ is in the region where our approximation does not hold, it is related to the optimal exponent γ of a parameter set. Since it starts at $1/L_0 = 0$, a parameter set with a smaller optimal γ must have a steeper growth near $\gamma = 0$, as the results in figure 4.14(b) show.

Also of note in figure 4.14(a) is the relationship between the effective energy per particle E_0/N and the exponent γ. It is evident that a larger exponent leads to a more negative E_0. If we examine the

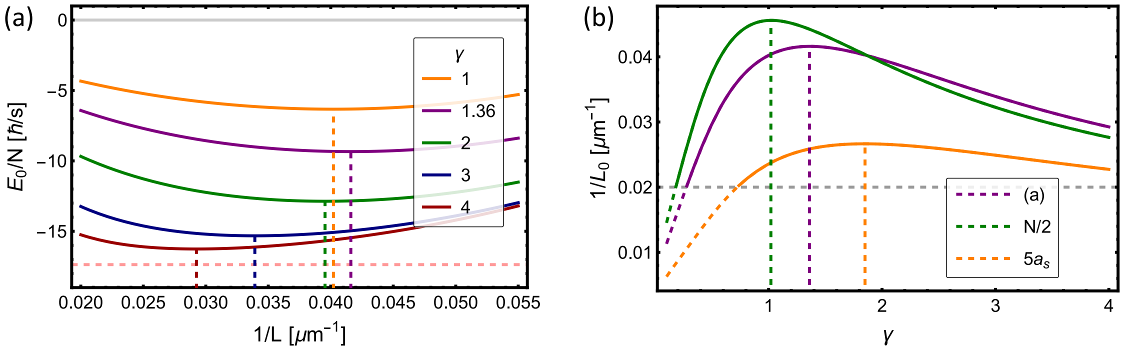

Figure 4.14: (a) Effective energy per particle E_0/N plotted against the inverse system size $1/L$ for five different choices of the envelope exponent γ. The droplet size L_0 corresponding to the minimum of E_0 is indicated by a dashed line in the corresponding color. The dashed red horizontal line indicates the value of the infinite-range quantum correction $E^{(\infty)}_{\text{qf,C}}/N$. The parameters are $N = 10^3$, $\xi = 50\,\mu\text{m}$, $I = -85$ Hz, $a_s = 100\,a_0$, $m = 87$ u, $\omega_R = 2\pi \times 3560$ Hz. (b) Inverse droplet size $1/L_0$ against the exponent in the envelope γ for three parameter sets. The first, with the same parameters as in subplot (a), is labeled "(a)". The set "$N/2$" uses identical parameters except that the number of atoms is halved to $N/2 = 500$. Finally, the parameter set "$5a_s$" uses the same parameters as subplot (a), but with five times the s-wave scattering length $5a_s = 500\,a_0$. The optimal exponent γ that leads to the densest droplet is indicated by a dashed vertical line. If $1/L_0 < 0.02\,\mu\text{m}^{-1}$, the condition is violated that $L/\xi < 1$ which is necessary for the approximation leading to analytical solvability. To indicate this, a gray horizontal line separates the region of applicability above from the pathological region below. The curves are drawn as dashed lines in the region where the approximation breaks down to further indicate this.

right-hand side of Eq. (4.80), we deduce that the correction term $(L/2\xi)^\gamma$ relative to the infinite-range order 1 decreases in magnitude as the exponent γ increases. Thus, a larger γ moves the effective energy E_0 closer to the value of $E^{(\infty)}_{\text{qf,C}}/N \approx -17.37$ Hz, Eq. (4.65), i.e. to more negative values.

4.4.7 Other envelope shapes: Both pump and cavity profile*

In this section we consider both the cavity and pump profiles, as shown in figure 4.8. For both profiles to have a significant contribution, the envelope of the cavity mode width ξ must be comparable to the system size in each respective dimension, and so must be the transverse width ξ_P of the pump mode. Studying figure 4.8 and Eq. (4.50) we find that the pump determines the envelope along the cavity axis x with ξ_P and, as before, the cavity determines the width ξ of the envelope along the pump axis y. The product of the cavity and pump field shape yields the width $1/\sqrt{1/\xi^2 + 1/\xi_P^2}$ of the envelope normal to the cavity-pump plane, which is the z-axis. In total, we thus obtain the three-dimensional Gaussian envelope characterized by $\boldsymbol{\xi}_{\text{CP}} = (\xi_P\,,\, \xi\,,\, 1/\sqrt{1/\xi^2 + 1/\xi_P^2})^T$ of the form

$$f^{(2)}_{\boldsymbol{\xi}_{\text{CP}}}(\boldsymbol{r}, \boldsymbol{r}') = \exp\left(-\frac{x^2}{\xi_P^2} - \frac{y^2}{\xi^2} - \left[\frac{1}{\xi^2} + \frac{1}{\xi_P^2}\right] z^2\right) \exp\left(-\frac{x'^2}{\xi_P^2} - \frac{y'^2}{\xi^2} - \left[\frac{1}{\xi^2} + \frac{1}{\xi_P^2}\right] z'^2\right). \tag{4.81}$$

Given three different envelope sizes along the axes, we consider the atoms in a rectangular cuboid volume $V = L_x L_y L_z$. Nonetheless, based on the generic model discussion in section 4.3, we know that as long as in each dimension it is $L_\nu/\xi_\nu < 1$, we can use our formalism and only need the spatial

---

*The discussed results are unpublished.

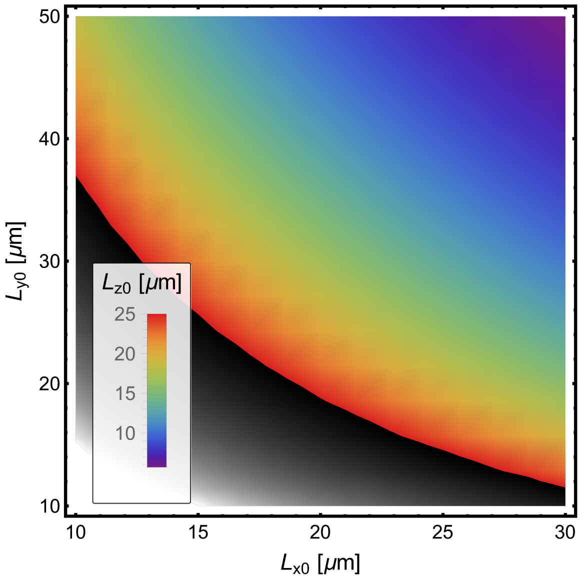

Figure 4.15: Combinations of (L_{x0}, L_{y0}, L_{z0}) that realize the energy minimum of the zero pressure condition $P_0 = 0$ with Eq. (4.85). The gray shaded region indicates that there are solutions, but they violate the global-range assumption $L_{z0} < \xi_z \approx 25\,\mu$m. We have set $\xi_P = 30\,\mu$m while the remaining parameters are the same as in figure 4.9.

average of the envelope as given by Eq. (4.24). It has the expression

$$\tilde{f}_{\boldsymbol{\xi}_{\mathrm{CP}}}(\mathbf{0},\mathbf{0}) = \frac{\pi^3\xi^2\xi_P^2\left[\operatorname{erf}\left(\frac{L_x}{2\xi_P}\right)\operatorname{erf}\left(\frac{L_y}{2\xi}\right)\operatorname{erf}\left(\frac{L_z\sqrt{\xi^2+\xi_P^2}}{2\xi\xi_P}\right)\right]^2}{L_x^2L_y^2L_z^2\left(\frac{1}{\xi^2}+\frac{1}{\xi_P^2}\right)}\,. \tag{4.82}$$

We still consider the same periodic signature $v(\boldsymbol{r},\boldsymbol{r}')$ of the interaction, see Eq. (4.51), so we immediately obtain the roton mode from Eq. (4.44) of the form

$$\Omega = \sqrt{2\omega_R\left(2\omega_R + 2nU + \frac{IN}{2}\tilde{f}_{\boldsymbol{\xi}_{\mathrm{CP}}}(\mathbf{0},\mathbf{0})\right)}\,, \tag{4.83}$$

as we did for Eq. (4.55). Analogously, we acquire the effective energy with the mean-field energy $E_{\mathrm{mf}} = gN^2/(2L_xL_yL_z)$ as

$$E_0 = \frac{gN^2}{2L_xL_yL_z} + \frac{1}{2}\left(\Omega - \omega_{\boldsymbol{k}}\right)\,. \tag{4.84}$$

Based on this, we can verify the droplet conditions (C1)-(C3), Eq. (4.1), by the derivative to obtain the pressure

$$P_0 = -\left(\frac{\partial E_0}{\partial V}\right)_N = -\frac{1}{3}\left(\frac{1}{L_yL_z}\frac{\partial E_0}{\partial L_x} + \frac{1}{L_xL_z}\frac{\partial E_0}{\partial L_y} + \frac{1}{L_xL_y}\frac{\partial E_0}{\partial L_z}\right)_N\,. \tag{4.85}$$

Hence, the zero pressure condition is underdetermined for a set of parameters to obtain the corresponding (L_{x0}, L_{y0}, L_{z0}) of the droplet.

Figure 4.15 shows the solutions of system extensions $L_{x,y,z0}$ for $P_0 = 0$ of Eq. (4.85). We see that a narrower droplet in one direction is a trade-off with an increased extension of the droplet in the other directions. The curve, where the droplet size in the z axis is as big as its envelope, is determined by the respective extension in the x and y plane. A possibility to lift the ambiguity would be to couple the ratio of the extensions in each dimension to the ratios of the envelope sizes, for example, $L_z/L_x = \xi_z/\xi_x$ and $L_z/L_y = \xi_z/\xi_y$. Then the studies we have performed for the previous section for the cube could be transferred to the rectangular cuboid without having to evaluate high dimensional plots for the droplet solutions. Similarly, the results obtained for the cube or cuboid-shaped atomic volume can be generalized to arbitrary d-dimensional shapes as long as some equivalent of the approximation in Eq. (4.24) can be applied.

4.5 – Translation invariant envelope engineered in a multi-mode cavity

The envelope of a single transversal mode, as studied in the preceding sections, is just one way to engineer a cavity-induced long-range interaction. In this section, we explore the possibilities established in the setup of an almost degenerate confocal cavity of Refs. [79, 187–190]. A large number of cavity modes contribute to the effective long-range interaction in such a setup. To create a translation invariant cavity-induced interaction, two main details have to be meticulously prepared in the experiment. The atoms are placed in only one half-plane of the cavity at a distance from the center of the cavity much larger than the interaction range ξ. This is done to suppress interactions with the mirror image [79]. In addition, an extra beam is used to cancel the remaining non-translation invariant contributions in the cavity-induced interaction [79]. Under these assumptions, a translation invariant effective long-range interaction can be engineered, such as

$$V_C(y, y') = I \cos[k(y - y')] \exp\left(-\frac{|y - y'|^2}{\xi^2}\right) . \tag{4.86}$$

Here, we study a one-dimensional system in the axis of the pump y. Droplet formation for this type of long-range interaction has been studied by quantum Monte Carlo techniques in a system confined in an external optical lattice in Ref. [181]. A similar effective interaction can be created in a ring cavity and has been studied for droplets in the superradiant regime, i.e. in a lattice, with mean-field methods in Ref. [182].

The total effective Hamiltonian is

$$\begin{aligned} \hat{H} = &\int_{-\frac{L}{2}}^{+\frac{L}{2}} dy \left\{ \hat{\psi}^\dagger(y) \left[-\frac{\nabla^2}{2m} + \frac{U}{2} \hat{\psi}^\dagger(y)\hat{\psi}(y) \right] \hat{\psi}(y) \right\} \\ &+ \frac{1}{2} \int_{-\frac{L}{2}}^{+\frac{L}{2}} dy \int_{-\frac{L}{2}}^{+\frac{L}{2}} dy' \left\{ \hat{\psi}^\dagger(y)\hat{\psi}(y) V_C(y, y') \hat{\psi}^\dagger(y')\hat{\psi}(y') \right\} . \end{aligned} \tag{4.87}$$

Following the generic approach of section 4.3, we verify $\tilde{f}_\xi^{(\mathrm{ti})}(p, p') \ll \tilde{f}_\xi^{(\mathrm{ti})}(0, 0)$ for $p, p' \neq 0$, Eq. (4.24), for the translation invariant envelope $f_\xi^{(\mathrm{ti})}(y, y') = \exp(-|y - y'|^2/\xi^2)$. We have to consider the special case $p = -p'$ in the same way as we had the special case $p = p' = 0$ before so that the estimate can be performed analogous to that of Eq. (4.52). The transformation $\tilde{f}_\xi^{(\mathrm{ti})}(p, p')$ for $p \neq -p'$ is again suppressed by at least $1/(\pi j_\nu)^2$ compared to $\tilde{f}_\xi^{(\mathrm{ti})}(0, 0)$ for $L < \xi$, so that

$$\tilde{f}_\xi^{(\mathrm{ti})}(p, p') = \int_{-\frac{L}{2}}^{+\frac{L}{2}} \frac{dy}{L} \int_{-\frac{L}{2}}^{+\frac{L}{2}} \frac{dy'}{L} \left\{ e^{-ipy} e^{-ip'y'} e^{-\frac{|y-y'|^2}{\xi^2}} \right\} \approx \delta_{p,0} \tilde{f}_\xi^{(\mathrm{ti})}(0, 0) . \tag{4.88}$$

Hence, we have confirmed that we only need to consider the spatial average of the envelope

$$\tilde{f}_\xi^{(\mathrm{ti})}(0, 0) = \frac{\xi^2}{L^2} \left(e^{-\frac{L^2}{\xi^2}} - 1 \right) + \frac{\sqrt{\pi}\xi}{L} \mathrm{erf}\left(\frac{\mathrm{L}}{\xi} \right) . \tag{4.89}$$

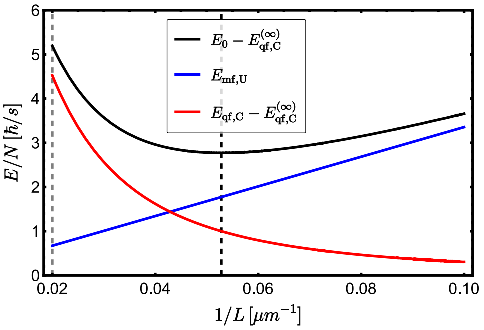

Figure 4.16: Effective energy per particle E_0/N and its constituents for the multi-mode cavity system realizing a translation-invariant long-range interaction versus the inverse system size $1/L$. The system size independent energy shift of the infinite-range interaction term $E^{(\infty)}_{\mathrm{qf,C}}$ is subtracted. The droplet size L_0 at the minimum of the total system energy E_0 is marked by the black dashed line. The parameters are $\omega_R = 2\pi \times 3560$ Hz, $\mathcal{I} = -21.25$ Hz, $N = 10^3$, $\xi = 50\,\mu$m, and $gn_0/\omega_R = 1.6 \times 10^{-4}$.

We can then apply the theory discussed in section 4.3.5 for a translation invariant long-range interaction. Since the wavenumber is non-zero, $k \neq 0$, the homogeneous mean-field $E_{\mathrm{mf,U}} = UN^2/2L$ is unaffected by the cavity-induced interaction. As discussed in section 4.3.5, the translation invariance of $v(y, y') = \cos[k(y - y')]$ restricts the coupling to be momentum conserving, so that the Fourier coefficients of the periodic signature $v(y, y')$ are all $v_{-k,k} = 1/2$ and $\underline{\tilde{v}}$ is diagonal. We know from Eq. (4.41) the dispersion including the long-range interaction

$$\mathcal{E}_p = \sqrt{\frac{p^2}{2m}\left(\frac{p^2}{2m} + 2nU + IN\tilde{f}^{(\mathrm{ti})}_{\xi}(0,0)\sum_{\sigma=\pm}\delta_{\sigma p,k}\right)}\,, \tag{4.90}$$

For $I < 0$ rotons emerge at $p = \pm k$ that are part of the dispersion and precisely those we visualized in figure 4.6. This is a notable difference from the case of the non-translation invariant cavity-induced interaction that we studied in section 4.4. The roton correction of the translation invariant interaction involves a roton at each $k \in \mathcal{K}_C$, i.e. here at $p = \pm k$. The multiplicity of the roton mode influences the cavity-induced quantum correction following Eq. (4.42) and we obtain

$$E_{\mathrm{qf,C}} = \mathcal{E}_k - \omega_k\,, \tag{4.91}$$

since the zero-point motion of each roton contributes.

The effective energy $E_0 = E_{\mathrm{mf,U}} + E_{\mathrm{qf,C}}$ of the competition between the multi-mode cavity-induced quantum correction $E_{\mathrm{qf,C}}$, Eq. (4.91), and the contact interaction mean-field $E_{\mathrm{mf,U}} = UN^2/2L$ is shown in figure (4.16). We observe that the repulsive mean-field energy scaling as $\propto 1/L$ is counteracted by the cavity-induced zero-point motions of the rotons $E_{\mathrm{qf,C}}$ to form the energy minimum of the equilibrium. The dependence on the system size of the rotons encoded in the spatial average of the envelope $\tilde{f}^{(\mathrm{ti})}_{\xi}(0,0)$ determines that and how the quantum correction manages to compete with the mean-field. Expanding the spatial average of the envelope around $L/\xi = 0$ yields

$$\tilde{f}^{(\mathrm{ti})}_{\xi}(0,0) = 1 - \frac{L^2}{6\xi^2} + \mathcal{O}\left(\frac{L^4}{\xi^4}\right)\,. \tag{4.92}$$

The translation invariant cavity-induced interaction with a Gaussian envelope thus again has an infinite-range interaction term $E^{(\infty)}_{\mathrm{qf,C}}$ and a leading L^2 dependence on the spatial extension. Note that the infinite-range term is again crucial to counteract self-evaporation to satisfy (C3), but is not involved in conditions (C1) and (C2) of Eq. (4.1). We conclude from Eqs. (4.91) and (4.92) that the quantum droplet is realized by the multi-mode engineered interaction as it was for the single transversal mode envelope previously in section 4.4. Applying the same approximations as for the analytical study of the single-mode cavity, we find a qualitatively similar description of the effective energy

$$E_0(N,L) = E^{(\infty)}_{\mathrm{qf,C}} + \frac{UN^2}{2L} + \frac{k_{\mathcal{E}}}{2}L^2\,. \tag{4.93}$$

The prefactor of the quantum self-confinement mechanism is

$$k_{\mathcal{E}} = \frac{-IN}{6\xi^2\sqrt{1+(4nU+IN)/4\omega_R}} \approx \frac{-IN}{6\xi^2\sqrt{1+IN/4\omega_R}}\,. \tag{4.94}$$

It shows that the quantum self-confinement is qualitatively the same $\propto L^2$ as for the factorized interaction, see Eq. (4.63). However, there are quantitative differences because of the different dimensionality and the discussed prefactor due to the multiplicity of the roton mode.
Comparing the effective energy, Eq. (4.93), with the minimal model, Eq. (4.2), we get the parameters $a(N) = UN^2/2$ and $b(N) = k_{\mathcal{E}}/2 > 0$. Since here we study a one-dimensional system $V = L$, the final parameter is $c = -3$. To fulfill the conditions for a droplet, the contact interaction must be positive $U > 0$, so we get $a(N) > 0$. Thus we have again a droplet realization of (D3) according to the classification Eq. (4.4).

4.6 – Outlook

The novel type of droplet and its mathematical description opens up many new opportunities for further study. We discuss some of them in this section.

One could consider the effective energy E_0 of the droplet in terms of Landau theory for a second-order phase transition. This would be invaluable in studying the formation of the droplet. To briefly recap the Landau theory, we follow Ref. [191]. In the homogeneous system of our purpose, this theory originally considers the free enthalpy expanded to the form

$$G(T,\varphi) = G(T,0) + \frac{a(T)}{V}\varphi^2 + \frac{b(T)}{V^3}\varphi^4\,, \tag{4.95}$$

for the order parameter

$$\varphi = \int_V d^d\boldsymbol{r}\psi(\boldsymbol{r}) \begin{cases} = 0, \text{if } T > T_C \\ \neq 0, \text{if } T < T_C \end{cases}\,, \tag{4.96}$$

that has a trivial solution or nontrivial solution depending on the control parameter T. The equilibrium value of the order parameter should minimize Eq. (4.95) such that

$$\left(\frac{\partial G}{\partial \varphi}\right)_T = \frac{2a(T)}{V}\varphi + \frac{4b(T)}{V^3}\varphi^3 \overset{!}{=} 0\,. \tag{4.97}$$

There are three solutions for the equilibrium order parameter

$$\varphi_0 = 0 \qquad \wedge \qquad \varphi_0 = \pm\sqrt{-V^2\frac{a(T)}{2b(T)}}\,. \tag{4.98}$$

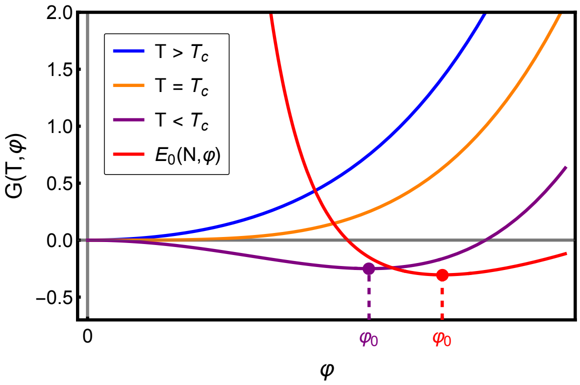

Figure 4.17: Free enthalpy in the Landau theory $G(T, \varphi)$ against the order parameter φ for the control parameter above the critical value (blue), at the critical value (orange), and below the critical value (purple). For the latter, we denote the finite equilibrium value of the order parameter by φ_0. The free enthalpy plot is adapted from Ref. [191]. In addition, we display the effective energy Eq. (4.100) in red with its equilibrium order parameter, i.e. the cavity-induced droplet.

Which solution is the stable one is determined by the second derivative

$$\left(\frac{\partial G}{\partial \varphi}\right)_T \bigg|_{\varphi=\varphi_0} \overset{!}{>} 0\,, \tag{4.99}$$

so that the order parameter minimizes the potential. The minimum condition Eq. (4.99) combined with Eqs. (4.96) and (4.98) imply that $a(T)$ must change sign at the critical value of the control parameter T_C [191]. It must be $0 < a(T > T_C)$ and $a(T < T_C) < 0$ as visualized in figure 4.17.

Returning to our results, let us compare the free enthalpy ansatz of the Landau theory Eq. (4.95) with the effective energy of the one-dimensional droplet, Eq. (4.93), that has the expression

$$\begin{aligned} E_0(N, \varphi = \sqrt{1/L}) &= E^{(\infty)}_{\mathrm{qf,C}}(N) + \frac{UN^2}{2L} + \frac{k_{\mathcal{E}}(N)}{2} L^2 \\ &= E_{\mathrm{qf,C}}(N, \varphi \to \infty) + \frac{UN^2}{2}\varphi^2 + \frac{k_{\mathcal{E}}(N)}{2}\varphi^{-4}\,, \end{aligned} \tag{4.100}$$

where we have chosen the supposed order parameter to be $\varphi = \sqrt{1/L}$. We have sketched this in figure 4.17. Simply from a mathematical perspective, this cannot have a solution $\varphi = 0$ unless $k_{\mathcal{E}} = 0$. This requires that the cavity-induced interaction is absent $I = 0$. Minimizing Eq. (4.100) with respect to the order parameter, like Eq. (4.97), will yield the equivalent result to finding the equilibrium size of the droplet by the zero pressure condition, i.e. $\varphi_0 = 1/L_0$. However, these solutions do not take into account that the theory in its current state is only valid for the global-range interaction $\varphi_0 = 1/L_0 \overset{!}{>} 1/\xi$. Furthermore, in the regime where no droplets are produced, the equilibrium solution φ_0 has complex values instead of φ_0 in Landau theory. Note as well that the order parameter for fluids and gases, both quantum and not, is the square root of the density $\sqrt{n}$ [3]. A description of the droplet state and its formation in a Landau theory would be a powerful tool, but conceptual issues need to be resolved, or our first gullible ansatz for the potential Eq. (4.100) needs to be extensively reworked. Resolving the open question we raise in the next paragraph will help in this endeavor.

Another aspect we view as important is to find a description of the droplet wave function based on an extended Gross-Pitaevskii-like equation. Both established types of quantum droplets are described by such a nonlinear Schrödinger equation, as discussed in section 4.2. Often these descriptions are found by a local density approximation for the condensate order parameter ψ_0. Under this assumption, the density varies slowly with respect to the wavelength of the dominant excitations. For the cavity BEC, we would need to consider the wavelength of the light field, since it selects the roton mode. However, deriving the appropriate equation for the cavity BEC droplet wavefunction raises some conceptual issues. First, the effective ground state energy E_0 cannot be expressed by an energy functional that depends only on the condensate order parameter. In fact, we have found that this is a general problem in the droplet class (D3). Therefore, it seems inevitable to re-derive the zero-point energy quantum correction while closely following the wave function of the condensate mean-field $\psi_0(\boldsymbol{r})$. To perform the derivation analytically, a local density approximation must be applied to $\psi_0(\boldsymbol{r})$ in the sense that it was done for the envelope in Eq. (4.24). One of the benefits of an extended Gross-Pitaevskii-like equation would be to give a more accurate prediction for the droplet that forms in an actual experiment. An extension of the Gross-Pitaevskii equation for the droplet would allow us to determine the shape of the droplet and how it deals with external trapping potentials and their release, which are required in the preparation and handling of the BEC.

An additional avenue worth exploring would be to go to other regimes of the interaction range. In this thesis, we have always discussed a cavity-induced interaction with a global range $L/\xi < 1$. Such a restriction was motivated to keep the Bogoliubov theory analytically solvable because, for the global interaction, we were able to show that only a single atomic excitation mode is modified by the interaction. To put it differently, the roton is effectively so narrow in dispersion that only its central momentum needs to be considered, see figure 4.6. If we were to go to cavity-induced interactions with less than global range $L/\xi > 0$, then the finite width of the roton would have to be respected. Looking at the dispersion, figure 4.6, neighboring modes of $p = \pm k$ would be significantly coupled by the long-range interaction and thus involved in the diagonalization that unveils the eigenmodes. The diagonalization is certainly numerically possible [182]. Furthermore, an evaluation of the cavity-induced quantum correction $E_{\mathrm{qf,C}}$ in the continuum limit might be necessary if a large part of the dispersion is roton-like. We have also used the global-range approximation to make sure that the mean-field is homogeneous, see section 4.3.2. If we go to $L/\xi > 1$ we will find a significant contribution of the cavity already at the mean-field level.
It seems valuable to derive an analytical description of the non-global interaction, considering the quantum Monte-Carlo study of droplets from this type of interaction in Ref. [181]. There, in a lattice model, a distinction is made between strongly glued and weakly glued droplets, the former being those with global-range interaction and the latter those with only local interactions $\xi \ll L_0$. Qualitative differences between the two cases in view of the stability and the order of the phase transition are predicted [181].

In Ref. [171] an effective single-mode description for the Bose-Bose mixture has been derived based on the density and the spin excitation branches of the mixture. We have explored that if such a Bose-Bose mixture is placed in the cavity, the cavity couples at the Bogoliubov level to only one of the excitation branches or the single effective branch of the condensate. Thus, the formalism we have developed is directly applicable to the generalized system. We can imagine a situation in the cavity mixture setup where the mean-field energy is tuned to zero by a Feshbach resonance. In this case, only the attractive quantum correction of the cavity-induced roton and the repulsive LHY correction of the mixture remain in the energy functional. Their interplay could realize a pure quantum droplet without any classical mean-field.

In the thesis, long-range interactions with an exponential decay were studied. Conversely, typical long-range interactions have an algebraic decay. Examples are the Coloumb interaction or the dipolar interaction, Eq. (4.12). It would be interesting to study long-range interactions that combine exponential decay with algebraic decay, similar to the Yukawa potential $e^{-\alpha m r}/r$. Such interaction potentials have been developed in multimode cavities $\cos(kr)e^{-r/\xi}/\sqrt{r/\xi}$ to create optical lattices with sound [79]. These would physically use photons to mediate the interaction. However, by engineering the vacuum fluctuations of the optical cavity, an interaction is realized that effectively selects a roton mode by the periodic signature and then has an algebraically decaying interaction with an effectively massive mediation if we compare the exponential decay to that of the Yukawa potential.

So far in this chapter, we have only dealt with the effective atom-only picture of cavity BEC. Remarkably, the Bogoliubov theory we have developed, with its approximations and treatment of the envelope, can be applied directly to the full field Hamiltonian Eq. (4.47), which includes the full cavity dynamics. From this, we could study droplet signatures in the cavity light or formation of the droplet in the recoil-resolved regime. As we have seen in figure 2.9 in the recoil resolved regime there is a pronounced plateau near the Dicke phase transition where the excitation energy of the soft mode polariton has already vanished but the homogeneous phase is still stable. The existence of this zero-energy excitation was recently verified in an experiment [192]. In this plateau region, we can expect a zero-energy excitation of the droplet, so that a periodic density modulation arises from the beyond mean-field fluctuations. Since the coherence between the periods of the density modulation is maintained, this would constitute a quantum supersolid due to cavity quantum fluctuations. Notably, because of the envelope creating the global droplet on which the density grating acts, this supersolid would be nonstiff as explored for the classical mean-field of a multimode realization in a ring cavity [182].

We have already mentioned in the previous discussion that very close to the phase transition there is a large quantum depletion of the homogeneous mean-field. Thus, this should be taken into account in the narrow regime where we propose to investigate the formation of the quantum supersolid. However, it is also important to study since we have found that operating close to the phase transition is a great way to optimize the droplet.

With the established theory at hand and knowing that it applies to the full cavity BEC field Hamiltonian, higher-order Hamiltonian beyond-Bogoliubov effects can be studied. To do so, we would simply have to combine the approach of the previous chapter 3 [A] with the approximations and light field shapes developed in this chapter [C, D], which are straightforward to amalgamate. The corrections to the leading order terms of the droplet are quite rich. They include the Bose gas LHY correction, Eq. (2.27), neighboring modes of the roton, further terms in the envelope expansion, Eq. (4.60), and the Beliaev damping effects investigated in chapter 3. Without actually performing the calculation, it is difficult to estimate whether their combined effect is beneficial or detrimental to the formation of the droplet. However, considering that the droplet is founded on the interplay of weak s-wave scattering and a finite-size roton correction, it seems relevant to at least explore these next-order corrections of the system.

Another phenomenon of interest for droplets are vortices. Vortices have been studied in the cavity BEC and it has been shown that they alter the energy potential such that the superradiant Dicke transition is shifted and its universality class could be modified [193]. Furthermore, the cavity mediates an interaction between the vortices similar to the cavity-mediated interaction of the atoms. Therefore, inducing vortices will lead to significant changes in the droplet.

In this thesis we have also discussed the parallels between the cavity BEC and the hybrid atom-optomechanical setup, see sections 2.3.10 and 3.4. It is only logical to investigate the possibility of droplet formation in these systems, and indeed such investigations are already underway. A Λ-level scheme like the one in the atom-optomechanical system, see figure 2.13, can also be implemented in the cavity BEC so that the two Bose species of the $|\pm\rangle$ internal atomic state are created [76].

4.7 – Conclusions

We derive an analytical description of a dilute Bose gas with the interplay of two types of interactions. On the one hand, the atoms of the Bose gas undergo a contact interaction, i.e. an effectively infinitesimal short-range interaction. On the other hand, the atoms interact at long-range via a density-density interaction. To treat this latter interaction analytically, we discuss it in the regime where the interaction range is global. Each atom can be correlated with every other atom in the gas. We provide a Bogoliubov theory for this generic system. Effectively, only a few distinct modes are affected by the long-range interaction. If its range is finite, as determined by the envelope function characterizing its spatial decay, its coupling strength in momentum space is dependent on the system size. A locally attractive long-range interaction produces roton modes in the excitation spectrum of the atomic gas. Consequently, the softness of these rotons is influenced by changes in system size. Since the leading ground state energy correction from quantum fluctuations is the zero-point motion of the rotons, the quantum energy correction depends on the system size. It can compete with the mean-field energy of the Bose gas to form a quantum droplet.

The few roton modes from the long-range interaction manage to destabilize the gas of stable mean-field. The discovered mechanism is drastically different from the established quantum droplets in dipolar Bose gases and Bose-Bose mixtures [45, 58, 59, 174]. In these systems, the mean-field is destabilized utilizing Feshbach resonances. The quantum fluctuation corrections of the contact and dipolar interaction contribute to a stabilization mechanism and a liquid self-bound state emerges. We generalize the notion of a quantum droplet to include finite-size effects such as the distinct roton modes, which provide an energy correction that is not extensive. This naturally leads to a new class of droplets that can only persist in the thermodynamics of finite-size systems. We show that the droplets introduced here are of this novel type.

Subsequently, we apply the theory to the single-mode cavity BEC system. In this setup, the light field shape is determined by the longitudinal and transversal functions describing the light mode. The cavity-mediated interaction leads to the formation of a single distinct roton mode. It is tunable by cavity parameters such as the pump laser power, the cavity pump detuning, or the transversal size of the pump and cavity light fields. We derive the effective energy potential analytically. Its leading terms are the mean-field energy of the Bose gas, the quantum correction induced in the limit of the infinite interaction range of the cavity, and a correction to this infinite-range quantum correction characterized by the finite-range interaction envelope. The minimization of the energy potential with respect to the system size determines the size of the self-bound quantum droplet. Only the mean-field and the finite-range correction of the quantum fluctuations are involved in the interplay that determines the minimum. Their algebraic dependencies determine the classification of the droplet as a novel type.

Furthermore, we provide a description of the droplet mechanism in thermodynamic terms. The mean-field of the stable Bose gas contributes a positive pressure. This is countered by the cavity-induced quantum fluctuations, which create a negative pressure. The competition between the two underlies the emergence of the mechanically stable droplet with its positive bulk compressibility. Notably, the bulk modulus and hence the speed of sound in the quantum liquid is reduced compared to that of the Bose gas without the cavity. The droplet criteria of pressure and compressibility are unaffected by the infinite-range correction term in the effective energy potential, which carries no information about the interaction envelope or the system size. However, this term is the leading term in the chemical potential and it is essential that it is negative to avoid self-evaporation of the droplet. We investigate the role of the finite temperature for the droplet in the single cavity mode setup and reveal a critical temperature for droplet formation.

The effective energy potential can be modified by the size and shape of the envelope, which characterize the long-range interaction. Their modification changes the properties of the quantum droplet such as its size and confinement. We find that the optimal profile of the envelope is sensitive to the remaining parameters of the setup.

Another modification of the interaction is the addition of symmetries. We study a translation invariant interaction that can be induced in multi-mode cavities. Our results show that the discovered droplet mechanism is qualitatively upheld despite the different physical origins of the interaction properties. However, the modification of the interaction brings quantitative differences, e.g. in the droplet size. A contributing aspect is the emergence of multiple roton modes, which, in contrast to the interaction of the single mode cavity, are part of the dispersion of the Bose gas. Notably, multiple roton modes add their zero-point energy to the correction of the ground state energy.

We present a new type of quantum liquid droplet that relies on a long-range atom-atom interaction which can be engineered by a cavity. Thus, we demonstrate that cavity BEC can be used to simulate quantum bound and aggregate states with the unprecedented control and observability that the cavity setup provides. In particular, we emphasize that not only is the strength of the interaction potential continuously tunable during an experiment, but also its profile can be adjusted, leading to qualitative changes in the effective energy potential of the droplet. It can be used to further explore new quantum many-body states in driven-dissipative systems. The self-bound nature of the system thus opens avenues for the study of nucleation, quantum sensing, and interferometry, and is potentially viable for long-term operation of cold gas setups and hence quantum computing.

5 – Summary and Outlook

In this thesis, we studied the intricate quantum fluctuations in a cavity BEC system. The setup places a condensate of atoms in an optical resonator. Each atom is modeled by a two-level system and its transition is pumped far off-resonance by the standing wave of a retroreflected laser transversal to the cavity axis. The atoms and the cavity light become coupled strongly on a quantum level due to the Purcell effect for the Rayleigh scattering processes. In the BEC exists a weak atom-atom interaction modeled by s-wave scattering. Quantum fluctuations arise in the atomic sector and in parallel emerge in the quantum light field due to their coupling. In the cavity BEC the strength of the pump laser driving the internal transition of the atoms is proportional to the coupling between the atoms and the quantum fluctuations in the cavity. This parameter is easily accessible and finely tunable in the experiment. We demonstrated in this thesis that the quantum fluctuations, which we study, and hence the phenomena arising from them are directly influenced by such accessible parameters. The setup realizes a rich phase diagram where the fluctuations are fundamental for the quantum phase transitions [23, 25, 26, 36]. Light lost from the cavity can be detected and, hence, the system and its dynamics can be studied in situ [28]. We have explored and successfully shown in this thesis that this provides an exceptional platform to realize, investigate, control, and exploit quantum fluctuation phenomena. In particular, decoherence effects and novel aggregate states of matter have been the two focus points of the thesis.

In the first project, we explored decoherence and exercising control over it. The particular effects under investigation arise from intrinsic damping due to quantum fluctuations in the weakly interacting condensate. These create phonon-like damping that takes the form of Landau and Beliaev damping processes. Due to the entanglement between the cavity and the atoms the damping couples to both sectors. Intriguingly, the damping couples stronger to the cavity photon mode than it does within the atoms. We revealed exotic spectral properties of the dissipative bath. It shows competition between damping and antidamping channels and sub-Ohmic signatures. The latter is connected to non-Markovian dynamics and exciting coherence effects. We established that the dissipative bath is controllable by tuning typical parameters of experiments. In addition, thermal effects were included and quantified.

Subsequently, we studied the signatures of the quantum dissipative bath in the system observables. We noticed that the central quantum system of polaritons is renormalized by a Stokes shift. Quantitative results were presented that the Stokes shift translates to a measurable shift of the critical point of the quantum phase transition. The transition and phase are related to the Dicke phase transition and the Dicke model [23], one of the fundamental models of light-matter interaction [24]. Further, we showed that there are signatures of the dissipation in observable fluctuations beyond the Stokes shift effects. In the cavity BEC the respective observables can be measured in situ and we showed how they are influenced by a change in the tuning of external parameters.

Intricate quantum dissipation with sub-Ohmic damping, $1/f$ noise, non-Markovian dynamics, and strong memory effects have only really developed into a field of research after the turn of the millennium, driven by dephasing and relaxation of, e.g., Josephson qubits with their $1/f$ noise [148]. Understanding and simulating the dissipative dynamics of quantum systems is not only relevant to qubits, molecular, and biological physics, but also reservoir engineering, which is seen as a resource to control quantum computing setups [30, 31, 129, 130, 136–138, 143, 148]. The setup investigated here expands on the typically studied systems like the spin-boson model and involves strong light-matter coupling with hybridization of the two and study of the dissipation effects in the vicinity of a non-equilibrium quantum phase transition.

In the second project, we investigated the aggregate state of a quantum droplet which is a novel state of matter realized by the competition of an attractive and a repulsive interaction. The state has zero pressure, positive compressibility, and negative chemical potential and is therefore the thermodynamically stable state of a self-bound quantum liquid [5]. A generic minimal model of the effective ground state energy can satisfy the quantum droplet criteria for different regimes of its model parameters. Based on these parameter regimes we introduced a systematic classification of quantum droplets. This novel classification is founded on an effective energy potential and therefore droplets with finite-size effects are contained in our formalism. We found that one of the droplet classes has been neither predicted nor found in an experiment. A generic long-range interaction of the type realized in the cavity BEC was constructed. The interaction has a periodic signature and a spatial decay inspired by transversal light field modes where the decay is exponential. We described this property of the long-range interaction by an envelope function. We developed a Bogoliubov theory to solve the quantum corrections around the mean-field analytically. For analytical solvability, we assume that the envelope varies slowly in position space compared to the excitations of the finite system. The equivalent statement is that the Fourier transformation of the envelope must be narrow. In leading order, the quantum correction is the zero-point energy of distinct roton modes induced by the long-range interaction. The coupling of the long-range interaction in reciprocal space depends on the size of the system relative to the interaction range. With the softness of the rotons depending on the system size, the quantum correction is system-size dependent as well. Consequently, the correction competes with the mean-field and a quantum droplet can form.

Having developed the generic formalism, we applied it to the single-mode cavity BEC setup, and in particular, the long-range interaction engineered in it by the interplay of the cavity mode and the pump field. We uncovered how the zero-point energy of a single distinct roton selected by the light field momentum interplays with the mean-field of the repulsive interaction within the Bose gas. It became evident that the roton in a finite-size system can facilitate the formation of a droplet. We showed that corrections to the notion that the cavity-induced interaction is infinite-range are essential for the formation of the droplet. These corrections modify the roton mode. For a long-range interaction with a global range, the first-order expansion around infinite-range interaction is accurate and allowed us to derive an analytical model for the droplet. This model for the effective energy of mean-field and quantum correction yields an analytic solution for the droplet size. Furthermore, it shows that the self-confinement is qualitatively similar to harmonic trapping. Thus, we have demonstrated a droplet of the previously found novel droplet class. Subsequently, we studied how the droplet can be optimized by typical tuning parameters of an experiment and successfully described these results by the analytical model. We provided a thermodynamic interpretation in terms of pressure, compressibility, and chemical potential of the ensemble. In addition, we derived finite temperature effects and expose a critical temperature for a droplet to exist. Furthermore, we studied other exponential interaction drop-offs of other shapes and symmetries. Interactions of different geometries and symmetries have already been realized in the cavity BEC [35, 70, 79]. Painting the cavity-mediated interaction so that the setup offers near endless freedom in molding the potential has been proposed very recently [78]. The setup can then be utilized to test characteristics of long-range interactions and probe the emergence of novel many-body quantum states like the self-bound quantum liquid droplets or beyond-mean-field supersolids based on our predictions of qualitatively tuning the stabilizing mechanism provided by the fluctuations. Notably, this novel quantum state would then be realized in a driven-dissipative system where the physics of phase transitions is subject to active research. The exploration of this physics relates to nucleation processes, supercold helium physics, and superconductivity [10, 39, 40, 163–165]. From there even a connection to the fundamental physics of our universe could be raised in the context of emergence [5].

Taking a broader view, in both parts of this thesis we have investigated novel quantum many-body phenomena using the vacuum of the electromagnetic field in a cavity to facilitate, tune, and observe them. Our motivation, as we conceptualized in the introduction, is to employ quantum simulations [1] to aid the development and testing of theories for phenomena that emerge throughout physics and in particular in many-body condensed matter which have proven difficult to model. The challenge of many-body scenarios effects that are unpredictable from fundamental theories is common throughout physics [4]. However, the mathematical mechanisms underlying the emergences are the same all over [4, 5].

Our projects revealed quantum dissipative phenomena that go beyond basic reservoir models and a new type of quantum droplet. Underlying the two phenomena is the interplay of s-wave scattering in the weakly interacting dilute Bose condensate and the coupling of the atoms to the cavity light field. The driven-dissipative system produced by this setup then can host effects from both the competition and the complementation of the two interactions. In the cavity BEC setup, the nondestructive measurements and hence in situ observation can be performed. Furthermore, the light-matter coupling is freely adjustable even during an experimental run. If Feshbach resonances are utilized, even the other interaction of the s-wave scattering can be tuned so that the entire interaction landscape is modifiable in an experiment. Thus, we provide testable theoretical predictions of intriguing quantum physics in a realizable setup which now await their experimental scrutiny.

Appendix

A.1 – Bogoliubov transformation

We start with the second-order terms of the Hamiltonian of the Bose gas in momentum space, Eq. (2.20),

$$\hat{H}_2 = {\sum_{\boldsymbol{p}}}' \left[\left(\frac{\boldsymbol{p}^2}{2m} + nU \right) \hat{\psi}^\dagger_{\boldsymbol{p}} \hat{\psi}_{\boldsymbol{p}} + \frac{nU}{2} \left(\hat{\psi}^\dagger_{\boldsymbol{p}} \hat{\psi}^\dagger_{-\boldsymbol{p}} + \hat{\psi}_{-\boldsymbol{p}} \hat{\psi}_{\boldsymbol{p}} \right) + \frac{m(nU)^2}{2\boldsymbol{p}^2} \right] , \tag{A.1}$$

and apply the Bogoliubov transformation, Eq. (2.21),

$$\hat{\psi}_{\boldsymbol{p}} = u_{\boldsymbol{p}} \hat{\varphi}_{\boldsymbol{p}} - v^*_{\boldsymbol{p}} \hat{\varphi}^\dagger_{-\boldsymbol{p}} , \qquad \hat{\psi}^\dagger_{\boldsymbol{p}} = u^*_{\boldsymbol{p}} \hat{\varphi}^\dagger_{\boldsymbol{p}} - v_{\boldsymbol{p}} \hat{\varphi}_{-\boldsymbol{p}} . \tag{A.2}$$

Utilizing $u_{-\boldsymbol{p}} = u_{\boldsymbol{p}}$ and $v_{-\boldsymbol{p}} = v_{\boldsymbol{p}}$, we get

$$\begin{aligned} \hat{H}_2 = {\sum_{\boldsymbol{p}}}' \Bigg[& \left(\frac{\boldsymbol{p}^2}{2m} + nU \right) \left(|u_{\boldsymbol{p}}|^2 \hat{\varphi}^\dagger_{\boldsymbol{p}} \hat{\varphi}_{\boldsymbol{p}} + |v_{\boldsymbol{p}}|^2 \hat{\varphi}_{-\boldsymbol{p}} \hat{\varphi}^\dagger_{-\boldsymbol{p}} - u^*_{\boldsymbol{p}} v^*_{\boldsymbol{p}} \hat{\varphi}^\dagger_{\boldsymbol{p}} \hat{\varphi}^\dagger_{-\boldsymbol{p}} - v_{\boldsymbol{p}} u_{\boldsymbol{p}} \hat{\varphi}_{-\boldsymbol{p}} \hat{\varphi}_{\boldsymbol{p}} \right) \\ & + \frac{nU}{2} \left([u^{*2}_{\boldsymbol{p}} + v^{*2}_{\boldsymbol{p}}] \hat{\varphi}^\dagger_{\boldsymbol{p}} \hat{\varphi}^\dagger_{-\boldsymbol{p}} + [u^2_{\boldsymbol{p}} + v^2_{\boldsymbol{p}}] \hat{\varphi}_{-\boldsymbol{p}} \hat{\varphi}_{\boldsymbol{p}} - [u^*_{\boldsymbol{p}} v_{\boldsymbol{p}} + v^*_{\boldsymbol{p}} u_{\boldsymbol{p}}] [\hat{\varphi}^\dagger_{\boldsymbol{p}} \hat{\varphi}_{\boldsymbol{p}} + \hat{\varphi}_{-\boldsymbol{p}} \hat{\varphi}^\dagger_{-\boldsymbol{p}}] \right) + \frac{m(nU)^2}{2\boldsymbol{p}^2} \Bigg] . \end{aligned} \tag{A.3}$$

We now apply the commutation relation $[\hat{\varphi}_{-\boldsymbol{p}}, \hat{\varphi}^\dagger_{-\boldsymbol{p}}] = 1$ and exchange terms in the $\boldsymbol{p}$-sum between $\boldsymbol{p}$ and $-\boldsymbol{p}$ to obtain

$$\begin{aligned} \hat{H}_2 = {\sum_{\boldsymbol{p}}}' \Bigg[& \left(\frac{\boldsymbol{p}^2}{2m} + nU \right) \left([|u_{\boldsymbol{p}}|^2 + |v_{\boldsymbol{p}}|^2] \hat{\varphi}^\dagger_{\boldsymbol{p}} \hat{\varphi}_{\boldsymbol{p}} + |v_{\boldsymbol{p}}|^2 - u^*_{\boldsymbol{p}} v^*_{\boldsymbol{p}} \hat{\varphi}^\dagger_{\boldsymbol{p}} \hat{\varphi}^\dagger_{-\boldsymbol{p}} - v_{\boldsymbol{p}} u_{\boldsymbol{p}} \hat{\varphi}_{-\boldsymbol{p}} \hat{\varphi}_{\boldsymbol{p}} \right) \\ & + \frac{nU}{2} \left([u^{*2}_{\boldsymbol{p}} + v^{*2}_{\boldsymbol{p}}] \hat{\varphi}^\dagger_{\boldsymbol{p}} \hat{\varphi}^\dagger_{-\boldsymbol{p}} + [u^2_{\boldsymbol{p}} + v^2_{\boldsymbol{p}}] \hat{\varphi}_{-\boldsymbol{p}} \hat{\varphi}_{\boldsymbol{p}} - [u^*_{\boldsymbol{p}} v_{\boldsymbol{p}} + v^*_{\boldsymbol{p}} u_{\boldsymbol{p}}] [2 \hat{\varphi}^\dagger_{\boldsymbol{p}} \hat{\varphi}_{\boldsymbol{p}} + 1] \right) + \frac{m(nU)^2}{2\boldsymbol{p}^2} \Bigg] . \end{aligned} \tag{A.4}$$

In view of the target to diagonalize the Hamiltonian, i.e. the $\hat{\varphi}^\dagger_{\boldsymbol{p}} \hat{\varphi}^\dagger_{-\boldsymbol{p}}$ and $\hat{\varphi}_{-\boldsymbol{p}} \hat{\varphi}_{\boldsymbol{p}}$ terms must cancel, we obtain the diagonalization condition, Eq. (2.23),

$$-\left(\frac{\boldsymbol{p}^2}{2m} + nU \right) u_{\boldsymbol{p}} v_{\boldsymbol{p}} + \frac{nU}{2} \left(u^2_{\boldsymbol{p}} + v^2_{\boldsymbol{p}} \right) = 0 . \tag{A.5}$$

We discussed in the main text that the coefficients have to adhere to the characteristic equation for hyperbolic functions which is

$$[\hat{\varphi}_{\boldsymbol{p}}, \hat{\varphi}^\dagger_{\boldsymbol{p}'}] = u_{\boldsymbol{p}} u^*_{\boldsymbol{p}'} [\hat{\psi}_{\boldsymbol{p}}, \hat{\psi}^\dagger_{\boldsymbol{p}'}] + v^*_{\boldsymbol{p}} v_{\boldsymbol{p}'} [\hat{\psi}^\dagger_{-\boldsymbol{p}}, \hat{\psi}_{-\boldsymbol{p}'}] = (u_{\boldsymbol{p}} u^*_{\boldsymbol{p}'} - v^*_{\boldsymbol{p}} v_{\boldsymbol{p}'}) \delta^{(3)}_{\boldsymbol{p},\boldsymbol{p}'} \quad \Rightarrow \quad |u_{\boldsymbol{p}}|^2 - |v_{\boldsymbol{p}}|^2 = 1 , \tag{A.6}$$

so that the transformation is canonical. We thus take the ansatz, Eq. (2.22),

$$u_{\boldsymbol{p}} = \cosh(\alpha_{\boldsymbol{p}}) , \qquad v_{\boldsymbol{p}} = \sinh(\alpha_{\boldsymbol{p}}) , \tag{A.7}$$

and insert it into the diagonalization condition, which yields

$$\begin{aligned}-\left(\frac{\boldsymbol{p}^2}{2m}+nU\right)\cosh(\alpha_{\boldsymbol{p}})\sinh(\alpha_{\boldsymbol{p}})+\frac{nU}{2}\left(\cosh(\alpha_{\boldsymbol{p}})^2+\sinh(\alpha_{\boldsymbol{p}})^2\right)&=0\\ -\left(\frac{\boldsymbol{p}^2}{2m}+nU\right)\sinh(2\alpha_{\boldsymbol{p}})+nU\cosh(2\alpha_{\boldsymbol{p}})&=0\\ \tanh(2\alpha_{\boldsymbol{p}})&=\frac{nU}{\frac{\boldsymbol{p}^2}{2m}+nU}\,,\end{aligned}\tag{A.8}$$

where using the hyperbolic identities $\cosh^2(\alpha_{\boldsymbol{p}})+\sinh^2(\alpha_{\boldsymbol{p}})=\cosh(2\alpha_{\boldsymbol{p}})$ and $2\cosh(\alpha_{\boldsymbol{p}})\sinh(\alpha_{\boldsymbol{p}})=\sinh(2\alpha_{\boldsymbol{p}})$ we have attained Eq. (2.24) for the transformation parameter $\alpha_{\boldsymbol{p}}$. Having now obtained the transformation coefficients $u_{\boldsymbol{p}}$ and $v_{\boldsymbol{p}}$, we can reinsert them into the second-order Hamiltonian to find the eigenfrequencies as well as their zero-point motion that are founded on the $[\hat\varphi_{-\boldsymbol{p}},\hat\varphi^\dagger_{-\boldsymbol{p}}]=1$ commutation. We get

$$\hat H_2=\sum_{\boldsymbol{p}}{}'\left[\left(\frac{\boldsymbol{p}^2}{2m}+nU\right)\left(\cosh(2\alpha_{\boldsymbol{p}})\hat\varphi^\dagger_{\boldsymbol{p}}\hat\varphi_{\boldsymbol{p}}+\sinh(\alpha_{\boldsymbol{p}})^2\right)-\frac{nU}{2}\sinh(2\alpha_{\boldsymbol{p}})\left(2\hat\varphi^\dagger_{\boldsymbol{p}}\hat\varphi_{\boldsymbol{p}}+1\right)+\frac{m(nU)^2}{2\boldsymbol{p}^2}\right].\tag{A.9}$$

We now use the identities $\cosh(\mathrm{artanh}(u))=(1-u^2)^{-1/2}$, $\sinh(\mathrm{artanh}(u))=u(1-u^2)^{-1/2}$, and $\sinh(\mathrm{artanh}(u)/2)^2=[(1-u^2)^{-1/2}-1]/2$ to find the expression

$$\begin{aligned}\hat H_2=\sum_{\boldsymbol{p}}{}'&\left[\left(\frac{\frac{\boldsymbol{p}^2}{2m}+nU}{\sqrt{1-\left(\frac{nU}{\frac{\boldsymbol{p}^2}{2m}+nU}\right)^2}}-\frac{nU}{\sqrt{1-\left(\frac{nU}{\frac{\boldsymbol{p}^2}{2m}+nU}\right)^2}}\frac{nU}{\frac{\boldsymbol{p}^2}{2m}+nU}\right)\hat\varphi^\dagger_{\boldsymbol{p}}\hat\varphi_{\boldsymbol{p}}\right.\\ &\left.+\frac{1}{2}\left(-\frac{\boldsymbol{p}^2}{2m}-nU+\frac{\frac{\boldsymbol{p}^2}{2m}+nU}{\sqrt{1-\left(\frac{nU}{\frac{\boldsymbol{p}^2}{2m}+nU}\right)^2}}-\frac{nU}{\sqrt{1-\left(\frac{nU}{\frac{\boldsymbol{p}^2}{2m}+nU}\right)^2}}\frac{nU}{\frac{\boldsymbol{p}^2}{2m}+nU}\right)+\frac{m(nU)^2}{2\boldsymbol{p}^2}\right]\\ =\sum_{\boldsymbol{p}}{}'&\left[\frac{\left(\frac{\boldsymbol{p}^2}{2m}+nU\right)^2-(nU)^2}{\sqrt{\left(\frac{\boldsymbol{p}^2}{2m}+nU\right)^2-(nU)^2}}\hat\varphi^\dagger_{\boldsymbol{p}}\hat\varphi_{\boldsymbol{p}}+\frac{1}{2}\left(-\frac{\boldsymbol{p}^2}{2m}-nU+\frac{\left(\frac{\boldsymbol{p}^2}{2m}+nU\right)^2-(nU)^2}{\sqrt{\left(\frac{\boldsymbol{p}^2}{2m}+nU\right)^2-(nU)^2}}\right)+\frac{m(nU)^2}{2\boldsymbol{p}^2}\right]\\ =\sum_{\boldsymbol{p}}{}'&\left[\sqrt{\frac{\boldsymbol{p}^2}{2m}\left(\frac{\boldsymbol{p}^2}{2m}+2nU\right)}\hat\varphi^\dagger_{\boldsymbol{p}}\hat\varphi_{\boldsymbol{p}}+\frac{1}{2}\left(\sqrt{\frac{\boldsymbol{p}^2}{2m}\left(\frac{\boldsymbol{p}^2}{2m}+2nU\right)}-\frac{\boldsymbol{p}^2}{2m}-nU\right)+\frac{m(nU)^2}{2\boldsymbol{p}^2}\right]\\ =\sum_{\boldsymbol{p}}{}'&\left[\omega_{\boldsymbol{p}}\hat\varphi^\dagger_{\boldsymbol{p}}\hat\varphi_{\boldsymbol{p}}+\frac{1}{2}\left(\omega_{\boldsymbol{p}}-\frac{\boldsymbol{p}^2}{2m}-nU+\frac{m(nU)^2}{\boldsymbol{p}^2}\right)\right]\,,\end{aligned}\tag{A.10}$$

where we have obtained the second-order terms of Eq. (2.26) with the Bogoliubov dispersion, Eq. (2.25),

$$\omega_{\boldsymbol{p}}=\sqrt{\frac{\boldsymbol{p}^2}{2m}\left(\frac{\boldsymbol{p}^2}{2m}+2nU\right)}\,,\tag{A.11}$$

and the energy correction

$$E_{\mathrm{qf}}=\frac{1}{2}\sum_{\boldsymbol{p}}{}'\left[\omega_{\boldsymbol{p}}-\frac{\boldsymbol{p}^2}{2m}-nU+\frac{m(nU)^2}{\boldsymbol{p}^2}\right]\,.\tag{A.12}$$

Other ways of performing this diagonalization are available and since we exploit it in chapter 4 we introduce also the method using quasi-position operators $\hat{x}_{\boldsymbol{p}}$ and quasi-momentum operators $\hat{y}_{\boldsymbol{p}}$ of Ref. [183]. These operators are defined as

$$\hat{x}_{\boldsymbol{p}} = \sqrt{\frac{m}{\boldsymbol{p}^2}}\left(\hat{\psi}_{\boldsymbol{p}} + \hat{\psi}^\dagger_{-\boldsymbol{p}}\right)\,, \qquad \hat{y}_{\boldsymbol{p}} = -i\sqrt{\frac{\boldsymbol{p}^2}{4m}}\left(\hat{\psi}_{-\boldsymbol{p}} - \hat{\psi}^\dagger_{\boldsymbol{p}}\right)\,, \tag{A.13a}$$

$$[\hat{x}_{\boldsymbol{p}}, \hat{y}_{\boldsymbol{p}}] = i\delta^{(3)}_{\boldsymbol{p},\boldsymbol{p}'}\,, \qquad \hat{x}_{-\boldsymbol{p}} = \hat{x}^\dagger_{\boldsymbol{p}}\,, \qquad \hat{y}_{-\boldsymbol{p}} = \hat{y}^\dagger_{\boldsymbol{p}}\,. \tag{A.13b}$$

We start from Eq. (2.20/A.1) and exchange terms in the $\boldsymbol{p}$-sum as well as commute operators to obtain

$$\begin{aligned}
\hat{H}_2 &= \frac{1}{2}\sum_{\boldsymbol{p}}{}'\Bigg[\frac{\boldsymbol{p}^2}{2m}\left(\hat{\psi}^\dagger_{\boldsymbol{p}}\hat{\psi}_{\boldsymbol{p}} + \hat{\psi}_{-\boldsymbol{p}}\hat{\psi}^\dagger_{-\boldsymbol{p}}\right) + nU\left(\hat{\psi}_{-\boldsymbol{p}}\hat{\psi}_{\boldsymbol{p}} + \hat{\psi}^\dagger_{\boldsymbol{p}}\hat{\psi}_{\boldsymbol{p}} + \hat{\psi}_{-\boldsymbol{p}}\hat{\psi}^\dagger_{-\boldsymbol{p}} + \hat{\psi}^\dagger_{\boldsymbol{p}}\hat{\psi}^\dagger_{-\boldsymbol{p}}\right) \\
&\qquad - \frac{\boldsymbol{p}^2}{2m} - nU + \frac{m(nU)^2}{\boldsymbol{p}^2}\Bigg] \\
&= \frac{1}{2}\sum_{\boldsymbol{p}}{}'\Bigg[-\frac{\boldsymbol{p}^2}{4m}\left(\hat{\psi}_{-\boldsymbol{p}} - \hat{\psi}^\dagger_{\boldsymbol{p}}\right)\left(\hat{\psi}_{\boldsymbol{p}} - \hat{\psi}^\dagger_{-\boldsymbol{p}}\right) + \left(\frac{\boldsymbol{p}^2}{4m} + nU\right)\left(\hat{\psi}_{-\boldsymbol{p}} + \hat{\psi}^\dagger_{\boldsymbol{p}}\right)\left(\hat{\psi}_{\boldsymbol{p}} + \hat{\psi}^\dagger_{-\boldsymbol{p}}\right) \\
&\qquad - \frac{\boldsymbol{p}^2}{2m} - nU + \frac{m(nU)^2}{\boldsymbol{p}^2}\Bigg] \\
&= \frac{1}{2}\sum_{\boldsymbol{p}}{}'\left[\hat{y}_{\boldsymbol{p}}\hat{y}_{-\boldsymbol{p}} + \frac{\boldsymbol{p}^2}{2m}\left(\frac{\boldsymbol{p}^2}{2m} + 2nU\right)\hat{x}_{-\boldsymbol{p}}\hat{x}_{\boldsymbol{p}} - \frac{\boldsymbol{p}^2}{2m} - nU + \frac{m(nU)^2}{\boldsymbol{p}^2}\right].
\end{aligned} \tag{A.14}$$

Another exchange of terms in the sum, in particular $\hat{y}_{\boldsymbol{p}}\hat{y}_{-\boldsymbol{p}}$, yields

$$\hat{H}_2 = \frac{1}{2}\sum_{\boldsymbol{p}}{}'\left[\hat{y}^\dagger_{\boldsymbol{p}}\hat{y}_{\boldsymbol{p}} + \omega^2_{\boldsymbol{p}}\hat{x}^\dagger_{\boldsymbol{p}}\hat{x}_{\boldsymbol{p}} - \frac{\boldsymbol{p}^2}{2m} - nU + \frac{m(nU)^2}{\boldsymbol{p}^2}\right]. \tag{A.15}$$

The reverse transformation [183]

$$\hat{x}_{\boldsymbol{p}} = \sqrt{\frac{1}{2\omega_{\boldsymbol{p}}}}\left(\hat{\varphi}_{\boldsymbol{p}} + \hat{\varphi}^\dagger_{-\boldsymbol{p}}\right)\,, \qquad \hat{y}_{\boldsymbol{p}} = -i\sqrt{\frac{\omega_{\boldsymbol{p}}}{2}}\left(\hat{\varphi}_{-\boldsymbol{p}} - \hat{\varphi}^\dagger_{\boldsymbol{p}}\right), \tag{A.16}$$

yields the second-order terms $\hat{H}_2 = E_{\text{qf}} + \sum_{\boldsymbol{p}}{}'[\omega_{\boldsymbol{p}}\hat{\varphi}^\dagger_{\boldsymbol{p}}\hat{\varphi}_{\boldsymbol{p}}]$ in Eq. (2.26).

A.2 – Lee-Huang-Yang Correction

The LHY correction of the ground state energy is obtained by evaluating E_{qf}, Eq. (A.12), in the continuum limit with $\rho = |\boldsymbol{p}|$ that yields the expression

$$\begin{aligned}
E_{\text{qf}} &= \frac{V}{2(2\pi)^3}\int_{\mathbb{R}^3} d^3\boldsymbol{p}\left\{\omega_{\boldsymbol{p}} - \frac{\boldsymbol{p}^2}{2m} - nU + \frac{m(nU)^2}{\boldsymbol{p}^2}\right\} \\
&= \frac{V}{(2\pi)^2}\int_0^\infty d\rho\left\{\rho^2\sqrt{\frac{\rho^2}{2m}\left(\frac{\rho^2}{2m} + 2nU\right)} - \frac{\rho^4}{2m} - nU\rho^2 + m(nU)^2\right\}.
\end{aligned} \tag{A.17}$$

The substitution $\mathcal{E} = \rho^2/2m$ leads to

$$E_{\text{qf}} = \frac{Vm^{3/2}}{2^{3/2}\pi^2}\int_0^\infty d\mathcal{E}\left\{\mathcal{E}\sqrt{\mathcal{E} + 2nU} - \mathcal{E}^{\frac{3}{2}} - nU\sqrt{\mathcal{E}} + \frac{(nU)^2}{2\sqrt{\mathcal{E}}}\right\}. \tag{A.18}$$

The antiderivative of the first term of the integrand is found with the substitution $v = u + 2nU$ as

$$\begin{aligned}\int du \left\{u\sqrt{u+2nU}\right\} = \int dv \left\{v^{\frac{3}{2}} - 2nU\sqrt{v}\right\} &= \frac{2}{5}v^{\frac{5}{2}} - \frac{4}{3}nUv^{\frac{3}{2}} + C \\ &= \frac{2}{15}(u+2nU)^{\frac{3}{2}}(3u-4nU) + C\,. \end{aligned} \tag{A.19}$$

This is used to obtain Eq. (2.27), i.e.,

$$\begin{aligned} E_{\mathrm{qf}} &= \frac{Vm^{3/2}}{2^{3/2}\pi^2}\left[\frac{2}{15}(\mathcal{E}+2nU)^{\frac{3}{2}}(3\mathcal{E}-4nU) - \frac{2}{5}\mathcal{E}^{\frac{5}{2}} - \frac{2}{3}nU\mathcal{E}^{\frac{3}{2}} + (nU)^2\sqrt{\mathcal{E}}\right]_0^\infty \\ &= \frac{Vm^{3/2}}{2^{3/2}\pi^2}\lim_{\mathcal{E}\to\infty}\left[\frac{2}{5}\mathcal{E}^{\frac{5}{2}} + \frac{2}{3}nU\mathcal{E}^{\frac{3}{2}} - (nU)^2\sqrt{\mathcal{E}} + \mathcal{O}\left(\frac{1}{\sqrt{\mathcal{E}}}\right) - \frac{2}{5}\mathcal{E}^{\frac{5}{2}} - \frac{2}{3}nU\mathcal{E}^{\frac{3}{2}} + (nU)^2\sqrt{\mathcal{E}}\right] \\ &\quad - \frac{Vm^{3/2}}{2^{3/2}\pi^2}\frac{-16\sqrt{2}}{15}(nU)^{\frac{5}{2}} \\ &= \frac{8Vm^{3/2}}{15\pi^2}(nU)^{\frac{5}{2}}\,. \end{aligned} \tag{A.20}$$

A.3 – Thermal correction of the Bose gas

The thermal energy correction Eq. (2.31) is evaluated in the continuum limit following the procedure in Ref. [62]. We have

$$E_{\mathrm{th}} = \frac{1}{\beta}\sum_{\boldsymbol{p}}{}' \ln\left(1-e^{-\beta\omega_{\boldsymbol{p}}}\right) \to \frac{V}{(2\pi)^3\beta}\int d^3\boldsymbol{p}\Big\{\ln\left(1-e^{-\beta\omega_{\boldsymbol{p}}}\right)\Big\}\,. \tag{A.21}$$

Like in the previous section it is $\rho = |\boldsymbol{p}|$ and $\mathcal{E} = \rho^2/2m$ is substituted to obtain

$$E_{\mathrm{th}} = \frac{V}{2\pi^2\beta}\int_0^\infty d\rho\Big\{\rho^2\ln\left(1-e^{-\beta\omega_\rho}\right)\Big\} = \frac{Vm^{3/2}}{2\pi^2\beta}\int_0^\infty d\mathcal{E}\left\{\sqrt{\mathcal{E}}\ln\left[1-\exp\left(-\beta\sqrt{\mathcal{E}^2+2nU\mathcal{E}}\right)\right]\right\}\,. \tag{A.22}$$

Subsequently, partial integration is applied to attain

$$E_{\mathrm{th}} = -\frac{Vm^{3/2}}{2\pi^2\beta}\int_0^\infty d\mathcal{E}\left\{\frac{2}{3}\mathcal{E}^{\frac{3}{2}}\frac{\mathcal{E}+nU}{\sqrt{\mathcal{E}^2+2nU\mathcal{E}}}\frac{\beta}{\exp\left(+\beta\sqrt{\mathcal{E}^2+2nU\mathcal{E}}\right)-1}\right\}\,. \tag{A.23}$$

The substitution with $u = \sqrt{2\beta^2 nU\mathcal{E}}$ yields

$$E_{\mathrm{th}} = \frac{-Vm^{3/2}}{6\pi^2\beta^4(nU)^{3/2}}\int_0^\infty du\left\{u^2\frac{\frac{u^4}{2\beta^2(nU)^2}+u^2}{\sqrt{\frac{u^4}{4\beta^2(nU)^2}+u^2}}\frac{1}{\exp\left(\sqrt{\frac{u^4}{4\beta^2(nU)^2}+u^2}\right)-1}\right\}\,. \tag{A.24}$$

In the low-temperature limit $\beta\to\infty$ this is vastly simplified to the form

$$E_{\mathrm{th}} = \frac{-Vm^{3/2}}{6\pi^2\beta^4(nU)^{3/2}}\int_0^\infty du\left\{\frac{u^3}{e^u-1}\right\} = \frac{-Vm^{3/2}}{6\pi^2\beta^4(nU)^{3/2}}\frac{\pi^4}{15} = \frac{-Vm^{3/2}\pi^2}{90\beta^4(nU)^{3/2}}\,, \tag{A.25}$$

and Eq. (2.33) could be obtained.

A.4 – Transformation of the hybrid atom-optomechanical system

The effective field Hamiltonian for the hybrid atom-optomechanical system is with symmetric coupling $\lambda_{\text{ex}} = 0$ [114, 115]

$$\begin{aligned}\hat{H}_{\text{aom}} = \Omega_m \hat{a}^\dagger \hat{a} + \sum_{\nu=\pm} \int dz \left\{ \hat{\psi}^\dagger_\nu(z) \left[\nu \frac{\Omega_a}{2} - \omega_R \partial_z^2 - \frac{V}{2}\cos(2z) + \frac{U}{2} \sum_{\nu'=\pm} \hat{\psi}^\dagger_{\nu'}(z)\hat{\psi}_{\nu'}(z) \right] \hat{\psi}_\nu(z) \right\} \\ - \frac{\lambda}{2}(\hat{a} + \hat{a}^\dagger) \int dz \left\{ \cos(2z) \left[\hat{\psi}^\dagger_+(z)\hat{\psi}_-(z) + \hat{\psi}^\dagger_-(z)\hat{\psi}_+(z) \right] \right\}. \qquad \text{(A.26)}\end{aligned}$$

In comparison to Eq. (2.73) the system was shifted relative to the light field by a $\pi/2$ phase $\sin(2z) \to \cos(2z)$ and the external optical lattice potential $V_{\nu=\pm}(z) = -V\cos(2z)/2$ applied. Furthermore, the s-wave scattering interaction is assumed to be independent of the internal atomic state $U_{\nu\nu'} = U$. We strictly follow Ref. [115] through the derivation of Eq. (2.75) and a more detailed discussion can be found there. The atomic field operators are expanded in the Wannier functions $w(z - z_j)$ located at the lattice sites $z_j = j\pi$ with $j = 1, \dots, l$. This expansion reads

$$\hat{\psi}_\nu = \sum_{j=1}^{l} w(z - z_j)\hat{b}_{j\nu}\,. \qquad \text{(A.27)}$$

Treating the Wannier expansion in leading order terms and defining them as

$$\begin{aligned} J &= \int dz \left\{ w(z - z_j) \left[\omega_R \partial_z^2 + \frac{V}{2}\cos(2z) \right] w(z - z_{j+1}) \right\}, \\ \Lambda &= \lambda \int dz \Big\{ \cos(2z)|w(z)|^2 \Big\}, \qquad U_{\text{lat}} = U \int dz \Big\{ |w(z)|^4 \Big\}, \qquad \text{(A.28)}\end{aligned}$$

the Hamiltonian has the expression

$$\begin{aligned}\hat{H}_{\text{aom}} = \Omega_m \hat{a}^\dagger \hat{a} + \frac{\Omega_a}{2} \sum_{j=1}^{l} \sum_{\nu=\pm} \nu \hat{b}^\dagger_{j\nu}\hat{b}_{j\nu} - J \sum_{j=1}^{l-1} \sum_{\nu=\pm} \left(\hat{b}^\dagger_{j\nu}\hat{b}_{j+1\nu} + \hat{b}^\dagger_{j+1\nu}\hat{b}_{j\nu} \right) \\ + \frac{U_{\text{lat}}}{2} \sum_{j=1}^{l} \sum_{\nu,\nu'=\pm} \hat{b}^\dagger_{j\nu}\hat{b}^\dagger_{j\nu'}\hat{b}_{j\nu'}\hat{b}_{j\nu} - \frac{\Lambda}{2}(\hat{a} + \hat{a}^\dagger) \sum_{j=1}^{l} \left(\hat{b}^\dagger_{j+}\hat{b}_{j-} + \hat{b}^\dagger_{j-}\hat{b}_{j+} \right). \qquad \text{(A.29)}\end{aligned}$$

Its transformation to momentum space $\hat{b}_{k\nu} = \sum_{j=1}^{l} \hat{b}_{j\nu} e^{-ijk}/\sqrt{l}$ where the momentum index k runs from $-\pi$ to π in equidistant steps $2\pi/l$ yields [115]

$$\begin{aligned}\hat{H}_{\text{aom}} = \Omega_m \hat{a}^\dagger \hat{a} + \sum_{k,\nu} \left(\nu \frac{\Omega_a}{2} - 2J\cos(k) \right) \hat{b}^\dagger_{k\nu}\hat{b}_{k\nu} + \frac{U_{\text{lat}}}{2l} \sum_{k,p,q} \sum_{\nu,\nu'} \hat{b}^\dagger_{k+q\nu}\hat{b}^\dagger_{p-q\nu'}\hat{b}_{p\nu'}\hat{b}_{k\nu} \\ - \frac{\Lambda}{2}(\hat{a} + \hat{a}^\dagger) \sum_{k} \left(\hat{b}^\dagger_{k+}\hat{b}_{k-} + \hat{b}^\dagger_{k-}\hat{b}_{k+} \right). \qquad \text{(A.30)}\end{aligned}$$

Assuming the parameter regime $\lambda, nU \ll \Omega_m, \Omega_a$, the ground state of the system is $(k, \nu) = (0, -)$ [115]. Bogoliubov theory is performed around this mean-field state of the system with [115]

$$\hat{b}_{0-} \approx \hat{b}^\dagger_{0-} \approx \sqrt{\hat{n}_{0-}}\,, \qquad \hat{b}^\dagger_{0-}\hat{b}^\dagger_{0-}\hat{b}_{0-}\hat{b}_{0-} = \hat{n}_{0-}(\hat{n}_{0-} - 1)\,, \qquad \text{(A.31)}$$

$$\hat{n}_{0-} = N - \hat{b}^\dagger_{0+}\hat{b}_{0+} - \sum_{k\neq 0} \sum_{\nu} \hat{b}^\dagger_{k\nu}\hat{b}_{k\nu}\,. \qquad \text{(A.32)}$$

In second order of the fluctuations out of the mean-field n_{0-}, the Hamiltonian is ($n = N/l$) [115]

$$\begin{aligned} H_{\mathrm{aom}} = & \left(-\frac{\Omega_a}{2} - 2J + \frac{nU_{\mathrm{lat}}}{2}\right) N + \Omega_m \hat{a}^\dagger \hat{a} + (\Omega_a + nU_{\mathrm{lat}}) \hat{b}^\dagger_{0+} \hat{b}_{0+} \\ & + \sum_{k\neq 0,\nu} \left(\delta_{\nu,+}\Omega_a + 2J[1-\cos(k)] + nU_{\mathrm{lat}}\right) \hat{b}^\dagger_{k\nu} \hat{b}_{k\nu} - \frac{\Lambda\sqrt{N}}{2} (\hat{a} + \hat{a}^\dagger)(\hat{b}_{0+} + \hat{b}^\dagger_{0+}) \\ & - \frac{\Lambda}{2} (\hat{a} + \hat{a}^\dagger) \sum_{k\neq 0} \left(\hat{b}^\dagger_{k+}\hat{b}_{k-} + \hat{b}^\dagger_{k-}\hat{b}_{k+}\right) + \frac{nU_{\mathrm{lat}}}{2} \sum_{k\neq 0} \left(\hat{b}_{-k-}\hat{b}_{k-} + \hat{b}^\dagger_{k-}\hat{b}_{-k-}\right) . \end{aligned} \tag{A.33}$$

Under the assumption $nU_{\mathrm{lat}} \ll \Omega_a$ the off-diagonal terms for the + branch like $nU_{\mathrm{lat}}\hat{b}_{-k+}\hat{b}_{k+}/2$ are neglected. Hence, the Bogoliubov transformation only needs to address the − branch

$$\hat{c}_{k-} = u_k \hat{c}_{k-} + v_k \hat{c}_{-k-} , \tag{A.34}$$

and $\hat{c}_{k+} = \hat{b}_{k+}$. A canonical transformation must satisfy $u_k^2 - v_k^2 = 1$ and we find the eigenmodes via

$$\begin{pmatrix} 2J[1-\cos(k)] + nU_{\mathrm{lat}} & nU_{\mathrm{lat}} \\ -nU_{\mathrm{lat}} & -2J[1-\cos(-k)] - nU_{\mathrm{lat}} \end{pmatrix} \begin{pmatrix} u_k \\ v_k \end{pmatrix} = \omega_{k-} \begin{pmatrix} u_k \\ v_k \end{pmatrix} . \tag{A.35}$$

The eigenvalues are, Eq. (2.76),

$$\omega_{k-} = 2J[1-\cos(k)] \sqrt{1 + \frac{nU_{\mathrm{lat}}}{J[1-\cos(k)]}} , \tag{A.36}$$

and the eigenvectors are [115]

$$u_k = \sqrt{\frac{2J[1-\cos(k)] + nU_{\mathrm{lat}} + \omega_{k-}}{2\omega_{k-}}} , \qquad v_k = \sqrt{\frac{2J[1-\cos(k)] + nU_{\mathrm{lat}} - \omega_{k-}}{2\omega_{k-}}} . \tag{A.37}$$

The result of the transformations is the Hamiltonian, Eq. (2.75), [115]

$$\begin{aligned} \hat{H}_{\mathrm{lat}} = & \, \Omega_m \hat{a}^\dagger \hat{a} + \Omega_a \hat{c}^\dagger_{0+} \hat{c}_{0+} + \sum_{k\neq 0,\nu} \omega_{k\nu} \hat{c}^\dagger_{k\nu} \hat{c}_{k\nu} - \frac{\Lambda\sqrt{N}}{2} (\hat{a} + \hat{a}^\dagger)(\hat{c}_{0+} + \hat{c}^\dagger_{0+}) \\ & - \frac{\Lambda}{2} (\hat{a} + \hat{a}^\dagger) \sum_{k\neq 0} \left(u_k[\hat{c}^\dagger_{k-}\hat{c}_{k+} + \hat{c}^\dagger_{k+}\hat{c}_{k-}] + v_k[\hat{c}_{k-}\hat{c}_{-k+} + \hat{c}^\dagger_{-k+}\hat{c}^\dagger_{k-}]\right) + \mathrm{const} , \end{aligned} \tag{A.38}$$

where, in addition, it was employed that $\Omega_a + nU_{\mathrm{lat}} \approx \Omega_a$, $\hat{c}_{0+} = \hat{b}_{0+}$, and $\omega_{k+} = \Omega_a + 2J[1-\cos(k)] + nU_{\mathrm{lat}}$.

A.5 – From the cavity BEC system-bath Hamiltonian to its spectral densities

The system-bath Hamiltonian $\hat{H} = \hat{H}_S + \hat{H}_B + \hat{H}_{SB}$ of Eqs. (3.38) to (3.40) is

$$\begin{aligned} \hat{H} = & - \delta_C \hat{a}^\dagger \hat{a} + \omega_1 \hat{\varphi}^\dagger_1 \hat{\varphi}_1 + \lambda_0 \big(\hat{a} + \hat{a}^\dagger\big) \big(\hat{\varphi}_1 + \hat{\varphi}^\dagger_1\big) + {\sum_{\boldsymbol{p}\in\mathcal{P}}}' \Big[\omega_{0,\boldsymbol{p}} \hat{\varphi}^\dagger_{0,\boldsymbol{p}} \hat{\varphi}_{0,\boldsymbol{p}} + \omega_{1,\boldsymbol{p}} \hat{\varphi}^\dagger_{1,\boldsymbol{p}} \hat{\varphi}_{1,\boldsymbol{p}}\Big] \\ & + \Big[\lambda\big(\hat{a} + \hat{a}^\dagger\big) + \eta\big(\hat{\varphi}_1 + \hat{\varphi}^\dagger_1\big)\Big] \big(\hat{L}_1 - \hat{B}_1\big) + \eta\big(u_1 \hat{\varphi}_1 - v_1 \hat{\varphi}^\dagger_1\big)\big(- \hat{L}^\dagger_2 + \hat{B}^\dagger_2\big) \\ & + \eta\big(u_1 \hat{\varphi}^\dagger_1 - v_1 \hat{\varphi}_1\big)\big(- \hat{L}_2 + \hat{B}_2\big) . \end{aligned} \tag{A.39}$$

As discussed in the main text we must evaluate the correlator of the system-bath coupling action $\langle S_{SB}^2\rangle_B$ which is the expression

$$\begin{aligned}
&\langle S_{SB}^2\rangle_B = \int_0^\beta d\tau \int_0^\tau d\tau' \left\langle H_{SB}(\tau)H_{SB}(\tau')\right\rangle_B \\
&= \int_0^\beta d\tau \int_0^\tau d\tau' \bigg\langle \bigg(\Big[\lambda\big(a(\tau)+a^*(\tau)\big)+\eta\big(\varphi_1(\tau)+\varphi_1^*(\tau)\big)\Big]\Big(L_1(\tau)-B_1(\tau)\Big) \\
&\qquad + \eta\Big(u_1\varphi_1(\tau)-v_1\varphi_1^*(\tau)\Big)\Big(-L_2^*(\tau)+B_2^*(\tau)\Big)+\eta\Big(u_1\varphi_1^*(\tau)-v_1\varphi_1(\tau)\Big)\Big(-L_2(\tau)+B_2(\tau)\Big)\bigg)\times \\
&\quad \times\bigg(\Big[\lambda\big(a(\tau')+a^*(\tau')\big)+\eta\big(\varphi_1(\tau')+\varphi_1^*(\tau')\big)\Big]\Big(L_1(\tau')-B_1(\tau')\Big) \\
&\qquad + \eta\Big(u_1\varphi_1(\tau')-v_1\varphi_1^*(\tau')\Big)\Big(-L_2^*(\tau')+B_2^*(\tau')\Big)+\eta\Big(u_1\varphi_1^*(\tau')-v_1\varphi_1(\tau')\Big)\Big(-L_2(\tau')+B_2(\tau')\Big)\bigg)\bigg\rangle_B .
\end{aligned} \tag{A.40}$$

We expressed the bath average, Eq. (3.44), in the form

$$\langle\cdot\rangle_B = \frac{1}{\mathcal{Z}_B}\int \mathcal{D}\left[\varphi^*,\varphi\right](\cdot)\, e^{-S_B[\varphi^*,\varphi]} \tag{A.41}$$

with, Eq. (3.39),

$$H_B = {\sum_{\boldsymbol{p}\in\mathcal{P}}}' \left[\omega_{0,\boldsymbol{p}}\varphi_{0,\boldsymbol{p}}^*\varphi_{0,\boldsymbol{p}}+\omega_{1,\boldsymbol{p}}\varphi_{1,\boldsymbol{p}}^*\varphi_{1,\boldsymbol{p}}\right] . \tag{A.42}$$

We use that since $\varphi_{i,\boldsymbol{p}}$ are the normal modes of $\hat{H}_B$ it is

$$\langle\varphi_{i,\boldsymbol{p}}(\tau)\varphi_{j,\boldsymbol{p}'}(\tau')\rangle_B = \left\langle\varphi_{i,\boldsymbol{p}}^*(\tau)\varphi_{j,\boldsymbol{p}'}^*(\tau')\right\rangle_B = 0\,. \tag{A.43}$$

Therefore, we can derive that

$$\left\langle L_{1,2}^{(*)}(\tau)B_{1,2}^{(*)}(\tau')\right\rangle_B = \left\langle B_{1,2}^{(*)}(\tau)L_{1,2}^{(*)}(\tau')\right\rangle_B = 0\,. \tag{A.44}$$

The correlator determining the influence action expressed in Eq. (3.45) hence is

$$\begin{aligned}
\langle S_{SB}^2\rangle_B = \int_0^\beta d\tau \int_0^\tau d\tau' \bigg\{ &\Big[\lambda\big(a(\tau)+a^*(\tau)\big)+\eta\big(\varphi_1(\tau)+\varphi_1^*(\tau)\big)\Big]\Big\langle L_1(\tau)L_1(\tau')+B_1(\tau)B_1(\tau')\Big\rangle_B\times \\
&\times\Big[\lambda\big(a(\tau')+a^*(\tau')\big)+\eta\big(\varphi_1(\tau')+\varphi_1^*(\tau')\big)\Big] \\
&-\Big[\lambda\big(a(\tau)+a^*(\tau)\big)+\eta\big(\varphi_1(\tau)+\varphi_1^*(\tau)\big)\Big]\Big\langle L_1(\tau)L_2^*(\tau')+B_1(\tau)B_2^*(\tau')\Big\rangle_B\eta\Big(u_1\varphi_1(\tau')-v_1\varphi_1^*(\tau')\Big) \\
&-\Big[\lambda\big(a(\tau)+a^*(\tau)\big)+\eta\big(\varphi_1(\tau)+\varphi_1^*(\tau)\big)\Big]\Big\langle L_1(\tau)L_2(\tau')+B_1(\tau)B_2(\tau')\Big\rangle_B\eta\Big(u_1\varphi_1^*(\tau')-v_1\varphi_1(\tau')\Big) \\
&-\eta\Big(u_1\varphi_1(\tau)-v_1\varphi_1^*(\tau)\Big)\Big\langle L_2^*(\tau)L_1(\tau')+B_2^*(\tau)B_1(\tau')\Big\rangle_B\Big[\lambda\big(a(\tau')+a^*(\tau')\big)+\eta\big(\varphi_1(\tau')+\varphi_1^*(\tau')\big)\Big] \\
&+\eta^2\Big(u_1\varphi_1(\tau)-v_1\varphi_1^*(\tau)\Big)\Big\langle L_2^*(\tau)L_2^*(\tau')+B_2^*(\tau)B_2^*(\tau')\Big\rangle_B\Big(u_1\varphi_1(\tau')-v_1\varphi_1^*(\tau')\Big) \\
&+\eta^2\Big(u_1\varphi_1(\tau)-v_1\varphi_1^*(\tau)\Big)\Big\langle L_2^*(\tau)L_2(\tau')+B_2^*(\tau)B_2(\tau')\Big\rangle_B\Big(u_1\varphi_1^*(\tau')-v_1\varphi_1(\tau')\Big) \\
&-\eta\Big(u_1\varphi_1^*(\tau)-v_1\varphi_1(\tau)\Big)\Big\langle L_2(\tau)L_1(\tau')+B_2(\tau)B_1(\tau')\Big\rangle_B\Big[\lambda\big(a(\tau')+a^*(\tau')\big)+\eta\big(\varphi_1(\tau')+\varphi_1^*(\tau')\big)\Big] \\
&+\eta^2\Big(u_1\varphi_1^*(\tau)-v_1\varphi_1(\tau)\Big)\Big\langle L_2(\tau)L_2^*(\tau')+B_2(\tau)B_2^*(\tau')\Big\rangle_B\Big(u_1\varphi_1(\tau')-v_1\varphi_1^*(\tau')\Big) \\
&+\eta^2\Big(u_1\varphi_1^*(\tau)-v_1\varphi_1(\tau)\Big)\Big\langle L_2(\tau)L_2(\tau')+B_2(\tau)B_2(\tau')\Big\rangle_B\Big(u_1\varphi_1^*(\tau')-v_1\varphi_1(\tau')\Big)\bigg\} .
\end{aligned} \tag{A.45}$$

We now compute the correlators in the interaction picture $\varphi_{i,\boldsymbol{p}}(\tau) = \varphi_{i,\boldsymbol{p}} e^{-\omega_{i,\boldsymbol{p}}\tau}$ and $\varphi^*_{i,\boldsymbol{p}}(\tau) = \varphi^*_{i,\boldsymbol{p}} e^{\omega_{i,\boldsymbol{p}}\tau}$ so that

$$\left\langle \varphi^*_{i,\boldsymbol{p}}(\tau)\varphi_{j,\boldsymbol{p}'}(\tau')\right\rangle_B = \delta_{i,j}\delta^{(2)}_{\boldsymbol{p},\boldsymbol{p}'} n_B(\omega_{i,\boldsymbol{p}})\,, \qquad \left\langle \varphi_{i,\boldsymbol{p}}(\tau)\varphi^*_{j,\boldsymbol{p}'}(\tau')\right\rangle_B = \delta_{i,j}\delta^{(2)}_{\boldsymbol{p},\boldsymbol{p}'} [1 + n_B(\omega_{i,\boldsymbol{p}})]\,. \tag{A.46}$$

For convenience, we define

$$\begin{aligned} \mathcal{U}_{1\boldsymbol{p}} &= u_{0,\boldsymbol{p}} u_{1,\boldsymbol{p}}\,, & \mathcal{U}_{2\boldsymbol{p}} &= v_{0,\boldsymbol{p}} v_{1,\boldsymbol{p}}\,, \\ \mathcal{V}_{1\boldsymbol{p}} &= u_{0,\boldsymbol{p}} v_{1,\boldsymbol{p}}\,, & \mathcal{V}_{2\boldsymbol{p}} &= v_{0,\boldsymbol{p}} u_{1,\boldsymbol{p}}\,, \end{aligned} \tag{A.47}$$

so that Eq. (3.41) becomes

$$\hat{L}_1 = {\sum_{\boldsymbol{p}\in\mathcal{P}}}' \left[(\mathcal{U}_{1\boldsymbol{p}} + \mathcal{U}_{2\boldsymbol{p}}) \left(\hat{\varphi}^\dagger_{0,\boldsymbol{p}} \hat{\varphi}_{1,\boldsymbol{p}} + \hat{\varphi}^\dagger_{1,\boldsymbol{p}} \hat{\varphi}_{0,\boldsymbol{p}} \right) \right]\,, \tag{A.48a}$$

$$\hat{B}_1 = {\sum_{\boldsymbol{p}\in\mathcal{P}}}' \left[(\mathcal{V}_{1\boldsymbol{p}} + \mathcal{V}_{2\boldsymbol{p}}) \left(\hat{\varphi}_{1,-\boldsymbol{p}} \hat{\varphi}_{0,\boldsymbol{p}} + \hat{\varphi}^\dagger_{0,\boldsymbol{p}} \hat{\varphi}^\dagger_{1,-\boldsymbol{p}} \right) \right]\,, \tag{A.48b}$$

$$\hat{L}_2 = {\sum_{\boldsymbol{p}\in\mathcal{P}}}' \left[\mathcal{V}_{2\boldsymbol{p}} \hat{\varphi}^\dagger_{0,\boldsymbol{p}} \hat{\varphi}_{1,\boldsymbol{p}} + \mathcal{V}_{1\boldsymbol{p}} \hat{\varphi}^\dagger_{1,\boldsymbol{p}} \hat{\varphi}_{0,\boldsymbol{p}} \right]\,, \tag{A.48c}$$

$$\hat{B}_2 = {\sum_{\boldsymbol{p}\in\mathcal{P}}}' \left[\mathcal{U}_{1\boldsymbol{p}} \hat{\varphi}_{1,-\boldsymbol{p}} \hat{\varphi}_{0,\boldsymbol{p}} + \mathcal{U}_{2\boldsymbol{p}} \hat{\varphi}^\dagger_{0,\boldsymbol{p}} \hat{\varphi}^\dagger_{1,-\boldsymbol{p}} \right]\,. \tag{A.48d}$$

Hence, we find the first correlator

$$\begin{aligned} \left\langle L_1(\tau) L_1(\tau')\right\rangle_B &= {\sum_{\boldsymbol{p}\in\mathcal{P}}}' \Big[\big(\mathcal{U}_{1\boldsymbol{p}} + \mathcal{U}_{2\boldsymbol{p}}\big)^2 \big(\langle \varphi^*_{0,\boldsymbol{p}}(\tau)\varphi_{0,\boldsymbol{p}}(\tau')\rangle_B \langle \varphi_{1,\boldsymbol{p}}(\tau)\varphi^*_{1,\boldsymbol{p}}(\tau')\rangle_B \\ &\qquad + \langle \varphi_{0,\boldsymbol{p}}(\tau)\varphi^*_{0,\boldsymbol{p}}(\tau')\rangle_B \langle \varphi^*_{1,\boldsymbol{p}}(\tau)\varphi_{1,\boldsymbol{p}}(\tau')\rangle_B \big) \Big] \\ &= {\sum_{\boldsymbol{p}\in\mathcal{P}}}' \Big[\big(\mathcal{U}_{1\boldsymbol{p}} + \mathcal{U}_{2\boldsymbol{p}}\big)^2 \big(n_B(\omega_{0,\boldsymbol{p}})[1 + n_B(\omega_{1,\boldsymbol{p}})] e^{-(\omega_{1,\boldsymbol{p}} - \omega_{0,\boldsymbol{p}})(\tau - \tau')} \\ &\qquad + [1 + n_B(\omega_{0,\boldsymbol{p}})] n_B(\omega_{1,\boldsymbol{p}}) e^{+(\omega_{1,\boldsymbol{p}} - \omega_{0,\boldsymbol{p}})(\tau - \tau')} \big) \Big]\,. \end{aligned} \tag{A.49}$$

Utilizing

$$\begin{aligned} n_B(\omega_{0,\boldsymbol{p}})[1 + n_B(\omega_{1,\boldsymbol{p}})] &= \frac{1}{e^{\beta\omega_{0,\boldsymbol{p}}} - 1} \left[1 + \frac{1}{e^{\beta\omega_{1,\boldsymbol{p}}} - 1} \right] = \frac{1}{e^{\beta\omega_{0,\boldsymbol{p}}} - 1} \left[\frac{e^{\beta\omega_{1,\boldsymbol{p}}} - 1}{e^{\beta\omega_{1,\boldsymbol{p}}} - 1} + \frac{1}{e^{\beta\omega_{1,\boldsymbol{p}}} - 1} \right] \\ &= \frac{e^{\beta\omega_{1,\boldsymbol{p}}}}{\Big(e^{\beta\omega_{0,\boldsymbol{p}}} - 1\Big)\Big(e^{\beta\omega_{1,\boldsymbol{p}}} - 1\Big)} = \frac{e^{\beta\omega_{1,\boldsymbol{p}}}}{\Big(e^{\beta\omega_{0,\boldsymbol{p}}} - 1\Big)\Big(e^{\beta\omega_{1,\boldsymbol{p}}} - 1\Big)} \frac{e^{\beta\omega_{1,\boldsymbol{p}}} - 1 - e^{\beta\omega_{0,\boldsymbol{p}}} + 1}{e^{\beta\omega_{1,\boldsymbol{p}}} - e^{\beta\omega_{0,\boldsymbol{p}}}} \\ &= \left[\frac{1}{e^{\beta\omega_{0,\boldsymbol{p}}} - 1} - \frac{1}{e^{\beta\omega_{1,\boldsymbol{p}}} - 1} \right] \frac{1}{1 - e^{-\beta(\omega_{1,\boldsymbol{p}} - \omega_{0,\boldsymbol{p}})}} = [n_B(\omega_{0,\boldsymbol{p}}) - n_B(\omega_{1,\boldsymbol{p}})] \frac{e^{\beta(\omega_{1,\boldsymbol{p}} - \omega_{0,\boldsymbol{p}})}}{e^{\beta(\omega_{1,\boldsymbol{p}} - \omega_{0,\boldsymbol{p}})} - 1} \\ &= [n_B(\omega_{0,\boldsymbol{p}}) - n_B(\omega_{1,\boldsymbol{p}})] \left[1 + n_B(\omega_{1,\boldsymbol{p}} - \omega_{0,\boldsymbol{p}}) \right]\,, \end{aligned} \tag{A.50a}$$

$$[1 + n_B(\omega_{0,\boldsymbol{p}})] n_B(\omega_{1,\boldsymbol{p}}) = [n_B(\omega_{0,\boldsymbol{p}}) - n_B(\omega_{1,\boldsymbol{p}})]\, n_B(\omega_{1,\boldsymbol{p}} - \omega_{0,\boldsymbol{p}})\,, \tag{A.50b}$$

we get, with the definition of $\omega^L_{\boldsymbol{p}} = \omega_{1,\boldsymbol{p}} - \omega_{0,\boldsymbol{p}}$,

$$\begin{aligned} \left\langle L_1(\tau) L_1(\tau')\right\rangle_B = {\sum_{\boldsymbol{p}\in\mathcal{P}}}' \Big[\big(\mathcal{U}_{1\boldsymbol{p}} + \mathcal{U}_{2\boldsymbol{p}}\big)^2 [n_B(\omega_{0,\boldsymbol{p}}) - n_B(\omega_{1,\boldsymbol{p}})] \times \\ \times \left(\left[1 + n_B(\omega^L_{\boldsymbol{p}})\right] e^{-\omega^L_{\boldsymbol{p}}(\tau - \tau')} + n_B(\omega^L_{\boldsymbol{p}}) e^{+\omega^L_{\boldsymbol{p}}(\tau - \tau')} \right) \Big]\,. \end{aligned} \tag{A.51}$$

We apply the free thermal Green's function $D_\omega(\tau)$, Eq. (3.14), such that

$$\big\langle L_1(\tau)L_1(\tau')\big\rangle_B = \sum_{\boldsymbol{p}\in\mathcal{P}}{}^{\prime} \Big[\big(\mathcal{U}_{1\boldsymbol{p}}+\mathcal{U}_{2\boldsymbol{p}}\big)^2 \mathcal{N}^L_{\boldsymbol{p}} D_{\omega^L_{\boldsymbol{p}}}(\tau-\tau')\Big]\,, \tag{A.52}$$

if we define Eq. (3.51)

$$\mathcal{N}^L_{\boldsymbol{p}} = n_B(\omega_{0,\boldsymbol{p}}) - n_B(\omega_{1,\boldsymbol{p}})\,. \tag{A.53}$$

In the analogous fashion, we calculate the correlator

$$\begin{aligned}\big\langle B_1(\tau)B_1(\tau')\big\rangle_B =& \sum_{\boldsymbol{p}\in\mathcal{P}}{}^{\prime} \Big[\big(\mathcal{V}_{1\boldsymbol{p}}+\mathcal{V}_{2\boldsymbol{p}}\big)^2 \big(\langle\varphi_{0,\boldsymbol{p}}(\tau)\varphi^*_{0,\boldsymbol{p}}(\tau')\rangle_B\langle\varphi_{1,-\boldsymbol{p}}(\tau)\varphi^*_{1,-\boldsymbol{p}}(\tau')\rangle_B \\ &+ \langle\varphi^*_{0,\boldsymbol{p}}(\tau)\varphi_{0,\boldsymbol{p}}(\tau')\rangle_B\langle\varphi^*_{1,-\boldsymbol{p}}(\tau)\varphi_{1,-\boldsymbol{p}}(\tau')\rangle_B\big)\Big] \\ =& \sum_{\boldsymbol{p}\in\mathcal{P}}{}^{\prime} \Big[\big(\mathcal{V}_{1\boldsymbol{p}}+\mathcal{V}_{2\boldsymbol{p}}\big)^2 \big([1+n_B(\omega_{0,\boldsymbol{p}})][1+n_B(\omega_{1,\boldsymbol{p}})]e^{-(\omega_{0,\boldsymbol{p}}+\omega_{1,\boldsymbol{p}})(\tau-\tau')} \\ &+ n_B(\omega_{0,\boldsymbol{p}})n_B(\omega_{1,\boldsymbol{p}})e^{+(\omega_{0,\boldsymbol{p}}+\omega_{1,\boldsymbol{p}})(\tau-\tau')}\big)\Big]\,,\end{aligned} \tag{A.54}$$

where we use $\omega_{i,-\boldsymbol{p}} = \omega_{i,\boldsymbol{p}}$. Utilizing

$$\begin{aligned}[1+n_B(\omega_{0,\boldsymbol{p}})][1+n_B(\omega_{1,\boldsymbol{p}})] &= \frac{e^{\beta\omega_{0,\boldsymbol{p}}}}{e^{\beta\omega_{0,\boldsymbol{p}}}-1}\frac{e^{\beta\omega_{1,\boldsymbol{p}}}}{e^{\beta\omega_{1,\boldsymbol{p}}}-1} = \frac{e^{\beta(\omega_{0,\boldsymbol{p}}+\omega_{1,\boldsymbol{p}})}}{\Big(e^{\beta\omega_{0,\boldsymbol{p}}}-1\Big)\Big(e^{\beta\omega_{1,\boldsymbol{p}}}-1\Big)}\frac{e^{\beta(\omega_{0,\boldsymbol{p}}+\omega_{1,\boldsymbol{p}})}-1}{e^{\beta(\omega_{0,\boldsymbol{p}}+\omega_{1,\boldsymbol{p}})}-1} \\ &= \frac{\Big(e^{\beta\omega_{0,\boldsymbol{p}}}-1\Big)\Big(e^{\beta\omega_{1,\boldsymbol{p}}}-1\Big)+e^{\beta\omega_{0,\boldsymbol{p}}}-1+e^{\beta\omega_{1,\boldsymbol{p}}}-1}{\Big(e^{\beta\omega_{0,\boldsymbol{p}}}-1\Big)\Big(e^{\beta\omega_{1,\boldsymbol{p}}}-1\Big)}\frac{e^{\beta(\omega_{0,\boldsymbol{p}}+\omega_{1,\boldsymbol{p}})}}{e^{\beta(\omega_{0,\boldsymbol{p}}+\omega_{1,\boldsymbol{p}})}-1} \\ &= [1+n_B(\omega_{0,\boldsymbol{p}})+n_B(\omega_{1,\boldsymbol{p}})]\,[1+n_B(\omega_{0,\boldsymbol{p}}+\omega_{1,\boldsymbol{p}})]\,, \qquad \text{(A.55a)} \\ n_B(\omega_{0,\boldsymbol{p}})n_B(\omega_{1,\boldsymbol{p}}) &= [1+n_B(\omega_{0,\boldsymbol{p}})+n_B(\omega_{1,\boldsymbol{p}})]\,n_B(\omega_{0,\boldsymbol{p}}+\omega_{1,\boldsymbol{p}})\,, \qquad \text{(A.55b)}\end{aligned}$$

we attain, with the definition $\omega^B_{\boldsymbol{p}} = \omega_{0,\boldsymbol{p}}+\omega_{1,\boldsymbol{p}}$,

$$\begin{aligned}\big\langle B_1(\tau)B_1(\tau')\big\rangle_B =& \sum_{\boldsymbol{p}\in\mathcal{P}}{}^{\prime} \Big[\big(\mathcal{V}_{1\boldsymbol{p}}+\mathcal{V}_{2\boldsymbol{p}}\big)^2 [1+n_B(\omega_{0,\boldsymbol{p}})+n_B(\omega_{1,\boldsymbol{p}})]\times \\ &\times\Big(\,[1+n_B(\omega^B_{\boldsymbol{p}})]\,e^{-\omega^B_{\boldsymbol{p}}(\tau-\tau')}+n_B(\omega^B_{\boldsymbol{p}})e^{+\omega^B_{\boldsymbol{p}}(\tau-\tau')}\Big)\Big] \\ =& \sum_{\boldsymbol{p}\in\mathcal{P}}{}^{\prime} \Big[\big(\mathcal{V}_{1\boldsymbol{p}}+\mathcal{V}_{2\boldsymbol{p}}\big)^2 \mathcal{N}^B_{\boldsymbol{p}} D_{\omega^B_{\boldsymbol{p}}}(\tau-\tau')\Big]\,,\end{aligned} \tag{A.56}$$

where we apply the definition

$$\mathcal{N}^B_{\boldsymbol{p}} = 1+n_B(\omega_{0,\boldsymbol{p}})+n_B(\omega_{1,\boldsymbol{p}})\,, \tag{A.57}$$

given in Eq. (3.51). Because they always occur alongside each other in Eq. (A.45), the Landau term and the Beliaev term are combined into a single handy correlation function

$$K_{11}(\tau-\tau') = \big\langle L_1(\tau)L_1(\tau')\big\rangle_B + \big\langle B_1(\tau)B_1(\tau')\big\rangle_B\,. \tag{A.58}$$

We discuss in the main text that the treatment in imaginary time and stationary states assumes detailed balance and where necessary we do so by construction. The two correlators we have derived until here in the appendix inherently have the required symmetry $\tau \to \beta - \tau$. This is also true for

$$\begin{aligned}\big\langle L_2(\tau)L_2(\tau')\big\rangle_B &= \sum_{\boldsymbol{p}\in\mathcal{P}} \Big[\mathcal{V}_{1\boldsymbol{p}}\mathcal{V}_{2\boldsymbol{p}}\big(\langle\varphi^*_{0,\boldsymbol{p}}(\tau)\varphi_{0,\boldsymbol{p}}(\tau')\rangle_B\langle\varphi_{1,\boldsymbol{p}}(\tau)\varphi^*_{1,\boldsymbol{p}}(\tau')\rangle_B \\ &\qquad + \langle\varphi_{0,\boldsymbol{p}}(\tau)\varphi^*_{0,\boldsymbol{p}}(\tau')\rangle_B\langle\varphi^*_{1,\boldsymbol{p}}(\tau)\varphi_{1,\boldsymbol{p}}(\tau')\rangle_B\big)\Big] \\ &= \sum_{\boldsymbol{p}\in\mathcal{P}} \Big[\mathcal{V}_{1\boldsymbol{p}}\mathcal{V}_{2\boldsymbol{p}}\mathcal{N}^L_{\boldsymbol{p}} D_{\omega^L_{\boldsymbol{p}}}(\tau-\tau')\Big] = \big\langle L^*_2(\tau)L^*_2(\tau')\big\rangle_B\,, \end{aligned} \tag{A.59}$$

and for

$$\begin{aligned}\big\langle B_2(\tau)B_2(\tau')\big\rangle_B &= \sum_{\boldsymbol{p}\in\mathcal{P}} \Big[\mathcal{U}_{1\boldsymbol{p}}\mathcal{U}_{2\boldsymbol{p}}\big(\langle\varphi_{0,\boldsymbol{p}}(\tau)\varphi^*_{0,\boldsymbol{p}}(\tau')\rangle_B\langle\varphi_{1,-\boldsymbol{p}}(\tau)\varphi^*_{1,-\boldsymbol{p}}(\tau')\rangle_B \\ &\qquad + \langle\varphi^*_{0,\boldsymbol{p}}(\tau)\varphi_{0,\boldsymbol{p}}(\tau')\rangle_B\langle\varphi^*_{1,-\boldsymbol{p}}(\tau)\varphi_{1,-\boldsymbol{p}}(\tau')\rangle_B\big)\Big] \\ &= \sum_{\boldsymbol{p}\in\mathcal{P}} \Big[\mathcal{U}_{1\boldsymbol{p}}\mathcal{U}_{2\boldsymbol{p}}\mathcal{N}^B_{\boldsymbol{p}} D_{\omega^B_{\boldsymbol{p}}}(\tau-\tau')\Big] = \big\langle B^*_2(\tau)B^*_2(\tau')\big\rangle_B\,. \end{aligned} \tag{A.60}$$

Again we combine them as

$$K_{22}(\tau-\tau') = \big\langle L_2(\tau)L_2(\tau')\big\rangle_B + \big\langle B_2(\tau)B_2(\tau')\big\rangle_B\,. \tag{A.61}$$

For the remaining correlation functions, we have to construct the symmetry to satisfy the assumption that the bath is to a good approximation in equilibrium. Note that

$$\big\langle L_1(\tau)L_2(\tau')\big\rangle_B = \langle L^*_2(\tau)L_1(\tau')\rangle_B = \big\langle L_2(\beta-\tau)L_1(\beta-\tau')\big\rangle_B = \big\langle L_1(\beta-\tau)L^*_2(\beta-\tau')\big\rangle_B\,, \tag{A.62a}$$

$$\big\langle B_1(\tau)B_2(\tau')\big\rangle_B = \langle B^*_2(\tau)B_1(\tau')\rangle_B = \big\langle B_2(\beta-\tau)B_1(\beta-\tau')\big\rangle_B = \big\langle B_2(\beta-\tau)B_1(\beta-\tau')\big\rangle_B\,, \tag{A.62b}$$

so that we substitute

$$\left.\begin{array}{l}\big\langle L_1(\tau)L_2(\tau')\big\rangle_B\,, \big\langle L_2(\tau)L_1(\tau')\big\rangle_B\,, \\ \big\langle L_1(\tau)L^*_2(\tau')\big\rangle_B\,, \big\langle L^*_2(\tau)L_1(\tau')\big\rangle_B\end{array}\right\} \to \frac{1}{2}\left[\big\langle L_1(\tau)L_2(\tau')\big\rangle_B + \big\langle L_2(\tau)L_1(\tau')\big\rangle_B\right]\,, \tag{A.63a}$$

$$\left.\begin{array}{l}\big\langle B_1(\tau)B_2(\tau')\big\rangle_B\,, \big\langle B_2(\tau)B_1(\tau')\big\rangle_B\,, \\ \big\langle B_1(\tau)B^*_2(\tau')\big\rangle_B\,, \big\langle B^*_2(\tau)B_1(\tau')\big\rangle_B\end{array}\right\} \to \frac{1}{2}\left[\big\langle B_1(\tau)B_2(\tau')\big\rangle_B + \big\langle B_2(\tau)B_1(\tau')\big\rangle_B\right]\,.$$

The Landau term is

$$\begin{aligned}\frac{1}{2}\left[\big\langle L_1(\tau)L_2(\tau')\big\rangle_B + \big\langle L_2(\tau)L_1(\tau')\big\rangle_B\right] &= \frac{1}{2}{\sum_{\boldsymbol{p}\in\mathcal{P}}}' \Big[\big(\mathcal{U}_{1\boldsymbol{p}} + \mathcal{U}_{2\boldsymbol{p}}\big)\big(\mathcal{V}_{1\boldsymbol{p}} + \mathcal{V}_{2\boldsymbol{p}}\big)\times \\ \times\big(\langle\varphi^*_{0,\boldsymbol{p}}(\tau)\varphi_{0,\boldsymbol{p}}(\tau')\rangle_B\langle\varphi_{1,\boldsymbol{p}}(\tau)\varphi^*_{1,\boldsymbol{p}}(\tau')\rangle_B &+ \langle\varphi_{0,\boldsymbol{p}}(\tau)\varphi^*_{0,\boldsymbol{p}}(\tau')\rangle_B\langle\varphi^*_{1,\boldsymbol{p}}(\tau)\varphi_{1,\boldsymbol{p}}(\tau')\rangle_B\big)\Big] \\ &= \frac{1}{2}{\sum_{\boldsymbol{p}\in\mathcal{P}}}' \Big[\big(\mathcal{U}_{1\boldsymbol{p}} + \mathcal{U}_{2\boldsymbol{p}}\big)\big(\mathcal{V}_{1\boldsymbol{p}} + \mathcal{V}_{2\boldsymbol{p}}\big)\mathcal{N}^L_{\boldsymbol{p}} D_{\omega^L_{\boldsymbol{p}}}(\tau-\tau')\Big]\,, \end{aligned} \tag{A.64}$$

the Beliaev term is

$$\begin{aligned}\frac{1}{2}\left[\big\langle B_1(\tau)B_2(\tau')\big\rangle_B + \big\langle B_2(\tau)B_1(\tau')\big\rangle_B\right] &= \frac{1}{2}{\sum_{\boldsymbol{p}\in\mathcal{P}}}' \Big[\big(\mathcal{V}_{1\boldsymbol{p}} + \mathcal{V}_{2\boldsymbol{p}}\big)\big(\mathcal{U}_{1\boldsymbol{p}} + \mathcal{U}_{2\boldsymbol{p}}\big)\times \\ \times\big(\langle\varphi_{0,\boldsymbol{p}}(\tau)\varphi^*_{0,\boldsymbol{p}}(\tau')\rangle_B\langle\varphi_{1,-\boldsymbol{p}}(\tau)\varphi^*_{1,-\boldsymbol{p}}(\tau')\rangle_B &+ \langle\varphi^*_{0,\boldsymbol{p}}(\tau)\varphi_{0,\boldsymbol{p}}(\tau')\rangle_B\langle\varphi^*_{1,-\boldsymbol{p}}(\tau)\varphi_{1,-\boldsymbol{p}}(\tau')\rangle_B\big)\Big] \\ &= \frac{1}{2}{\sum_{\boldsymbol{p}\in\mathcal{P}}}' \Big[\big(\mathcal{V}_{1\boldsymbol{p}} + \mathcal{V}_{2\boldsymbol{p}}\big)\mathcal{U}_{1\boldsymbol{p}} + \mathcal{U}_{2\boldsymbol{p}}\big)\mathcal{N}^B_{\boldsymbol{p}} D_{\omega^B_{\boldsymbol{p}}}(\tau-\tau')\Big]\,, \end{aligned} \tag{A.65}$$

and we combine them to

$$K_{12}(\tau-\tau') = \frac{-1}{2}\left[\left\langle L_1(\tau)L_2(\tau')\right\rangle_B + \left\langle L_2(\tau)L_1(\tau')\right\rangle_B + \left\langle B_1(\tau)B_2(\tau')\right\rangle_B + \left\langle B_2(\tau)B_1(\tau')\right\rangle_B\right] . \tag{A.66}$$

Note the minus sign to include the minus sign in Eq. (A.45).
Analogously, we treat the final correlation functions

$$\left\langle L_2(\tau)L_2^*(\tau')\right\rangle_B , \left\langle L_2^*(\tau)L_2(\tau')\right\rangle_B \to \frac{1}{2}\left[\left\langle L_2(\tau)L_2^*(\tau')\right\rangle_B + \left\langle L_2^*(\tau)L_2(\tau')\right\rangle_B\right] , \tag{A.67}$$

$$\left\langle B_2(\tau)B_2^*(\tau')\right\rangle_B , \left\langle B_2^*(\tau)B_2(\tau')\right\rangle_B \to \frac{1}{2}\left[\left\langle B_2(\tau)B_2^*(\tau')\right\rangle_B + \left\langle B_2^*(\tau)B_2(\tau')\right\rangle_B\right] , \tag{A.68}$$

that yield the expressions

$$\frac{1}{2}\left[\left\langle L_2(\tau)L_2^*(\tau')\right\rangle_B + \left\langle L_2^*(\tau)L_2(\tau')\right\rangle_B\right] = \frac{1}{2}\sum_{\boldsymbol{p}\in\mathcal{P}}{}' \Big[(\mathcal{V}_{1\boldsymbol{p}}^2 + \mathcal{V}_{2\boldsymbol{p}}^2)\mathcal{N}_{\boldsymbol{p}}^L D_{\omega_{\boldsymbol{p}}^L}(\tau-\tau')\Big] , \tag{A.69a}$$

$$\frac{1}{2}\left[\left\langle B_2(\tau)B_2^*(\tau')\right\rangle_B + \left\langle B_2^*(\tau)B_2(\tau')\right\rangle_B\right] = \frac{1}{2}\sum_{\boldsymbol{p}\in\mathcal{P}}{}' \Big[(\mathcal{U}_{1\boldsymbol{p}}^2 + \mathcal{U}_{2\boldsymbol{p}}^2)\mathcal{N}_{\boldsymbol{p}}^B D_{\omega_{\boldsymbol{p}}^B}(\tau-\tau')\Big] , \tag{A.69b}$$

$$K_{2^*2}(\tau-\tau') = \frac{1}{2}\left[\left\langle L_2(\tau)L_2^*(\tau')\right\rangle_B + \left\langle L_2^*(\tau)L_2(\tau')\right\rangle_B + \left\langle B_2(\tau)B_2^*(\tau')\right\rangle_B + \left\langle B_2^*(\tau)B_2(\tau')\right\rangle_B\right] . \tag{A.69c}$$

We have calculated all the correlation functions that occur in Eq. (A.45) and insert them such that we designate them to which degree of freedom a or φ_1 of the system they couple to

$$\begin{aligned}\left\langle S_{SB}^2\right\rangle_B = \frac{1}{4}\int_0^\beta d\tau \int_0^\beta d\tau' \Big\{ &(a(\tau)+a^*(\tau))K_C(\tau,\tau')(a(\tau')+a^*(\tau')) \\ &+ (a(\tau)+a^*(\tau))K_{AC}(\tau,\tau')(\varphi_1(\tau')+\varphi_1^*(\tau')) + (\varphi_1(\tau)+\varphi_1^*(\tau))K_{AC}(\tau,\tau')(a(\tau')+a^*(\tau')) \\ &+ (\varphi_1(\tau)+\varphi_1^*(\tau))K_A(\tau,\tau')(\varphi_1(\tau')+\varphi_1^*(\tau')) - (\varphi_1(\tau)-\varphi_1^*(\tau))K_{\dot{A}}(\tau,\tau')(\varphi_1(\tau')-\varphi_1^*(\tau'))\Big\} \\ = \frac{1}{2}\int_0^\beta d\tau \int_0^\beta d\tau' \Big\{ &-\delta_C q_C(\tau)K_C(\tau,\tau')q_C(\tau') + \sqrt{-\delta_C\omega_1}q_C(\tau)K_{AC}(\tau,\tau')q_A(\tau') \\ &+ \sqrt{-\delta_C\omega_1}q_A(\tau)K_{AC}(\tau,\tau')q_C(\tau') + \omega_1 q_A(\tau)K_A(\tau,\tau')q_A(\tau) \\ &+ \frac{1}{\omega_1}\dot{q}_A(\tau)K_{\dot{A}}(\tau,\tau')\dot{q}_A(\tau')\Big\} ,\end{aligned} \tag{A.70}$$

where $q_C = (a+a^*)/\sqrt{-2\delta_C}$ as well as $q_A = (\varphi_1+\varphi_1^*)/\sqrt{2\omega_1}$ and we introduced

$$K_C(\tau-\tau') = 2\lambda^2 K_{11}(\tau-\tau') , \tag{A.71a}$$

$$K_{AC}(\tau-\tau') = 2\lambda\eta(u_1-v_1)\big[K_{11}(\tau-\tau') - K_{12}(\tau-\tau')\big] , \tag{A.71b}$$

$$K_A(\tau-\tau') = \eta^2(u_1-v_1)^2\big[2K_{11}(\tau-\tau') + K_{2^*2}(\tau-\tau') + K_{22}(\tau-\tau') - 4K_{12}(\tau-\tau')\big] , \tag{A.71c}$$

$$K_{\dot{A}}(\tau-\tau') = \frac{\eta^2}{(u_1-v_1)^2}\big[K_{2^*2}(\tau-\tau') - K_{22}(\tau-\tau')\big] . \tag{A.71d}$$

Now we use Eq. (3.15), i.e.

$$K(\tau) = \int_0^\infty d\omega\, G(\omega)D_\omega(\tau) , \tag{A.72}$$

to extract the spectral densities $G^{L,B}_{\nu}(\omega)$ with $\nu = \{C, AC, A, \dot{A}\}$

$$G^{L}_{C}(\omega) = \sideset{}{'}\sum_{\boldsymbol{p}\in\mathcal{P}} \Big[2\lambda^2\big(\mathcal{U}_{1\boldsymbol{p}} + \mathcal{U}_{2\boldsymbol{p}}\big)^2 \mathcal{N}^{L}_{\boldsymbol{p}}\delta(\omega - \omega^{L}_{\boldsymbol{p}})\Big]\,, \tag{A.73a}$$

$$G^{B}_{C}(\omega) = \sideset{}{'}\sum_{\boldsymbol{p}\in\mathcal{P}} \Big[2\lambda^2\big(\mathcal{V}_{1\boldsymbol{p}} + \mathcal{V}_{2\boldsymbol{p}}\big)^2 \mathcal{N}^{B}_{\boldsymbol{p}}\delta(\omega - \omega^{B}_{\boldsymbol{p}})\Big]\,, \tag{A.73b}$$

$$G^{L}_{AC}(\omega) = \sideset{}{'}\sum_{\boldsymbol{p}\in\mathcal{P}} \Big[\lambda\eta(u_1 - v_1)\big[2\big(\mathcal{U}_{1\boldsymbol{p}} + \mathcal{U}_{2\boldsymbol{p}}\big)^2 - \big(\mathcal{U}_{1\boldsymbol{p}} + \mathcal{U}_{2\boldsymbol{p}}\big)\big(\mathcal{V}_{1\boldsymbol{p}} + \mathcal{V}_{2\boldsymbol{p}}\big)\big]\mathcal{N}^{L}_{\boldsymbol{p}}\delta(\omega - \omega^{L}_{\boldsymbol{p}})\Big]\,, \tag{A.73c}$$

$$G^{B}_{AC}(\omega) = \sideset{}{'}\sum_{\boldsymbol{p}\in\mathcal{P}} \Big[\lambda\eta(u_1 - v_1)\big[2\big(\mathcal{V}_{1\boldsymbol{p}} + \mathcal{V}_{2\boldsymbol{p}}\big)^2 - \big(\mathcal{U}_{1\boldsymbol{p}} + \mathcal{U}_{2\boldsymbol{p}}\big)\big(\mathcal{V}_{1\boldsymbol{p}} + \mathcal{V}_{2\boldsymbol{p}}\big)\big]\mathcal{N}^{B}_{\boldsymbol{p}}\delta(\omega - \omega^{B}_{\boldsymbol{p}})\Big]\,, \tag{A.73d}$$

$$G^{L}_{A}(\omega) = \sideset{}{'}\sum_{\boldsymbol{p}\in\mathcal{P}} \Big[\eta^2(u_1 - v_1)^2 \frac{5(\mathcal{U}_{1\boldsymbol{p}} + \mathcal{U}_{2\boldsymbol{p}})^2 - 4(\mathcal{U}_{1\boldsymbol{p}} + \mathcal{U}_{2\boldsymbol{p}})(\mathcal{V}_{1\boldsymbol{p}} + \mathcal{V}_{2\boldsymbol{p}}) - 1}{2}\mathcal{N}^{L}_{\boldsymbol{p}}\delta(\omega - \omega^{L}_{\boldsymbol{p}})\Big]\,, \tag{A.73e}$$

$$G^{B}_{A}(\omega) = \sideset{}{'}\sum_{\boldsymbol{p}\in\mathcal{P}} \Big[\eta^2(u_1 - v_1)^2 \frac{5(\mathcal{V}_{1\boldsymbol{p}} + \mathcal{V}_{2\boldsymbol{p}})^2 - 4(\mathcal{U}_{1\boldsymbol{p}} + \mathcal{U}_{2\boldsymbol{p}})(\mathcal{V}_{1\boldsymbol{p}} + \mathcal{V}_{2\boldsymbol{p}}) + 1}{2}\mathcal{N}^{B}_{\boldsymbol{p}}\delta(\omega - \omega^{B}_{\boldsymbol{p}})\Big]\,, \tag{A.73f}$$

$$G^{L}_{\dot{A}}(\omega) = \sideset{}{'}\sum_{\boldsymbol{p}\in\mathcal{P}} \Big[\frac{\eta^2}{(u_1 - v_1)^2}\frac{(\mathcal{V}_{1\boldsymbol{p}} - \mathcal{V}_{2\boldsymbol{p}})^2}{2}\mathcal{N}^{L}_{\boldsymbol{p}}\delta(\omega - \omega^{L}_{\boldsymbol{p}})\Big]\,, \tag{A.73g}$$

$$G^{B}_{\dot{A}}(\omega) = \sideset{}{'}\sum_{\boldsymbol{p}\in\mathcal{P}} \Big[\frac{\eta^2}{(u_1 - v_1)^2}\frac{(\mathcal{U}_{1\boldsymbol{p}} - \mathcal{U}_{2\boldsymbol{p}})^2}{2}\mathcal{N}^{B}_{\boldsymbol{p}}\delta(\omega - \omega^{B}_{\boldsymbol{p}})\Big]\,. \tag{A.73h}$$

Therefore, we have derived Eqs. (3.49) to (3.52) and Eq. (3.55a)

$$G^{L,B}_{\nu}(\omega) = \gamma_{\nu} \sideset{}{'}\sum_{\boldsymbol{p}\in\mathcal{P}} \left[f^{L,B}_{\nu}(\boldsymbol{p})\mathcal{N}^{L,B}_{\boldsymbol{p}}\delta(\omega - \omega^{L,B}_{\boldsymbol{p}})\right]\,, \tag{A.74}$$

with $\gamma_{\nu} \in \{\lambda^2\,,\, \lambda\eta(u_1 - v_1)\,,\, \eta^2(u_1 - v_1)^2\,,\, \eta^2/(u_1 - v_1)^2\}$ and

$$f^{L}_{C}(\boldsymbol{p}) = 2\big(\mathcal{U}_{1\boldsymbol{p}} + \mathcal{U}_{2\boldsymbol{p}}\big)^2\,, \qquad f^{B}_{C}(\boldsymbol{p}) = 2\big(\mathcal{V}_{1\boldsymbol{p}} + \mathcal{V}_{2\boldsymbol{p}}\big)^2\,, \tag{A.75a}$$

$$\begin{aligned} f^{L}_{AC}(\boldsymbol{p}) &= 2\big(\mathcal{U}_{1\boldsymbol{p}} + \mathcal{U}_{2\boldsymbol{p}}\big)^2 - \big(\mathcal{U}_{1\boldsymbol{p}} + \mathcal{U}_{2\boldsymbol{p}}\big)\big(\mathcal{V}_{1\boldsymbol{p}} + \mathcal{V}_{2\boldsymbol{p}}\big)\,,\\ f^{B}_{AC}(\boldsymbol{p}) &= 2\big(\mathcal{V}_{1\boldsymbol{p}} + \mathcal{V}_{2\boldsymbol{p}}\big)^2 - \big(\mathcal{U}_{1\boldsymbol{p}} + \mathcal{U}_{2\boldsymbol{p}}\big)\big(\mathcal{V}_{1\boldsymbol{p}} + \mathcal{V}_{2\boldsymbol{p}}\big)\,, \end{aligned} \tag{A.75b}$$

$$\begin{aligned} f^{L}_{A}(\boldsymbol{p}) &= \frac{5(\mathcal{U}_{1\boldsymbol{p}} + \mathcal{U}_{2\boldsymbol{p}})^2 - 4(\mathcal{U}_{1\boldsymbol{p}} + \mathcal{U}_{2\boldsymbol{p}})(\mathcal{V}_{1\boldsymbol{p}} + \mathcal{V}_{2\boldsymbol{p}}) - 1}{2}\,,\\ f^{B}_{A}(\boldsymbol{p}) &= \frac{5(\mathcal{V}_{1\boldsymbol{p}} + \mathcal{V}_{2\boldsymbol{p}})^2 - 4(\mathcal{U}_{1\boldsymbol{p}} + \mathcal{U}_{2\boldsymbol{p}})(\mathcal{V}_{1\boldsymbol{p}} + \mathcal{V}_{2\boldsymbol{p}}) + 1}{2}\,, \end{aligned} \tag{A.75c}$$

$$f^{L}_{\dot{A}}(\boldsymbol{p}) = \frac{(\mathcal{V}_{1\boldsymbol{p}} - \mathcal{V}_{2\boldsymbol{p}})^2}{2}\,, \qquad f^{B}_{\dot{A}}(\boldsymbol{p}) = \frac{(\mathcal{U}_{1\boldsymbol{p}} - \mathcal{U}_{2\boldsymbol{p}})^2}{2}\,. \tag{A.75d}$$

Note that due to hyberbolic identities $\mathcal{U}^2_{1\boldsymbol{p}} + \mathcal{U}^2_{2\boldsymbol{p}} = \mathcal{V}^2_{1\boldsymbol{p}} + \mathcal{V}^2_{2\boldsymbol{p}} + 1$ it is

$$f^{L}_{C}(\boldsymbol{p}) = f^{B}_{C}(\boldsymbol{p}) + 2\,, \quad f^{L}_{AC}(\boldsymbol{p}) = f^{B}_{AC}(\boldsymbol{p}) + 2\,, \quad f^{L}_{A}(\boldsymbol{p}) = f^{B}_{A}(\boldsymbol{p}) + \frac{3}{2}\,, \quad f^{L}_{\dot{A}}(\boldsymbol{p}) = f^{B}_{\dot{A}}(\boldsymbol{p}) - \frac{1}{2}\,. \tag{A.76}$$

A.6 – Series expansion of spectral densities

We analyze the functions determining the spectral density characteristics $f_{\nu}(W)/|g'(W)|$, see Eqs. (3.58) to (3.62). In particular, we focus here on the vicinity of the Landau to Beliaev damping boundary at ω_1 where $W(\omega = \omega_1) = 0$. The singularity is of the cusp type which is evident from the two leading order terms of the derivatives' asymptotic analysis Eq. (3.63)

$$\begin{aligned}\frac{d}{dW}\frac{f_C^B}{|g'_B|} &\sim -\frac{a_C}{\sqrt{W}} + b_C\,, \qquad & a_C &= \frac{1}{\sqrt{2nU}}\left(1 + \frac{(2\omega_R - \overline{\omega}_P + nU)(2\omega_R - \overline{\omega}_P + 2nU)}{\omega_1^2}\right),\\ & & b_C &= \frac{1}{\omega_1}\left(\frac{2\omega_R - \overline{\omega}_P}{nU} + \right) - \frac{(2\omega_R - \overline{\omega}_P + nU)(2\omega_R - \overline{\omega}_P + 2nU)}{\omega_1^3}\,,\end{aligned} \tag{A.77a}$$

$$\begin{aligned}\frac{d}{dW}\frac{f_{AC}^B}{|g'_B|} &\sim -\frac{a_{AC}}{\sqrt{W}} + b_{AC} \qquad & a_{AC} &= \frac{1}{\sqrt{2nU}}\left(1 + \frac{(2\omega_R - \overline{\omega}_P + nU)(2\omega_R - \overline{\omega}_P + 2nU)}{2\omega_1^2}\right),\\ & & b_{AC} &= \frac{2\omega_R - \overline{\omega}_P}{2\omega_1 nU} - \frac{(2\omega_R - \overline{\omega}_P + nU)(2\omega_R - \overline{\omega}_P + 2nU)}{2\omega_1^3}\,,\end{aligned} \tag{A.77b}$$

$$\begin{aligned}\frac{d}{dW}\frac{f_A^B}{|g'_B|} &\sim -\frac{a_A}{\sqrt{W}} + b_A\,, \qquad & a_A &= \frac{1}{4\sqrt{2nU}}\left(3 + \frac{(2\omega_R - \overline{\omega}_P + nU)(2\omega_R - \overline{\omega}_P + 2nU)}{\omega_1^2}\right),\\ & & b_A &= \frac{1}{2\omega_1}\left(\frac{2\omega_R - \overline{\omega}_P}{nU} - 1\right) - \frac{(2\omega_R - \overline{\omega}_P + nU)(2\omega_R - \overline{\omega}_P + 2nU)}{4\omega_1^3}\,,\end{aligned} \tag{A.77c}$$

$$\begin{aligned}\frac{d}{dW}\frac{f_{\dot{A}}^B}{|g'_B|} &\sim -\frac{a_{\dot{A}}}{\sqrt{W}} + b_{\dot{A}}\,, \qquad & a_{\dot{A}} &= \frac{-1}{4\sqrt{2nU}}\left(1 - \frac{(2\omega_R - \overline{\omega}_P)(2\omega_R - \overline{\omega}_P + nU)}{\omega_1^2}\right),\\ & & b_{\dot{A}} &= \frac{-1}{4\omega_1}\left(\frac{2\omega_R - \overline{\omega}_P}{nU} - 1\right) - \frac{(2\omega_R - \overline{\omega}_P)(2\omega_R - \overline{\omega}_P + nU)}{4\omega_1^3}\,.\end{aligned} \tag{A.77d}$$

We compute their antiderivative to obtain the approximate behavior of the spectral densities around the cusp singularity $W = 0$. The constants of the antiderivatives $C_\nu = f_\nu^B(W = 0)/|g'_B(W = 0)|$ are determined by the finite value at the cusp. This yields the series expansion for the spectral densities Eq. (3.64)

$$\frac{f_C^B(W)}{|g'_B(W)|} \sim C_C - 2a_C\sqrt{W} + b_C W\,, \qquad C_C = \frac{2\omega_R - \overline{\omega}_P + 2nU}{\omega_1}\,, \tag{A.78a}$$

$$\frac{f_{AC}^B(W)}{|g'_B(W)|} \sim C_{AC} - 2a_{AC}\sqrt{W} + b_{AC} W\,, \qquad C_{AC} = \frac{2\omega_R - \overline{\omega}_P + 2nU}{2\omega_1}\,, \tag{A.78b}$$

$$\frac{f_A^B(W)}{|g'_B(W)|} \sim C_A - 2a_A\sqrt{W} + b_A W\,, \qquad C_A = \frac{2\omega_R - \overline{\omega}_P + 2nU}{4\omega_1}\,, \tag{A.78c}$$

$$\frac{f_{\dot{A}}^B(W)}{|g'_B(W)|} \sim C_{\dot{A}} - 2a_{\dot{A}}\sqrt{W} + b_{\dot{A}} W\,, \qquad C_{\dot{A}} = \frac{2\omega_R - \overline{\omega}_P}{4\omega_1}\,. \tag{A.78d}$$

Note that in the limit of $nU, \overline{\omega}_P \ll \omega_R$ the checkerboard frequency is $\omega_1 \approx 2\omega_R - \overline{\omega}_P + nU$ and the expansion parameters a_ν, b_ν, and C_ν are significantly simplified and $\tanh(2\alpha_1) = nU/(2\omega_R - \overline{\omega}_P + nU)$, Eq. (3.36), can be utilized.

A.7 – Bogoliubov theory of the generic long-range envelope interaction model

Let us quickly validate the linear-order of quantum fluctuations for the expansion of the atomic field operator Eq. (4.28)

$$\hat{\psi}(\boldsymbol{r}) = \sqrt{n} + \hat{\phi}(\boldsymbol{r}) = \sqrt{n} + \frac{1}{\sqrt{V}}\sum_{\boldsymbol{p}}{}' e^{i\boldsymbol{p}\boldsymbol{r}}\hat{\phi}_{\boldsymbol{p}}\,, \tag{A.79}$$

applied to the generic atomic field Hamiltonian, Eq. (4.17), which has the form

$$\begin{aligned}\hat{H} = &\int_V d^d\boldsymbol{r} \left\{ \hat{\psi}^\dagger(\boldsymbol{r}) \left[-\frac{\nabla^2}{2m} + \frac{U}{2}\hat{\psi}^\dagger(\boldsymbol{r})\hat{\psi}(\boldsymbol{r}) \right] \hat{\psi}(\boldsymbol{r}) \right\} \\ &+ \frac{I}{2} \int_V d^d\boldsymbol{r} \int_V d^d\boldsymbol{r'} \Big\{ \hat{\psi}^\dagger(\boldsymbol{r})\hat{\psi}(\boldsymbol{r}) v(\boldsymbol{r},\boldsymbol{r'}) f_{\boldsymbol{\xi}}(\boldsymbol{r},\boldsymbol{r'}) \hat{\psi}^\dagger(\boldsymbol{r'})\hat{\psi}(\boldsymbol{r'}) \Big\} . \end{aligned} \tag{A.80}$$

In linear order in $\phi(\boldsymbol{r})$ around the homogeneous mean-field derived in the main text with $\mu_{\mathrm{mf}} = Un$ it is

$$\begin{aligned}\hat{H}_1 = &\sqrt{n} \int_V d^d\boldsymbol{r} \left\{ \left[-\frac{\nabla^2}{2m} \right] \hat{\phi}(\boldsymbol{r}) + Un\big(\hat{\phi}(\boldsymbol{r}) + \hat{\phi}^\dagger(\boldsymbol{r})\big) - \mu_{\mathrm{mf}}\big(\hat{\phi}(\boldsymbol{r}) + \hat{\phi}^\dagger(\boldsymbol{r})\big) \right\} \\ &+ In^{\frac{3}{2}} \int_V d^d\boldsymbol{r} \left\{ \big(\hat{\phi}(\boldsymbol{r}) + \hat{\phi}^\dagger(\boldsymbol{r})\big) \int_V d^d\boldsymbol{r'} \Big\{ v(\boldsymbol{r},\boldsymbol{r'}) f_{\boldsymbol{\xi}}(\boldsymbol{r},\boldsymbol{r'}) \Big\} \right\} \\ = &\frac{\sqrt{n}}{\sqrt{V}} \sum_{\boldsymbol{p}}{}' \frac{\boldsymbol{p}^2}{2m} \hat{\phi}_{\boldsymbol{p}} \int_V d^d\boldsymbol{r} \Big\{ e^{i\boldsymbol{pr}} \Big\} \\ &+ I\frac{n^{3/2}}{\sqrt{V}} \sum_{\boldsymbol{p}}{}' \sum_{\boldsymbol{k},\boldsymbol{k'}} \int_V d^d\boldsymbol{r} \Big\{ \big(\hat{\phi}_{\boldsymbol{p}} e^{i\boldsymbol{pr}} + \hat{\phi}^\dagger_{\boldsymbol{p}} e^{-i\boldsymbol{pr}}\big) \int_V d^d\boldsymbol{r'} \Big\{ v_{\boldsymbol{k},\boldsymbol{k'}} e^{i\boldsymbol{kr}} e^{i\boldsymbol{k'r'}} f_{\boldsymbol{\xi}}(\boldsymbol{r},\boldsymbol{r'}) \Big\} \Big\} \\ = &\frac{\sqrt{n}}{\sqrt{V}} \sum_{\boldsymbol{p}}{}' \frac{\boldsymbol{p}^2}{2m} \hat{\phi}_{\boldsymbol{p}} V \delta^{(d)}_{\boldsymbol{p},\boldsymbol{0}} + IN^{\frac{3}{2}} \sum_{\boldsymbol{p}}{}' \sum_{\boldsymbol{k},\boldsymbol{k'}} v_{\boldsymbol{k},\boldsymbol{k'}} \big(\hat{\phi}_{\boldsymbol{p}} \delta^{(d)}_{-\boldsymbol{p},\boldsymbol{k}} + \hat{\phi}^\dagger_{\boldsymbol{p}} \delta^{(d)}_{\boldsymbol{p},\boldsymbol{k}}\big) \delta^{(d)}_{\boldsymbol{0},\boldsymbol{k'}} \tilde{f}_{\boldsymbol{\xi}}(\boldsymbol{0},\boldsymbol{0}) = 0 . \end{aligned} \tag{A.81}$$

The terms of linear order vanish because we presuppose that the Fourier coefficient $v_{\boldsymbol{k},\boldsymbol{0}} = 0$ and $\boldsymbol{p} = 0$ is omitted from the sum.

The Hamiltonian of second-order is

$$\begin{aligned}\hat{H}_2 = &\int_V d^d\boldsymbol{r} \left\{ \hat{\phi}^\dagger(\boldsymbol{r}) \left[-\frac{\nabla^2}{2m} + 2Un - \mu_{\mathrm{mf}} \right] \hat{\phi}(\boldsymbol{r}) + \frac{Un}{2} \left[\hat{\phi}(\boldsymbol{r})\hat{\phi}(\boldsymbol{r}) + \hat{\phi}^\dagger(\boldsymbol{r})\hat{\phi}^\dagger(\boldsymbol{r}) \right] \right\} \\ &+ In \int_V d^d\boldsymbol{r} \left\{ \hat{\phi}^\dagger(\boldsymbol{r})\hat{\phi}(\boldsymbol{r}) \int_V d^d\boldsymbol{r'} v(\boldsymbol{r},\boldsymbol{r'}) f_{\boldsymbol{\xi}}(\boldsymbol{r},\boldsymbol{r'}) \right\} \\ &+ \frac{In}{2} \int_V d^d\boldsymbol{r} \Big\{ \big(\hat{\phi}(\boldsymbol{r}) + \hat{\phi}^\dagger(\boldsymbol{r})\big) \int_V d^d\boldsymbol{r'} \Big\{ v(\boldsymbol{r},\boldsymbol{r'}) f_{\boldsymbol{\xi}}(\boldsymbol{r},\boldsymbol{r'}) \big(\hat{\phi}(\boldsymbol{r'}) + \hat{\phi}^\dagger(\boldsymbol{r'})\big) \Big\} \Big\} \\ = &\frac{1}{V} \sum_{\boldsymbol{p},\boldsymbol{p'}}{}' \int_V d^d\boldsymbol{r} \Big\{ \hat{\phi}^\dagger_{\boldsymbol{p}} e^{-i\boldsymbol{pr}} \left[\frac{\boldsymbol{p}'^2}{2m} + Un \right] e^{i\boldsymbol{p'r}} \hat{\phi}_{\boldsymbol{p'}} + \frac{Un}{2} \left[\hat{\phi}_{\boldsymbol{p}}\hat{\phi}_{\boldsymbol{p'}} e^{i(\boldsymbol{p}+\boldsymbol{p'})\boldsymbol{r}} + \hat{\phi}^\dagger_{\boldsymbol{p}}\hat{\phi}^\dagger_{\boldsymbol{p'}} e^{-i(\boldsymbol{p}+\boldsymbol{p'})\boldsymbol{r}} \right] \Big\} \\ &+ \frac{In}{2V} \sum_{\boldsymbol{p},\boldsymbol{p'}}{}' \sum_{\boldsymbol{k},\boldsymbol{k'}} \int_V d^d\boldsymbol{r} \big(\hat{\phi}_{\boldsymbol{p}} e^{i\boldsymbol{pr}} + \hat{\phi}^\dagger_{\boldsymbol{p}} e^{-i\boldsymbol{pr}}\big) v_{\boldsymbol{k},\boldsymbol{k'}} e^{i\boldsymbol{kr}} \int_V d^d\boldsymbol{r'} e^{i\boldsymbol{k'r'}} f_{\boldsymbol{\xi}}(\boldsymbol{r},\boldsymbol{r'}) \big(\hat{\phi}_{\boldsymbol{p'}} e^{i\boldsymbol{p'r'}} + \hat{\phi}^\dagger_{\boldsymbol{p'}} e^{-i\boldsymbol{p'r'}}\big) \\ = &\sum_{\boldsymbol{p}}{}' \left(\left[\frac{\boldsymbol{p}^2}{2m} + Un \right] \hat{\phi}^\dagger_{\boldsymbol{p}}\hat{\phi}_{\boldsymbol{p}} + \frac{Un}{2} \left[\hat{\phi}_{-\boldsymbol{p}}\hat{\phi}_{\boldsymbol{p}} + \hat{\phi}^\dagger_{\boldsymbol{p}}\hat{\phi}^\dagger_{-\boldsymbol{p}} \right] \right) \\ &+ \frac{IN}{2} \tilde{f}_{\boldsymbol{\xi}}(\boldsymbol{0},\boldsymbol{0}) \sum_{\boldsymbol{p},\boldsymbol{p'}}{}' \sum_{\boldsymbol{k},\boldsymbol{k'}} \left[v_{\boldsymbol{k},\boldsymbol{k'}} \big(\hat{\phi}_{\boldsymbol{p}} \delta^{(d)}_{-\boldsymbol{p},\boldsymbol{k}} + \hat{\phi}^\dagger_{\boldsymbol{p}} \delta^{(d)}_{\boldsymbol{p},\boldsymbol{k}}\big) \big(\hat{\phi}_{\boldsymbol{p'}} \delta^{(d)}_{-\boldsymbol{p'},\boldsymbol{k'}} + \hat{\phi}^\dagger_{\boldsymbol{p'}} \delta^{(d)}_{\boldsymbol{p'},\boldsymbol{k'}}\big) \right] \\ = &\sum_{\boldsymbol{p}}{}' \left(\left[\frac{\boldsymbol{p}^2}{2m} + Un \right] \hat{\phi}^\dagger_{\boldsymbol{p}}\hat{\phi}_{\boldsymbol{p}} + \frac{Un}{2} \left[\hat{\phi}_{-\boldsymbol{p}}\hat{\phi}_{\boldsymbol{p}} + \hat{\phi}^\dagger_{\boldsymbol{p}}\hat{\phi}^\dagger_{-\boldsymbol{p}} \right] \right) \\ &+ \frac{IN}{2} \tilde{f}_{\boldsymbol{\xi}}(\boldsymbol{0},\boldsymbol{0}) \sum_{\boldsymbol{p},\boldsymbol{p'}}{}' \sum_{\boldsymbol{k},\boldsymbol{k'}} \left[v_{\boldsymbol{k},\boldsymbol{k'}} \big(\hat{\phi}_{\boldsymbol{p}} \delta^{(d)}_{-\boldsymbol{p},\boldsymbol{k}} + \hat{\phi}^\dagger_{\boldsymbol{p}} \delta^{(d)}_{\boldsymbol{p},\boldsymbol{k}}\big) \big(\hat{\phi}_{\boldsymbol{p'}} \delta^{(d)}_{-\boldsymbol{p'},\boldsymbol{k'}} + \hat{\phi}^\dagger_{\boldsymbol{p'}} \delta^{(d)}_{\boldsymbol{p'},\boldsymbol{k'}}\big) \right] . \end{aligned} \tag{A.82}$$

Utilizing the commutation of operators and exchange of terms in the same way as in the Bogoliubov theory of the Bose gas, see appendix A.1, we find Eq. (4.31) as

$$\begin{aligned}
\hat{H}_2 &= \frac{1}{2}\sum_{\boldsymbol{p}}{}' \left[\frac{\boldsymbol{p}^2}{2m}\left(\hat{\phi}^\dagger_{\boldsymbol{p}}\hat{\phi}_{\boldsymbol{p}} + \hat{\phi}_{-\boldsymbol{p}}\hat{\phi}^\dagger_{-\boldsymbol{p}}\right) + nU\left(\hat{\phi}_{-\boldsymbol{p}} + \hat{\phi}^\dagger_{\boldsymbol{p}}\right)\left(\hat{\phi}_{\boldsymbol{p}} + \hat{\phi}^\dagger_{-\boldsymbol{p}}\right) - \frac{\boldsymbol{p}^2}{2m} - nU\right] \\
&\quad + \frac{IN}{2}\tilde{f}_{\boldsymbol{\xi}}(\boldsymbol{0},\boldsymbol{0})\sum_{\boldsymbol{p},\boldsymbol{p}'}{}' \sum_{\boldsymbol{k},\boldsymbol{k}'\in\mathcal{K}_C}\left[\left(\hat{\phi}_{\boldsymbol{p}}\delta^{(d)}_{-\boldsymbol{p},\boldsymbol{k}} + \hat{\phi}^\dagger_{\boldsymbol{p}}\delta^{(d)}_{\boldsymbol{p},\boldsymbol{k}}\right)v_{\boldsymbol{k},\boldsymbol{k}'}\left(\hat{\phi}_{\boldsymbol{p}'}\delta^{(d)}_{-\boldsymbol{p}',\boldsymbol{k}'} + \hat{\phi}^\dagger_{\boldsymbol{p}'}\delta^{(d)}_{\boldsymbol{p}',\boldsymbol{k}'}\right)\right] \\
&= \frac{1}{2}\sum_{\boldsymbol{p}}{}' \left[\frac{\boldsymbol{p}^2}{2m}\left(\hat{\phi}^\dagger_{\boldsymbol{p}}\hat{\phi}_{\boldsymbol{p}} + \hat{\phi}_{-\boldsymbol{p}}\hat{\phi}^\dagger_{-\boldsymbol{p}}\right) + nU\left(\hat{\phi}_{-\boldsymbol{p}} + \hat{\phi}^\dagger_{\boldsymbol{p}}\right)\left(\hat{\phi}_{\boldsymbol{p}} + \hat{\phi}^\dagger_{-\boldsymbol{p}}\right) - \frac{\boldsymbol{p}^2}{2m} - nU\right] \\
&\quad + \frac{IN}{2}\tilde{f}_{\boldsymbol{\xi}}(\boldsymbol{0},\boldsymbol{0})\sum_{\boldsymbol{k},\boldsymbol{k}'\in\mathcal{K}_C}\left[(\hat{\phi}_{-\boldsymbol{k}} + \hat{\phi}^\dagger_{\boldsymbol{k}})v_{\boldsymbol{k},\boldsymbol{k}'}(\hat{\phi}_{-\boldsymbol{k}'} + \hat{\phi}^\dagger_{\boldsymbol{k}'})\right]. \qquad \text{(A.83)}
\end{aligned}$$

By introducing the quasi-position and quasi-momentum operators, Eq. (4.32), [183]

$$\hat{x}_{\boldsymbol{p}} = \sqrt{\frac{m}{\boldsymbol{p}^2}}\left(\hat{\phi}_{\boldsymbol{p}} + \hat{\phi}^\dagger_{-\boldsymbol{p}}\right), \qquad \hat{y}_{\boldsymbol{p}} = -i\sqrt{\frac{\boldsymbol{p}^2}{4m}}\left(\hat{\phi}_{-\boldsymbol{p}} - \hat{\phi}^\dagger_{\boldsymbol{p}}\right), \qquad \text{(A.84a)}$$

$$[\hat{x}_{\boldsymbol{p}}, \hat{y}_{\boldsymbol{p}}] = i\delta^{(d)}_{\boldsymbol{p},\boldsymbol{p}'}, \qquad \hat{x}_{-\boldsymbol{p}} = \hat{x}^\dagger_{\boldsymbol{p}}, \qquad \hat{y}_{-\boldsymbol{p}} = \hat{y}^\dagger_{\boldsymbol{p}}, \qquad \text{(A.84b)}$$

we obtain Eq. (4.33) by exchanging terms under the double sum

$$\begin{aligned}
\hat{H}_2 &= \frac{1}{2}\sum_{\boldsymbol{p}}{}' \left[\hat{y}_{-\boldsymbol{p}}\hat{y}_{\boldsymbol{p}} + \frac{\boldsymbol{p}^2}{2m}\left(\frac{\boldsymbol{p}^2}{2m} + 2nU\right)\hat{x}_{-\boldsymbol{p}}\hat{x}_{\boldsymbol{p}} - \frac{\boldsymbol{p}^2}{2m} - nU\right] \\
&\quad + \frac{IN}{2}\tilde{f}_{\boldsymbol{\xi}}(\boldsymbol{0},\boldsymbol{0})\sum_{\boldsymbol{k},\boldsymbol{k}'\in\mathcal{K}_C}\left[v_{\boldsymbol{k},-\boldsymbol{k}'}\frac{|\boldsymbol{k}||\boldsymbol{k}'|}{m}\hat{x}_{-\boldsymbol{k}}\hat{x}_{\boldsymbol{k}'}\right]. \qquad \text{(A.85)}
\end{aligned}$$

Next we denote $\mathcal{K}_C = \{\boldsymbol{k}_1, \ldots, \boldsymbol{k}_{\tilde{d}}\}$ and

$$\hat{\vec{x}} = \begin{pmatrix}\hat{x}_1 \\ \hat{x}_2 \\ \vdots \\ \hat{x}_{\tilde{d}}\end{pmatrix}, \quad \hat{\vec{y}} = \begin{pmatrix}\hat{y}_1 \\ \hat{y}_2 \\ \vdots \\ \hat{y}_{\tilde{d}}\end{pmatrix}, \quad \underline{\tilde{v}} = \begin{pmatrix}
v_{\boldsymbol{k}_1,-\boldsymbol{k}_1}\frac{|\boldsymbol{k}_1|^2}{m} & v_{\boldsymbol{k}_1,-\boldsymbol{k}_2}\frac{|\boldsymbol{k}_1||\boldsymbol{k}_2|}{m} & \cdots & v_{\boldsymbol{k}_1,-\boldsymbol{k}_{\tilde{d}}}\frac{|\boldsymbol{k}_1||\boldsymbol{k}_{\tilde{d}}|}{m} \\
v_{\boldsymbol{k}_2,-\boldsymbol{k}_1}\frac{|\boldsymbol{k}_2||\boldsymbol{k}_1|}{m} & v_{\boldsymbol{k}_2,-\boldsymbol{k}_2}\frac{|\boldsymbol{k}_2|^2}{m} & \cdots & v_{\boldsymbol{k}_2,-\boldsymbol{k}_{\tilde{d}}}\frac{|\boldsymbol{k}_2||\boldsymbol{k}_{\tilde{d}}|}{m} \\
\vdots & \vdots & \ddots & \vdots \\
v_{\boldsymbol{k}_{\tilde{d}},-\boldsymbol{k}_1}\frac{|\boldsymbol{k}_{\tilde{d}}||\boldsymbol{k}_1|}{m} & \cdots & \cdots & v_{\boldsymbol{k}_{\tilde{d}},-\boldsymbol{k}_{\tilde{d}}}\frac{|\boldsymbol{k}_{\tilde{d}}|^2}{m}
\end{pmatrix}, \qquad \text{(A.86)}$$

such that Eq. (4.35) is attained

$$\hat{H}_2 = \frac{1}{2}\sum_{\boldsymbol{p}\notin\mathcal{K}_C}{}' \left[\hat{y}^\dagger_{\boldsymbol{p}}\hat{y}_{\boldsymbol{p}} + \omega^2_{\boldsymbol{p}}\hat{x}^\dagger_{\boldsymbol{p}}\hat{x}_{\boldsymbol{p}} - \frac{\boldsymbol{p}^2}{2m} - nU\right] + \frac{1}{2}\left[\hat{\vec{y}}^\dagger\mathbb{I}_{\tilde{d}\times\tilde{d}}\hat{\vec{y}} + \hat{\vec{x}}^\dagger\underline{h}\hat{\vec{x}} - \sum_{j=1}^{\tilde{d}}\left(\frac{\boldsymbol{k}_j}{2m} + Un\right)\right], \qquad \text{(A.87)}$$

with Eq. (4.36)

$$\underline{h} = \begin{pmatrix}
\omega_1^2 + IN\tilde{f}_{\boldsymbol{\xi}}(\boldsymbol{0},\boldsymbol{0})\tilde{v}_{11} & IN\tilde{f}_{\boldsymbol{\xi}}(\boldsymbol{0},\boldsymbol{0})\tilde{v}_{12} & \cdots & IN\tilde{f}_{\boldsymbol{\xi}}(\boldsymbol{0},\boldsymbol{0})\tilde{v}_{1\tilde{d}} \\
IN\tilde{f}_{\boldsymbol{\xi}}(\boldsymbol{0},\boldsymbol{0})\tilde{v}_{21} & \omega_2^2 + IN\tilde{f}_{\boldsymbol{\xi}}(\boldsymbol{0},\boldsymbol{0})\tilde{v}_{22} & \cdots & IN\tilde{f}_{\boldsymbol{\xi}}(\boldsymbol{0},\boldsymbol{0})\tilde{v}_{2\tilde{d}} \\
\vdots & \vdots & \ddots & \vdots \\
IN\tilde{f}_{\boldsymbol{\xi}}(\boldsymbol{0},\boldsymbol{0})\tilde{v}_{\tilde{d}1} & \cdots & \cdots & \omega_{\tilde{d}}^2 + IN\tilde{f}_{\boldsymbol{\xi}}(\boldsymbol{0},\boldsymbol{0})\tilde{v}_{\tilde{d}\tilde{d}}
\end{pmatrix}. \qquad \text{(A.88)}$$

In section 4.3.5 we discuss two generic cases of the long-range interaction. If the interaction is translation invariant, it holds that $v_{\boldsymbol{k},-\boldsymbol{k}'} = \delta^{(d)}_{\boldsymbol{k},\boldsymbol{k}'} v_{\boldsymbol{k},-\boldsymbol{k}}$ and hence Eq. (A.85) is diagonal of the form

$$\hat{H}_2^{(\mathrm{ti})} = \frac{1}{2}\sum_{\boldsymbol{p}}{}' \left[\hat{y}^\dagger_{\boldsymbol{p}}\hat{y}_{\boldsymbol{p}} + \frac{\boldsymbol{p}^2}{2m}\left(\frac{\boldsymbol{p}^2}{2m} + 2Un + 2IN\tilde{f}_{\boldsymbol{\xi}}(\boldsymbol{0},\boldsymbol{0}) \sum_{\boldsymbol{k}\in\mathcal{K}_C} \delta^{(d)}_{\boldsymbol{p},\boldsymbol{k}} v_{-\boldsymbol{k},\boldsymbol{k}}\right)\hat{x}^\dagger_{\boldsymbol{p}}\hat{x}_{\boldsymbol{p}} - \frac{\boldsymbol{p}^2}{2m} - Un\right], \tag{A.89}$$

with the dispersion, Eq. (4.41),

$$\mathcal{E}_{\boldsymbol{p}} = \sqrt{\frac{\boldsymbol{p}^2}{2m}\left(\frac{\boldsymbol{p}^2}{2m} + 2Un + 2IN\tilde{f}_{\boldsymbol{\xi}}(\boldsymbol{0},\boldsymbol{0}) \sum_{\boldsymbol{k}\in\mathcal{K}_C} \delta^{(d)}_{\boldsymbol{p},\boldsymbol{k}} v_{-\boldsymbol{k},\boldsymbol{k}}\right)}\,. \tag{A.90}$$

In the second case, that $|\boldsymbol{k}_i| = |\boldsymbol{k}_j|$ and $\tilde{v}_{ij} = \tilde{v}$ for all $i, j = 1, \ldots, \tilde{d}$, the matrix coupling the quasi-position operators is

$$\underline{h} = \begin{pmatrix} \omega^2_{\boldsymbol{k}} + IN\tilde{f}_{\boldsymbol{\xi}}(\boldsymbol{0},\boldsymbol{0})\tilde{v} & IN\tilde{f}_{\boldsymbol{\xi}}(\boldsymbol{0},\boldsymbol{0})\tilde{v} & \cdots & IN\tilde{f}_{\boldsymbol{\xi}}(\boldsymbol{0},\boldsymbol{0})\tilde{v} \\ IN\tilde{f}_{\boldsymbol{\xi}}(\boldsymbol{0},\boldsymbol{0})\tilde{v} & \omega^2_{\boldsymbol{k}} + IN\tilde{f}_{\boldsymbol{\xi}}(\boldsymbol{0},\boldsymbol{0})\tilde{v} & \cdots & IN\tilde{f}_{\boldsymbol{\xi}}(\boldsymbol{0},\boldsymbol{0})\tilde{v} \\ \vdots & \vdots & \ddots & \vdots \\ IN\tilde{f}_{\boldsymbol{\xi}}(\boldsymbol{0},\boldsymbol{0})\tilde{v} & \cdots & \cdots & \omega^2_{\boldsymbol{k}} + IN\tilde{f}_{\boldsymbol{\xi}}(\boldsymbol{0},\boldsymbol{0})\tilde{v} \end{pmatrix}. \tag{A.91}$$

We recognize that

$$\underline{h} - \omega^2_{\boldsymbol{k}}\mathbb{I}_{\tilde{d}\times\tilde{d}} = IN\tilde{f}_{\boldsymbol{\xi}}(\boldsymbol{0},\boldsymbol{0})\tilde{v}\begin{pmatrix} 1 & 1 & \cdots & 1 \\ 1 & 1 & \cdots & 1 \\ \vdots & \vdots & \ddots & \vdots \\ 1 & \cdots & \cdots & 1 \end{pmatrix}, \tag{A.92}$$

is a singular matrix with rank 1. Therefore, $\omega^2_{\boldsymbol{k}}$ is an eigenvalue of $\underline{h}$ with multiplicity $\tilde{d} - 1$. Because

$$\underline{h} - [\omega^2_{\boldsymbol{k}} + \tilde{d}IN\tilde{f}_{\boldsymbol{\xi}}(\boldsymbol{0},\boldsymbol{0})\tilde{v}]\mathbb{I} = \begin{pmatrix} -(\tilde{d}-1)IN\tilde{f}_{\boldsymbol{\xi}}(\boldsymbol{0},\boldsymbol{0})\tilde{v} & IN\tilde{f}_{\boldsymbol{\xi}}(\boldsymbol{0},\boldsymbol{0})\tilde{v} & \cdots & IN\tilde{f}_{\boldsymbol{\xi}}(\boldsymbol{0},\boldsymbol{0})\tilde{v} \\ IN\tilde{f}_{\boldsymbol{\xi}}(\boldsymbol{0},\boldsymbol{0})\tilde{v} & -(\tilde{d}-1)IN\tilde{f}_{\boldsymbol{\xi}}(\boldsymbol{0},\boldsymbol{0})\tilde{v} & \cdots & IN\tilde{f}_{\boldsymbol{\xi}}(\boldsymbol{0},\boldsymbol{0})\tilde{v} \\ \vdots & \vdots & \ddots & \vdots \\ IN\tilde{f}_{\boldsymbol{\xi}}(\boldsymbol{0},\boldsymbol{0})\tilde{v} & \cdots & \cdots & -(\tilde{d}-1)IN\tilde{f}_{\boldsymbol{\xi}}(\boldsymbol{0},\boldsymbol{0})\tilde{v} \end{pmatrix}, \tag{A.93}$$

is trivially singular given the eigenvector $(1\ 1\ \cdots\ 1)^T/\sqrt{\tilde{d}}$ of $\underline{h}$, we acquire the remaining eigenvalue that is the single mode out of the dispersion Eq. (4.44)

$$\Omega = \sqrt{\omega^2_{\boldsymbol{k}} + \frac{\boldsymbol{k}^2}{m}IN\tilde{f}_{\boldsymbol{\xi}}(\boldsymbol{0},\boldsymbol{0})\tilde{d}\tilde{v}}\,. \tag{A.94}$$

A.8 – Estimates of the envelope transformation

Here, we illustrate in figure A.1 the validity of the inequalities Eqs. (4.52) and (4.76) for $L < \xi$ by numerical evaluation.

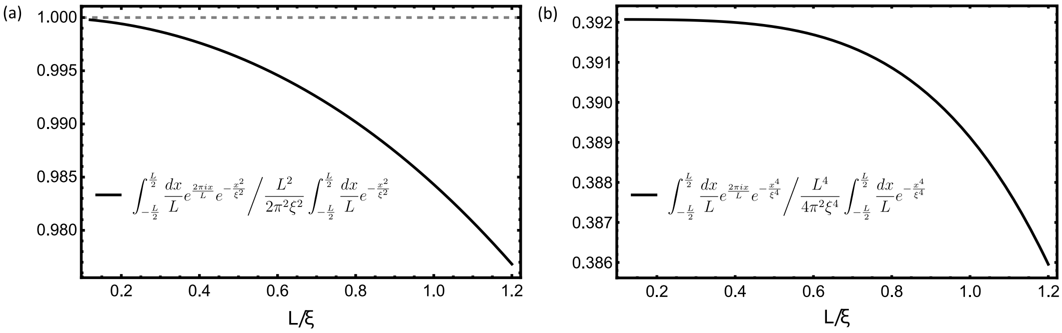

Figure A.1: Graphical visualization of the validity of Eq. (4.52) in (a) and of Eq. (4.76) in (b) in dependence of the system extension L relative to the envelope width ξ. The horizontal line in (a) marks the value of 1.

A.8.1 Gaussian envelope

The integral on the left-hand side of Eq. (4.52) is nonelementary and yields error functions with complex arguments

$$\int_{-\frac{L}{2}}^{+\frac{L}{2}} \frac{dx}{L} \Big\{ e^{ipx} e^{-\frac{x^2}{\xi^2}} \Big\} = \frac{\sqrt{\pi}\xi}{2L} e^{-\frac{\xi^2 p^2}{4}} \left[\operatorname{erf}\left(\frac{L - ip\xi^2}{2\xi} \right) + \operatorname{erf}\left(\frac{L + ip\xi^2}{2\xi} \right) \right] . \tag{A.95}$$

The atomic momenta are discrete values $p = 2\pi j/L$, where $j \in \mathbb{Z}$ and we introduce $\epsilon = pL = 2\pi j$ which we view as a large parameter $|\epsilon| \gg 1$ for $j \in \mathbb{Z} \setminus \{0\}$. Subsequently, we expand the integral in this parameter ϵ according to

$$\begin{aligned}
&\int_{-\frac{L}{2}}^{+\frac{L}{2}} \frac{dx}{L} \Big\{ e^{i\frac{\epsilon x}{L}} e^{-\frac{x^2}{\xi^2}} \Big\} = \int_{-\frac{1}{2}}^{+\frac{1}{2}} du \Big\{ e^{i\epsilon u} e^{-u^2 \frac{L^2}{\xi^2}} \Big\} = \frac{\sqrt{\pi}\xi}{2L} e^{-\frac{\xi^2\epsilon^2}{4L^2}} \left[\operatorname{erf}\left(\frac{L}{2\xi} - \frac{i\epsilon\xi}{2L} \right) + \operatorname{erf}\left(\frac{L}{2\xi} + \frac{i\epsilon\xi}{2L} \right) \right] \\
&= \left(-\frac{i}{\epsilon} - \frac{L^2}{\xi^2\epsilon^2} + \mathcal{O}\left(\epsilon^{-3}\right) \right) e^{\frac{i\epsilon}{2} - \frac{L^2}{4\xi^2} + \mathcal{O}\left(\epsilon^{-3}\right)} + \left(\frac{i}{\epsilon} - \frac{L^2}{\xi^2\epsilon^2} + \mathcal{O}\left(\epsilon^{-3}\right) \right) e^{-\frac{i\epsilon}{2} - \frac{L^2}{4\xi^2} + \mathcal{O}\left(\epsilon^{-3}\right)} \\
&= -\frac{i}{\epsilon} e^{-\frac{L^2}{4\xi^2}} \left(e^{\frac{i\epsilon}{2} + \mathcal{O}\left(\epsilon^{-3}\right)} - e^{-\frac{i\epsilon}{2} + \mathcal{O}\left(\epsilon^{-3}\right)} \right) - \left(\frac{L^2}{\xi^2\epsilon^2} + \mathcal{O}\left(\epsilon^{-3}\right) \right) e^{-\frac{L^2}{4\xi^2}} \left(e^{\frac{i\epsilon}{2} + \mathcal{O}\left(\epsilon^{-3}\right)} + e^{-\frac{i\epsilon}{2} + \mathcal{O}\left(\epsilon^{-3}\right)} \right) \\
&\approx \frac{2\sin(\epsilon/2)}{\epsilon} e^{-\frac{L^2}{4\xi^2}} - \frac{2L^2\cos(\epsilon/2)}{\xi^2\epsilon^2} = \cos(\pi j) \frac{L^2}{2\pi^2 j^2 \xi^2} e^{-\frac{L^2}{4\xi^2}} .
\end{aligned} \tag{A.96}$$

Using $e^{-u^2/4} < \sqrt{\pi}\operatorname{erf}(u/2)/u$ for $u \neq 0$, we obtain Eq. (4.52), i.e.

$$\left| \int_{-\frac{L}{2}}^{+\frac{L}{2}} \frac{dx}{L} \Big\{ e^{ipx} e^{-\frac{x^2}{\xi^2}} \Big\} \right| \approx \frac{L^2}{2\pi^2 j^2 \xi^2} e^{-\frac{L^2}{4\xi^2}} < \frac{L^2}{2\pi^2 j^2 \xi^2} \frac{\sqrt{\pi}\xi}{L} \operatorname{erf}\left(\frac{L}{2\xi} \right) = \frac{L^2}{2\pi^2 j^2 \xi^2} \int_{-\frac{L}{2}}^{+\frac{L}{2}} \frac{dx}{L} \Big\{ e^{-\frac{x^2}{\xi^2}} \Big\} . \tag{A.97}$$

A.8.2 Quartic exponent envelope

We evaluate the nonelementary integral on the left-hand side of Eq. (4.76) by its Taylor series and expand the solution in orders of $|\epsilon| = |pL| = |2\pi j| \gg 1$ for $j \in \mathbb{Z} \setminus \{0\}$ which yields

$$\begin{aligned}
&\int_{-\frac{L}{2}}^{+\frac{L}{2}} \frac{dx}{L} \left\{ e^{ipx} e^{-\frac{x^4}{\xi^4}} \right\} = \int_{-\frac{L}{2}}^{+\frac{L}{2}} \frac{dx}{L} \left\{ e^{i\epsilon\frac{x}{L}} \sum_{n=0}^{\infty} \frac{1}{n!} \left(-\frac{x^4}{\xi^4} \right)^n \right\} \\
&= \sum_{n=0}^{\infty} \left(\frac{(-1)^n}{n!} \left[ie^{-\frac{i\epsilon}{2} + \mathcal{O}\left(\epsilon^{-3}\right)} \left(\frac{1}{\epsilon} \left(\frac{L}{2\xi} \right)^{4n} - \frac{8in}{\epsilon^2} \left(\frac{L}{2\xi} \right)^{4n} + \mathcal{O}\left(\epsilon^{-3}\right) \right) \right.\right. \\
&\qquad\qquad \left.\left. - ie^{+\frac{i\epsilon}{2} + \mathcal{O}\left(\epsilon^{-3}\right)} \left(\frac{1}{\epsilon} \left(\frac{L}{2\xi} \right)^{4n} + \frac{8in}{\epsilon^2} \left(\frac{L}{2\xi} \right)^{4n} + \mathcal{O}\left(\epsilon^{-3}\right) \right) \right] \right) \\
&= \sum_{n=0}^{\infty} \left(\frac{(-1)^n}{n!} \left[\left(e^{-\frac{i\epsilon}{2} + \mathcal{O}\left(\epsilon^{-3}\right)} + e^{+\frac{i\epsilon}{2} + \mathcal{O}\left(\epsilon^{-3}\right)} \right) \left(\frac{8n}{\epsilon^2} \left(\frac{L}{2\xi} \right)^{4n} + \mathcal{O}\left(\epsilon^{-3}\right) \right) \right] \right) \\
&= 16\cos(\epsilon/2) \frac{-L^4}{16\epsilon^2\xi^4} e^{-\frac{L^4}{16\xi^4} + \mathcal{O}\left(\epsilon^{-3}\right)} + \mathcal{O}\left(\epsilon^{-3}\right) \approx -\cos(\pi j) \frac{L^4}{4\pi^2 j^2 \xi^4} e^{-\frac{L^4}{16\xi^4}} \,. \qquad \text{(A.98)}
\end{aligned}$$

It is

$$\int_{-\frac{L}{2}}^{+\frac{L}{2}} \left\{ \frac{dx}{L} e^{-\frac{x^4}{\xi^4}} \right\} = \frac{\xi}{2L} \left[\Gamma\left(\frac{1}{4}\right) - \Gamma\left(\frac{1}{4}, \frac{L^4}{16\xi^4}\right) \right] , \qquad \text{(A.99)}$$

and $e^{-(u/2)^4} < [\Gamma(1/4) - \Gamma(1/4, (u/2)^4)]/(2u)$ for $u \neq 0$, so that we find Eq. (4.76), i.e.

$$\begin{aligned}
\left| \int_{-\frac{L}{2}}^{+\frac{L}{2}} \frac{dx}{L} \left\{ e^{ipx} e^{-\frac{x^4}{\xi^4}} \right\} \right| \approx \frac{L^4}{4\pi^2 j^2 \xi^4} e^{-\frac{L^4}{16\xi^4}} &< \frac{L^4}{4\pi^2 j^2 \xi^4} \frac{\xi}{2L} \left[\Gamma\left(\frac{1}{4}\right) - \Gamma\left(\frac{1}{4}, \frac{L^4}{16\xi^4}\right) \right] \\
&= \frac{L^4}{4\pi^2 j^2 \xi^4} \int_{-\frac{L}{2}}^{+\frac{L}{2}} \frac{dx}{L} \left\{ e^{-\frac{x^4}{\xi^4}} \right\} . \qquad \text{(A.100)}
\end{aligned}$$

Bibliography

[A] L. Mixa, H. Keßler, A. Hemmerich, and M. Thorwart, *Enhancing exotic quantum fluctuations in a strongly entangled cavity BEC system*, Phys. Rev. Res. **6**, L012024 (2024).

[B] M. Radonjić, L. Mixa, A. Pelster, and M. Thorwart, *Nanomechanically-induced nonequilibrium quantum phase transition to a self-organized density wave of a Bose-Einstein condensate*, Phys. Rev. Res. **6**, 033094 (2024).

[C] L. Mixa, M. Radonjić, A. Pelster, and M. Thorwart, *Cavity-induced quantum droplets*, Phys. Rev. Res. **7**, 033216 (2025).

[D] L. Mixa, M. Radonjić, A. Pelster, and M. Thorwart, *Engineering quantum droplet formation by cavity-induced long-range interactions*, Phys. Rev. Res. **7**, 023204 (2025).

[1] R. P. Feynman, *Simulating physics with computers*, Int. J. Theor. Phys. **21**, 467 (1982).

[2] D. J. Griffiths, D. F. Schroeter, *Introduction to quantum mechanics*, 3rd ed., Cambridge University Press, 2018.

[3] A. Altland and B. D. Simons, *Condensed matter field theory*, Cambridge University Press, 2010.

[4] P. W. Anderson, *More is different*, Science **177**, 393 (1972).

[5] G. E. Volovik, *The universe in a helium droplet*, Oxford University Press, 2009.

[6] J. G. Bednorz and K. A. Müller, *Possible high T_c superconductivity in the Ba-La-Cu-O system*, Z. Physik B - Condensed Matter **64**, 189 (1986).

[7] X. Zhou, W.-S. Lee, M. Imada, N. Trivedi, P. Phillips, H.-Y. Kee, P. Törmä, and M. Eremets, *High-temperature superconductivity*, Nat. Rev. Phys. **3**, 462 (2021).

[8] J. Bardeen, L. N. Cooper, and J. R. Schrieffer, *Microscopic theory of superconductivity*, Phys. Rev. **106**, 162 (1957).

[9] J. Bardeen, L. N. Cooper, and J. R. Schrieffer, *Theory of superconductivity*, Phys. Rev. **108**, 1175 (1957).

[10] R. P. Feynman, *Superfluidity and superconductivity*, Rev. Mod. Phys. **29**, 205 (1957).

[11] A. Einstein, *Zur Quantentheorie der Strahlung*, Phys. Zeit. **18**, 121 (1917), Translation to English.

[12] S. Haroche and D. Kleppner, *Cavity quantum electrodynamics*, Physics Today **42**, 24 (1989).

[13] E. M. Purcell, *Spontaneous emission probabilities at radio frequencies*, Phys. Rev. **69(11)**, 681 (1946).

[14] S. Haroche and J.-M. Raimond, *Exploring the quantum: Atoms, cavities, and photons*, Oxford University Press, 2006.

[15] M. H. Anderson, J. R. Ensher, M. R. Matthews, C. E. Wieman, and E. A. Cornell, *Observation of Bose-Einstein condensation in a dilute atomic vapor*, Science **269**, 198 (1995).

[16] K. B. Davis, M.-O. Mewes, M. R. Andrews, N. J. van Druten, D. S. Durfee, D. M. Kurn, and W. Ketterle, *Bose-Einstein condensation in a gas of sodium atoms*, Phys. Rev. Lett. **75**, 3969 (1995).

[17] M. Greiner, O. Mandel, T. Esslinger, T. W. Hänsch, and I. Bloch, *Quantum phase transition from a superfluid to a Mott insulator in a gas of ultracold atoms*, Nature **415**, 39 (2002).

[18] A. Osterloh, L. Amico, G. Falci, and R. Fazio, *Scaling of entanglement close to a quantum phase transition*, Nature **416**, 608 (2002).

[19] L. Amico, R. Fazio, A. Osterloh, and V. Vedral, *Entanglement in many-body systems*, Rev. Mod. Phys. **80**, 517 (2008).

[20] C. A. Regal, M. Greiner, and D. S. Jin, *Observation of resonance condensation of fermionic atom pairs*, Phys. Rev. Lett. **92**, 040403 (2004).

[21] M. W. Zwierlein, C. A. Stan, C. H. Schunck, S. M. F. Raupach, A. J. Kerman, and W. Ketterle, *Condensation of pairs of fermionic atoms near a Feshbach resonance*, Phys. Rev. Lett. **92**, 120403 (2004).

[22] M. Bartenstein, A. Altmeyer, S. Riedl, S. Jochim, C. Chin, J. H. Denschlag, and R. Grimm, *Collective excitations of a degenerate gas at the BEC-BCS crossover*, Phys. Rev. Lett. **92**, 203201 (2004).

[23] K. Baumann, C. Guerlin, F. Brennecke, and T. Esslinger, *Dicke quantum phase transition with a superfluid gas in an optical cavity*, Nature **464**, 1301 (2010).

[24] R. H. Dicke, *Coherence in Spontaneous Radiation Processes*, Phys. Rev. **93**, 99 (1954).

[25] J. Klinder, H. Keßler, M. R. Bakhtiari, M. Thorwart, and A. Hemmerich, *Observation of a superradiant Mott insulator in the Dicke-Hubbard model*, Phys. Rev. Lett. **115**, 230403 (2015).

[26] R. Landig, L. Hruby, N. Dogra, M. Landini, R. Mottl, T. Donner, and T. Esslinger, *Quantum phases from competing short- and long-range interactions in an optical lattice*, Nature **532**, 7600 (2016).

[27] F. Mivehvar, F. Piazza, T. Donner, and H. Ritsch, *Cavity QED with quantum gases: new paradigms in many-body physics*, Adv. Phys. **70**, 1 (2021).

[28] F. Brennecke, R. Mottl, K. Baumann, R. Landig, T. Donner, and T. Esslinger, *Real-time observation of fluctuations at the driven-dissipative Dicke phase transition*, Proc. Natl. Acad. Sci. U.S.A. **110**, 11763 (2013).

[29] S. Lloyd, *Universal quantum simulators*, Science **273**, 1073 (1996).

[30] F. Verstraete, M. M. Wolf, and J. Ignacio Cirac, *Quantum computation and quantum-state engineering driven by dissipation*, Nat. Phys. **5**, 633 (2009).

[31] H. Weimer, M. Müller, I. Lesanovsky, P. Zoller, and H. P. Büchler, *A Rydberg quantum simulator*, Nat. Phys. **6**, 382 (2010).

[32] U. Weiss, *Quantum dissipative systems*, 4th ed., World Scientific, Singapore, 2012.

[33] S. Giorgini, *Damping in dilute Bose gases: A mean-field approach*, Phys. Rev. A **57**, 2949 (1998).

[34] G. Kónya, G. Szirmai, and P. Domokos, *Damping of quasiparticles in a Bose-Einstein condensate coupled to an optical cavity*, Phys. Rev. A **90**, 013623 (2014).

[35] R. Mottl, F. Brennecke, K. Baumann, R. Landig, T. Donner, and T. Esslinger, *Roton-type mode softening in a quantum gas with cavity-mediated long-range interactions*, Science **336**, 1570 (2012).

[36] D. Nagy, G. Szirmai, and P. Domokos, *Critical exponent of a quantum-noise-driven phase transition: The open-system Dicke model*, Phys. Rev. A **84**, 043637 (2011).

[37] P. Kapitza, *Viscosity of liquid helium below the λ-point*, Nature **141**, 74 (1938).

[38] L. Landau, *Theory of the Superfluidity of Helium II*, Phys. Rev. **60**, 356 (1941).

[39] D. S. Petrov, *Liquid beyond the van der Waals paradigm*, Nat. Phys. **14**, 211 (2018).

[40] F. Dalfovo, A. Lastri, L. Pricaupenko, S. Stringari, and J. Treiner, *Structural and dynamical properties of superfluid helium: A density-functional approach*, Phys. Rev. B **52**, 1193 (1995).

[41] L. Pitaevskii and S. Stringari, *Bose-Einstein condensation and superfluidity*, Oxford University Press, 2016.

[42] A. J. Leggett, *Can a solid be "superfluid"?*, Phys. Rev. Lett. **25**, 1543 (1970).

[43] M. H. W. Chan, R. B. Hallock, and L. Reatto, *Overview on solid ^{4}He and the issue of supersolidity*, J. Low Temp. Phys. **172**, 317 (2013).

[44] D. S. Petrov, *Quantum mechanical stabilization of a collapsing Bose-Bose mixture*, Phys. Rev. Lett. **115**, 155302 (2015).

[45] I. Ferrier-Barbut, H. Kadau, M. Schmitt, M. Wenzel, and T. Pfau, *Observation of quantum droplets in a strongly dipolar Bose gas*, Phys. Rev. Lett. **116**, 215301 (2016).

[46] T. D. Lee, K. Huang, and C. N. Yang, *Eigenvalues and eigenfunctions of a Bose system of hard spheres and its low-temperature properties*, Phys. Rev. **106**, 1135 (1957).

[47] R. Schützhold, M. Uhlmann, Y. Xu, and U. R. Fischer, *Mean-field expansion in Bose–Einstein condensates with finite-range interactions*, Int. J. Mod. Phys. B **20**, 3555 (2006).

[48] A. R. P. Lima and A. Pelster, *Quantum fluctuations in dipolar Bose gases*, Phys. Rev. A **84**, 041604 (2011).

[49] A. R. P. Lima and A. Pelster, *Beyond mean-field low-lying excitations of dipolar Bose gases*, Phys. Rev. A **86**, 063609 (2012).

[50] L. Santos, G. V. Shlyapnikov, and M. Lewenstein, *Roton–maxon spectrum and stability of trapped dipolar Bose–Einstein condensates*, Phys. Rev. Lett. **90**, 250403 (2003).

[51] D. H. J. O'Dell, S. Giovanazzi, and G. Kurizki, *Rotons in gaseous Bose-Einstein condensates irradiated by a laser*, Phys. Rev. Lett. **90**, 110402 (2003).

[52] L. Chomaz, R. M. W. van Bijnen, D. Petter, G. Faraoni, S. Baier, J. H. Becher, M. J. Mark, F. Wächtler, L. Santos, and F. Ferlaino, *Observation of roton mode population in a dipolar quantum gas*, Nat. Phys. **14**, 442 (2018).

[53] D. Petter, G. Natale, R. M. W. van Bijnen, A. Patscheider, M. J. Mark, L. Chomaz, and F. Ferlaino, *Probing the roton excitation spectrum of a stable dipolar Bose gas*, Phys. Rev. Lett. **122**, 183401 (2019).

[54] L. Tanzi, E. Lucioni, F. Fama, J. Catani, A. Fioretti, C. Gabbanini, R. N.Bisset, L. Santos, and G. Modugno, *Observation of a dipolar quantum gas with metastable supersolid properties*, Phys. Rev. Lett. **122**, 130405 (2019).

[55] F. Böttcher, J.-N. Schmidt, M. Wenzel, J. Hertkorn, M. Guo, T. Langen, and T. Pfau, *Transient supersolid properties in an array of dipolar quantum droplets*, Phys. Rev. X **9**, 011051 (2019).

[56] L. Chomaz, D. Petter, P. Ilzhöfer, G. Natale, A. Trautmann, C. Politi, G. Durastante, R. M. W. van Bijnen, A. Patscheider, M. Sohmen, M. J. Mark, and F. Ferlaino, *Long-lived and transient supersolid behaviors in dipolar quantum gases*, Phys. Rev. X **9**, 021012 (2019).

[57] N. Bogoliubov, *On the theory of superfluidity*, J. Phys. (USSR) **11**, 23 (1947).

[58] C. R. Cabrera, L. Tanzi, J. Sanz, B. Naylor, P. Thomas, P. Cheiney, and L. Tarruell, *Quantum liquid droplets in a mixture of Bose-Einstein condensates*, Science **359**, 301 (2018).

[59] G. Semeghini, G. Ferioli, L. Masi, C. Mazzinghi, L. Wolswijk, F. Minardi, M. Modugno, G. Modugno, M. Inguscio, and M. Fattori, *Self-bound quantum droplets of atomic mixtures in free space*, Phys. Rev. Lett. **120**, 235301 (2018).

[60] D. S. Petrov and G. E. Astrakharchik, *Ultradilute low-dimensional liquids*, Phys. Rev. Lett. **117**, 100401 (2016).

[61] L. D. Landau and E. M. Lifshitz, *Quantum mechanics: Non-relativistic theory*, 3rd ed., Elsevier Science, 1981.

[62] A. Pelster, *Bose-Einstein-Kondensation*, Lecture notes, 2004.

[63] M. Macêdo-Lima and L. Madeira, *Scattering length and effective range of microscopic two-body potentials*, Rev. Bras. Ensino Fís. **45**, e20230079 (2023).

[64] M. Born, *Quantenmechanik der Stoßvorgänge*, Z. Physik **38**, 803 (1926).

[65] H. Kleinert, *Path integrals in quantum mechanics, statistics, polymer physics, and financial markets*, 5th ed., World Scientific Publishing Company, 2009.

[66] M. Lewenstein, A. Sanpera, and V. Ahufinger, *Ultracold atoms in optical lattices: Simulating quantum many-body systems*, Oxford University Press, 2012.

[67] A. Kamenev, *Field theory of non-equilibrium systems*, Cambridge University Press, 2023.

[68] F. Schwabl, *Statistical mechanics*, 2nd ed., Springer-Verlag Berlin Heidelberg, (2006).

[69] K. Baumann, R. Mottl, F. Brennecke, and T. Esslinger, *Exploring symmetry breaking at the Dicke quantum phase transition*, Phys. Rev. Lett. **107**, 140402 (2011).

[70] J. Léonard, A. Morales, P. Zupancic, T. Esslinger, and T. Donner, *Supersolid formation in a quantum gas breaking a continuous translational symmetry*, Nature **543**, 7643 (2017).

[71] J. Klinder, H. Keßler, M. Wolke, L. Mathey, and A. Hemmerich, *Dynamical phase transition in the open Dicke model*, Proc. Natl. Acad. Sci. U.S.A. **112**, 3290 (2015).

[72] H. Keßler, P. Kongkhambut, C. Georges, L. Mathey, J. G. Cosme, and A. Hemmerich, *Observation of a dissipative time crystal*, Phys. Rev. Lett. **127**, 043602 (2021).

[73] P. Kongkhambut, J. Skulte, L. Mathey, J. G. Cosme, A. Hemmerich, and H. Keßler, *Observation of a continuous time crystal*, Science **377**, 670 (2022).

[74] P. Kongkhambut, J. G. Cosme, J. Skulte, M. A. Moreno-Armijos, L. Mathey, A. Hemmerich, and H. Keßler, *Observation of a phase transition from a continuous to a discrete time crystal*, Rep. Prog. Phys. **87**, 080502 (2024).

[75] X. Li, D. Dreon, P. Zupancic, A. Baumgärtner, A. Morales, W. Zheng, N. R. Cooper, T. Donner, and T. Esslinger, *First order phase transition between two centro-symmetric superradiant crystals*, Phys. Rev. Res. **3**, L012024 (2021).

[76] B. Gábor, D. Nagy, A. Dombi, T. W. Clark, F. I. B. Williams, K. V. Adwaith, A. Vukics, and P. Domokos, *Ground-state bistability of cold atoms in a cavity*, Phys. Rev. A **107**, 023713 (2023).

[77] S. Ostermann, V. Walther, and S. F. Yelin, *Superglass formation in an atomic BEC with competing long-range interactions*, Phys. Rev. Research **4**, 023074 (2022).

[78] M. Bonifacio, F. Piazza, and T. Donner, *Laser-painted cavity-mediated interactions in a quantum gas*, PRX Quantum **5**, 040332 (2024).

[79] Y. Guo, R. M. Kroeze, B. P. Marsh, S. Gopalakrishnan, J. Keeling, and B. L. Lev, *An optical lattice with sound*, Nature **599**, 211 (2021).

[80] X. Zhang, Y. Chen, Z. Wu, J. Wang, J. Fan, S. Deng, and H. Wu, *Observation of a superradiant quantum phase transition in an intracavity degenerate Fermi gas*, Science **373**, 1359 (2021).

[81] A.-S. Walter, Z. Zhu, M. Gächter, J. Minguzzi, S. Roschinski, K. Sandholzer, K. Viebahn, and T. Esslinger, *Quantization and its breakdown in a Hubbard–Thouless pump*, Nat. Phys. **19**, 1471 (2023).

[82] Z. Zhu, M. Gächter, A.-S. Walter, K. Viebahn, and T. Esslinger, *Reversal of quantized Hall drifts at noninteracting and interacting topological boundaries*, Science **384**, 317 (2024).

[83] D. F. Walls and G. J. Milburn, *Quantum optics*, Springer, Berlin, Heidelberg, 2008.

[84] Ph. W. Courteille, *Quantum mechanics applied to atoms and light*, Courses on Physics (lecture notes), 30.10.2024.

[85] M. Motsch, M. Zeppenfeld, P. W. H. Pinkse, and G. Rempe, *Cavity-enhanced Rayleigh scattering*, New J. Phys. **12**, 063022 (2010).

[86] H. Tanji-Suzuki, I. D. Leroux, M. H. Schleier-Smith, M. Cetina, A. T. Grier, J. Simon, and V. Vuletic, *Interaction between atomic ensembles and optical resonators: Classical description*, arXiv:1104.3594 (2011).

[87] E. T. Jaynes and F. W. Cummings, *Comparison of quantum and semiclassical radiation theories with application to the beam maser*, Proc. IEEE **51**, 89 (1963).

[88] C. Maschler, I. B. Mekhov, and H. Ritsch, *Ultracold atoms in optical lattices generated by quantized light fields*, Eur. Phys. J. D **46**, 545 (2008).

[89] J. Klinner, *Experiments with ultra-cold atomic ensembles in optical resonators with ultra-high finesse and narrow linewidth*, Verlag Dr. Hut (2009).

[90] M. Wolke, *Laserkühlung in optischen Resonatoren unter der Rückstoßgrenze*, Verlag Dr. Hut (2012).

[91] H. Keßler, *Resonator-kontrollierte Materiewellen-Superradianz*, Verlag Dr. Hut (2016).

[92] J. S. Klinder, *Vom dynamischen Phasenübergang im offenen Dicke Modell zum Dicke-Hubbard Modell*, Verlag Dr. Hut (2016).

[93] P. Kongkhambut, *Realizing dissipative time crystals in an atom-cavity system*, Dissertation (2024).

[94] A. Aspect, E. Arimondo, R. Kaiser, N. Vansteenkiste, and C. Cohen-Tannoudji, *Laser cooling below the one-photon recoil energy by velocity-selective coherent population trapping*, Phys. Rev. Lett. **61**, 826 (1988).

[95] J. Dalibard and C. Cohen-Tannoudji, *Laser cooling below the Doppler limit by polarization gradients: Simple theoretical models*, J. Opt. Soc. Am. B **6**, 2023 (1989).

[96] H. J. Metcalf and P. Van Der Straten, *Laser cooling and trapping*, Springer, New York, NY, 1999.

[97] T. Esslinger, I. Bloch, and T. W. Hänsch, *Bose-Einstein condensation in a quadrupole-Ioffe-configuration trap*, Phys. Rev. A **58**, R2664 (1998).

[98] J. Klinner, M. Wolke, and A. Hemmerich, *Increased efficiency of rf-induced evaporative cooling by utilizing gravity*, Phys. Rev. A **81**, 043414 (2010).

[99] H. Keßler, J. Klinder, M. Wolke, and A. Hemmerich, *Optomechanical atom-cavity interaction in the sub-recoil regime*, New J. Phys. **16**, 053008 (2014).

[100] D. Nagy, G. Szirmai, and P. Domokos, *Self-organization of a Bose-Einstein condensate in an optical cavity*, Eur. Phys. J. D **48**, 127 (2008).

[101] P. Domokos and H. Ritsch, *Collective cooling and self-organization of atoms in a cavity*, Phys. Rev. Lett. **89**, 253003 (2002).

[102] I. B. Mekhov, C. Maschler, and H. Ritsch, *Cavity-enhanced light scattering in optical lattices to probe atomic quantum statistics*, Phys. Rev. Lett. **98**, 100402 (2007).

[103] I. B. Mekhov, C. Maschler, and H. Ritsch, *Light scattering from ultracold atoms in optical lattices as an optical probe of quantum statistics*, Phys. Rev. A **76**, 053618 (2007).

[104] I. B. Mekhov, C. Maschler, and H. Ritsch, *Probing quantum phases of ultracold atoms in optical lattices by transmission spectra in cavity quantum electrodynamics*, Nat. Phys. **3**, 319 (2007).

[105] D. Nagy, G. Kónya, G. Szirmai, and P. Domokos, *Dicke-model phase transition in the quantum motion of a Bose-Einstein condensate in an optical cavity*, Phys. Rev. Lett. **104**, 130401 (2010).

[106] C. Emary and T. Brandes, *Quantum chaos triggered by precursors of a quantum phase transition: the Dicke model*, Phys. Rev. Lett. **90**, 044101 (2003).

[107] F. Piazza, P. Strack, and W. Zwerger, *Bose–Einstein condensation versus Dicke–Hepp–Lieb transition in an optical cavity*, Ann. Phys. (N. Y.) **339**, 135 (2013).

[108] C. Maschler and H. Ritsch, *Cold atom dynamics in a quantum optical lattice potential*, Phys. Rev. Lett. **95**, 260401 (2005).

[109] S. B. Jäger, T. Schmit, G. Morigi, M. J. Holland, and R. Betzholz, *Lindblad master equations for quantum systems coupled to dissipative bosonic modes*, Phys. Rev. Lett. **129**, 063601 (2022).

[110] N. Defenu, T. Donner, T. Macrì, G. Pagano, S. Ruffo, and A. Trombettoni, *Long-range interacting quantum systems*, Rev. Mod. Phys. **95**, 035002 (2023).

[111] M. R. Bakhtiari, A. Hemmerich, H. Ritsch, and M. Thorwart, *Nonequilibrium phase transition of interacting bosons in an intra-cavity optical lattice*, Phys. Rev. Lett. **114**, 123601 (2015).

[112] T. Wu, S. Ray, and J. Kroha, *Temporal bistability in the dissipative Dicke-Bose-Hubbard system*, Ann. Phys. (Berl.) **536**, 2300505 (2024).

[113] N. Mann, A. Pelster, and M. Thorwart, *Tuning the order of the nonequilibrium quantum phase transition in a hybrid atom-optomechanical system*, New J. Phys. **21**, 113037 (2019).

[114] N. Mann and M. Thorwart, *Enhancing nanomechanical squeezing by atomic interactions in a hybrid atom-optomechanical system*, Phys. Rev. A **98**, 063804 (2018).

[115] N. Mann, *Nonequilibrium fluctuations and phase transitions in hybrid quantum systems*, Dissertation, 2019.

[116] W. V. Liu, *Theoretical study of the damping of collective excitations in a Bose-Einstein condensate*, Phys. Rev. Lett. **79**, 4056 (1997).

[117] L. P. Pitaevskii and S. Stringari, *Landau damping in dilute Bose gases*, Phys. Lett. A **235**, 398 (1997).

[118] M. Guilleumas and L. P. Pitaevskii, *Temperature-induced resonances and Landau damping of collective modes in Bose-Einstein condensed gases in spherical traps*, Phys. Rev. A **61**, 013602 (1999).

[119] B. Jackson and E. Zaremba, *Accidental suppression of Landau damping of the transverse breathing mode in elongated Bose-Einstein condensates*, Phys. Rev. Lett. **89**, 150402 (2002).

[120] M. Guilleumas and L. P. Pitaevskii, *Landau damping of transverse quadrupole oscillations of an elongated Bose-Einstein condensate*, Phys. Rev. A **67**, 053607 (2003).

[121] B. Jackson and E. Zaremba, *Landau damping in trapped Bose condensed gases*, New J. Phys. **5**, 88 (2003).

[122] S. Tsuchiya and A. Griffin, *Landau damping of Bogoliubov excitations in two- and three-dimensional optical lattices at finite temperatures*, Phys. Rev. A **72**, 053621 (2005).

[123] S. T. Beliaev, *Energy-spectrum of a non-ideal Bose gas*, Sov. Phys. JETP **34**, 323 (1958).

[124] E. Hodby, O. M. Maragò, G. Hechenblaikner, and C. J. Foot, *Experimental observation of Beliaev coupling in a Bose-Einstein condensate*, Phys. Rev. Lett. **86**, 2196 (2001).

[125] Yu. Kagan and L. A. Maksimov, *Damping of trapped Bose-Einstein condensate oscillations at zero temperature*, Phys. Rev. A **64**, 053610 (2001).

[126] N. Katz, J. Steinhauer, R. Ozeri, and N. Davidson, *Beliaev damping of quasiparticles in a Bose-Einstein condensate*, Phys. Rev. Lett. **89**, 220401 (2002).

[127] G. Kónya, G. Szirmai, D. Nagy, and P. Domokos, *Photonic tuning of Beliaev damping in a superfluid*, Phys. Rev. A **89**, 051601 (2014).

[128] G. Kónya, D. Nagy, G. Szirmai, and P. Domokos, *Nonequilibrium polariton dynamics in a Bose-Einstein condensate coupled to an optical cavity*, Phys. Rev. A **98**, 063608 (2018).

[129] X. You, A. A. Clerk, and J. Koch, *Positive- and negative-frequency noise from an ensemble of two-level fluctuators*, Phys. Rev. Res. **3**, 013045 (2021).

[130] P. M. Mutter and G. Burkard, *Fingerprints of qubit noise in transient cavity transmission*, Phys. Rev. Lett. **128**, 236801 (2022).

[131] S. Gröblacher, A. Trubarov, N. Prigge, G. D. Cole, M. Aspelmeyer, and J. Eisert, *Observation of non-Markovian micromechanical Brownian motion*, Nat. Commun. **6**, 1 (2015).

[132] D. Rosenberg, P. Nalbach, and D. D. Osheroff, *Memory effects in amorphous solids below 20 mK*, Phys. Rev. Lett. **90**, 195501 (2003).

[133] N.-H. Tong and M. Vojta, *Signatures of a noise-induced quantum phase transition in a mesoscopic metal ring*, Phys. Rev. Lett. **97**, 016802 (2006).

[134] Q. Si, S. Rabello, K. Ingersent, and J. L. Smith, *Locally critical quantum phase transitions in strongly correlated metals*, Nature **413**, 6858 (2001).

[135] P. Gegenwart, T. Westerkamp, C. Krellner, Y. Tokiwa, S. Paschen, C. Geibel, F. Steglich, E. Abrahams, and Q. Si, *Multiple energy scales at a quantum critical point*, Science **315**, 969 (2007).

[136] H.-G. Duan, P. Nalbach, R. J. D. Miller, and M. Thorwart, *Intramolecular vibrations enhance the quantum efficiency of excitonic energy transfer*, Photosynth. Res. **144**, 137 (2020).

[137] A. Jha, P.-P. Zhang, V. Tiwari, L. Chen, M. Thorwart, R. J. D. Miller, and H.-G. Duan, *Unraveling quantum coherences mediating primary charge transfer processes in photosystem II reaction center*, Sci. Adv. **10**, eadk1312 (2024).

[138] F. Otterpohl, D. Keefer, S. Mukamel, and M. Thorwart, *Coherent ultrafast stimulated x-ray Raman spectroscopy of dissipative conical intersections*, Phys. Rev. Lett. **133**, 098001 (2024).

[139] H. Kirchberg, M. Thorwart, and A. Nitzan, *Charge transfer through redox molecular junctions in nonequilibrated solvents*, J. Phys. Chem. Lett. **11**, 1729 (2020).

[140] H. Kirchberg and M. Thorwart, *Time-resolved probing of the nonequilibrium structural solvation dynamics by the time-dependent Stokes shift*, J. Phys. Chem. B **124**, 5717 (2020).

[141] G. Gurski, H. Kirchberg, P. Nalbach, and M. Thorwart, *Single-molecule junctions sensitive to binary solvent mixtures*, Phys. Rev. B **106**, 075413 (2022).

[142] G. Gurski, H. Kirchberg, P. Nalbach, and M. Thorwart, *Hydration shell effects in ac-driven single-molecule junctions*, Phys. Rev. B **107**, 165413 (2023).

[143] N. Breckwoldt, T. Posske, and M. Thorwart, *Bath-induced decoherence in finite-size Majorana wires at non-zero temperature*, New J. Phys. **24**, 013033 (2022).

[144] M. Thorwart, *Quantum statistics with path integrals*, Lecture notes, 2023.

[145] G.-L. Ingold, *Path integrals and their application to dissipative quantum systems, in: Coherent evolution in noisy environments*, Springer, Berlin, Heidelberg, 2002, pp. 1–53.

[146] A. J. Leggett, S. Chakravarty, A. T. Dorsey, M. P. A. Fisher, A. Garg, and W. Zwerger, *Dynamics of the dissipative two-state system*, Rev. Mod. Phys. **59**, 1 (1987).

[147] F. Otterpohl, P. Nalbach, and M. Thorwart, *Hidden phase of the spin-boson model*, Phys. Rev. Lett. **129**, 120406 (2022).

[148] A. Chin and M. Turlakov, *Coherent-incoherent transition in the sub-Ohmic spin-boson model*, Phys. Rev. B **73**, 075311 (2006).

[149] P. Nalbach and M. Thorwart, *Ultraslow quantum dynamics in a sub-Ohmic heat bath*, Phys. Rev. B **81**, 054308 (2010).

[150] D. Kast and J. Ankerhold, *Persistence of coherent quantum dynamics at strong dissipation*, Phys. Rev. Lett. **110**, 010402 (2013).

[151] C. Duan, Z. Tang, J. Cao, and J. Wu, *Zero-temperature localization in a sub-Ohmic spin-boson model investigated by an extended hierarchy equation of motion*, Phys. Rev. B **95**, 214308 (2017).

[152] D. Nagy and P. Domokos, *Nonequilibrium quantum criticality and non-Markovian environment: Critical exponent of a quantum phase transition*, Phys. Rev. Lett. **115**, 043601 (2015).

[153] D. Nagy and P. Domokos, *Critical exponent of quantum phase transitions driven by colored noise*, Phys. Rev. A **94**, 063862 (2016).

[154] J. Schwinger, *Brownian motion of a quantum oscillator*, J. Math. Phys. **2**, 407 (1961).

[155] L. V. Keldysh, *Diagram technique for nonequilibrium processes*, Sov. Phys. JETP **20**, 1018 (1965).

[156] E. G. D. Torre, S. Diehl, M. D. Lukin, S. Sachdev, and P. Strack, *Keldysh approach for nonequilibrium phase transitions in quantum optics: Beyond the Dicke model in optical cavities*, Phys. Rev. A **87**, 023831 (2013).

[157] L. M. Sieberer, M. Buchhold, and S. Diehl, *Keldysh field theory for driven open quantum systems*, Rep. Prog. Phys. **79**, 096001 (2016).

[158] F. Napoli, M. Sassetti, and U. Weiss, *Two-phonon processes in the two-state dynamics*, Phys. B: Condens. Matter **202**, 80 (1994).

[159] J. Klinder, H. Keßler, Ch. Georges, J. Vargas, and A. Hemmerich, *Bose-Einstein condensates in an optical cavity with sub-recoil bandwidth*, Appl. Phys. B **122**, 1 (2016).

[160] I. Dorofeyev, *Dynamics and stationarity of two coupled arbitrary oscillators interacting with separate reservoirs*, J. Stat. Phys. **162**, 218 (2016).

[161] A. Garg, J. N. Onuchic, and V. Ambegaokar, *Effect of friction on electron transfer in biomolecules*, J. Chem. Phys. **83**, 4491 (1985).

[162] H. Grabert, P. Schramm, and G.-L. Ingold, *Localization and anomalous diffusion of a damped quantum particle*, Phys. Rev. Lett. **58**, 1285 (1987).

[163] S. Stringari, and J. Treiner, *Systematics of liquid helium clusters*, J. Chem. Phys. **87**, 5021 (1987).

[164] J. Dupont-Roc, M. Himbert, N. Pavloff, and J. Treiner, *Inhomogeneous liquid* ^{4}*He: A density functional approach with a finite-range interaction*, J. Low Temp. Phys. **81**, 31 (1990).

[165] M. Casas, F. Dalfovo, A. Lastri, Ll. Serra, and S. Stringari, *Density functional calculations for* ^{4}*He droplets*, Z. Phys. D **35**, 67 (1995).

[166] M. Schmitt, M. Wenzel, F. Böttcher, I. Ferrier-Barbut, and T. Pfau, *Self-bound droplets of a dilute magnetic quantum liquid*, Nature **539**, 259 (2016).

[167] F. Böttcher, J.-N. Schmidt, J. Hertkorn, K. S. H. Ng, S. D. Graham, M. Guo, T. Langen, and T. Pfau, *New states of matter with fine-tuned interactions: quantum droplets and dipolar supersolids*, Rep. Prog. Phys. **84**, 012403 (2021).

[168] L. Chomaz, I. Ferrier-Barbut, F. Ferlaino, B. Laburthe-Tolra, B. L. Lev, and T. Pfau, *Dipolar physics: A review of experiments with magnetic quantum gases*, Rep. Prog. Phys. **86**, 026401 (2022).

[169] D. M. Larsen, *Binary mixtures of dilute bose gases with repulsive interactions at low temperature*, Ann. Phys. (N. Y.) **24**, 89 (1963).

[170] Q. Gu and L. Yin, *Phonon stability and sound velocity of quantum droplets in a boson mixture*, Phys. Rev. B **102**, 220503 (2020).

[171] Y. Xiong and L. Yin, *Effective single-mode model of a binary boson mixture in the quantum droplet region*, Phys. Rev. A 105, 053305 (2022).

[172] H. Hu, J. Wang, and X.-J. Liu, *Microscopic pairing theory of a binary Bose mixture with interspecies attractions: Bosonic BEC-BCS crossover and ultradilute low-dimensional quantum droplets*, Phys. Rev. A **102**, 043301 (2020).

[173] H. Hu and X.-J. Liu, *Consistent theory of self-bound quantum droplets with bosonic pairing*, Phys. Rev. Lett. **125**, 195302 (2020).

[174] T. G. Skov, M. G. Skou, N. B. Jørgensen, and J. J. Arlt, *Observation of a Lee-Huang-Yang fluid*, Phys. Rev. Lett. **126**, 230404 (2021).

[175] F. Wächtler, and L. Santos, *Quantum filaments in dipolar Bose-Einstein condensates*, Phys. Rev. A **93**, 061603(R) (2016).

[176] T. Donner, *Dipolar quantum gases go supersolid*, Physics **12**, 38 (2019).

[177] A. Pelster, *Supersolide dipolare Quantengase*, Physik Journal **18** (6), 20 (2019).

[178] D. Y. Kim and M. H. W. Chan, *Absence of supersolidity in solid helium in porous vycor glass*, Phys. Rev. Lett. **109**, 155301 (2012).

[179] J. Sánchez-Baena, C. Politi, F. Maucher, F. Ferlaino, and T. Pohl, *Heating a dipolar quantum fluid into a solid*, Nat. Commun. **14**, 1868 (2023).

[180] P. Karpov and F. Piazza, *Crystalline droplets with emergent color charge in many-body systems with sign-changing interactions*, Phys. Rev. A **100**, 061401 (2019).

[181] P. Karpov and F. Piazza, *Light-induced quantum droplet phases of lattice bosons in multimode cavities*, Phys. Rev. Lett. **128**, 103201 (2022).

[182] N. Masalaeva, H. Ritsch, and F. Mivehvar, *Tuning photon-mediated interactions in a multimode cavity: From supersolid to insulating droplets hosting phononic excitations*, Phys. Rev. Lett. **131**, 173401 (2023).

[183] P. Tommasini, E. J. V. de Passos, A. F. R. de Toledo Piza, M. S. Hussein, and E. Timmermans, *Bogoliubov theory for mutually coherent condensates*, Phys. Rev. A **67**, 023606 (2003).

[184] A. E. Leanhardt, T. A. Pasquini, M. Saba, A. Schirotzek, Y. Shin, D. Kielpinski, D. E. Pritchard, and W. Ketterle, *Cooling Bose-Einstein condensates below 500 picokelvin*, Science **301**, 1513 (2003).

[185] C. Deppner et al., *Collective-mode enhanced matter-wave optics*, Phys. Rev. Lett. **127**, 100401 (2021).

[186] N. Gaaloul et al., *A space-based quantum gas laboratory at picokelvin energy scales*, Nat. Commun. **13**, 7889 (2022).

[187] A. J. Kollár, A. T. Papageorge, K. Baumann, M. Armen, and B. L. Lev, *An adjustable-length cavity and Bose–Einstein condensate apparatus for multimode cavity QED*, New J. Phys. **17**, 043012 (2015).

[188] A. J. Kollár, A. T. Papageorge, V. D. Vaidya, Y. Guo, J. Keeling, and B. L. Lev, *Supermode-density-wave-polariton condensation with a Bose–Einstein condensate in a multimode cavity*, Nat. Commun. **8**, 14386 (2017).

[189] V. D. Vaidya, Y. Guo, R. M. Kroeze, K. E. Ballantine, A. J. Kollár, J. Keeling, and B. L. Lev, *Tunable-range, photon-mediated atomic interactions in multimode cavity QED*, Phys. Rev. X **8**, 011002 (2018).

[190] Y. Guo, R. M. Kroeze, V. D. Vaidya, J. Keeling, and B. L. Lev, *Sign-changing photon-mediated atom interactions in multimode cavity quantum electrodynamics*, Phys. Rev. Lett. **122**, 193601 (2019).

[191] W. Nolting, *Theoretical physics 8*, Springer International Publishing, 2018.

[192] A. Bolian, P. Kongkhambut, C. Georges, Roy D. Jara Jr., J. Vargas, J. Klinder, J. G. Cosme, H. Keßler, and A. Hemmerich, *Observation of a zero-energy excitation mode in the open Dicke model*, arXiv:2502.12155 (2025).

[193] N. Masalaeva and F. Mivehvar, *Rotational superradiance in a time-reversal symmetry-broken quantum gas inside an optical cavity*, arXiv:2404.10131 (2024).

Acknowledgements

Throughout this stage of my life, which now culminates in this thesis, I have been fortunate that many people had a positive influence on me, both professionally and privately, and I want to express my gratitude to all of you.

Special thanks go to Prof. Michael Thorwart. As my supervisor, he allowed me as much freedom as I could bear, yet anytime I required support, he provided knowledge and motivation. I never left a conversation with him feeling less than positive, and he always greatly encouraged me to forge my individual path. This provided me with an environment where I could devise new theories and approaches. In his way, he fostered the great development in me during the years of my PhD, especially as a student of physics, but also as a person.

I would like to thank Prof. Andreas Hemmerich and Dr. Hans Keßler. Through the intriguing exchange I enjoyed with them, their influence on me was a source of inspiration and yielded a great enhancement of my work. I want to highlight the effort of Hans Keßler to always explain the experimental setup and provide helpful answers to any of my questions.

In the latter part of my PhD, I was fortunate to work together with Prof. Axel Pelster and Dr. Milan Radonjić. With them, I had numerous discussions where any question could lead to hours of conversation about physics. That is to say, I learned a lot, not just physics, but also that proposing any cute idea comes with the responsibility of meticulously scrutinizing it. I want to express my gratitude towards them and my wish to enjoy many more such conversations. Furthermore, I want to thank Axel Pelster that from the moment I got to know him, I could rely on his guidance and support.

Immense thanks go to my parents for always encouraging and supporting me in all my interests and my decisions, even if it was to get a PhD in physics.

Eidesstattliche Versicherung

Hiermit versichere ich an Eides statt, die vorliegende Dissertationsschrift selbst verfasst und keine anderen als die angegebenen Hilfsmittel und Quellen benutzt zu haben.

Sofern im Zuge der Erstellung der vorliegenden Dissertationsschrift generative Künstliche Intelligenz (gKI) basierte elektronische Hilfsmittel verwendet wurden, versichere ich, dass meine eigene Leistung im Vordergrund stand und dass eine vollständige Dokumentation aller verwendeten Hilfsmittel gemäß der Guten wissenschaftlichen Praxis vorliegt. Ich trage die Verantwortung für eventuell durch die gKI generierte fehlerhafte oder verzerrte Inhalte, fehlerhafte Referenzen, Verstöße gegen das Datenschutz- und Urheberrecht oder Plagiate.

Hamburg, den 30.09.2025 Unterschrift: